The University of Nottingham

Hybrid Metal-Carbon Nanostructures for Energy-Related Applications

Carlos Herreros Lucas

Thesis submitted to the University of Nottingham for the degree of Doctor of Philosophy

June 2017

It’s the little details that are vital.
Little things make big things happen.

John Wooden

Abstract

Recent technological advances such as the transition from non-renewable to renewable energy have been intimately related to the development of new nanostructured materials. A rational thinking is required for the development of nanomaterials with functional properties by targeting the combination of two or more nanocomponents with different properties, and preparation methodologies ensuring the utilisation of cheaper and abundant materials such as non-precious metals. Therefore, the main motivation of this work is to expand the frontiers of knowledge for the preparation of functional nanomaterials by designing hybrid carbon nanostructures suitable for energy storage applications containing a range of electrochemically active nanocomponents including molecules, nanoparticles and metal coordination polymers.

The first chapter describes a general overview of the current approaches within the energy area to prepare uncoupled carbon nanostructures as well as the strategies to combine them with several active components (i.e. molecular metal clusters, nanoparticles and metal coordination polymers). Relevant concepts for this thesis such as electrochemical storage mechanisms, differences between hybrid and composite nanomaterials, synergetic effects and the distinction between ex situ and in situ synthetic approaches are discussed in the introductory chapter. For the sake of clarity, only the most relevant examples of hybrid carbon nanostructures from the literature will be highlighted and discussed. Before describing the hybridisation of carbon with molecules, nanoparticles and metal-coordination polymers, different carbon nanostructures will be analysed on their own due to their outstanding electrochemical properties.

After the introductory chapter (Chapter 1), the thesis is followed by two parts: Part A and B. Part A, which is divided in two chapters (Chapter 2 and 3), gathers only carbon nanostructure investigations. In Chapter 2, a facile and solvent-free method is proposed for the development of few-layer graphene nanostructure from carbon tubular nanofibers. In Chapter 3, the synthesis of hollow carbon cages on the surface of carbon nanostructures is thoroughly investigated to elucidate their novel mechanism of formation.

The preparation and electrochemical characterization of metal-carbon nanostructures by combining carbon nanostructure with a molecular metal cluster, metal oxide nanoparticles and metal coordination polymers are discussed in Part B. In Chapter 4 the extreme confinement inside hollow tubular carbon nanotubes is investigated to overcome the intrinsic low stability of molecular Mn_{12} cluster during the electrochemical process. In Chapter 5, the synthesis of metal oxide nanoparticles is carried out in the presence of hollow tubular carbon nanofibers (what we called "in situ synthesis") where special attention is paid to the carbon surface functionalization. Only the metal oxide-carbon hybrids of interest produced in previous chapter are extensively characterized by electrochemical means to elucidate the effect of confinement with respect to their electrochemical stability. In Chapter 6, a correlation between the structure and chemical composition of a coordinated metal polymer and its electrochemical performance is established in order to gain a better understanding of the alkali intercalation/deintercalation process.

One of the key findings in this thesis has been the encapsulation of electrochemically active species, shows promising results not only due to the electron transfer between the guest specie and the host carbon nanostructure, but also to the improvement in the stability during electrochemical cycling. In addition, it has been observed that the electrochemical performance of metal-carbon nanohybrids depends dramatically on the synthetic process that determines the interaction between the nanocomponents and, therefore, the synergetic effect.

To sum up, the work developed in this thesis contributes to the area of hybrid metal-carbon nanostructures for energy-storage applications, including new synthetic protocols and strategies, novel hybrid materials with confined electrochemical components, advanced understanding on the electrochemical-structure relationships and important concepts related to durability/recyclability.

Acknowledgements

I would like to express my gratitude to Dr. Maria del Carmen Giménez López and Prof. Andrei N. Khlobystov for their continued support during my PhD study. Their help, patience, criticism and immense knowledge are greatly appreciated.

I would like to thank Dr. Michael Fay for performing all the TEM experiments during my thesis.

I would like to thank the technical staff in advanced Materials Group. Special thanks to Dr Nigel Neate and Dr. Martin Roe for training me to use scanning electron microscope.

I would like to thank Ms. Emily Smith for her assistance in using XPS characterization technique.

I would like to thank Dr. Andrew Osborne for his help in using Nova Software.

I would like to thank the Nottingham Nanocarbon group members for their continuous support over the years.

I would like to thanks all MSci project students working with me, specially, Robert J. E. Westbrook and Alana Murphy. I would like to thank also all the technical staff, in particular Mark Guyler.

Finally, I would like to thank my girlfriend Yolanda and my family for their constant love and support, specially, throughout writing this thesis.

Table of contents

Part B2: Functional networks with carbon nanostructures

Chapter 1

Development of hybrid metal carbon nanostructures for energy storage: Challenges and strategies

1.1 Energy storage and their mechanisms

Energy storage refers to devices that collect energy to be used at a later time. Batteries are the most popular and store energy as chemical and deliver as electrical, playing a dual role. Volta first demonstrated that electric current could be produced by stacking several pairs of alternating copper (positive electrode-cathode: reduction takes place) and zinc (negative electrode-anode: oxidation takes place) separated by cloth soaked in brine (Figure 1a). Despite the two centuries since Volta's discovery and the evolution to the current lithium battery (Figure 1b), there is still room for new and novel types of materials which can overcome the current limitations of battery technology (i.e. ion diffusion within the solid) to achieve the performance demanded by industry (high specific energy and power density) (Figure 1c).

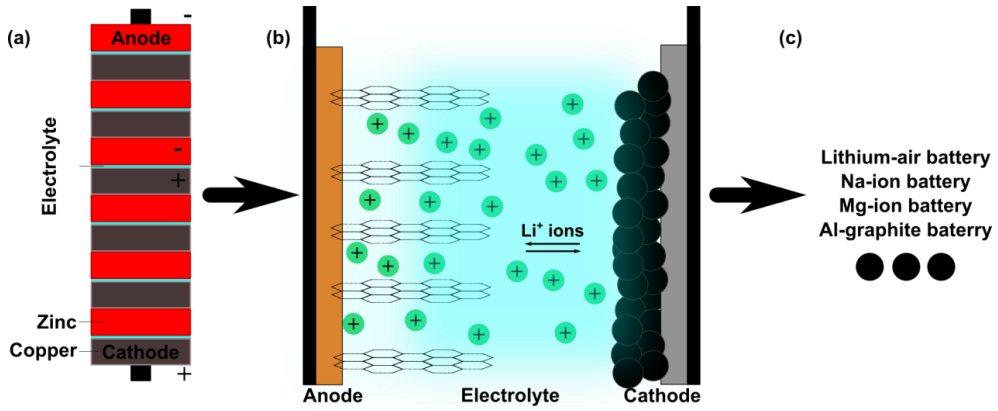

Figure 1. Schematic representation of (a) initial voltaic pile, (b) current lithium ion battery and (c) proposed future batteries, which are expected to have much better electrochemical performance and cyclability, safer and made of green and low-cost materials.[1]

In contrast to batteries, capacitors lead to high currents and high specific power so electrochemical processes occur at the surface, being not limited by solid-state diffusion. However, they show poor specific energy. Once chemical knowledge was applied to capacitors, turning them into supercapacitors (or ultracapacitors), their specific energy increased more than conventional capacitors and approaching the batteries values. This is a result of a new process called pseudocapacitance, which arises when reversible redox reactions (Faradaic) occur at or near the surface of a material in contact with an electrolyte. It is important to mention that this mechanism is completely different to the electrochemical double-layer (EDL) observed in traditional

capacitors where ions are adsorbed on the surface of the electrode due to electrostatic interactions (Figure 2a).

Conway identified several Faradaic mechanisms that can result in capacitive electrochemical features:[2] (b) underpotential deposition, (c) redox pseudocapacitance and (d) intercalation pseudocapacitance. Underpotential deposition (Figure 2b) takes place when metal ions are adsorbed at a different electrode surfaces well above their redox potential.[3-4] On the other hand, redox pseudocapacitance (Figure 2c) occurs when ions are electrochemically adsorbed onto the surface with a Faradaic charge-transfer (oxygen groups in carbon, metals…),[5-6] while intercalation pseudocapacitance (Figure 2d) arises when ions intercalate into channels or layers of a redox-active material accompanied by a faradaic charge-transfer with no crystallographic phase change.[7-9]

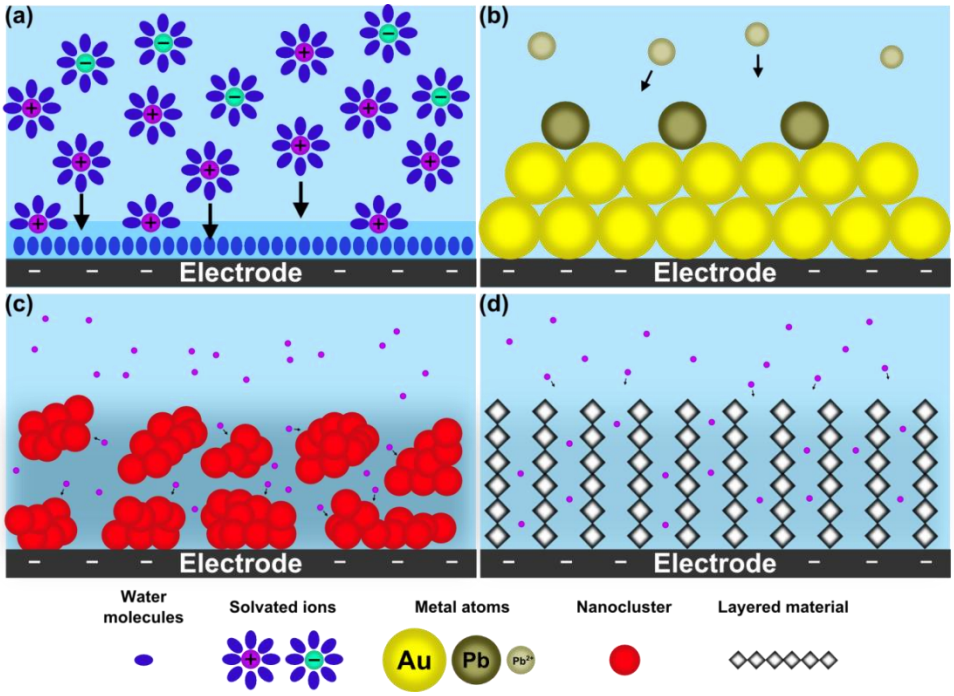

Figure 2. Schematic representation of energy storage mechanisms: (a) electrical double layer (EDL) in a liquid at contact with a negatively-charge solid, (b) underportential deposition (i.e. Pb on gold surface: $Au + nPb^{2+} + 2ne^- \rightarrow Au{\cdot}nPb_{ads}$), (c) redox pseudocapacitance (i.e. ruthenium nanoparticles: $RuO_x(OH)_y + nH^+ + ne^- \leftrightarrow RuO_{x-n}(OH)_{y+n}$) and (d) intercalation pseudocapacitance (i.e. lithium intercalation: $Nb_2O_5 + nLi^+ + ne^- \leftrightarrow Li_nNB_2O_5$).

Therefore, chemistry along with engineering has still a lot to contribute to the development of new energy devices.

1.2 Current challenges

Nowadays, one of the main challenges in our society is to fill the energetic gap between supply and demand. This challenge has become very important due to not only the huge increase in population (from 1.6 billion on 1900 to 7.43 billion on 2016)[10] but also the energy consumption (from ~50 exajoules (EJ, 10^{18}J) on 1900 to higher than 550 EJ on 2016).[11] Additionally, it is important to cope with the future energetic demand while changing towards renewable sources, such as biomass, solar, wind or hydropower, in order to achieve the desired reduction of CO_2 emissions and dangerous waste.

Despite to the fact that, little by little, more and more houses are getting powered from electrical energy from renewable sources, the dependence of these technologies on the climatic conditions is currently one of the main drawbacks. One approach to overcome such limitation is by combining energy storage and conversion devices. For example, a battery is charged by a solar panel while the sun shines and discharged during the night. However, the large-scale storage limitation, these approaches cannot be transfer to industry due to the challenging demanded performance.

The lack of environmentally friendly materials at lower price and requirement for high stability and safety are hindering a wide commercial distribution of nanomaterials. Nowadays, the extensive use of electrochemical technology for many mobile applications such as electric vehicles (EV)[12] is restricted by the expensive Pt, being the best-known catalyst for the electrolysis of water.[13] Rechargeable batteries lose voltage and capacity each charging cycle, leading to their replacement after several cycles. For example, lithium iron phosphate batteries reach, according to the manufacturer, more than 5000 cycles with a 70% loss of the total capacity.[14] Furthermore, lithium cobalt oxide, which offers high energy density as a cathode in lithium batteries, presents safety risks. Therefore, the discovery of new electrochemical storage mechanisms as well as the development of novel materials with outstanding electrochemical storage properties for a high number of cycles is urgently required in order to cope with the future technological advances of our society.

1.3 Carbon nanostructures and their energy storage properties

Among all the nanocomponents, carbon nanostructures (i. e. fullerenes, carbon nano-onions, carbon nanotubes, carbon nanohorns or graphene) have received a lot of interest due to the outstanding properties for a wide range of applications. In fact, carbons have been frequently used for more than 100 years as an electrode due to their ability to withstand very high temperature, good mechanical properties, high current carrying capacity and fast electron transfer.[15]

The synthesis of carbon nanotubes, which are made of layers of graphene (Figure 3a) parallel to the growth axis forming a set of concentric cylinders, has been greatly improved since their first discovery by S. Iijima in 1991.[16] Nowadays, it is possible to synthesise hollow tubular carbon nanostructures in large quantities with a selective control over their length, thickness, diameter, internal structure as well as orientating their assembly.[17-19] As a consequence, a wide library of hollow tubular nanostructures is fully available varying from narrow single-wall nanotubes (~1 nm) and multi-walled nanotubes (~10nm, Figure 3b) to wide carbon nanofibers (~100 nm, Figure 3c). In this context, it is important to highlight that carbon nanofibers (CNF) have been shown to play an important role for the stabilization of nanoparticles, specifically, at high temperatures[20] and during many electrochemical cycles[21] as a consequence of their corrugated internal surface (Figure 3c, right-hand-side), which is dictated by the presence of internal graphitic structure formed by stacked-nanocones. Thus, the step-edges have been demonstrated as a physical anchoring point that stabilises nanoparticle, facilitating also the arrangement of nanoparticles inside CNF.[22]

The synthesis of highly pure graphitized nanostructures is based on a bottom-up approach (i. e. chemical vapour deposition), where a carbon containing molecule is adsorbed on the surface of a catalyst and reacted under harsh conditions, and it is extended to other carbon nanostructures such as carbon nano-onions (Figure 3d) or graphene (Figure 3a) by simply controlling the synthetic parameters (i. e. catalyst, carbon source or temperature). For example, spherical carbon nano-onions, with a typical size in the range of 1-

100 nm,[23] can be synthesized using a bottom-up approach both by a hard or soft templating strategy, having a control over the size, porosity or interior (hollow or metallic). The hard templating strategy is based on the formation of the graphitic carbon shell under harsh conditions (i. e. chemical vapour deposition) on the surface of a spherical template or catalyst (i. e. silica or metal nanoparticles), which could subsequently be removed via acid treatment.[24] Alternatively, soft templating strategy does not require a catalyst so a sacrificial template, such as nano-diamond, is thermally annealed at high temperatures (i. e. 1700^{o}C) under inert atmosphere.[25-26]

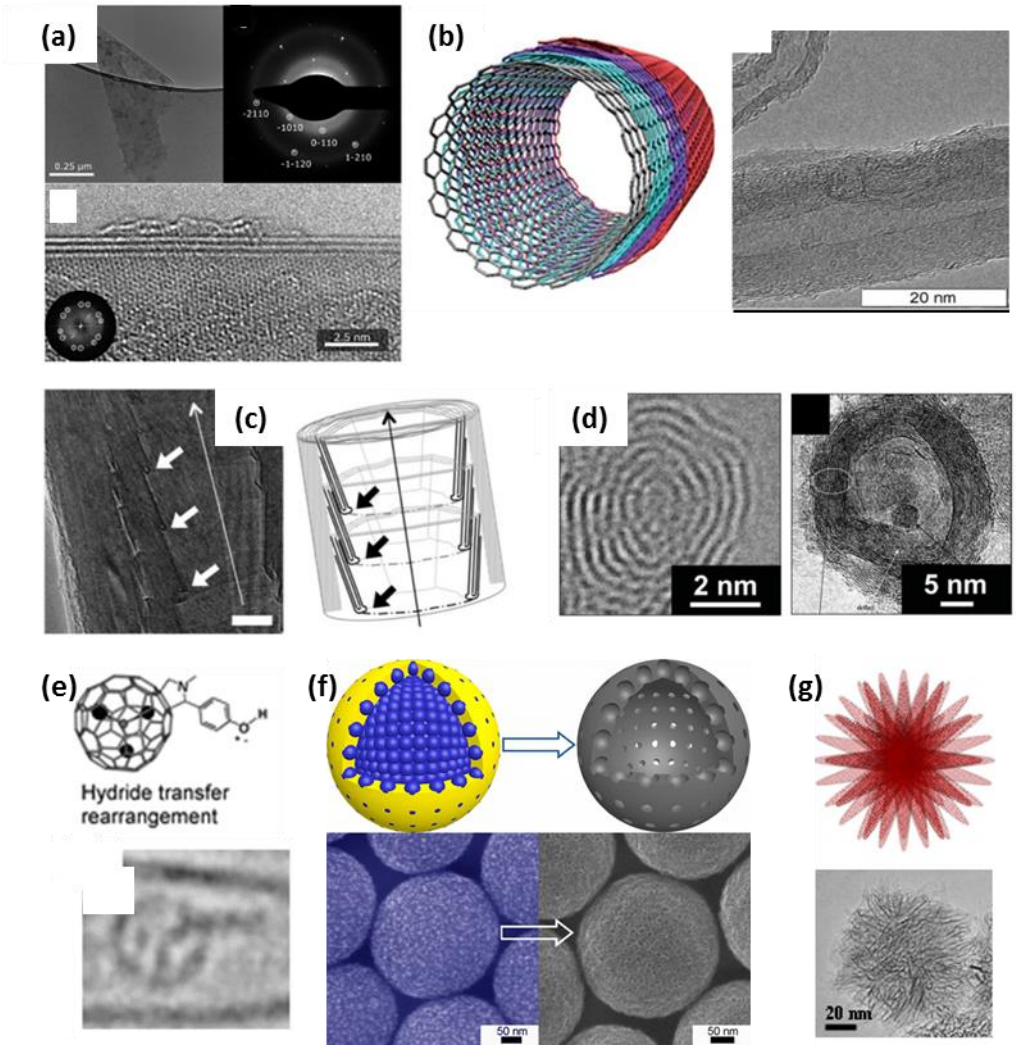

Figure 3. Schematic representation of (a) graphene[43], (b), multi-walled nanotubes (MWNTs), (c) graphitized carbon nanofibers (CNFs), (d) carbon nano-onions[44], (e) functionalized endohedral fullerene inside single-walled carbon nanotube[36], (f) mesoporous carbon and (g) nanohorn.[42]

Alternatively, a top-down synthesis of graphene can be carried out by using graphite as the source. Hence, mechanical (Scotch tape),[27-28] chemical

(solution-based exfoliation, graphite oxide exfoliation), electrochemical and physical routes have been already investigated.[29-31] In the chemical approach, the oxidation to graphene oxide facilitates the exfoliation, as Van der Waals forces are weakened, but a post-treatment (to from reduced graphene oxide) is required to restore the conductivity of the nanostructure.[32-33] In the physical approaches, despite their simplicity, the exfoliating agent used during ball-milling can limit the applicability of the resultant exfoliated graphene.[34-35] Furthermore, the mechanical and electrochemical approaches are limited by a low yield.

The synthesis and properties of other carbon nanostructures such as fullerenes (Figure 3e), mesoporous carbon (Figure 3f) or nanohorns (Figure 3g) are outside of the scope of this discussion.[36-42]

The electrochemical storage mechanism of all carbon nanostructures is mainly based on electrochemical double-layer (EDL) where ions are adsorbed on the surface of the electrode due to electrostatic interactions. Thus, the major research objective in this field is to establish the relationship between the electrode area (including pore structure) with the capacitance. For example, a near-ideal graphitic spacing between SWNTs was observed when introducing and drying liquids into the as-grown SWNTs forest as the surface tension of the liquid and the strong van der Waals interactions "zip" the SWNTs together. Despite of the observed packing, the tube separation is sufficient to allow for full surface coverage thus retaining its surface area. As a consequence, the resulted highly-densely packed and aligned SWNTs showed a specific capacitance of 80 F/g, being roughly twice the capacitance of free-standing SWNTs.[45] Furthermore, hollow carbon nano-onions synthesized using Ni nanoparticles as a template show excellent high-rate cycle performance with high electrochemical reversibility[46] while nanodiamond-derived carbon nano-onions commonly show capacitance values of up to 52 F g^{-1} in aqueous 1M H_2SO_4.[47] More interestingly, ~500 F/g capacitance has been projected for an ideal single layer of graphene-based EDLC, if the entire surface fully utilized.[48] It is important to highlight that such an electrode would constitute a record in carbon electrode material but preparation of such material remains still a great challenge.

In order to overcome the moderate specific capacitance of carbon-based electrodes as a consequence of the double layer mechanism, [49] different strategies such as designing ionic liquid mixtures for improving the cell voltage or utilizing pore sizes that match the electrolyte ion size have been investigated.[50-52] For instance, it has being reported that carbon materials achieve approximately 150 F/g in ionic liquid electrolytes for optimum carbon pore sizes.[53]

Alternatively, the surface functionalization strategy adds reversible redox reactions (pseudocapacitance mechanism) at the surface of the carbon material in contact with an electrolyte. It is important to highlight that functional groups have less influence on capacitance in organic medium than aqueous one.[54] In the last decade a number of studies have shown the high performance of heteroatom (nitrogen, oxygen, or sulfur)–enriched carbons for supercapacitors. For example, nitrogen in the carbon network, especially in the form of pyridone and/or pyridine, affects the electron density and enhances the charge affinity of the carbon material.[55] Therefore, chemical knowledge has being employed as a major tool to enhance both the performance and stability of carbon nanostructures.

The incorporation of such heteroatoms into the carbon structure is carried out by two main strategies: direct growth of carbon nanostructure in the presence of heteroatom-containing molecules [56-60] or post-synthesis method (i. e. treatment of an already formed carbon nanostructure).[61-62] While the two approaches have shown promising results, post-synthesis method has advantages; for instance, the as-grown carbon nanostructures (CNs) can be purified, shortened and functionalized before doping. For example, generating nanopores in the matrix of graphene and subsequently nitrogen-doping of the active sites along the pore opening was reported as a simple way to synthesize doped carbon nanostructures.[63] In addition, graphene edges have been selectively functionalized (i. e. nitrogen, hydrogen, carboxylic acid, sulfonic acid, chloride, bromide, iodide, phosphorus, selenium and antimony) by ball milling in the presence of heteroatom source.[64-69] Such selective incorporation of heteroatoms in both these examples is due to higher reactivity of the edge atoms of graphitic planes as compared to the defect-free basal planes.[70-71]

1.4 Recent advantages of metal-carbon nanostructures for energy storage applications: nanocomposite and nanohybrid

In the 20th century, the size of materials has become increasingly important and as a result a new scientific discipline called "Nanotechnology" has arisen, encompassing science, engineering and technology. By definition, nanotechnology is the branch of the technology involving the fabrication and manipulation of structures (smaller than 100 nm in dimensions) with new physicochemical properties independent on those observed at the bulk and atomic scale. The first acknowledgement of this new area is attributed to the brilliant Nobel Laureate physicist Richard Feynman where, in his famous lecture *"There is Plenty of Room at the Bottom"*, he discussed the idea of writing the entire 24 volumes of the Encyclopaedia Britannica on the head of a pin.[72]

The most fascinating aspect of nanotechnology concerns the unique and size-dependent properties and phenomena that arise within this size regime. For example, the equilibrium of forces in the nanoworld is different from that observed in the larger, macroscopic world: owing of the small mass of the objects, gravitational forces are less important, whereas electrostatic interactions and van der Waals forces are of huge significance.[73]

Field	Example	Description
Energy	Lithium ion battery	Less flammable, quicker charging, more efficient, lighter weight and hold electrical charge longer.
Environmental	Paper towel	Woven from tiny wires of potassium manganese oxide that can absorb 20 times its weight in oil for clean-up applications
Medical	Quantum dots	Semiconducting nanocrystal that can enhance biological imaging for medical diagnostic. They offer optical detection up to 1000 times better than conventional dyes and render significantly more information.
Electronic	OLED	Organic light-emitting diodes that offer brighter images in a flat format, as well as wider viewing angles, lighter weight, better picture density, lower power consumption and longer lifetimes.
	MRAM	Magnetic random access memory enabled by nanometer-scale magnetic tunnel junctions that can quickly and effectively save data.

Table 1. Role of some nanomaterials in different sectors of today's society.

Furthermore, the properties of matter at nanoscale may not be as predictable as those observed at larger scales. Because of their small size, nanomaterials exhibit novel and significantly improved physical, chemical and biological properties. However, most of the important changes in behaviour are caused by

the emergence of a totally new phenomenon such as quantum confinement, a typical example of which is found in semiconductor nanoparticles that have luminescence properties and thus colours that critically depend on their core size.[74] Therefore, one of the great challenges in research is to attain complete understanding of the unique properties and phenomena only observed at the nanoscale and consequently control the arrangement and characteristics of nanoobjects. This is largely motivated by applications, as the development of unique nanoscale structures has the potential to revolutionise the world and significant progress has already been made. Thus, nowadays, different nanoscale materials are already playing a significant role in industry, communications, medicine, computing, and even in the household (Table 1). [75]

The fabrication of nanoscale materials is based on two main approaches: (i) "Bottom-up" or "from small to large" and (ii) "Top-down" or "from large to small".[76] The former strategy involves the arrangement of smaller components, such as atoms and molecules, and exploits a range of fundamental chemical interactions (e.g. hydrogen bonding, Van der Waals, π-π stacking interactions) to form a larger complex assembly. The best example of the "Bottom-up" concept appears extensively in nature in the form of DNA which utilises hydrogen bonding to organise the helical superstructure (Figure 4).[77]

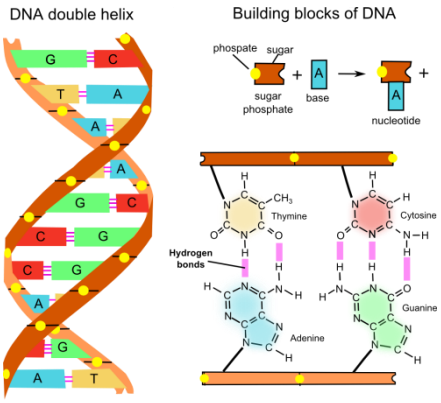

Figure 4: Schematic representation of DNA and its building blocks. DNA molecule is composed of two helical strands held together by hydrogen bonds between the base pairs. The shapes and chemical structure of the bases allow hydrogen bonds to form efficiently only between Adenine-Thymine (A-T) and between Guanine-Cytosine (G-C).[77]

In addition to the extraordinary properties exhibited by individual nanostructures, it is now understood that by combining two or more nanoscale materials (building blocks or components) to form a new heterostructure (**Figure 5)**, where various components possessing different properties can be incorporated into a single composite material, enables multi-functionality to be accessed. The formation of such hierarchical nanostructures can also allow for new properties and applications that are not available with just the individual components.[78]

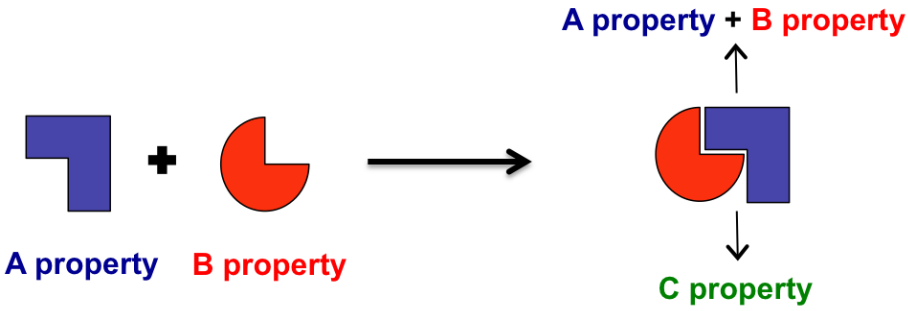

Figure 5: Schematic representation of the integration of two nanoscale components into novel hybrid nanomaterials, which can either incorporate the functional properties of the individual nanoscale components showing multifunctionality (additive) or can couple with each other to yield new properties (non-additive) that are fundamentally different from that of isolated components.

In this context, it is mandatory to define terms such as "hybrid" and "composite" as they have been interchangeable in the research community for a long time. Hence, and following the distinction provided in the review by Elder.[79] Nanocarbon composites are materials in which the nanocarbon is mechanically mixed with the other component (i. e. polymer) with the purpose of combine the intrinsic properties of the individual (i. e. high conductivity of CNs with transparency of polymer).[80] The nanocarbon content tends to be rather low (0.1-5wt%). More importantly, even though composites materials are already commercially available, their properties are not ideal as a consequence of inhomogeneous mixing and poor interfacial adhesion between the two components of the composite.[81]

In contrast, nanocarbon hybrids are materials in which the second component is deposited onto the surface of the nanocarbon.[82] Thus, the close proximity and similar size of the two phases introduce the interface as a powerful new parameter, leading to synergistic properties.

In this section, different hybridization for electrochemical storage applications will be reviewed, with a focus on in molecule-, nanoparticle-, and metal coordination polymer-carbon nanostructures. The combination of such active materials with carbon nanostructure creates the possibility of a large capacitance from the combination of dual storage mechanism from the EDLC and pseudocapacitance (Faradaic).[83] It is important to highlight that, overall, there are two strategies to synthesize nanocarbon hybrids: i) directly from molecular precursors (in situ) or ii) through the attachment of pre-synthesized building blocks via anchor molecules (ex situ). Specifically, in the ex situ (or building block) approach, the two components are first produced separately with their desired dimensions and morphology. They are then modified with a suitable functional group or molecular linker, and finally combined using covalent, non-covalent (van der Waals, π- π interaction) or electrostatic interactions. Conversely, in the in situ route one of the hybrid components is synthesized in the presence of the other (or both components simultaneously). Hence, one component can affect the synthesis of the other in terms of size, crystal structure, and morphology.[84]

1.4.1 Carbon nanostructures with molecules

Electrochemically active molecules (organic or inorganic metal complexes) have been demonstrated to increase the energy storage of the capacitor due to their electron transfer (redox process) with the electrode surface.[85-91] Redox flow batteries would be a practical example where at least one electrode comprises a movable solution of an electroactive material, which is reduced (or oxidised) to store (or release) the energy.[92]

Alternatively, researchers have been developing different approaches to enhance the molecule-electrode surface interaction. By using carbon nanostructures as an electrode, molecule-electrode surface interaction can be controlled either by a covalent (grafting) or non-covalent (π-stacking, encapsulation) approach. In this section, examples of the synthesis of molecule-carbon nanostructures by using covalent and non-covalent routes are firstly summarised. Subsequently, special attention to the encapsulation effect in the electrochemical storage is discussed. Finally, relevant examples of polyoxometalates molecules will be overviewed.

1.4.1.1 General synthesis of molecule-carbon nanostructures

1.4.1.1.1 Covalent bonding (grafting)

The reactivity of the carbon nanostructure depends on its curvature. For example, it is estimated that the free energies of activation and reaction associated with Diels-Alder reactions on carbon-based materials decreases while the curvature increases.[93] Therefore, the lack of curvature makes graphene less reactive in terms of covalent chemistry and even more prone to establish strong van der Waals or π-π interactions.

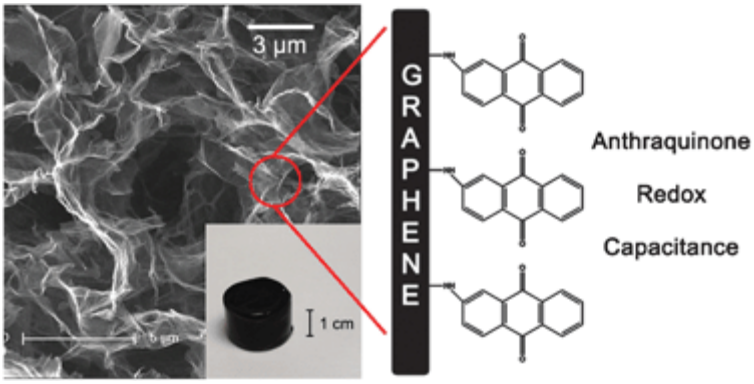

Figure 6. Additional redox capacitance mainly due to covalently bonded 2-Aminoanthraquinone increases the specific capacitance of pure graphene hydrogel (193 F/g) to 258 F/g at a current density of 0.3 A/g.[97]

The mentioned low reactivity can be overcome by introducing defects on the carbon structure (i. e. chemical by the incorporation of hetero-atoms or physical by the vacancy of carbon atoms within the honeycomb carbon lattice) or by free radical reactions. With respect to the former, the covalent modification of graphene oxide with ferrocene produced single-layer graphene oxide sheets with interesting application in detection, for instance, of H_2O_2. [94-95] With respect to the latter, free radicals can be generated from diazonium salts or benzoyl peroxide, reacting with the sp^2 carbon atoms of the graphene. For example, 2-aminoanthraquinone (AAQ) was covalently grafted onto the surface of carbon nanotubes [96] and chemically modified graphene.[97] Interestingly, an AAQ/graphene composite produced a much improved specific capacitance of 258 F/g as a consequence of the additional pseudocapacitance provided by the covalently bonded molecule (Figure 6). It is important to highlight the need of a controlled covalent modification of the carbon nanostructure, as it modifies the honeycomb carbon lattice, and therefore, the conductivity of the sheets.[98-99] On the other hand, covalent bonding is more effective method than the π-π stacking interaction where the molecule can easily diffuse away from the electrode surface into the bulk solution thus resulting stability and sensitivity of the hybrid material.[100]

1.4.1.1.2 Non-covalent interaction (π- π interactions)

π -π interactions occur in many systems such as vertical nucleobase pair stabilization in the double helical structure of DNA and RNA, packing of aromatic molecules in crystals and in many host-guest systems, and so on.[101-102]

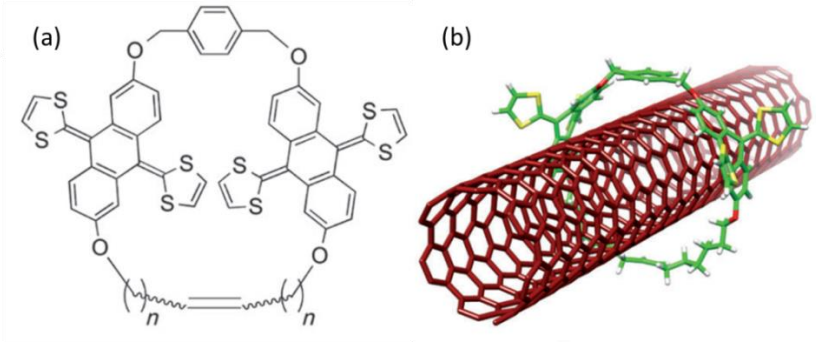

Figure 7. (a) Structure of the first mechanically interlocked derivate of SWNTs. (b) Energy minimized model which shows significant positive interaction with the macrocycle.[108]

In the case of carbon nanostructures, π-π interactions are the dominating supramolecular forces due to the presence of sp^2 carbon. Hence, molecules (such as benzene, TTF or porphyrins) have been dispersed on the surface of graphene and tubular carbon nanostructures.[103-106] For example, the self-assembly of graphitic carbon nitride (g-C_3N_4) and carbon nanotubes was driven by π-π stacking and electrostatic interactions.[107] De Juan et al. have successfully reported for the first time the exTTF-SWNT interaction to template the formation of mechanically interlocked derivatives of SWNTs[108] (Figure 7). Furthermore, a third component (i. e. peptides) has been dispersed on the surface of multiwalled carbon nanotubes using pyrene (π-π interactions) as a linker.[109]

More importantly, the molecule can substantially affect the properties of the carbon nanostructures via π-π interactions. For instance, the dispersity of SWNTs in water was reported for the first time by Nakashuma's team by adsorbing the pyrene derivative onto the walls of SWNTs through π-π interactions.[110] The electrical properties of graphene were tuned with different π-stacking organic molecules (porphyrins, naphthalene homologues and ferrocene) by Chowdhury and co-workers. They showed that the conductivity

of graphene can be enhanced via no covalently functionalized.[111] Recently, it has been demonstrated that π- π stacking at a carbon-ionic liquid interface can modify the operation voltage of supercapacitor device by up to 30%.[112] Furthermore, only extended layering of ionic liquids surrounded amorphous carbon surface was observed due to the π- π stacking between sp^2 carbon in the amorphous carbon and the imidazolium cation in ionic liquids (Figure 8).[113]

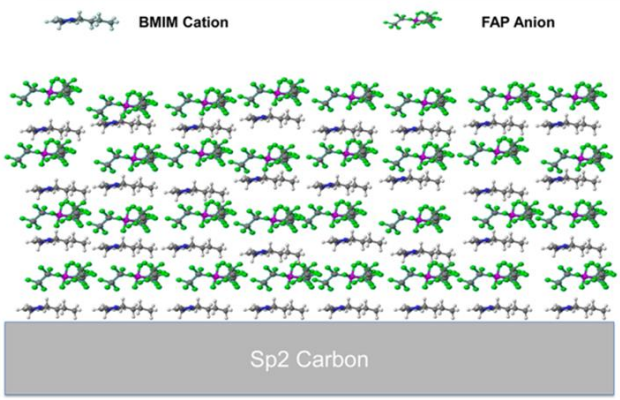

Figure 8. Proposed "lamella-like" structure of solvation layers of 1-butyl-3-methyllimidazolium tris(pentafluoroethyl)trifluorophosphate ion liquid (BMIM-FAP) on the sp^2 carbon surface by Gong and co-workers.[113]

1.4.1.1.3 Encapsulation of molecules

More importantly, an intimate contact between molecules and the carbon nanostructure without any covalent modification can also be achieved by the encapsulation into hollow carbon nanostructures, having advantage of the empty space inside. Since the first encapsulation into SWNTs using C_{60} as guest specie,[114] the fundamental knowledge has increased significantly.[115-118] For example, it has been demonstrated that the encapsulation of molecules also affects the electric conductivity of CNTs, due to the charge transfer between the encapsulated molecules and CNTs. For example, the encapsulation of a cathechol molecule inside MWNTs mediated an electrochemical oxidation of hydrazine ~20 times faster than empty MWNTs. More importantly, it was possible to distinguish among the encapsulated and physisorbed catechol moieties by electrochemistry, showing the charge transfer between the encapsulated molecule and the CNTs.[119]

Furthermore, encapsulation of organic active materials (i.e. organic polymers) in carbon nanotubes revealed applicability towards high electrochemical-storage. This approach avoids the high self-discharge and low practical capacity of organic polymer electrodes.[120] For example, PANI nanowires were confined within a 10 nm-diameter multiwalled carbon nanotube (MWCNT) porous membrane through an *in situ* electro-polymerization method. It is observed that the CNT inhibit the structural change of the confined polyaniline (PANI) chains during multiple charging-discharging cycles, increasing the lifetime of the device. Thus, the hybrid showed an electrochemical capacitance of 296 F/g at a current density of 1.6 A/g with a capacitance loss of less than 5% after 2000 charging-discharging cycles.[121]

Similar improvement of stability was reported by Kawasaky et al. 9,10-antraquinone (AQ) and 9,10-phenantreneuquinone (PhQ) molecules were encapsulated inside of SWNT. As expected, the dissolution of quinone molecules was supressed by the encapsulation, overcoming the undesired capacity fading (Figure 9).[122] Wang et al, synthesized S-CNTs@CNTs hybrid by completely filling the inside of a large amorphous carbon nanotube (~200 nm in diameter) with both small carbon nanotubes and a high amount of sulfur

(S, 85.2%). The obtained electrode material demonstrated superior high-rate cycling performance due to the encapsulation.[123] While the promising results have been obtained for the stability during cycling, attention should be paid to the size of the internal nanotube cavities as they affect the diffusion of the electrolyte (or reactant), potentially limiting the overall performance.

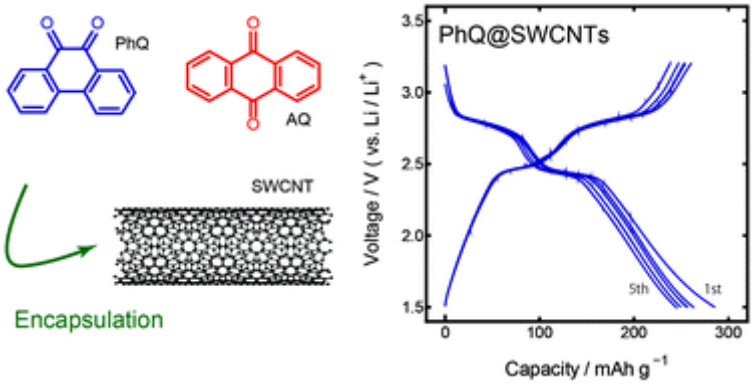

Figure 9. Quinone molecules encapsulated in the SWCNTs can store Li-ions reversibly overcoming via encapsulation the undesired capacity fading, which comes from the dissolution of quinone molecules into the electrolyte.[122]

1.4.1.2 Molecular metal clusters with carbon nanostructures

Polyoxometalates (POMs) are polyatomic ions, usually anions that consist of one or more transition metal oxyanions linked together by shared oxygen atoms to form a large, closed three-dimensional framework. It is important to mention that POMs are molecular metal oxides with reversible redox properties, which makes them attractive building blocks for energy storage applications (Figure 10).[124-126]

Initially, several molecular frameworks were dispersed on the carbon surface (i. e. graphene, carbon nanotubes or carbon black) to form POM/C ex situ hybrid.[127-129] For example, a much larger capacitance than the theoretical one, as calculated from the redox changes in POM ($[PMo_{12}O_{40}]^{3-}$) when deposited on rGO, is observed.[130] Khan et. al., reported the support of tungsten addenda mixed heteropolymolybdate ($PMo_{12-x}W_xO_4O_3$, PMoW) on the poly(dimethyl diallyl ammonium chloride) (PDDA) functionalized graphene (PDDA-rGO). The cationic polymer was employed as a linker to adsorb both rGO and POMs through electrostatic interactions. The resulting ex

situ hybrid exhibited a fast ion transport and high rate specific capacitance.[131] It is important to mention that despite the several examples of immobilization or encapsulation of POMs (i. e. inside silica structures),[132-133] to the best of our knowledge, the electrochemical properties of POMs encapsulated in hollow carbon nanostructures have not been reported. Song. et. al, demonstrated the tuneable synthesis of POMs on the surface of SWNTs by controlling the ultrasonication intensity and time. However, the material obtained (POM-CNTs) showed discharge capacities only up to 100 cycles.[134]

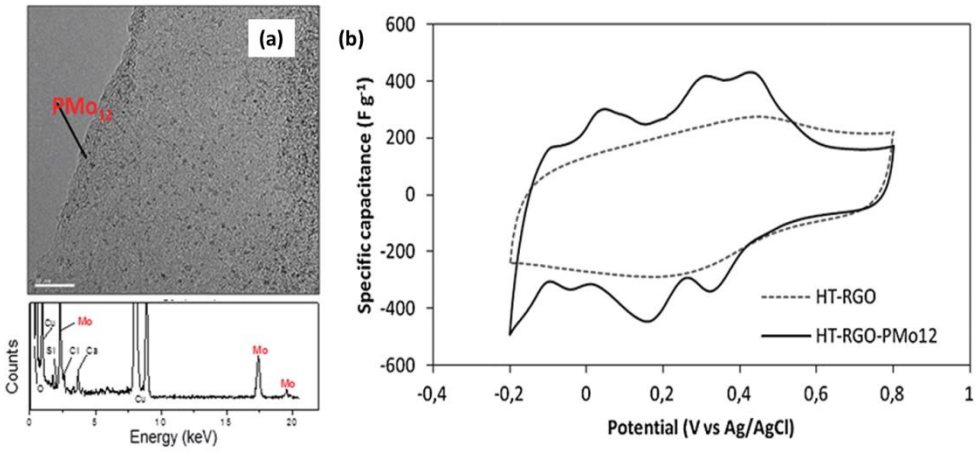

Figure 10. (a) Simultaneous incorporation of polyoxometalate ($H_3PMo_{12}O_{40}10H_2O$ or PMo12) with reduced graphene oxide (HT-GO) exhibits a 30% increase in specific capacitance due to the combination of two storage mechanisms (double layer and faradaic) in the hybrid (b), being 215 F/g and 276 F/g the specific capacitance in 1M H_2SO_4 of HT-RGO and HT-RGO-PMo12, respectively.[125] Scale bar is (a) 10 nm.

Additionally, the attention was also focused on creating stronger molecule-carbon interactions. For example, Derouich et al., reported a controlled electrochemically grafting of diazonium modified polyoxometalates (POMs) on the carbon surface, demonstrating a robust attachment with a control layer thickness.[135] More interestingly, it has recently being demonstrated that such close molecule-carbon interaction enables the charge transfer between the diazonium modified POM and the graphene substrate.[136]

1.4.2 Nanoparticles with carbon nanostructures

In contrast to their bulk counterparts, nanoparticles (NPs) exhibit a large surface-to-volume ratio[137] and quantum size effects.[139-142] Briefly, the electronic states and coordination environment of surface atoms of a nanoparticle can undergo dramatic changes when its size decreases to certain range, [143-144] for example, 19 nm NiO nanoparticles showed the largest specific capacitance in comparison to 31 and 48 nm NiO NPs (140, 114 and 101 F/g, respectively).[145] The surface atoms are also dependent on the nanoparticle morphology (spherical, cubic, or octahedral) as this typically exposes one set of specific crystallographic planes. Then, each crystallographic plane shows specific coordination environment and electronic state, determining, for instance, the resultant activation barrier for chemisorbing or dissociating reactant molecules.[146] Thus, Pt nanocubes showed a higher catalytic reactivity than polyhedron or the truncated cubes.[147]

1.4.2.1 Synthesis and properties of nanoparticles-carbon nanostructures

A large number of synthetic approaches for a great variety of nanoparticles (Figure 11) are available after several decades of intense research efforts and many of them have been widely employed: solid-state methods (involving grinding and firing the mixture of metal oxides, nitrates or carbonates),[148-149] chemical vapour deposition,[150] solvothermal,[151] microwave, [152] hot-injection, [153] precipitation [154] and electrochemical methods.[155] It is important to mention that many of these protocols are constantly revised and modified. For example, gold nanoparticles, which were initially synthesized via single phase reduction in water, introduced by Turkevich et al. [156-157] was, subsequently refined by Frens, [158] and extended to a two-phase Liquid-Liquid system by Brust.[159]

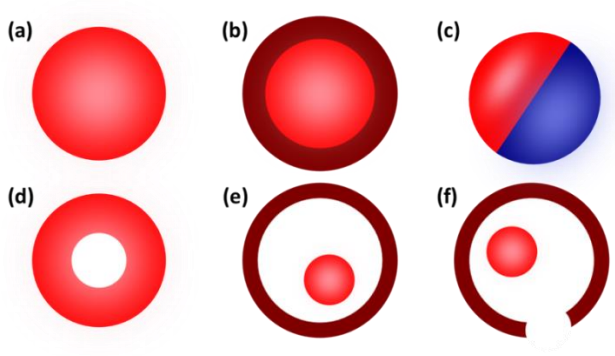

Figure 11. Schematic representation showing the wide range of (spherical) nanoparticles: (a) M-NP, (b) M'-M core-shell NP,[160-163] (c) N-M Janus NP,[164] (d) void@M hollow NP,[165] (e) M-M' yolk-shell NP [166-168] and (f) M-M' open-mouthed yolk-shell NP.[169]

In this section, relevant examples about the synthesis of NP-carbon nanostructures via ex situ (conventional) or in situ approach are summarized. Afterwards, attention is focused towards the synthetic routes to encapsulate NPs inside carbon nanostructures to establish whether the encapsulation has an effect on the electrochemical properties of the metal-carbon hybrids.

1.4.2.1.1 Ex situ synthetic approach

As discussed previously, the ex situ (or conventional) route is based on a physical mixing of two preformed components (nanoparticles and the carbon nanostructure) using either a linker (surfactant) or functionalized carbon nanostructure (i. e. oxygen groups). Thus, a wide range of pseudocapacitance nanoparticles (NiO, V_2O_5, Fe_3O_4, CuO, *etc*.) have been combined with a nanoconductor such as carbon-black, acetylene black, carbon nanotubes or graphene, to form an ex situ hybrid electrode.[170-172] It is known that such dispersion of nanoparticles onto carbon nanostructures provides both conductivity of the film and separation of nanoparticles from each other, thus maximizing their total surface area. For example, the simple addition of carbon nanotubes to 2D MnO_2 nanoplatelets increased not only their specific capacitance but also the conductivity and the robustness of the film.[173]

However, the need to chemically modify the carbon nanostructure, the nanoparticle or both, can be detrimental to the overall performance of the hybrid material. Additionally, an ex situ approach is commonly based on non-covalent interactions, such as van der Waals or electrostatic interactions, so a

weak nanoparticle-carbon interaction is expected.[174-179] As a result, despite the initial increase in the capacity by dispersing MnO_2 NPs on conductive polymers, [180] the electrochemical stability of the hybrid is severely limited by nanoparticle agglomeration.[181-183]

1.4.2.1.2 In situ synthetic approach

Alternatively, superior durability and higher cycle performance is reported for in situ hybrid nanomaterials formed by a chemical reaction (i. e. growing NPs on the CNs surface via covalent bonding) as compared to ex situ hybrids. In a study by Yira et al., a direct thermal decomposition of palladium acetyalacetonate in the presence of carboxyl-functionalized MWNTs (MWNTS-COOH) leads to Pd-MWNT-COOH hybrid material, where Pd NPs were uniformly distributed and strongly anchored onto the MWNT-COOH surface. It is important to mention that the carboxyl groups are commonly used as nucleation sites for the deposition of preformed metal NPs and hence favouring the formation of highly dispersed and stable composite materials.[184-187] More importantly, the in situ Pd-MWNT-COOH hybrid revealed a greater electrochemical performance in comparison to the isostructural ex situ hybrid (Figure 12).[188] Therefore, it should be emphasized that this type of hybrid material/electrode is by no means a simple mixture of two components, but a true nanocomposite, featuring interactions at the atomic/molecular level between the components.189]

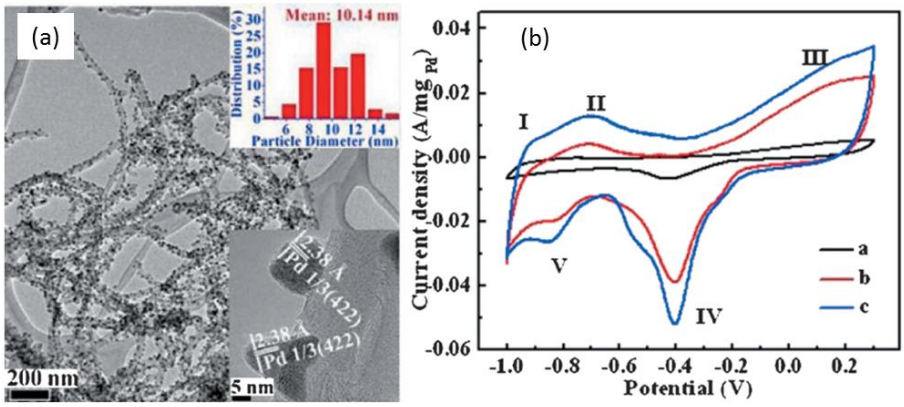

Figure 12. (a) TEM image of Pd-MWNTs-COOH. Inset particle-size histrograms (top) and HRTEM images (bottom) of the corresponding nanohybrid. (b) Electrochemical characterization of bare PdNPs (a, black), ex situ Pd-MWNTs (b, red) and in situ Pd-MWNTs-COOH hybrid (c, blue) in 1M KOH at a scan rate of 50 mV/s at room temperature.[188]

Similar methodology has been extended to other NPs independently of their composition or morphology (i. e. Au, MoO_3, WS_2, and bimetallic PdCo), all of which show synergistic properties as the electrochemical performance of the metal-carbon hybrid is not a simple sum of its components, but much superior compared to both NP and CNs.[190-193] Moreover, the optimized in situ synthesis of a c-$CoMn_2$/C hybrid, which revealed similar electrocatalytic activity to the commercial Pt/C catalyst, showed a superior catalytic durability (> 91.5% retention of ORR current on the c-$CoMn_2$/C hybrid with respect to 71.6% on Pt/C after a continuous chronoamperometric period of 50 h)[194] (Figure 13). Therefore, the in situ synthesis is not only a promising approach for enhancing the electrochemical performance by synergetic effects but it can also improve the cyclability.

During the in situ synthesis, despite the strong bonding between the nanoparticle species and the carbon substrate, a control over nanoparticle morphology can be also achieved. For example, Duan et al. specifically control the shape of Mn_3O_4 NPs during their growth on nitrogen-doped graphene sheets through a two-step liquid-phase process at different temperatures.[195] Briefly, irregular Mn_3O_4 nuclei were formed when graphene oxide sheets (GO) were initially combined with $Mn(Ac)_2$ and ammonia. Then, the simultaneous deoxygenation and nitrogen doping at high pressure and elevated temperatures facilitated the growth of Mn_3O_4 into a sphere, cube, or ellipsoid-like nanoparticle under different reaction conditions. Interestingly, the corresponding materials without nitrogen doping were also prepared and, surprisingly large Mn_3O_4 nanoparticles were observed, resulting in a poor monodispersity. As a result, it is suggested that nitrogen atoms doped into the graphitic lattice acted as anchoring sites leading to a strong nanoparticle-support bonding.

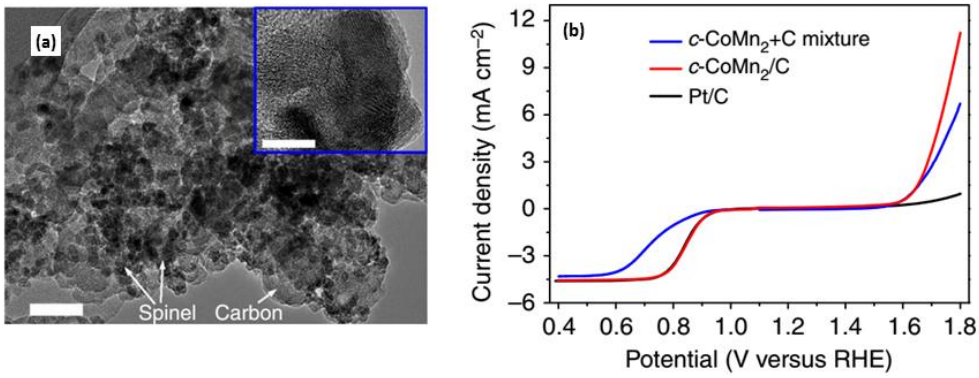

Figure 13. (a) TEM image of prepared c-$CoMn_2$/C hybrid (sacle bar, 50 nm). Inset shows anchoring of a single spinel nanoparticle on carbon (scale bar, 10 nm). (b) Comparison of ORR and OER activities of c-$CoMn_2$+C mixture (or ex situ hybrid), c- $CoMn_2$/C in situ hybrid and Pt/C catalyst in 0.1M KOH solution.[194]

1.4.2.2 Encapsulation of nanoparticles and properties

The previous approaches (ex situ and in situ) can be applied when synthesizing nanoparticles inside carbon nanostructures: (1) ex situ synthesis by filling hollow carbon nanostructures (i. e. muti-walled nanotubes) with preformed nanoparticles (Figure 14a) or (2) the in situ synthesis by synthesizing nanoparticles inside the hollow carbon structure (Figure 14b), growth of carbon nanostructures on the surface of nanoparticles (carbon coating, Figure 14c) or the simultaneous synthesis of both the nanoparticles and the carbon nanostructure.[196]

In the first approach (Figure 14a), preformed nanoparticles are encapsulated into the empty cavities of carbon tubular structures. Initially, the use of supercritical conditions was highly desirable due to the high diffusion resistance for the nanoparticles along the narrow internal channels of SWNTs and MWNTs (1-20 nm). However, the opening of MWNTs or the Ostwald ripening of nanoparticles, which increases the nanoparticle size, during the filling in supercritical conditions were some of the reported side effects.[197-198] Alternatively, the use of graphitized carbon nanofibers (CNF) showed an advantage with respect the filling conditions due to their large internal diameter (50-100 nm).[199]

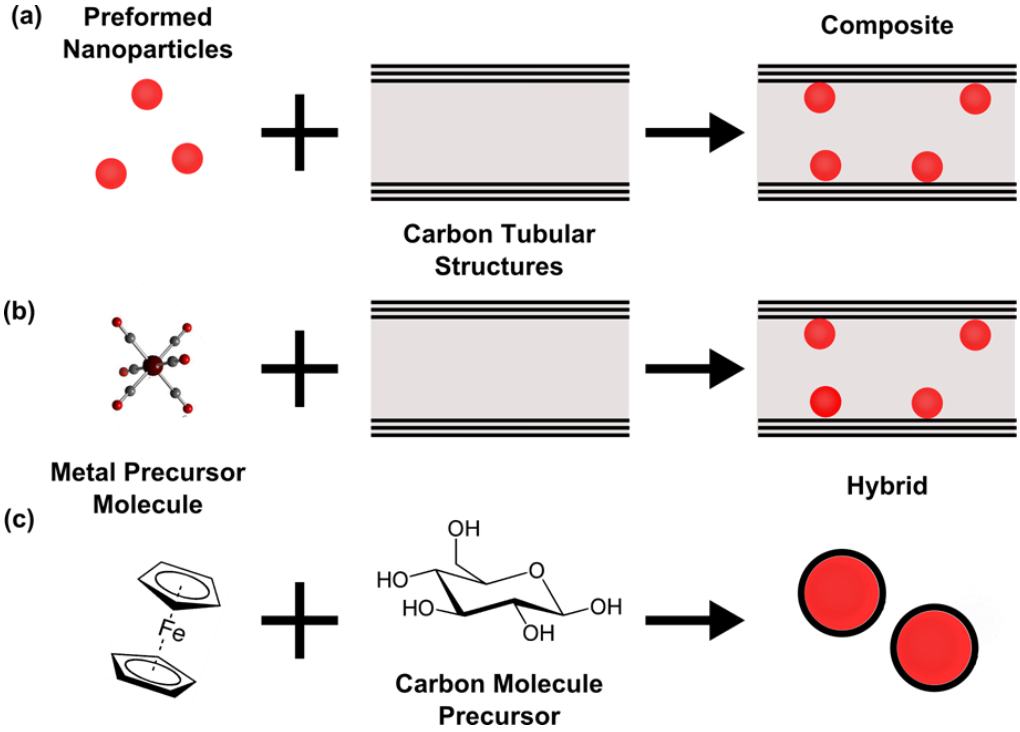

Figure 14. Schematic representation of the synthesis of (a) encapsulated nanoparticle inside tubular carbon nanostructures by wet impregnation, leading to NP@TCN ex situ hybrid. In contrast, the in situ synthesis of nanoparticles in the cavities by using a metal precursor molecule (b) or the carbonization in the presence of a carbon precursor molecule such as glucose (c) results in hybrid materials with stronger NP-carbon interaction.

In situ synthesis of nanoparticles within the interior of narrow carbon tubular nanostructure (Figure 14b) has been carried out mainly by a thermal decomposition of a metal containing molecule.[200-201] For example, a series of noble metal and metal oxide nanoparticles (Pd, Au, Pt, Ru, Fe_3O_4, CoO) have been encapsulated inside end-opened carbon nanotubes by wet impregnation followed by thermal annealing.[202-203] It is important to mention that hollow tubular carbon nanostructures are used as a template of inorganic structures, known as nanoreactor. For instance, nanoribbons of molybdenum/tungsten disulphide $[MoS_2]_n$ are formed through the reaction of metal hexacarbonyls ($M(CO)_6$, M = Mo or W) with iodide anions and, subsequently, with hydrogen sulphide.[204]

The carbon coating route (Figure 14c) is more versatile so the nanoparticle morphology determines the carbon nanostructure while leading to an intimate metal-carbon contact.[205] For example, spherical Co NPs, formed during the arc-discharge process, were encapsulated by the carbon atoms decomposed from the ethanol to finally form the Co@C nanocapsules.[206] This approach

has been extended to the formation of ternary structures where the resulting carbon structure serves as the skeleton for the subsequent synthesis of NPs.[207-208] For example, ternary nickel cobalt sulfide nanosheets/carbon nanotubes core-shell nanomaterial were fabricated via a two-step method by the initial in situ growth of CNT on the metallic Ni mesh, followed by the hydrothermal synthesis of Ni-Co-S nanosheets.[209] The as-prepared hybrid material delivers a high specific capacity of 222mA h/g at 4 A/g owing to the intimate contact of highly conductive CNTs with high redox-active Ni-Co-S nanosheets.

Apart from using molecules [210-211] or polymers [212] as the source of carbon, Hasin et al. reported the utilization of carbon nanostructures as a carbon source for the coating. Hence, graphene oxide (GO), which contains only a few layers of carbon,[214] was used for the synthesis of Co_2C. [213] Briefly, a simple ammonia-evaporation method leads to the synthesis of a Co_3O_4/GO hybrid material which is subsequently converted into Co_2C by thermal reduction in a H_2/N_2 atmosphere. At low annealing temperatures under a reducing atmosphere, graphene is formed and simultaneously reacts with Co_3O_4 NPs to form mesoporous Co_2C.[213]

The development of nanoparticles@carbon nanostructures has received a lot of attention as the host-guest interactions (confinement effect) have an impact in the hybrid properties, such as an enhancement of the catalytic activity of nanoparticles.[215] In situ metal-carbon hybrid exhibited a much better performance (reduction of charge overpotential in the formation of Li_2O_2) with respect to their counterparts (nanoparticles supported on CNT surface). This phenomenon was further studied by density functional theory (DFT) calculations which revealed an increased electron density on CNT surface due to the encapsulation of “guest” noble metal nanoparticles.[202] With respect to nanoparticle stability, Baaziz et al. reported that confinement effect of Co NPs inside carbon nanotubes improves the resistance towards oxidation of “naked" metal Co NPs.[216-217] Additionally, Co@carbon catalyst revealed high chemical stability in acid media due to the protective graphitic layers.[218] As a result, the encapsulation of nanoparticle has promising results not only from performance but also from the stability point of view.

1.4.3 Carbon nanostructures with metal-coordination polymers

Metal-coordination polymers (MCPs), or more popularly known as metal-organic frameworks (MOFs), are crystalline porous hybrid materials comprising coupling units (metal ions or metal-oxo units) coordinated by electron-donating organic ligands.[219-222] One of the reasons of their popularity is their outstanding properties such as (i) extremely low density (~0.13 g/cm^3) with very high surface areas (up to 10,000m^2/g),[223] being higher than those of other porous materials such as zeolites and carbons, and (ii) their flexibility to respond dynamically to external factors such as guest-molecules, temperature or pressure.[224-226] All these properties, together with their molecular nature, which enables a unique level of control over their structure, chemical and physical properties at the nanoscale, suggest MCP as a great candidate for a wide range of applications such as electrochemical storage.[227-228]

In this section, however, we focus our attention on a type of metal-organic framework (MOF), a metal coordination polymer: Prussian blue. While Prussian Blue does not enable the same nanoscale synthetic control as the ligand linker is restricted to cyanide in contrast to the wide library of organic ligands in the case of MOFs, Prussian blue also presents a porous and flexible 3D metal-cyanide framework with the potential to exploit the redox-active properties of the metal centres.[229]

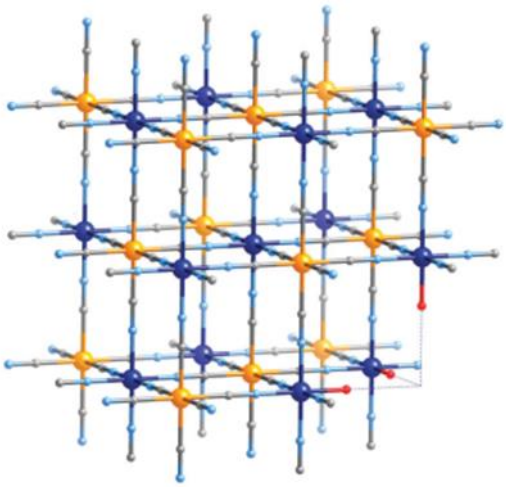

Figure 15. Schematic representation of a cobalt hexacyanoferrate (CoHCF) framework with formula $A_xCo_y[Fe(CN)_6]\cdot nH_2O$ (A: alkali ions, which have been omitted for clarity, C: grey; N:light blue; Co: blue; Fe: yellow; O: red).

The general formula of metal hexacyanoferrate (A-MHCFs) or Prussian blue analogues (PBA) is $A_xM[Fe(CN)_6]_{1-y}\cdot m_y\cdot H_2O$, where x,y = stoichiometric numbers, A = alkali metal cation, M = N-coordinated transition metal ion, m = hexacyanoferrate vacancy (Figure 15). It is important to mention that the electro-neutrality of the network (for instance, in K-CoHCF) is ensured during the synthesis by adjusting the number of hexacyanometallate (i.e. $[Fe(CN)_6]^{3-}$) vacancies with the amount of alkaline ions (K^+) initially introduced in the structure. Hence, the coordination spheres of the N-coordinated transition metal sites (i. e. Co^{II}) neighbouring to a vacancy is completed by water molecules (leading to an average $CoN_{6-p}O_p$ coordination sphere). Large interstitial "A sites" within the structure can accommodate zeolitic water or alkali insertion ions. In addition, MHCFs framework structure has wide channels between the A sites, allowing for the rapid insertion and removal of monovalent alkali cations and multivalent cations.[230] For example, NiHCFs showed a good stability and outstanding properties for the separation of ions ($Cs^+ > Rb^+ > K^+ > Na^+ > Li^+$).[231]

The earliest investigation of these type redox-active framework materials showed the ability to switch between the different redox states of the metal centres, being later exploited to modulate conducting, magnetic, gas adsorption and even optical properties.[232-234] Thus, both the N-coordinated and C-coordinated transition metals can be electrochemically active in this structure having an effect on their performance with respect to electrochemical storage. For example, Mn centres show higher insertion potential of Na cations than Fe centre in MnHCFs, producing higher power and energy output than FeHCFs.[235] It is worth mentioning that a high alkali cation concentration in the MHCF framework is highly desired for a full application in ion batteries. Goodenough's group has recently synthesized Na-MnHCF with a high concentration of sodium cations.[236] Interestingly, the hydrated sample exhibited high reversibility but, surprisingly, a single plateau for voltage profiles, which seems inconsistent with two redox processes Mn^{2+}/Mn^{3+} and Fe^{2+}/Fe^{3+}. It was proposed that the two-redox processes brought close in potential is due to the removal of lattice water. This example highlights that the in-depth mechanistic understanding of Prussian blue materials is still lacking

and further explorations are needed to achieve satisfactory electrochemical performance.[237-239]

1.4.3.1 Synthesis and properties of Prussian blue-carbon nanostructures

Prussian blue analogues (PBA) have been considered as ideal candidate electrode materials for supercapacitors based on their high chemical stability, wide potential window and excellent electroactivity in neutral electrolytes containing alkali metal cations [240-242] in comparison to metal oxide/hydroxide or conductive polymers which preferentially operate in highly corrosive electrolytes. The synthesis of PBA has evolved from the primarily amorphous electrodeposition on a surface electrode [243] or co-precipitation of the metal salt (M) with the corresponding hexacyanometallate [244] to more sophisticated synthetic nanostructures with a control over their morphology (i.e. hollow or core/shell PBA nanoparticles)[245-246] or the guest specie (i. e. drugs).[247] As the combination with conductive carbon nanostructures overcomes the intrinsic poor conductivity of PBA [248-249], only relevant examples of PBA-carbon hybrid from the literature, with attention in their electrochemical properties, are discussed below.

Similar to previous hybridization, the synthesis is carried out by either an ex situ or in situ approach. As example of the former, nano-sized insoluble MHFCs (FeHCF, NiHCF and CoHCF), which were prepared by a simple co-precipitation method, were physically mixed with conductive carbon and showed the specific capacitances of 425, 574.7 and 261.56 F/g (at 0.2 A/g), respectively.[250] CuHCF were uniformly coating carbon fibers, which were used both as the substrate and the current collector, and investigated as a positive electrode (due to their pseudocapacitance) for the fabrication of a flexible asymmetric supercapacitor device.[251] CoHCF nanoparticles were physically dispersed via sonication in the presence of CNTs, exhibiting the expected increase of the surface area due to better particle dispersion.[252]

On the other hand, in situ synthesis of MHCF-C hybrids was also investigated due to the strong interfacial interaction between the components. Capping-free FeHCF grown on graphene oxide facilitated by the hydrophilic sites on the graphene surface and showed a high electron transfer and

enhancement of sensitivity.[253] Additionally, in situ synthesis of FeHCF on carbon chains assured fast charge transfer and ion diffusion as a high performance sodium ion battery.[254] Dou, et. al performed the in situ synthesis of FeHCF in the presence of carbon black and compared with bare FeHCF in order to understand the role of vacancies.[255] Firstly, it was observed that carbon had an effect in the $Fe(CN)_6$ vacancy content (i.e. 0.07 and 0.15 for PB@C hybrid and bare PB respectively) as well as in the PB crystal morphology: much smaller PB crystal anchored on the carbon compared to the size of bare PB. With respect to their electrochemical properties, unusually, bare PB exhibited only one distinct voltage plateau at 3.0-2.7V (Figure 16a, pink) whereas PB@C electrode showed a two sets of redox plateaus (Figure 16a, blue) and redox peaks in the anodic/cathodic scan (Figure 16b, blue). Even though the presence of carbon, the authors claimed that the higher electrochemical performance of PB@C hybrid with respect to bare PB is based on the presence of lower vacancy content within the framework (Figure 16c). Thus, according to first-principles calculations, the density of states (DOS) of $Fe^{LS}(C)$ atoms neighbouring the vacancy are largely affected and the unoccupied peak states of $Fe^{LS}(C)$ nearly disappeared (Figure 16d), indicating the electrochemical degradation of the neighbouring $Fe^{LS}(C)$ for reaction with Na intercalation/deintercalation.

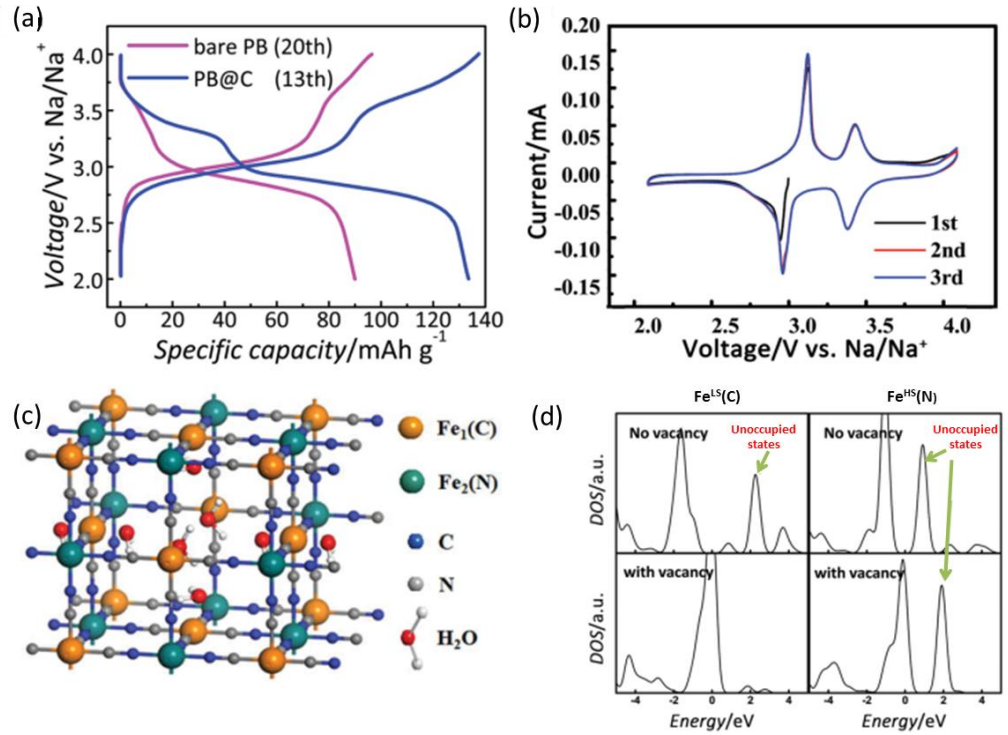

Figure16. (a) Galvanostatic charge-discharge profiles of PB@C and bare PB at 50 mA/g. (b) cyclic voltammetry curves of PB@C at a scan rate of 0.1mV/s. (c) Crystal structure with Fe^{HS}(N) vacancies, where C, N. Fe^{HS}(N), and Fe^{LS} (C) are represented by grey, blue, green and orange balls, respectively. The red and white balls represent O and H in the water molecules, respectively. (d) Density of states projected on the nearest Fe^{LS} (C) and Fe^{HS} (N) atoms with and without Fe^{HS} (N) vacancy.[255]

Very recently, a one-pot Prussian blue/polypyrrole/graphene oxide ternary hybrid was successfully prepared through the spontaneous polymerization of pyrrole and formation of PB nanocubes on GO.[256] The formation of the nanohybrid is based on the initial strong adsorption of pyrrole on the GO surface, via hydrogen bonding between the N-H group in the polymer and the hydroxyl groups in the graphene oxide. Subsequently, Fe^{3+} is reduced to Fe^{2+} by pyrrole on the surface of GO, acting as nucleation points for the formation of insoluble PB nanocubes. It is important to stress that the specific capacitance of the ternary hybrid (525.4 F/g at 5A/g) is far superior to the performance of binary materials (262.5, 246.8 and 97.5 F/g for PPy-PB, PB-GO and PPy-GO, respectively), being attributed to the synergistic effect of pseudocapacitance from PB and PPy on the double-layer capacitance from GO.

1.5 Concluding remarks

A general overview of all the different nanocomponents used towards electrochemical energy storage in the literature have been discussed in this chapter, with special attention given to the rational thinking of how to prepare functional nanostructures so that the synthesis dramatically affects the electrochemical properties.

Carbon nanostructures (i. e. graphene, carbon nanotubes, carbon nanofibers and carbon nano-onions) themselves are one of the greatest candidates towards energy-related application due to their outstanding properties such as electrical conductivity. Their intrinsic performance have been overcome by different strategies, for example, enhancing their surface area by exfoliation, doping the structure with heteroatoms which affects the electron density along the carbon lattice or by combining with other species.

With regard to the latter, this chapter has reviewed the combination of different carbon nanostructures with more electrochemically active components such as organic molecules (i.e. antraquinone), inorganic molecules (i.e. polyoxometalates), nanoparticles (i.e. monometallic, bimetallic, spherical, core-shell) or metal-coordination polymers (i.e. metal hexacyanoferrates).

From all the synthetic approaches, there are two main concepts that will be expanded throughout this thesis. The first concept is to reduce the resistance at the nanoscale between the different components. For example, it is been observed that the synthesis of nanoparticles in the presence of the carbon nanostructure (*in situ* hybrid) exhibited a higher electrochemical performance in comparison to the ex situ (or conventional) hybrid, where preformed nanoparticles are physically dispersed on the carbon nanostructure. It is important to note that the control of the morphology of the nanoparticle is crucial towards the electrochemical properties of the hybrid material.

Secondly, the encapsulation of electrochemically active species has shown promising results towards energy-related applications not only due to the electron transfer between the guest specie and the host carbon nanostructure, but also due to the improvement over the stability during cycling.

Overall, development of new materials through new synthetic protocols as well as the fundamental understanding of their electrochemical storage mechanisms could make renewable energy much more efficient and cheaper, making possible the total replacement of the traditional fossil fuel technologies.

1.6 References

1. X. Zhang, Y. Tang, F. Zhang and C. S. Lee, Adv. Energy Mater., 2016, **6**, 1502588.
2. B. E. Conway, Kluwer-Academic, 1999.
3. S. C. S. Lai, R. A. Lazenby, P. M. Kirkman and P. R. Unwin, Chem. Sci., 2015, **6**, 1126-1138.
4. I. Gurrappa and L. Binder, Sci. Technol. Adv. Mater., 2008, 9, 043001.
5. H. Liu, H. Song, X. Chen, S. Zhang, J. Zhou and Z. Ma, J. Power Sources, 2015, **285**, 303-309.
6. H. J. Lee, J. H. Lee, S-Y. Chung and J. W128. Choi, Angew. Chem., 2016, **128**, 4026-4030.
7. C. Chen, Y. Wen, X. Hu, X. Ji, M. Yan, L. Mai, P. Hu, B. Shan and Y. Huang, Nat. Commun., 2015, **6**, 6929.
8. H. D. Yoo, Y. Li, Y. Liang, Y. Lan, F. Wang and Y. Yao, ChemNanoMat, 2016, **2**, 688-691.
9. Y. Zhu, L. Peng, D. Chen and G. Yu, Nano Lett., 2016, **16**, 742-747.
10. http://www.worldometers.info/es/.
11. https://yearbook.enerdata.net/.
12. H. Tsuchiya and O. Kobayashi, Int. J. Hydrogen Energy, 2004, **29**, 985.
13. X. Wang, S-I. Choi, L. T. Roling, M. Luo, C. Ma, L. Zhang, M. Chi, J. Liu, Z. Xie, J. A. Herron, M. Mavrikakis and Y. Xia, Nat. Commun., 2015, **6**, 7594.
14. http://3xe-electric-cars.com/Winston Battery.
15. A. Ambrosi, C. K. Chua, A. Bonanni and M. Pumera, Chem. Rev., 2014, **114**, 7150-7188.
16. S. Iijima and T. Ichihashi, Nature, 1993, **363**, 603-605.
17. A. Eliseev, L. Yashina, M. Kharlamova and N. Kiselev (2011). One-Dimensional Crystals inside Single-Walled Carbon Nanotubes: Growth, Structure and Electronic Properties, Electronic Properties of Carbon Nanotubes, Prof. Jose Mauricio Marulanda (Ed.), InTech, DOI: 10.5772/19060.
18. T. Zhao, Q. Tang., Y. Liu, C. Zhu and X. Zhao, J. Nanomater., 2007, 84540.
19. H. Xie, R. Zhang, Y. Zhang, Z. Yin, M. Jian and F. Wei, Carbon, 2016, **98**, 157-161.
20. A. La Torre, M. C. Gimenez-Lopez, M. W. Fay, G. A. Rance, W. A. Solomonsz, T. W. Chamberlain, P. D. Brown and A. N. Khlobystov, ACS Nano, 2012, **6**, 2000–2007.
21. M. C. Gimenez-Lopez, A. Kurtoglu, D. A. Walsh and A. N. Khlobystov, Adv. Mater., 2016, **28**, 9103-9108.
22. M. C. Gimenez-Lopez, A. La Torre, M. W. Fay, P. D. Brown and A. N. Khlobystov, Angew. Chem., 2013, **52**, 2051-2054.
23. M. Zeiger, N. Jackel, V. N. Mochalin and V. Presser, J. Mater. Chem. A, 2016, 4, 3172–3196
24. G. Yang, H. Ham, T. Li and C. Du, Carbon 2012, **50**, 3753-3765.
25. K. Makgopa, P. M. Ejikeme, C. J. Jafta, K. Raju, M. Zeiger, V. Presser and K. I. Ozoemena, J. Mater. Chem. A 2015, **3**, 3480-3490.
26. G. Wang, X. Pan, J. N. Kumar and Y. Liu, Carbon, 2015, **83**, 180-182.
27. K. S. Novoselov, A. K. Geim, S. V. Morozov, D. Jiang, Y. Zhang, S. V. Dubonos, I. V. Grigorieva, and A. A. Firsov, Science, 2004, **306**, 666-669.
28. A. K. Geim and K. S. Novoselov, Nat. Materials, 2007, **6**, 183-191,
29. T. M. Swager, ACS Macro Lett., 2012, **1**, 3-5.
30. V. Eswaraiah, S. S. J. Aravind and S. Ramaprabhu, J. Mater. Chem., 2011, **21**, 6800-6803.
31. J. M. Tour, Chem. Mater., 2014, **26**, 163-171.

32. S. Stankovich, D. A. Dikin, R. D. Piner, K. A. Kohlhaas, A. Kleinhammes, Y. Jia, Y. Wu, S. T. Nguyen and R. S. Ruoff. Carbon, 2007, **45**, 1558–1565.
33. S. Park, J. An, I. Jung, R. D. Piner, S. J. An, X. Li, A. Velamakanni and R. S. Ruoff. Nano Lett., 2009, **9**, 1593-1597.
34. M. Lotya, Y. Hernandez, P. J. King, R. J. Smith, V. Nicolosi, L. S. Karlsson, F. M. Blighe, S. De, Z. Wang, I. T. McGovern, G. S. Duesberg and J. N. Coleman, J. Am. Chem. Soc., 2009, **131**, 3611–3620.
35. V. M. Samoilov, E. A. Danilov, A. V. Nikolaeva, G. A. Yerpuleva, N. N. Trofimova, S. S. Abramchuk and K. V. Ponkratov, Carbon, 2015, **84**, 38–46.
36. M. C. Gimenez-Lopez, A. Chuvilin, U. Kaiser and A. N. Khlobystov, Chem. Comm., 2011, **47**, 2116-2118.
37. T. Zhao, Q. Tang., Y. Liu, C. Zhu and X. Zhao, J. Nanomater., 2007, 84540.
38. M. A. Lebedeva, T. W. Chamberlain and A. N. Khlobystov, Chem. Rev., 2015, **115**, 11301-11351.
39. M. Zeiger, N. Jäckel, V. N. Mochalin and V. Presser, J. Mater, Chem. A, 2016, **4**, 3172-3196.
40. H. Zhang, O. Noonan, X. Huang, Y. Yang, C. Xu, L. Zhou and C. Yu, ACS Nano, 2016, **10**, 4579-4586.
41. W. Xin and Y. Song, RSC Adv., 2015, **5**, 83239-83285.
42. N. Karousis, I. Suarez-Martinez, C. P. Ewels and N. Tagmatarchis, Chem. Rev., 2016, **116**, 4850-4883.
43. C. Vallés, C. Drummond, H. Saadaoui, C. A. Furtado, M. He, O. Roubeau, L. Ortolani, M. Monthioux and A. Pénicaud, J. Am. Chem. Soc., 2008, **130**, 15802-15804.
44. K. Makgopa, P. M. Ejikeme, C. J. Jafta, K. Raju, M. Zeiger, V. Presser and K. I. Ozoemena, J. Mater. Chem. A, 2015, **3**, 3480-3490.
45. D. N. Futaba, K. Hata, T. Yamada, T. Hiraoka, Y. Hayamizu, Y. Kakudate, O. Tanaike, H. Hatori, M. Yumura and S. Iijima, Nat. Mater., 2006, **5**, 987-994.
46. S-M. Yoo, W. M. Choi, H. Baik, H-J. Shim, I. Song, M-S. Kwon, J. J. Bae, H. Kim, Y. H. Lee and J-Y. Choi, ACS Nano 2012, **6**, 6803-6811.
47. E. G. Bushueva, P. S. Galkin, A. V. Okotrub, L. G. Bulusheva, N. N. Gavrilov, V. L. Kuznetsov and S. I. Moiseekov, Phys. Status Solidi B, 2008, **245**, 2296-2299.
48. J. Xia, F. Chen, J. Li and N. Tao. Nat. Nanotechnol., 2009, **4**, 505–509.
49. Y. Huang, J. Liang and Y. Chen. Small, 2012, **8**, 1805–1834.
50. L. Hao, X. Li and L. Zhi. Adv. Mater., 2013, **25**, 3899–3904.
51. J. Chmiola, G. Yushin, Y. Gogotsi, C. Portet, P. Simon and P. L. Taberna. Science, 2006, **313**, 1760–1763.
52. R. Lin, P.-L. Taberna, S. Fantini, V. Presser, C. R. Perez, F. Malbosc, N. L. Rupesinghe, K. B. K. Teo, Y. Gogotsi and P. Simon. J. Phys. Chem. Lett., 2011, **2**, 2396–2401.
53. P. Simon and Y. Gogotsi. Nat. Mater., 2008, **7**, 845–854.
54. G. Moussa, C. M. Ghimbeu, P-L. Taberna, P. Simon and C. Vix-Guterl, Carbon, 2016, **105**, 628-637.
55. K. Jurewicz, K. Babel, R. Pietrzak, S. Delpeux and H. Wachowska, Carbon, 2006, **44**, 2368-2375.
56. Y. Tang, B. L. Allen, D. R. Kauffman and A. Star, J. Am. Chem. Soc., 2009, **131**, 13200-13201.
57. J. Vazquez-Arenas, D. Higgins, Z. Chen, M. Fowler and Z. Chen, J. Power Sources, 2011, **205**, 215-221.

58. R. Czerw, M. Terrones, J.-C.Charlier ,X. Blase ,B. Foley ,R. Kamalakaran ,N. Grobert , H. Terrones ,D. Tekleab, P. M. Ajayan, W. Blau, M. Rühle, and D. L. Carroll, Nano Letters, 2011, **1**, 457-560.
59. Y. T. Lee, N. S. Kim, S. Y. Bae, J. Park, S-C. Yu, H. Ryu and H. J. Lee, J. Phys. Chem. B, 2003, 107, 12958-12963.
60. X. Zhao, F. Li, R. Wang, J-M. Seo, H-J. Choi, S-M. Jung, J. Mahmood, I-Y. Jeon and J-B. Baek, Adv. Funct. Mater., 2017, 10.1002/adfm.201605717.
61. G.J. Sohn, H.J. Choi, I.Y. Jeon, D.W. Chang, L. Dai and J-B. Baek, ACS Nano, 2012, **6,** 6345-6355.
62. N. Gavrilov, I.A. Pašti, M. Mitri, J. Travas-Sejdi, G. Ciri, Marjanovi and S.V. Mentus, J. Power Sources, 2012, **220**, 306-316.
63. T. Palaniselvam, M. O. Valappil, R. Illathvalappil and S. Kurungot, Energy Environ. Sci., 2014, **7**, 1059-1067.
64. I-Y Jeon, H-J. Choi, M. J. Ju, I. T. Choi, K. Lim, J. Ko, H. K. Kim, J. C. Kim, J-J. Lee, D. Shin, S-M. Jung, J-M. Seo, M-J. Kim, N. Park, L. Dai and J-B. Baek, Sci. Rep., 2013, **3**, 2260.
65. Z. Jin, H. Nie, Z. Yang, J. Zhang, Z. Liu, X. Xu and S. Huang, Nanoscale, 2012, **4**, 6455-6460.
66. I-Y. Jeon, H-J. Choi, S-M. Jung, J-M. Seo, M-J. Kim, L. Dai and J-B. Baek, J. Am. Chem. Soc., 2013, **135**, 1386–1393.
67. I-Y. Jeon, H-J. Choi, M. Choi, J-M. Seo, S-M. Jung, M-J. Kim, S. Zhang, L. Zhang, Z. Xia, L. Dai, N. Park and J-B. Baek, Sci. Rep., 2013, **3**, 1810, 1–7.
68. C. Zhang, N. Mahmood, H. Yin, F. Liu and Y. Hou, Adv. Mater., 2013, **25**,4932–4937.
69. I-Y Jeon, H-J. Choi, H-J. Choi, S-M. Jung, M-J. Kim, J-M. Seo, S-Y. Bae, S. Yoo, G. Kim, H. Y. Jeong, N. Park and J-B Baek, Nat. Commun., 2015, **6**, 7123.
70. C. Banks, T. Davies, G. Wildgoose and R. Compton, Chem. Commun., 2005, 829-841.
71. D. K. Kampouris and C. E. Banks, Chem. Comm., 2010, **46**, 8986-8988.
72. R. P. Feyman, Engineering and Science, 1960, 22.
73. D. Jariwala, V. K. Sangwan, L. J. Lauhon, T. J. Marks and M. C. Hersan, Chem. Soc. Rev., 2013, **42**, 2824-2860.
74. G. Lota, K. Fic and E. Frackowiak, Energy Environ. Sci., 2011, **4**, 1592-1605.
75. B. Scrosati, J. Hassoun & Y-K. Sun, Energy Environ. Sci., 2011, **4**, 3287-3295.
76. M. G. Walter, E. L. Warren, J. R. McKone, S. W. Boettcher, Q. Mi, E. A. Santori and N. S. Lewis, Chem. Rev., 2010, **110**, 6446-6473.
77. L. M. Reddy, S. R. Gowda, M. M. Shaijumon and P. M. Ajayan, Adv. Mater., 2012, **24**, 5045-5064.
78. S. R. Sivakkumar, W. J. Kim, J-A. Choi, D. R. MacFarlane, M. Forsyth and D-W. Kim, J. Power Sources, 2007, **171**, 1062-1068.
79. D. Eder, Chem. Rev., 2010. **110**, 1348-1385.
80. C. J. Shearer, A. Cherevan and D. Eder, Adv. Mater., 2014, **26**, 2295-2318.
81. Y. Y. Huang and E. M. Terentjev, Adv. Funct. Mater. **2010**, 20, 4062-4068.
82. J. J. Vilatela and D. Eder , ChemSusChem 2012, **5**, 456-478.
83. H. T. Liu, P. He, Z. Y. Li, Y. Liu and J. H. Li, Electrochim. Acta, 2006, **51**, 1925–193.
84. A. S. Cherevan, P. Gebhardt, C. J. Shearer, M. Matsukawa, K. Domen and D. Eder , Energy Environ. Sci., 2014, **7**, 791-796.
85. G. Lota and E. Frackowiak, Electrochem. Commun., 2009, **11**, 87–90.
86. K. Fic, E. Frackowiak and F. Béguin, J. Mater. Chem., 2012, **22**, 24213–24223.

87. G. Lota, K. Fic and E. Frackowiak, Electrochem. Commun., 2011, **13**, 38–41.
88. E. Frackowiak, K. Fic, M. Meller and G. Lota, ChemSusChem, 2012, 5, 1181−1185.
89. J. Suarez-Guevara, V. Ruiz and P. Gomez-Romero, J. Mater. Chem. A, 2014, **2**, 1014–1021.
90. S. Roldán, M. Granda, R. Menéndez, R. Santamaría and C. Blanco, J. Phys. Chem. C, 2011, **115**, 17606–17611.
91. S. Roldán, M. Granda, R. Menéndez, R. Santamaría and C. Blanco, Electrochim. Acta, 2012, **83**, 241–246.
92. G. L. Soloveichik, Chem. Rev., 2015, **115**, 11533-11558.
93. B. Willocq, V. Lemaur, M. El Garah, A. Ciesielski, P. Samori, J.-M. Raquez, P-H. Dubois and J. Cornil, Chem. Comm., 2016, **52**, 7608-7611.
94. M. B. Avinash, K. S. Subrahmanyam, Y. Sundarayya and T. Govindaraju, Nanoscale, 2010, **2**, 1762-1766.
95. K. Deng, J. Zhou, and X. Li, Electrochimica Acta, 2013, **95**, 18–23.
96. M. A. Ghanem, I. Kocak, A. Al-Mayouf, M. AlHoshan and P. N. Bartlett, Electrochimica Acta, 2012, **68**, 74-80.
97. Q. Wu, Y. Sun, H. Bai and G. Shi, Phys. Chem. Chem. Phys., 2011, **13**, 11193−11198.
98. M. Vizuete, M. J. Gómez-Escalonilla, M. Barrejón, J. L. G. Fierro, M. Zhang, M. Yudasaka, S. Iikima, P. Atienzar, H. García and F. Langa, Phys. Chem. Chem. Phys., 2016, **18**, 1828-1837.
99. R. T. Jane and R. Lomoth, J. Mater. Chem. C, 2015, **3**, 6260-6265.
100. N. Xia, L. Liu, Z. Sun and B. Zhou, J. Nanomater., 2015, 892674.
101. C. A. Hunter and J. K. M. Sanders, J. Am. Chem. Soc., 1990, **112**, 5525−5534.
102. C. A. Hunter, M. N. Meah, M. N. and J. K. M. Sanders, J. Am. Chem. Soc., 1990, **112**, 5773−5780.
103. Z. Guo, J. Mao, Q. Ouyang, Y. Zhu, L. He, X. Lu, L. Liang, D. Ren, Y. Chen and J. Zhen, J. of Dispersion Sci. and Technology, 2009, **1**, 31.
104. H. Murakami, G. Nakamura, T. Nomura, T. Miyamoto and N. Najashima, J. Porphyrins Phtalocyanines, 2007, **11**, 418.
105. B. Kowalewska and P. J. Kulesza, Electroanalysis, 2009, **21**, 351-359.
106. G. Pognon, T. Brousse, L. Demarconnay and D, Bélanger, J. Power Sources, 2011, **196**, 4117–4122.
107. T. Y. Ma, S. Dai, M. Jaroniec and S. Z. Qiao, Angew. Chem. Int. Ed., 2014, **53**, 7281-7285.
108. A. de Juan, Y. Pouillon, L. Ruiz-González, A. Torres-Pardo, S. Casado, N. Martín, A. Rubio and E. M. Pérez, Angew. Chem., Int. Ed., 2014, **53**, 5394–5400.
109. K. S. Prasad, C. Walgama and S. Krishnan, RSC Adv., 2015, **5**, 11845-11849.
110. N. Nakashima, Y. Tomonari and H. Murakami, Chem. Lett., 2002, 638–639.
111. M. J. Deka and D. Chowdhury, J. Phys. Chem. C, 2016, **120**, 4121-4129.
112. M. Li, A. S. Westover, R. Carter, L. Oakes, N. Muralidharan, T. C. Boire, H-J. Sung and C. L. Pint, ACS Appl. Mater. Interfaces, 2016, **8**, 19558-19566.
113. X. Gong, A. Kozbial, F. Rose and L. Li, ACS Appl. Mater. Interfaces, 2015, **7**, 7078-7081.
114. B. W. Smith, M. Monthioux, and D. E. Luzzi, Chem. Phys. Lett., 1999, **315**, 31–36.
115. T. W. Chamberlain, A. M. Popov, A. A. Knizhnik, G. E. Samoilov, and A. N. Khlobystov, ACS Nano, 2010, **4**, 5203–5210.
116. D. A. Britz and A. N. Khlobystov, Chem. Soc. Rev., 2006, **35**, 637–659.
117. A. N. Khlobystov, D. A. Britz, J. Wang, S. A. O'Neil, M. Poliakoff, and G. A. D. Briggs, J. Mater. Chem., 2004, **14**, 2852–2857.

118. H. Song, Y. Ishii, A. Al-zubaidi, T. Sakai and S. Kawasaki, Phys. Chem. Chem, Phys., 2013, **15**, 5767-5770.
119. A. S. Kumar and P. Swetha, Lagmuir, 2010, **26**, 6874-6877.
120. J-K. Kim, Y. Kim, S. Park, H. Ko and Y. Kim, Energy Environ. Sci., 2016, **9**, 1264-1269.
121. R. Wang, Q. Wu, X. Zhang, Z. Yang, L. Gao, J. Ni and O. K. C. Tsui, J. Mater. Chem. A, 2016, **4**, 12602-12608.
122. Y. Ishii, K. Tashiro, K. Hosoe, A. Al-zubaidi and S. Kawasaki, Phys. Chem. Chem. Phys., 2016, **18**, 10411-10418.
123. F. Jin, S. Xiao, L. Lu and Y. Wang, Nano Lett., 2016, **16**, 440-447.
124. J. Suarez-Guevara, V. Ruiz and P. Gomez-Romero, Phys. Chem. Chem. Phys., 2014, **16**, 20411–20414.
125. J. S-G, V. Ruiz and P. Gomez-Romero, Phys. Chem. Chem. Phys, 2014, **16**, 20411-20414.
126. M. Yang, S. B. Hong, J. H. Yoon, D. S. Kim, S. W. Jeong, D. E. Yoo, T. J. Lee, K. G. Lee, S. J. Lee and B. G. Choi, ACS Appl. Mater. Interfaces, 2016, 8, 22220-22226.
127. W. Zhang, D. Du, D. Gunarratne, R. Colby, Y. Lin and J. Laskin, Electroanalysis, 2014, **6**, 178-183.
128. W. Chen, L. Huang, J. Hu, T. Li, F. Jia and Y.-F. Song, Phys. Chem. Chem. Phys., 2014, **16**, 19668–19673.
129. A. K. Cuentas-Gallegos, S. Lopez-Cortina, D. Pacheco-Catalan, E. Fuentes-Quezeda, H. Mosqueda and G. Orozco-Gamboa, J. Solid State Electrochem., 2016, **20**, 67.
130. K. Kume, N. Kawasaki, H. Wang, T. Yamada, H. Yoshikawa and K. Awaga, J. Mater. Chem. A, 2014, **2**, 3801-3807.
131. Y-H. Ding, J. Peng, H-Y. Lu, Y. Yuan and S-U Khan, RSC Adv., 2016, **6**, 81085-81091.
132. S. Pourbeyram, M. Moosavifar and V. Hasanzadeh, J. Electroanal. Chem., 2014, **714**, 19-24.
133. T. Okada, K. Miyamoto. T. Sakai and S. Mishima, ACS Catal., 2014, **4**, 73-78.
134. J. Hu, Y. C. Ji, W. Chen, C. Streb and Y-F. Song, Energy Environ. Sci., 2016, **9**, 1095-1101.
135. S. G. Derouich, C. Rinfray, G. Izzet, J. Pinson, J-J. Gallet, F. Kanoufi, A. Proust and C. Combellas, Langmuir, 2014, **30**, 2287-2296.
136. L. Huder, C. Rinfray, D. Rouchon, A. Bernayad, M. Baraket, G. Izzet, F. Lipp-Bregolin, G. Lapertot, L. Dubois, A. Proust, L. Jansen and F. Duclairoir, Langmuir, 2016, **32**, 4774–4783.
137. R. Rossetti, J. L. Ellison, J. M. Gibson and L. E. Brus, J. Chem. Phys., 1984, **80**, 4464.
138. M. Valden, X. Lai and D. W. Goodman, Science, 1998, **281**, 1647-1650.
139. Y. Guo, Y-F. Zhang, X-Y. Bao, T-Z. Han, Z. Tang, L-X Zhang, W-G. Zhu, E. G. Wang, Q. Niu, Z. Q. Qiu, J-F. Jia, Z-X. Zhao and Q-K. Xue, Science, 2004, **306**, 1915-1917.
140. J. A. Sichert, Y. Tong, N. Mutz, M. Vollmer. S. Fischer, K. Z. Milowska, R. G. Cortadella, B.Nickel, C. Cardenas-Daw, J. K. Stolarczyk, A. S. Urban, and J. Feldmann, Nano Lett., 2015, **15**, 6521-6527.
141. W. Sun, C. Quian, L. Wang, M. Wei, M. L. Mastronardi, G. Casillas, J. Breu and G. A. Ozin, Adv. Mater., 2015, **27**, 746-749.
142. Z. X. Gan, L. Z. Liu, H. Y. Wu, Y. L. Hao, Y. Shan, X. L. Wu and P. K. Chu, Appl. Phys. Lett., 2015, **106**, 233133.
143. M-H. Yeh, S-H. Chang, L-Y. Lin, H-L. Chou, R. Vittal, B-J. Hwang and K-C. Ho, Nano Energy, 2015, **17**, 241-253.
144. S. Hebié, T. W. Napporn, C. Morais and K. B. Kokoh, ChemPhysChem, 2016, **17**, 1454-1462.

145. K. Wang, X. Shi, Z. Zhang, X. Ma, Y. Lu and H. Wang, J. Alloy. Comp., 2015, **632**, 361-367.
146. S. Cao, F. F. Tao, Y. Tang, Y. Tang, Y. Li and J. Yu, Chem. Soc. Rev., 2016, **45**, 4747-4765.
147. C. Wang, H. Daimon, T. Onodera, T. Koda and S. Sun, Angew. Chem., Int. Ed., 2008, **47**, 3588–3591.
148. J. S. Armijo, Oxid. Met., 1969, **1**,171–198.
149. J. Lu, C. Zhan, T. Wu, J. Wen, Y. Lei, A. J. Kropf, H. Wu, D. J. Miller, J. W. Elan, Y-K. Sun, X. Qiu and K. Amine, Nat. Commun., 2014, **5**, 5693.
150. D. S. Choi, A. W. Robertson, J. H. Warner, S. O. Kim and H. Kim, Adv. Mater., 2016, **28**, 7115-7122.
151. G. Cai, X. Wang, M. Cui, P. Darmawan, J. Wang, A. L-S. Eh and P. S. Lee, Nano Energy, 2015, **12**, 258-267.
152. C. Blanco-Andujar, D. Ortega, P. Southern, Q. A. Pankhurst and N. T. K. Thanh, Nanoscale, 2015, **7**, 1768-1775.
153. J. J. L. Humphrey, S. Sadasivan, D. Plana, V. Celorrio, R. A. Tooze and D. J. Fermín, Chem. Eur. J., 2015, **21**, 12694-12701.
154. B. G. S. Raj, A. M. Asiri, J. J. Wu and S. Anandan, J. Alloy. Comp., 2015, **636**, 234-240.
155. D. Wang, Y. Yu, J. Zhu, S. Liu, D. A. Muller and H. D. Abruña, Nano Lett., 2015, **15**, 1343-1348.
156. B. V. Enüstün and J. Turkevich, J. Am. Chem. Soc., 1963, **85**, 3317-3328.
157. J. Turkevich, Gold Bull., 1985, **18**, 125.
158. G. Frens, Nat. Phys. Sci.1973, **241**, 20-22.
159. M. Brust, M. Walker, D. Bethell, D. J. Schiffrin and R. Whyman, J. Chem. Soc., 1994, 801-802.
160. D. Raciti, J. Kubal, C. Ma, M. Barclay, M. Gonzalez, M. Chi, J. Greeley, K. L. More and C. Wang, Nano Energy, 2016, **20**, 202-211.
161. A. Sahoo, S. K. Tripathy, N. Dehury and S. Patra, J. Mater. Chem. A, 2015, **3**, 19376-19383.
162. K. Eid, V. Malqras, P. He, K. Wang, A. Aldalbahi, S. M. Alshehri, Y. Yamauchi and L. Wang, RSC Adv., 2015, **5**, 31147-31152.
163. P. C. Pandey and G. Pandey, Catal. Sci. Technol., 2016, **6**, 3911-3917.
164. L. Chen, C. P. Deming, Y. Peng, P. Hu, J. Stofan and S. Chen, Nanoscale, 2016, **8**, 14565-14572.
165. B. Koo, H. Xiong, M. D. Slater, V. B. Prakapenka, M. Balasubraman, P. Podsiadlo, C. S. Johnson, T. Rajh and E. V. Shevchenko, Nano Lett., 2012, **12**, 2429-2435.
166. R. Purbia and S. Paria, Nanoscale, 2015, **7**, 19789-19873.
167. W. Shi, D. Du, B. Shen, C. Cui, L. Lu, L. Wang and J. Zhang, ACS Appl. Mater. Interfaces, 2016, **8**, 20831-20838.
168. Q. Shi, P. Zhang, Y. Li, H. Q. Xia, S. Fu, G. Ren, F. Chai, J. Jiang and F. Qu, New J. Chem., 2016, **40**, 818-824.
169. Xia, D. Wang and X. Tao, Chem. Sci., 2015, **6**, 4350-4357.
170. H. Y. Lee, S. W. Kim and H. Y. Lee, Electrochem. Solid-State Lett., 2001, **4**, A19–A22.
171. M. Zhi, C. Xiang, J. Li, M. Li and N. Wu, Nanoscale, 2012, **5**, 72–88.
172. D. Hanlon, C. Backes, T. M. Higgins, M. Hughes, A. O'Neill, P. J. King, N. McEvoy, G. S. Duesberg, B. M. Sanchez, H. Pettersson, V. Nicolosi and J. N. Coleman, Chem. Mater., 2014, **26**, 1751–1763.

173. T. M. Higgins, D. McAteer, J. C. M. Coelho, B. M. Sanchez, Z. Gholamvand, G. Moriarty, N. McEvoy, N. C. Berner, G. S. Duesberg, V. Nicolosi and J. N. Coleman, ACS Nano, 2014, **8**, 9567-9579.
174. Z. Chen, V. Augustyn, J. Wen, Y. W. Zhang, M. Q. Shen, B. Dunn and Y. F. Lu, Adv. Mater., 2011, **23**, 791.
175. Q. Li, W. Zhu, J. Fu, H. Zhang, G. Wu and S. Sun, Nano Energy, 2016, **24**, 1-9.
176. W. Yang , X. Wang , F. Yang , C. Yang and X. Yang , Adv. Mater., 2008, **20**, 2579-2587.
177. D. Belanger, T. Brousse and J. W. Long, Electrochem. Soc. Interface, 2008, **17**,49–52.
178. J. Kim, J. Lee, J. You, M-S. Park, M. S. A. Hossain, Y. Yamauchi and J. H. Kim, Mater. Horiz., 2016, **3**, 517-535.
179. V. A. Turek, Y. Francescato, P. Cadinu, C. R. Crick, L. Elliot, Y. Chen, V. Urland, A. P. Ivanov, L. Velleman, M. Hong, R. Vilar, S. A. Maier, V. Giannini and J. B. Edel, ACS Photonics, 2016, **3**, 35-42.
180. T. G. Yun, B. I. Hwang, S. Kim, S. Hyun and S. M. Han, ACS Appl. Mater. Interfaces, 2015, **7**, 9228-9234.
181. Z. Tang, C. Tang & H. Gong, Adv. Funct. Mater., 2012, **22**, 1272−1278.
182. Y. Huang, Y. Li, Z. Hu, G. Wei, J. Guo and J. Liu, J. Mater. Chem. A, 2013, **1**, 9809−9813.
183. C. Zhang, Y. Xie, M. Zhao, A. E. Pentecost, Z. Ling, J. Wang, D. Long, L. Ling and W. Qiao, ACS Appl. Mater. Interfaces, 2014, **6**, 9751−9759.
184. V. Georgakilas, D. Gournis, V. Tzitzios, L. Pasquato, D. M. Guldi and M. Prato, J. Mater. Chem. 2007, **17**, 2679–2694.
185. V. Lordi, N. Yao and J. Wei, Chem. Mater. 2001, **13**, 733–737.
186. M. S. Raghuveer, S. Agrawal, N. Bishop and G. Ramanath, Chem. Mater. 2006, **18**, 1390–1393.
187. R. Yu, L. Chen, Q. Liu, J. Lin, K.-L. Tan, S. C. Ng, H. S. O. Chan, G.-Q. Xu and T. S. A. Hor, Chem. Mater. 1998, **10**, 718–722.
188. Y. Wang, Q. He, J. Guo, H. Wei, K. Ding, H. Lin, S. Bhana, X. Huang, Z. Luo, T. D. Shen, S. Wei and Z. Guo, ChemElectroChem, 2015, **2**, 559-570.
189. D. P. Dubal, O. Ayyad, V. Ruiz and P. Gómez-Romero, Chem. Soc. Rev., 2015, **44**. 1777-1790.
190. S. Kaur, V. Bhalla and M. Kumar, ACS Appl. Mater. Interfaces, 2015, **7**, 1661-16624.
191. K. Zhou, W. Zhou, X. Liu, Y. Sang, S. Ji, W. Li, J. Lu, L. Li, W. Niu, H. Liu and S. Chen, Nano Energy, 2015, **12**, 510-520.
192. H. Xue, J. Tang, H. Gong, H. Guo, X. Fan, T. Wang, J. He and Y. Yamauchi, ACS Appl. Mater. Interfaces, 2016, **8**, 20766-20771.
193. K. Shiva, H. S. S. Ramakrishna, H. B. Rajendra, A. J. Bhattacharyya and C. N. R. Rao, Nano Energy, 2013, **2**, 787-793.
194. C. Li, X. Han, F. Cheng, Y. Hu, C. Chen and J. Chen, Nat. Commun., 2015, **6**, 7345.
195. J. Duan, S. Chen, S. Dai and S. Z. Qiao, Adv. Funct. Mater., 2014, **24**, 2072-2078.
196. X. Deng, B. Zhao, Y. Zhong, Y. Zhu and Z. Shao, J. Mater. Chem. A, 2016, **4**, 10403-10408.
197. J-Y. Chang, F-D. Mai, B. Lo, J-J. Chang, S-H. Tzing, A. Ghule and Y-C. Ling, Chem. Commun., 2003, 2362-2363.
198. A. La Torre, G. A. Rance, J. El Harfi, J. Li, D. J. Irvine, P. D. Brown and A. N. Khlobystov, Nanoscale, 2010, **2**, 1006-1010.

199. W. A. Solomonsz, G. A. Rance, B. J. Harris and A. N. Khlobystov, Nanoscale, 2013, **5**, 12200-1220.
200. J-P. Tessonnier, L. Pesant, G. Ehret, M. J. Ledoux and C. Pham-Huu, Appl. Catal. A, 2005, **288**, 203-210.
201. X. Pan, Z. Fan, W. Chen, Y. Ding, H. Luo and X. Bao, Nat. Mater., 2007, **6**, 507-511.
202. X. Huang, H. Yu, H. Tan, J. Zhu, W. Zhang, C. Wang, J. Zhang, Y. Wang, Y. Lv, Z. Zeng, D. Liu, J. Ding, Q. Zhang, M. Srinivasan, P. M. Ajayan, H. H. Hng and Q. Yan, Adv. Funct. Mater., 2014, **24**, 6516-6523.
203. X Liu, I. Marangon, G. Melinte, C. Wilhelm, C. Ménard-Moyon, B. P. Pichon, O. Ersen, K. Aubertin, W. Baaziz, C. Pham-Huu, S. Bégin-Colin, A. Bianco, F. Gazeau and D. Bégin, ACS Nano, 2014, **8**, 11290-11304.
204. A. Botos, J. Biskupek, T. W. Chamberlain, G. A. Rance, C. T. Stoppiello, J. Sloan, Z. Liu, K. Suenaga, U. Kaiser and A. N. Khlobystov, J. Am. Chem. Soc., 2016, **138**, 8175-8183
205. Y. Shen, J. Mater. Chem. A, 2015, **3**, 13114-13188.
206. H. Wang, C. Chen, Y. Zhang, L. Peng, S. Ma, T. Yang, H. Guo, Z. Zhang, D. S. Su and J. Zhang, Nat. Commun., 2015, **6**, 7181.
207. X. Mu, X. LLiu, K. Zhang, J. Li, J. Zhou, E. Xie and Z. Zhang, Electron. Mater. Lett., 2016, **12**, 296.
208. B. D. Boruah and A. Misra, RSC Adv., 2016, **6**, 36307-36313.
209. T. Peng, H. Yi, P. Sun, Y. Jing, R. Wang, H. Wang and X. Wang, J. Mater. Chem. A, 2016, **4**, 8888-8897.
210. Y. Luo, Z. Wang, Y. Fu, C. Jin, Q. Wei and R. Yang, J. Mater. Chem. A, 2016, **4**, 12583-12590.
211. Y. N. Ko, S. B. Park, S. H. Choi and Y. C. Kang, Sci. Rep., 2014, **4**, 5751.
212. M. Zhuang, X. Ou, Y. Dou, L. Zhang, Q. Zhang, R. Wu, Y. Ding, M. Shao and Z. Luo, Nano Lett., 2016, **16**, 4691-4698.
213. P. Hasin, J. Phys. Chem. C, 2014, **118**, 4726–4732.
214. M. J. McAllister, J. L. Li, D. H. Adamson, H. C. Schniepp, A. A. Abdala, J. Liu, M. Herrera-Alonso, D. L. Milius, R. Car, R. K. Prud'homme and I. A. Aksay, Chem. Mater., 2007, **19**, 4396–4404.
215. H. Zhang, X. Pan, J. Liu, W. Qian, F. Wei, Y. Huang and X. Bao. ChemSusChem, 2011, **4**, 975-980.
216. W. Baaziz, S. Begin-Colin, B. P. Pichon, I. Florea, O. Ersen, S. Zafeiratos, R. Barbosa, D. Begin and C. Pham-Huu, Chem. Mater., 2012, **24**, 1549-1551.
217. W. Baaziz, I. Florea, S. Moldovan, V. Papaefthimiou, S. Zafeiratos, S. Belgin-Colin, D. Begin, O. Ersen and C. Pham-Huu, J. Mater. Chem. A., 2015, **3**, 11203-11214.
218. T. Cao, D. Wang, J. Zhang, C. Cao and Y. Li, Chem. Eur. J. 2015, **21**, 14022-14029.
219. G. Férey, Dalton Trans., 2016, **45**, 4073-4089.
220. H. Furukawa, K. E. Cordova, M. O'Keeffe and O. M. Yaghi, Science, 2013, **341**, 1230444.
221. S. R. Batten, S. M. Neville and D. R. Turner, Coordination Polymers: Design, Analysis and Application, Royal Society of Chemistry, 2008.
222. J. E. Halls, A. Hernán-Gómez, A. D. Burrows and F. Marken, Dalton Trans., 2012, **41**, 1475-1480
223. O. M. Yaghi and H. Li, J. Am. Chem. Soc., 1995, **117**, 10401–10402.
224. J. Graham, D. R. Allan, A. Muszkiewicz, C. A. Morrison and S. A. Moggach, Angew. Chem. Int. Ed. 2011, **50**, 11138-11141.
225. M. Wang, X. Zhang, Y. Chen and D. Li, J. Phys. Chem. C, 2016, **120**, 5059-5066.

226. N. H. Alsmail, M. Suyentin, Y. Yan, R. Cabot, C. P. Krap, J. Lü, T. L. Easun, E. Bichoutskaia, W. Lewis, A. J. Blake and M. Schröder, Chem. Eur. J. 2014, **20**, 7317-7324.
227. D. M. D'Alessandro, Chem. Comm., 2016, **52**, 8957-8971.
228. W. Xia, A. Mahmood, R. Zou and Q. Xu, Energy Environ. Sci., 2015, **8**, 1837-1866.
229. C. D. Wessells, R. A. Huggins and Y. Cui, Nat. Commun., 2011, **2**, 550.
230. R. Y. Wang, C. D. Wessells, R. a. Huggins and Y. Cui, Nano Lett., 2013, **13**, 5748.
231. X. Hao, Y. Li and M. Pritzker, Sep. Purif. Technol., 2008, **63**, 407–414.
232. A. A. Karyakin, Electroanalysis, 2001, **13**, 813–819.
233. D. Maspoch, D. Ruiz-Molina and J. Veciana, Chem. Soc. Rev., 2007, **36**, 770–818.
234. B. Kong, C. Selomulya, G. F. Zheng and D. Y. Zhao, Chem. Soc. Rev., 2015, **44**, 7997–8018.
235. M. Pasta, R. Y. Wang, R. Ruffo, R. Qiao, H-W. Lee, B. Shyam, M. Guo, Y. Wang, L. A. Wray, W. Yang, M. F. Toney and Y. Cui, J. Mater. Chem. A, 2016, **4**, 4211-4223.
236. J. Song, L. Wang, Y. Lu, J. Liu, B. Guo, P. Xiao, J.-J. Lee, X.-Q. Yang, G. Henkelman and J. B. Goodenough, J. Am. Chem. Soc., 2015, **137**, 2658–2664.
237. A. Dostal, B. Meyer, F. Scholz, W. Schröder, A. M. Bond, F. Marken and S. J. Shaw, J. Phys. Chem., 1995, **99**, 2096-2103.
238. R. C. Millward, C. E. Madden, I. Sutherland, R. J. Morimer, S. Fletcher and F. Marken, Chem. Commun., 2001, 1994-1995.
239. S. Guo, J. Yi, Y. Sun and H. Zhou, Energy Environ. Sci., 2016, **9**, 2978-3006.
240. H. Jiang, Y.-T. Xu, T. Wang, P.-L. Zhu, S. Yu, Y. Yu, X.-Z. Fu, R. Sun and C.-P. Wong, Electrochim. Acta, 2015, **166**, 157–162.
241. K. Lu, D. Li, X. Gao, H. Dai, N. Wang and H. Ma, J. Mater. Chem. A, 2015, **3**, 16013–1601.
242. Y. Wang and Q. Chen, ACS Appl. Mater. Interfaces, 2014, **6**, 6196–6201.
243. S. Nakanishi, G. Lu, H. M. Kothari, E. W. Bohannan and J. A. Switzer, J. Am. Chem. Soc., 2003, **125**, 14998-14999.
244. C. Zhang, Y. Xu, M. Zhou, L. Liang, H. Dong, M. Wu, Y. Yang and Y. Lei, Adv. Funct. Mater., 2017, **27**, 10.1002/adfm.201604307.
245. L. Chang, S. Chang, W. Chen, W. Han, Z. Li, Z. Zhang, Y. Dai and D. Chen, RSC Adv., 2016, **6**, 96223-69228; Y. Wang and Q. W. Chen, ACS Appl. Mater. Interfaces, 2014, **6**, 6196–6201.
246. M. Hu, S. Furukawa, R. Ohtani, H. Sukegawa, Y. Nemoto, J. Reboul, S. Kitagawa and Y. Yamauchi. Angew. Chem., 2012, **124**, 1008-1012.
247. S. Mukherjee, B. R. Rao, B. Sreedhar, P. Paik and C. R. Patra, Chem. Commun., 2015, **51**, 7325-7328.
248. N. P. Wickramaratne, V. S. Perera, B.-W. Park, M. Gao, G. W. McGimpsey, S. D. Huang and M. Jaroniec, Chem. Mater., 2013, **25**, 2803–2811.
249. Y. Tang, W. Zhang, L. Xue, X. Ding, T. Wang, X. Liu, J. Liu, X. Li and Y. Huang, J. Mater. Chem. A, 2016, **4**, 6036-6041.
250. J. Chen, K. Huang and S. Liu, Electrochem. Commun., 2008, **10**, 1851–1855.
251. S. T. Senthikumar, J. Kim, Y. Wang, H. Huang and Y. Kim, J. Mater. Chem. A., 2016, **4**, 4934-4940.
252. Q. Wang, S. He, N. Wang, J. Zhao, J. Fang and W. Shen, New J. Chem., 2016, **40**, 3244-3251.
253. B. Kong, X. Sun, C. Selomulya, J. Tang, G. Zheng, Y. Wang and D. Zhao, Chem. Sci., 2015, **6**, 4029-4034.

254. D. Yan, J. Xu, X. Z. Liao, H. Wang, Y. S. He and Z. F. Ma, Chem. Commun., 2015, **51**, 8181-8184.
255. Y. Jiang, S. Yu, B. Wang, Y. Li, W. Sun, Y. Lu, M. Yan, B. Song and S. Dou, Adv. Funct. Mater. 2016, **26**, 5315-5321.
256. Y. Zou, Q. Wang, C. Xiang, Z. She, H. Chu, S. Qiu, F. Xu, S. Liu, C. Tang and L. Sun, Electrochim. Acta, 2016, **188**, 126-134.

Part A

Modification of carbon nanostructures towards energy-related applications

General statement

As mentioned in the previous chapter, especial attention has been focussed recently on the preparation and/or modification of carbon nanostructures (CNs) to improve their performance in a wide range of electrochemical applications. In the case of 2D carbon nanostructures, their optimised production from a top-down approach (i.e. exfoliation of graphite) requires harsh conditions. In Chapter 2, we aim to develop a large-scale, green, simple and cost-effective method for the production of 2D graphene nanoplatelets (GNP) from one-dimensional hollow carbon nanofibers (CNF). GNP are 1-15 nm thick graphitic nanoparticles with diameters ranging from sub-micrometre to 100 μm. One of the objectives here is to determine whether mechanical dry high-energy ball milling enables the release of nanographene stacks from the internal structure of CNFs, producing selectively high-quality GNP. Special attention will be also paid on the oxygen-containing groups on the GNP surface related to the hydrophilicity of the milled material that determines the electrochemical charge storage mechanism (i. e. double-layer capacitance or redox pseudocapacitance) of GNP. Thus, the effect of the milling time, as well as, the hydrophilicity of the GNP will be investigated in detail.

On the other hand, the preparation of carbon nanostructures from a bottom-up approach appears to be far more flexible than top-down approach due to the wide range of reactants, conditions or catalyst that can be used. For example, it has been reported that graphitic carbon shell (named as carbon nano-onions) can grow on the surface of nanoparticles during chemical vapour deposition (CVD), which allows the protection of the metal core against oxidation. In Chapter 3, we provide further insight into the mechanism formation of carbon onions, especially when the catalytic nanoparticle is supported on a two-dimensional carbon substrate. To study the role of the substrate during the carbon nano-onion formation, catalytic nanoparticles (Fe_3O_4 NPs) were dispersed and compared on two different carbon substrates.

Chapter 2

Quick chemical-free exfoliation of carbon nanofibers for high-performance few-layer graphene nanoplatelet supercapacitors

2.1. Introduction

Because of their unique large surface area, exceptional electrical conductivity and electrochemical stability, graphene-based materials hold a great promise as high-performance electrochemical capacitors and battery electrode materials in a variety of energy storage applications ranging from portable electronics to electric automotive vehicles. [1-5] Nevertheless, their market potential is currently hindered by the lack of simple, green and cost-effective methods for large-scale production in high yield of electrochemically active graphene-based materials.[6,7]

To address the above challenge, tremendous efforts have been made to develop top-down production methods of few-layer graphene materials including nanoplatelets and nanosheets using graphite as source of carbon.[8-10] The chemical exfoliation of graphite, popularly known as Hummers' method, produces graphene oxide via oxidation in harsh conditions after a day.[11] Apart from the environmental concerns,[12] one of the main drawbacks of this approach is that the oxygen-containing groups in the graphene oxide cannot so far be fully removed by chemical reduction that limits the electrical conductivity of the obtained material.[13-16]

Alternatively, graphite has been mechanically exfoliated in much shorter times by sonication in the presence of surfactants.[17-18] These methods tend to exhibit either high production rates or low defect contents, but not both. Although the intrinsic carbon structure is mainly maintained, unfortunately the presence of surfactants acting as stabilizers against aggregation or restacking hinders any further electrochemical applicability. Very recently, wet ball-milling has been also exploited as a one-step mechanical method for the mass-production of graphene nanosheets using large amounts of organic solvents such as N,N-dimethylformamide (DMF) and strong exfoliating agents.[19-21] Though it can be considered as low-cost alternative, it is not an environmentally friendly method.

Unlike carbon nanotubes, hollow carbon nanofibers are industrially available in large quantities and in an order-of-magnitude cheaper, making these nanostructures very attractive to address the cost issues faced by the current energy storage devices. Highly graphitised carbon nanofibers (CNF)

with large internal diameters (63 ± 26 nm) exhibit corrugated surfaces dictated by their internal graphitic structure composed by 13–15 nm stacked-nanocones with a typical nanocone thickness of 24 ± 8 nm (Figure 1).

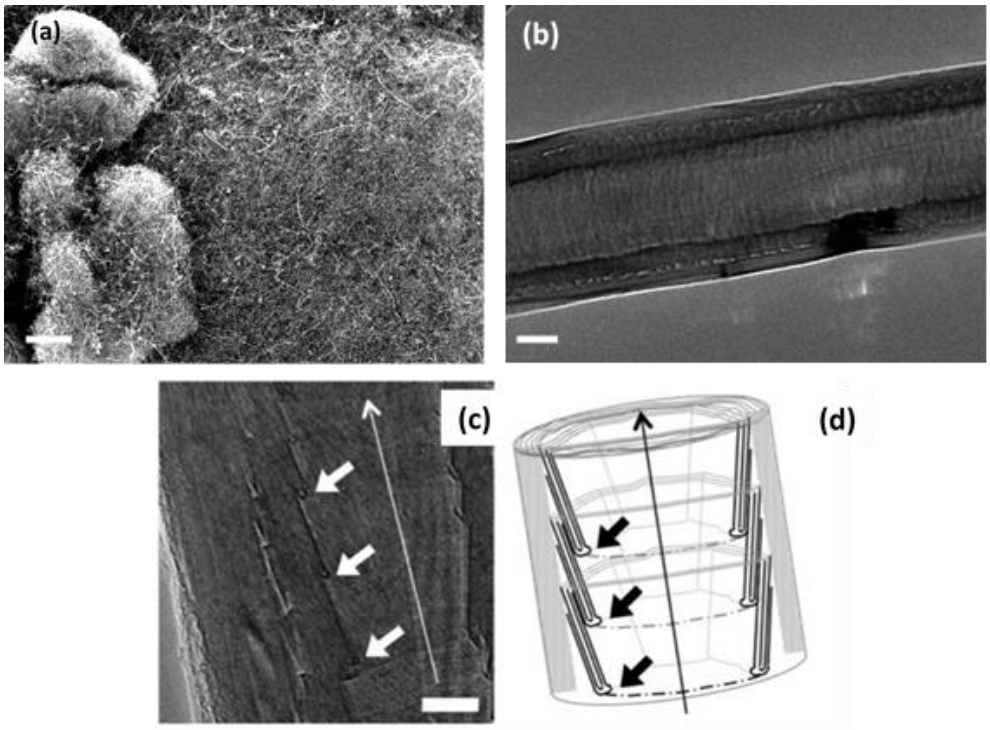

Figure 1. (a) FESEM and (b-c) HRTEM images of CNF at low and high magnification showing their internal corrugated structure (scale bars 25 µm, 100nm and 10 nm, respectively). (d) Schematic representation of a CNF. The long arrow in c and d indicates the main axes of the nanofibers, while the short arrows point to the internal step-edge of the CNF.

Interestingly, these graphene stacks can be potentially disassembled and exfoliated during mechanical ball milling to produce few-layer graphene nanoplatelets (GNP). Recent studies have shown that the corrugated graphitic interiors of CNF can be also used for controlling nanoparticle positions [22] and their growth. [23,24] Nevertheless, to the best of our knowledge, the interiors of hollow carbon nanofibers have not yet been investigated as source of carbon to produce few-layer graphene materials for energy storage applications using dry ball milling conditions in absence of exfoliating agents.[25]

In this study, we demonstrate for the first time the high-yield production of good-quality electrochemically active GNP in just 20 minutes from CNF via a one-step, low-cost and chemical-free process using mechanical ball milling. The as-prepared GNP without any purification step was investigated in detail using a number of different characterization techniques including microscopy,

spectroscopy, thermogravimetric, X-ray diffraction and electrochemistry. An unprecedented improvement in charge storage ability of GNP with respect to CNF of more than 30 times is reported here.

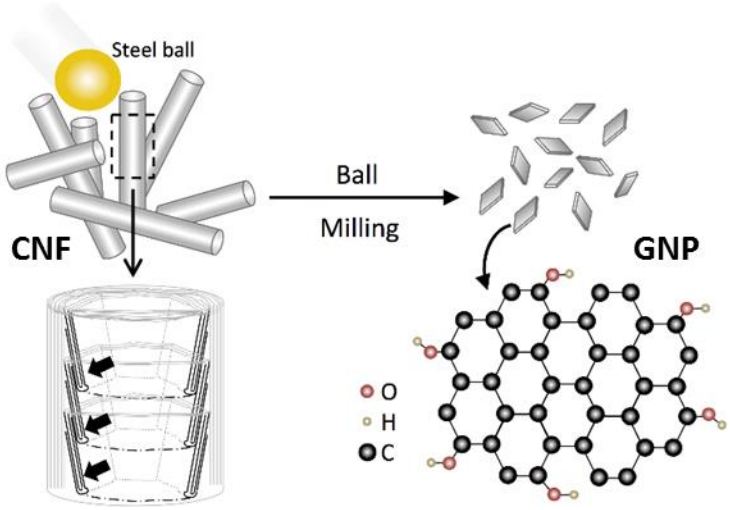

Scheme 1. Representation of the fabrication of electrochemically active GNP via dry high-energy ball milling (milling time: 20 min; vibrational frequency: 1800 rpm). The selected source of carbon, CNF, is composed by graphene stacked-nanocones that are disassembled, broken and exfoliated during ball milling in air. As result, GNP edges are mainly functionalized by hydroxyl groups (oxygen atoms in red; hydrogen atoms in grey), while the graphitic basal planes remain with minimal defects. A single layer of graphene is represented here for clarity.

2.2 Results and discussion

Conversion of CNF to GNP with an optimum energy storage ability was achieved after 20 min in a ~98% yield via mechanical ball milling (Scheme 1) using a high-energy ball mill instrument (1800 rpm) as described in the Method section. No further steps were required to obtained GNP, as no contamination was observed by energy-dispersive X-ray spectroscopy (EDS) from the ball milling process (metallic impurities) after 20 min (Figure 2b and Appendix II, Figure 1). GNP was then acid treated (8M HNO_3, 1 h reflux) to yield GNP_{AC}, in order to test electrochemical changes with an increase of the hydrophilic nature of the sample. To appraise the effect of milling on the electrochemical performance of GNP, CNF was subjected to different milling times (1, 5, 10, 20 and 30 min) under the same milling conditions. The ball milling process of CNF involves first the bond cleavage of graphitic C–C frameworks on the CNF external surface and the graphene nanocones, and then the physical delamination of the smashed graphene stacks (Scheme 1). Note

that short-times of high-energy ball milling are employed here to increase the degree of exfoliation and efficiency, while reducing the amount of fragmentation that otherwise will induce amorphous phases. In ambient atmosphere, the active carbon species (radicals and anions) generated at the unzipped edges react to give oxygenated functional groups (e.g. –OH, –C=O, –COOH) at the edges with minimal defects of the graphitic basal plane that will ensure high-quality GNP. As shown in Figure 2f, the presence of polar edge-oxygenated groups, due to the above mechanochemically driven reaction, clearly facilitates the solubility of GNP in a polar solvent such as water, enhancing their processability for energy storage devices.

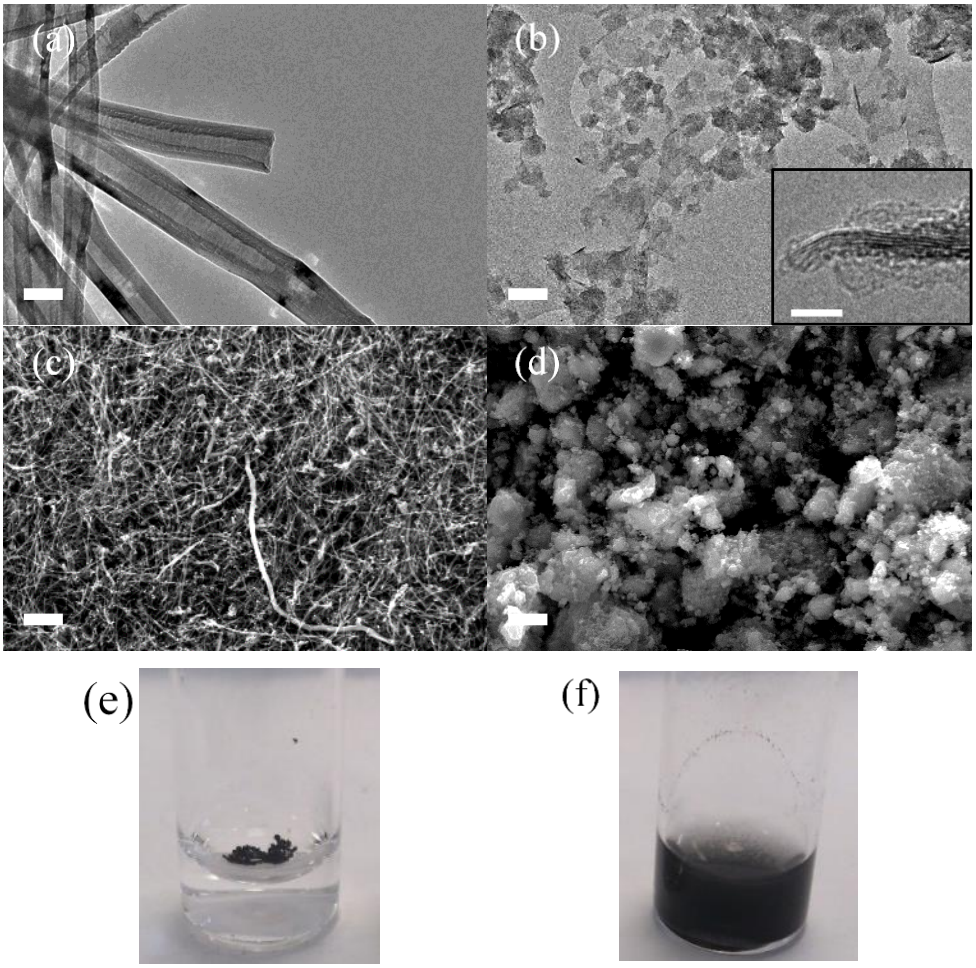

Figure 2. HRTEM images of CNF (a) and GNP (b) (scale bars: 100 nm). The inset in (b) confirms the retention of graphitization in a few-layer GNP (scale bar: 5 nm). FESEM images of CNF (c) and GNP (d) highlighting the structural changes as result of the ball milling process (scale bars: 5 μm). Images of CNF (e) and GNP (f) after sonication for 15 minutes in deionized water showing the improved dispersion of the latter.

High-resolution transmission electron microscopy (HRTEM) imaging combined with field emission scanning electron microscopy (FESEM) studies

reveal a complete transformation of CNF into GNP after a milling time of 20 min (Figure 2b). As shown in Appendix II, Figure 2, the milled material is composed only of graphitic nanoplatelets (with a size distribution between 20 and 50 nm) and no tubular carbon nanostructures can be observed, which is in agreement with the observed change in solubility. A high-magnification TEM image of a GNP oriented perpendicularly on the TEM grid (inset Figure 2b) exhibits a thickness of ~4 nm (11 graphene layers, approximately), that correlates well with the statistical analysis of 18 GNP obtained by atomic force microscopy (AFM) showing an average thickness of 6.4 ± 2.0 nm (Figure 3).

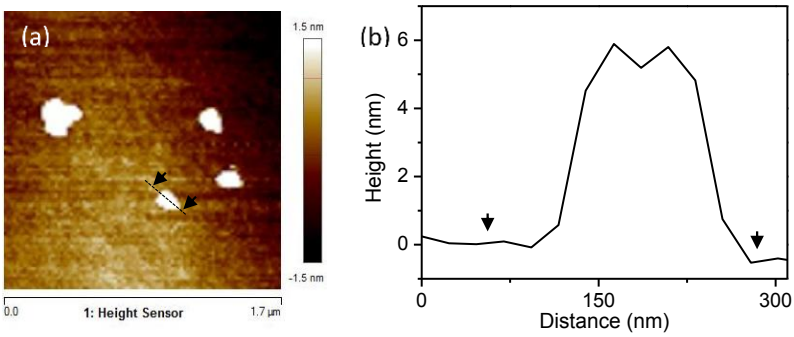

Figure 3. (a) AFM image of GNP on a silica surface and (b) the height profile taken across the dotted line on the AFM image. The GNP thickness is lower than 6 nm.

It is worth mentioning that the ball milling treatment of graphite under the same conditions does not lead to the same extent of exfoliation. Detailed SEM studies at different milling times (Figure 4c-h and Appendix II, Figure 3) clearly indicate a change on the morphology of the milled sample after just 5 min. Both low and high-magnification SEM images show a consistent morphology confirming further the high-yield transformation to GNP after 20 min. As we can see in these series of images, the milled material tends to agglomerate forming ball-like structures and the size of these agglomerates decreases with the milling time. Contamination from the milling process in form of metallic impurities was observed only after 30 min, as suggested by energy-dispersive X-ray spectroscopy (EDS) (Appendix II, Figure 4) and X-ray diffraction (XRD) data (Figure 4b). Surprisingly, when GNP is acid treated (GNP_{AC}), the sample morphology changes dramatically leading to a close laminar structure, as observed by SEM (Figure 5 and Appendix, Figure 5), that may affect the accessibility of the ions to the surface.

Thermogravimetric analysis (TGA) measurements for GNP (Figure 6a) in air present a gradual decomposition in the 250–700ºC temperature range. Below 350 ºC the small weight loss (8%) observed for GNP can be ascribed to the removal of oxygen functional groups, while the weight loss above this temperature (92%) can be solely attributed to the oxidation of pure carbon. GNP clearly decomposes at lower temperatures when compared with CNF.[26] A decrease in annealing temperatures with milling times is observed for all the milled samples (Figure 4a). However, no weight loss below 350ºC can be detected when CNF is milled less than 10 min. Figure 6b shows the XRD patterns for both GNP and CNF. The [002] peak at 26.5º of GNP is significantly broader and weaker compared to that observer for CNF suggesting solely a degree of edge-expansion due to the presence of oxygenated groups at the edges, while the graphitic basal plane remains intact.[27]

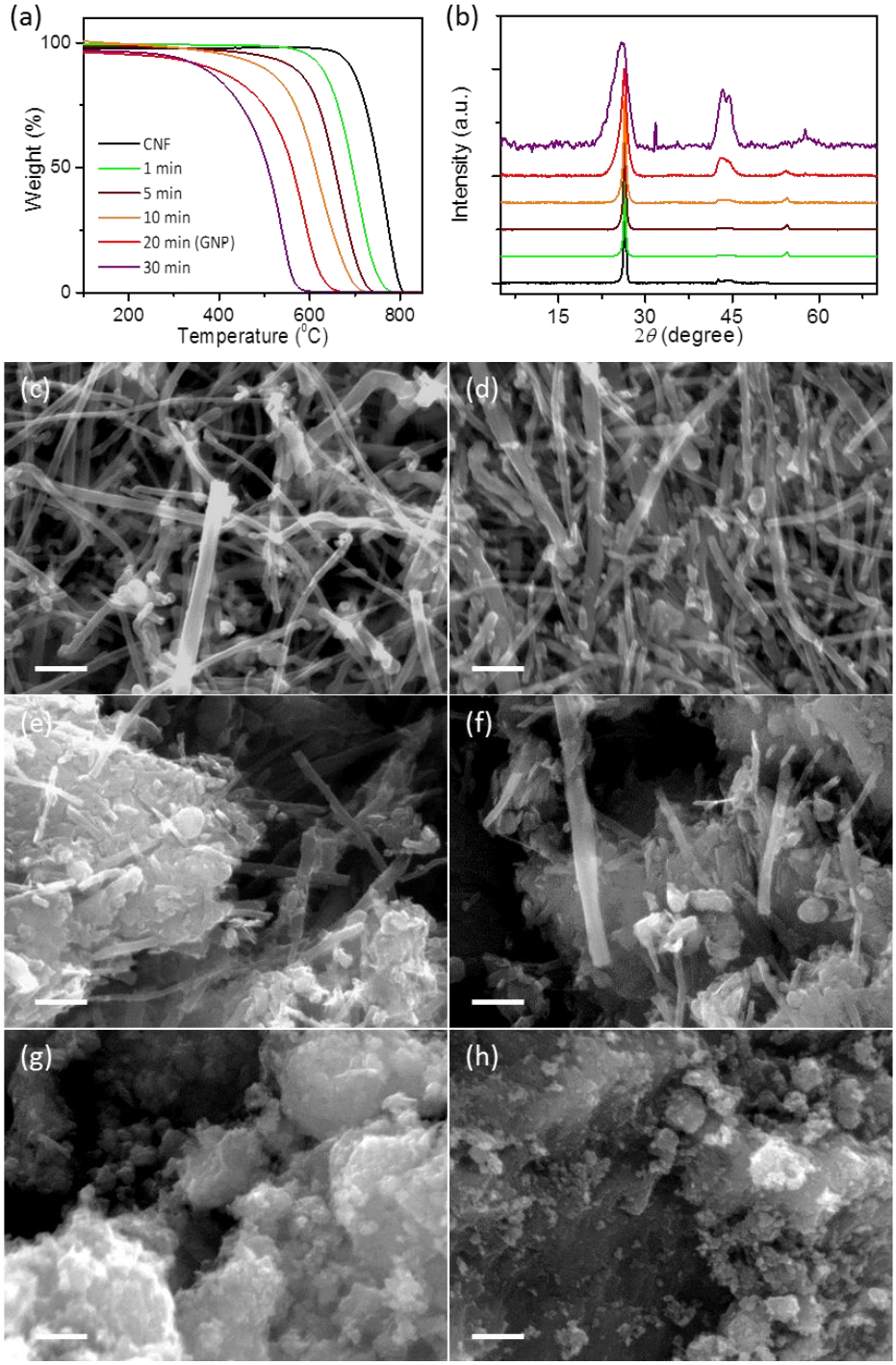

Figure 4. Comparison of TGA in air at a scan rate of 5°C/min (a) and powder XRD patters (normalized for the sake of comparison) (b) of pristine CNF (black) and milled samples after 1 (green), 5 (brown), 10 (orange), 20 (red) and 30 (purple) minutes, showing metallic contamination just after 30 minutes of milling. FESEM images of pristine CNF (c) and CNF milled after 1 (d), 5 (e), 10 (f), 20 (g) and 30 (h) minutes. Scale bars for all the images are 1 μm.

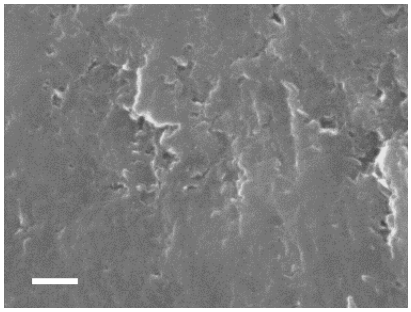

Figure 5. FESEM images of GNP after acid treatment (GNP_{AC}). Scale bars: 1 µm.

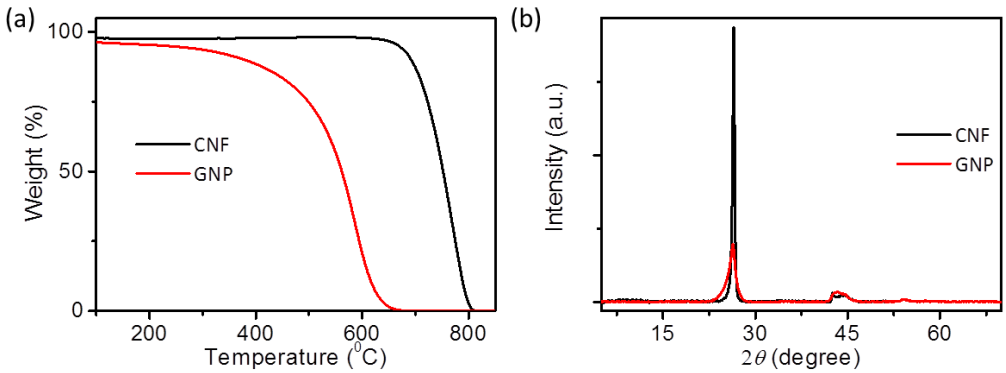

Figure 6. Comparison of TGA measurements (a) at a scan rate of 5°C/min in air and powder XRD patters (b) for CNF and GNP.

Further evidence for the chemical nature of the edge-functionalisation comes from X-ray photoelectron spectroscopy (XPS) measurements. As expected, only a pronounced C 1s peak at 284.6 eV for CNF with a trace amount of O at 532.5 eV (O/C = 0.01) (Figure 7a). After ball milling, an increase of 5 times in the O 1 s peak intensity relative to the C 1s peak (O/C = 0.05) confirms the presence of oxygen-rich groups in GNP that is in agreement with the TGA results (Figure 6a). The curve fittings of the high-resolution XPS O 1s and C 1s spectra show that the O component in GNP comes predominantly from C-OH (hydroxyl) groups (Figure 7b-d and 7f-h). It is worth mentioning that O=C-OH (carboxyl) groups (288.7 eV) will appear in GNP only after acid treatment that is in agreement with the EDS data (Appendix II, Figure 6).[28-29] Fourier transform infrared spectroscopic (FTIR) data for GNP show the characteristic vibration peak C-O at 1089 cm^{-1}, while for GNP_{AC} the most characteristic features are the adsorption bands corresponding to the C=O carbonyl stretching at 1720 cm^{-1} and the C-O stretching at 1313 cm^{-1} (Figure 7e).

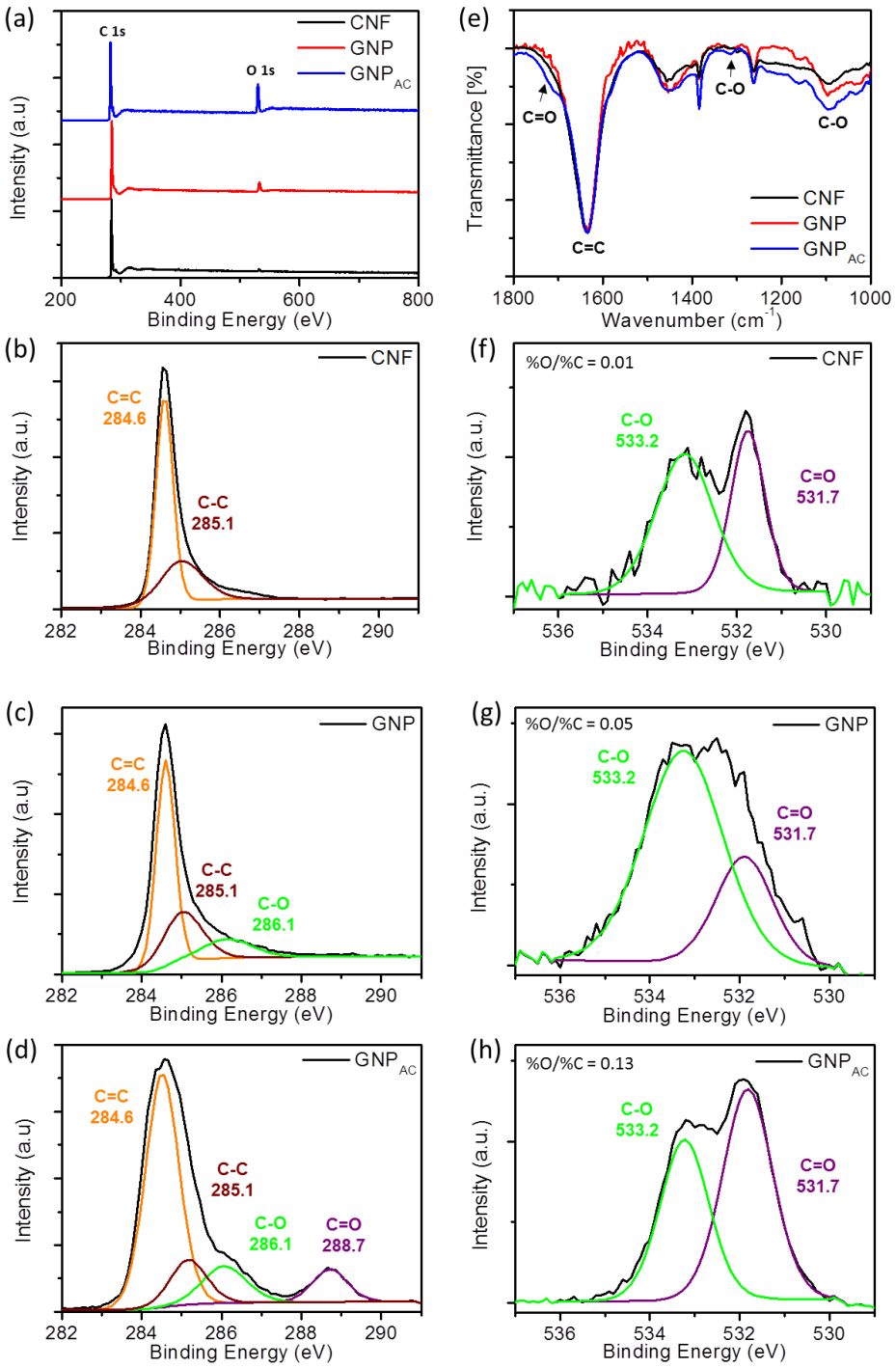

Figure 7. Comparison of the XPS wide-scan measurements for CNF, GNP and GNP_{AC}, showing a O/C relation of 0.01, 0.05 and 0.13, respectively (a). C 1s high-resolution XPS measurements of CNF (b) fitted with two components: C=C (284.6 eV) and C-C (285.1 eV), GNP (c) showing a new third component at 286.1 eV that corresponds to hydroxyl groups (C-O) and GNP_{AC} (d) fitted with the following contributions (nonoxygenated sp^2 C (284.6 eV), nonoxygenated sp^3 C (285.1 eV), hydroxyl groups (286.1 eV) and carboxyl groups (288.7 eV)). It is worth noting that the carboxyl groups (O=C-OH, 288.7 eV) appear in GNP only after acid treatment, no after milling process. FTIR data for CNF, GNP and GNP after acid treatment (e) assigning 1722 cm^{-1} (C=O stretching), 1630 cm^{-1} (C=C), 1384 cm^{-1} (C-O bending), 1313 cm^{-1} (C-O stretching) and 1089 cm^{-1} (hydroxyl C-O stretching) peaks. O 1s high-resolution XPS spectra of CNF (f), GNP (g) and GNP_{AC} (h). After ball milling the C-O component (in green) is

higher than the C=O component (in purple) for GNP, while after acid treatment for GNP_{AC} the C=O component is more intense than the C-O one.

The energy storage ability of a thin-film of GNP deposited on a glassy carbon electrode is extensively investigated in our study by cyclic voltammetry, galvanostatic charge-discharge measurements and electrochemical impedance spectroscopy in a three-electrode electrochemical cell using a nitrogen saturated aqueous solution of KOH (1M). To test the effect of increasing the hydrophilicity on the GNP surface, GNP_{AC} was also studied under the same experimental conditions. Figure 8c shows the cyclic voltammogram (CV) curves at 0.1V/s for GNP, GNP_{AC} and CNF. Trough ball milling, the ability of GNP to store charge, and thus its specific capacitance that is proportional to the area under the CV curve, has become 32 times higher (119 F/g) than the one observed for CNF (3.7 F/g) (Figure 8a). Note that the reported specific capacitance values are calculated from charging-discharging measurements (Figure 8b and 8d). Surprisingly, a short milling time such as just 1 min can increase 7 times the storage ability of the milled material (from 3.7 to 26.4 F/g). However, when CNF is subjected to milling times longer than 20 min, the specific capacitance of the milled materials decreases drastically (Figure 8a-b). The effect of milling on the rate capability of GNP can be clearly observed when variations of the specific capacitance with the current density for GNP and CNF are compared, showing much higher values for GNP in the investigated range (0.5 to 10A/g) (Appendix II, Figure 7). For both samples the specific capacitance decreases with the increase of current density. It is also worth mentioning that after acid treatment (GNP_{AC}) only a small change in the storage charge ability is observed (from 119 to 140 F/g). Comparison of the galvanostatic charging-discharging cycles for GNP, GNP_{AC} and CNF at the same current density of 0.5 A/g (Figure 8d) demonstrates a behaviour for GNP and GNP_{AC} that is a combined contribution from double-layer capacitance and redox pseudocapacitance, while a solely double-layer contribution is observed for CNF.

It is not surprising that after ball milling the studied milled samples show higher discharging times than CNF that exhibits an intrinsic small surface area (15-25 m^2/mg as provided by the supplier) and a poor wettability due to their high grade of graphitization (Figure 8b). Although GNP_{AC} shows slightly

longer discharging time than GNP, the charge–discharge curves for GNP are more symmetric (quick current/voltage response) and with much lower iR drop (lower contact resistance) than that obtained for GNP_{AC} (0.3 and 0.6 mV, respectively).[30] The latter is in agreement with the reduction in the internal resistance observed for GNP with respect to GNP_{AC}.

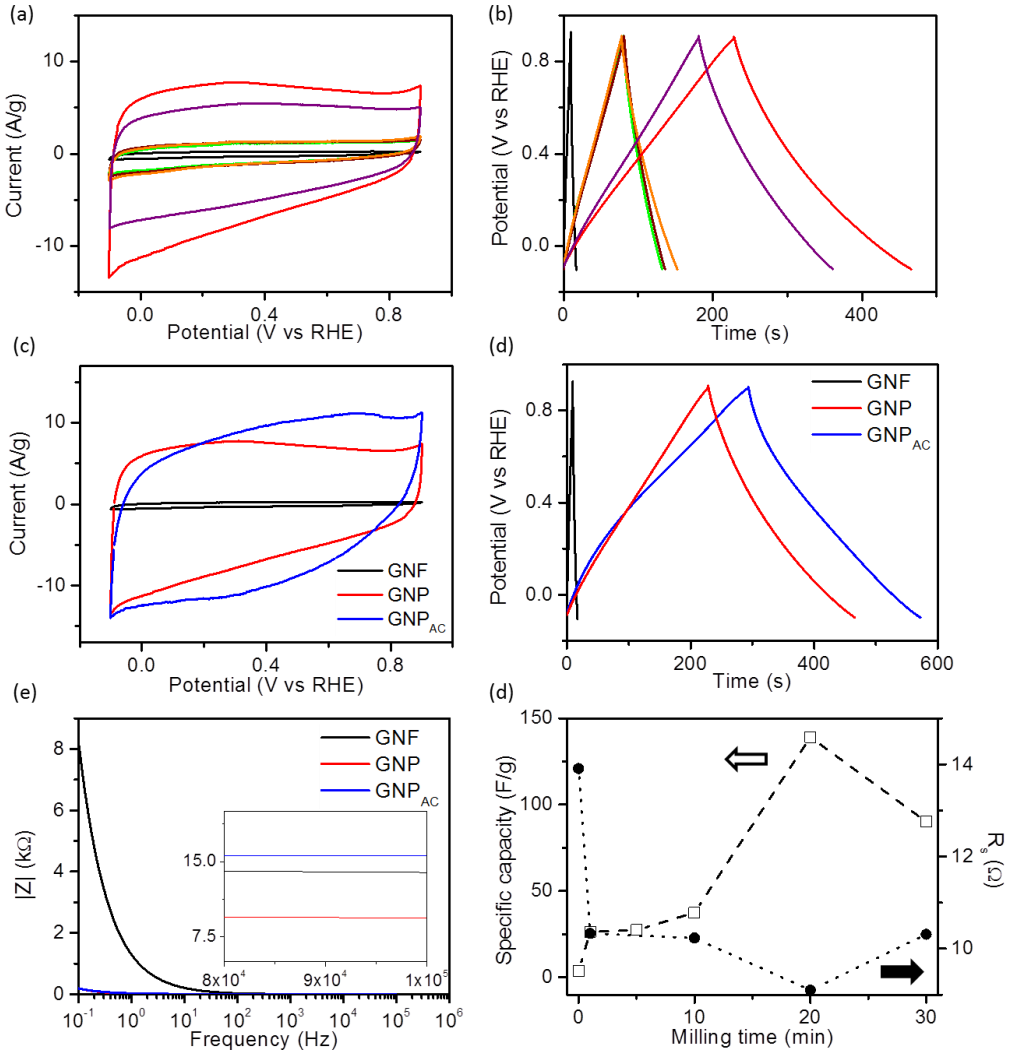

Figure 8. (a,c) Comparison of CV at 0.1V/s and (b,d) galvanostatic charging–discharging measurements at 0.5 A/g in 1M KOH of pristine (black) and milled CNF after 1 (green), 5 (brown), 10 (orange), 20 (red) and 30 minutes (purple) (a-b, respectively) and CNF, GNP and GNPAC (c-d, respectively). (e) Bode plots in the 10^{5}–10^{-1} frequency range with 5mV AC signal amplitude. (f) Correlation between the specific capacitance (F/g) (squares), based on galvanostatic charge-discharge cycles, and the solution resistance (Rs) (circles), obtained from the electrochemical impedance spectroscopy measurements, with the increasing milling time (1, 5, 10, 20 and 30 min).

To investigate this point further, we carried out electrochemical impedance spectroscopy (EIS) measurements for GNP and GNP_{AC} and compared them

with that observed for CNF.[31] Their Nyquist plots in the 0.1–10^5 Hz frequency range are shown in Appendix II, Figure 8.

In the high frequency region, the values obtained from the x-axis intercept of the Nyquist plots correspond to the ionic resistance (R_s) at electrode/electrolyte interface that can be also extracted from their Bode plots shown in the inset of Figure 8e.[32] After ball milling R_s decreases, as the value found for GNP (10.0 Ω) is lower than the one observed for CNF (13.5 Ω). Figure 8f clearly highlights the relationship between the ionic resistance (circles) and the specific capacitance (squares) over milling time, in which GNP shows a maximum value of storage ability with a minimum value of ionic resistance. The absence of a semi-circle and a high slope at low frequency in the GNP Nyquist plot indicates a low internal and charge-transfer resistance, suggesting that GNP is especially well suited for use as an electrode material toward electrochemical energy storage (Appendix II, Figure 9). The presence of oxygenated groups at the edges appears to improve the ionic diffusion of the electrolyte on the electrode surface leaving a more open structure.[33] However, when GNP is acid treated the R_s increases substantially (15.6 Ω). This can be explained by the change in the charge distribution, due to the acid decoration in GNP_{AC} on both the edges and the graphitic basal plane that affects the ionic accessibility to the carbon surface increasing the ionic resistance. This is in agreement with the change in morphology observed by SEM for GNP_{AC}.[34] Moreover, the appearance of a high-frequency semicircle in its Nyquist plot evidences an increase in the charge transfer resistance at the current collector/electrode interface (Appendix II, Figure 10). Thus, the acid treatment induces a resistive behaviour in GNP_{AC} that is in sharp contrast with the combined capacitive behaviour observed for GNP.

A comparison of the production rate of graphitised nanoplatelets for our method with the recently reported low-energy ball milling methods (≤ 500 rpm) using graphite as a source of carbon[35-37] further highlights the advantage of using CNF comprised of nanographene stacks under high-energy conditions. Taking into account the size of the ball mill container, the production rate for the method described here is 291 times higher. Comparing specific capacitance values, the value obtained for GNP is similar or higher to those reported for the

above low-energy ball milling methods. For example, commercially available graphite nanoplatelets (GNP_C) shows a much smaller specific capacitance (20 F/g) in comparison with the obtained GNP after milling CNF for 20 min (Appendix II, Figure 11), suggesting GNP a cheaper alternative to GNP_C (615.5F/$ and 264F/$, respectively)[38]. Moreover, due to the very short times used in our method (20 min compared to 48 h), no further purification steps (such as Soxhlet extraction in acid media, 48 h) are required to remove metallic impurities from the ball milling process. As we demonstrate above, a change in the distribution charges can affect the ionic accessibility to the carbon surface increasing the ionic resistance of the electrode, which can have detrimental effects on the storage ability performance of the material.

2.3 Conclusions

This is the first example in which the interiors of hollow carbon nanofibers have been exploited as source of carbon to produce few-layer graphene materials for energy storage applications with an optimized storage ability performance using dry ball milling conditions in absence of exfoliating agents. We have demonstrated a facile, low-cost and scalable method to produce high-quality, few-layer GNP from stacked-cup CNF by high-energy ball milling in high-yield in just 20 min showing a combined contribution from double-layer capacitance and redox pseudocapacitance. Previous attempts using one-dimensional carbon nanostructures such as carbon nanotubes, also under high-energy conditions (3000 rpm), yielded to mixtures of damaged carbon nanotubes together with the expected crumbed graphene sheets[37] highlighting the importance of the careful selection of the right source of carbon with the appropriated mechanical properties.

The major advantage of our ball milling approach to produce GNP over the tedious chemical processes (oxidation, sonication, separation and reduction) is that it is a very quick, one-pot and eco-friendly process in which no hazardous wet-chemicals are used producing minimal distortion on the graphitic basal plane. The production rate of our method, which does not require any purification step and yields GNP with a similar or much higher specific capacitance value, is much higher compared to those for the low-energy ball milling methods using graphite as source of carbon. Our approach opens up a

new strategy for GNP production towards energy storage applications from unexplored exotic multi-structured nanocarbon materials such as platelet or fishbone carbon nanofibers.

2.4 Experimental part

Preparation of graphene nanoplatelets

GNP was prepared from CNF produced by chemical vapor deposition (purchased from Pyrograph, 15-25m^2/g) via mechanical ball milling using a high-energy Retsch MM400 ball mill instrument (1800 rpm). In a typical experiment, 50 mg of CNF were placed into a stainless steel container (5 mL) with a stainless steel ball (10 mm diameter) and milled in air for 20 minutes to afford GNP (98% yield). Note that no further purifications steps are required. To investigate the ball milling effect on the electrochemical performance of the obtained milled materials, CNF was also milled at different milling times (1, 5, 10 and 30 minutes) under the same conditions. To produce GNP_{AC}, GNP (15 mg) was added into a round flask with 10 mL of HNO_3 (8M) and sonicated for 15 minutes before refluxing the mixture for 1 hour. The resultant mixture was diluted with deionized water and filtered through a 0.2 *μm pore size* PTFE membrane. The black solid was dried overnight under reduced pressure to give GNP_{AC}. Commercial graphene nanoplatelets (GNP) were purchased from Asbury (2299 GNP, 402 m^2/g).

Material characterization

HRTEM images and EDS measurements were performed using a Jeol 2100F transmission electron microscope at an accelerating voltage of 200 kV. TEM specimens were prepared by casting several drops of a suspension of the carbon material in hexane onto a copper-grid mounted "holey" carbon film before drying under a stream of nitrogen. SEM images were acquired on a field emission scanning electron microscope (XL30 FESEM) with 15 kV working voltage. AFM images were acquired by using a Fast Scan Bio (Bruker) with NanoScope Analysis 1.50 software. All the images presented in this article were acquired using tapping mode under ambient conditions and the samples were prepared by drop casting on a silica substrate a suspension of carbon material in hexane. TGA was carried out on a SDT Q-600 TA instrument over the range of 25-1,000 °C in air with a scan rate of 5 °C/min. Powder XRD patterns were recorded using a PANalytical diffractometer equipped with Cu Kα source (λ=1.5418Å). The data was analysed and processed using the X'

Pert Data software package. XPS measurements were recorded using a Kratos with monochromated Al Kα radiation (10 kV anode potential, 15 A emission current) in fixed analyser transmission mode (80 eV pass energy).

Electrochemical measurements

Electrochemical experiments were carried out on a computer-controlled potentiostat (Autolab 201A) at room temperature using a conventional three-electrode cell with a nitrogen saturated 1M KOH aqueous solution as electrolyte. A Pt wire and a reversible hydrogen reference electrode (RHE) were used as the counter and the reference electrode, respectively. All potentials were measured and reported versus the RHE at room temperature. 0.5 mg of carbon material was mixed with 0.03 mg of PTFE (0.5% in DI water), 0.1 mg of graphite powder (15%) and 0.5 mL of deionized water to form a homogeneous suspension after sonication. Subsequently, 10 µg of the suspension was placed onto the surface of glassy carbon electrode (GCE) using a micro syringe and the electrode was allowed to dry at room temperature before measurements. Prior to use, the working glassy GCE (3 mm in diameter) was polished mechanically with aqueous slurries of alumina powder (0.05 µm) and rinse with Mill-Q water and acetone, and allowed to dry under nitrogen. The specific capacitance (C_{sp}) in F/g was calculated using galvanostatic charging–discharging measurements using the following expression: $C_{sp} = (t_d \bullet I)/\Delta V$, where t_d (s), I (A/g) and ΔV (V) are the discharging time in galvanostatic cycles, the current density and the voltage window, respectively.

2.5 References

1. P. Simon and Y. Gogotsi, Nat. Mater., 2008, **7**, 845–854.
2. Y. Li, W. Zhou, H. Wang, L. Xie, Y. Liang, F. Wie, J-C. Idrobo, S. J. Pennycook and H. Dai, Nat. Nanotechnology, 2012, **7**, 394–400.
3. G. C. Liu, N. Z. Yu, D. Neff, A. Zhamu and Z. N. Jang, Nano Lett., 2010, **10**, 4863–4868.
4. H. Jang, Y. J. Park, X. Chen, T. Das, M-S. Kim and J-H. Ahm, Adv. Mater., 2016, **28**, 4184-4202.
5. L-H. Hu, F. Y. Wu, C-T. Lin and A. N. Khlobystov, Nat. Commun., 2013, **4**, 1687, 1–7.
6. P. R. Somani, S. P. Somani and M. Umeno, Chem. Phys. Lett., 2006, **430**, 56–59.
7. M. Zhu, J. Wang, B. C. Holoway, R. A. Outlaw, X. Zhao, K. Hou, V. Shutthanandan and D. M. Manos, Carbon, 2007, **45**, 2229–2234.
8. S. Pei and H-M. Cheng, Carbon, 2012, **50**, 3210–3228.
9. M. Zhao, Z-Y. Guo, O. Ambacher, C. E. Nebeol and R. Hoffmann, Carbon, 2015, **83**, 128–135.
10. A. M. Dimiev, G. Ceriotti, A. Metzger, N. D. Kim and J. M. Tour, ACS Nano, 2016, **10**, 274–279.
11. W. S. Hummers and R. E. Offeman, J. Am. Chem. Soc., 1958, **80**, 1339–1339.
12. J. D. Lamphene, B. Rogers, C. Luth, C. H. Bolster and S. K. Walker, Envir. Eng. Science, 2014, **31**, 350–359.
13. H. Wang, Y. Wang, Z. Hu and X. Wang, ACs Appl. Mater. Interfaces, 2012, **4**, 6827–6834.
14. A. Y. S. Eng, A. Ambrosi, C. K. Chua, F. Sanek, Z. Sofer and M. Pumera, Chem. Eur. J., 2013, **19**, 12673–12683.
15. B. Zhao, P. Liu, Y. Jiang, D. Pan, H. Tao, J. Song, T. Fang and W. Xu, J. Power Sources, 2012, **198**, 423–427.
16. M. Cai, D. Thorpe, D. H. Adamson and H. C. Schiepp, J. Mater. Chem., 2012, **22**, 24992–25002.
17. M. Lotya, Y. Hernandez, P. J. King, R. J. Smith, V. Nicolosi, L. S. Karlsson, F. M. Blighe, S. De, Z. Wang, I. T. McGovern, G. S. Duesberg and J. N. Coleman, J. Am. Chem. Soc., 2009, **131**, 3611–3620.
18. V. M. Samoilov, E. A. Danilov, A. V. Nikolaeva, G. A. Yerpuleva, N. N. Trofimova, S. S. Abramchuk and K. V. Ponkratov, Carbon, 2015, **84**, 38–46.
19. W. Zhao, M. Fang, F. Wu, H. Wu, L. Wang and G. Chen, J. Mater. Chem., 2010, **20**, 5817–5819.
20. V. León, M. Quintana, M. A. Herrero, J. L. G. Fierro, A. de la Hoz, M. Prato and E. Vázquez, Chem. Comm., 2011, **47**, 10936–10938.
21. V. León, A. M. Rodriguez, P. Prieto, M. Prato and E. Vázquez, ACS Nano, 2014, **8**, 563–571.
22. M. C. Gimenez-Lopez, A. La Torre, M. W. Fay, P. D. Brown and A. N. Khlobystov, Angew. Chem. Int. Ed., 2012, **52**, 2051–2054.
23. A. La Torre, M. C. Gimenez-Lopez, M. W. Fay, C. Herreros-Lucas, P. D. Brown and A. N. Khlobystov, Small, 2015, **11**, 23, 2756–2761.
24. A. La Torre, M. W. Fay, G. A. Rance, M. C. Gimenez-Lopez, W. Solomonsz, P. D. Brown and A. N. Khlobystov, Small, 2012, **8**, 1222–1228.
25. A. E. Del Rio-Castillo, C. Merino, E. Díez-Barra and E. Vázquez. Nano Res., 2014, **7**, 963–972.

26. R. Cruz-Silva, A. Morelos-Gómez, S. Vega-Díaz, F. Tristán-López, A. L. Elias, N. Perea-López, H. Muramatsu, T. Hayashi, K. Fujisawa, Y. A. Kim, M. Endo and M. Terrones, ACS Nano, 2013, **7**, 3, 2192–2204.
27. G. Titelman, V. Gelman, S. Bron, R. L. Khalfin, Y. Cohen and H. Bianco-Peled, Carbon, 2005, **43**, 641–649.
28. M. Wang, L. D. Duong, N. T. Mai, S. Kim, Y. Kim, H. Seo, Y. C. Kim, W. Jang, Y. Lee, J. Shur and J. Nam, ACS Appl. Mater. Interfaces, 2015, **7**, 1348–1354.
29. G. Lu, H. Wang, Y. Yang, T. Deng, C. Cheng, Y. Zhu and X. Hou, ACS Catal., 2015, **5**, 5636–5646.
30. H. Wang, L. Shi, T. Yan, J. Zhang, Q. Zhong and D. Zhang, J. Mater. Chem. A, 2014, **2**, 4739–4750.
31. I. Dumitrescu, P. R. Unwin and J. V. Macpherson, Electro. Comm., 2009, **11**, 2081–2084.
32. B. Abdulhakeem, B. Farshad, M. Damilola, T. Fatemeh, F. Mopeli, D. Julien and M. Ncholu, RSC Advances, 2014, **4**, 39066–39072.
33. Y. J. Oh, J. J. Yoo, Y. I. Kim, J. K. Yoon, H. N. Yoon, J. Kim and S. B. Park, Electrochimica Acta, 2014, **116**, 118–128.
34. J. R. Miller, R. A. Outlaw and B. C. Holloway, Science, 2010, **329**, 1637–1639.
35. I. Jeon, H-J. Choi, S-M. Jung, J-M. Seo, M-J. Kim, L. Dai and J-B. Baek, J. Am. Chem. Soc., 2013, **135**, 1386–1393.
36. I-Y. Jeon, H-J. Choi, M. Choi, J-M. Seo, S-M. Jung, M-J. Kim, S. Zhang, L. Zhang, Z. Xia, L. Dai, N. Park and J-B. Baek, Sci. Rep., 2013, **3**, 1810, 1–7.
37. C. S. Tiwary, B. Javvaji, C. Kumar, D. R. Mahapatra, S. Ozden, P. M. Ajayan and K. Chattopadhyay, Carbon, 2015, **89**, 217-224.
38. S. H. Aboutalebi, A. T. Chidembo, M. Salari, K. Konstantinov, D. Wexler, H. K. Liu and S. X. Dou, Energy Environ. Sci., 2011, **4**, 1855-1865.

Chapter 3

Growth of hollow nano-cages on defective graphene flakes driven by the agglomeration and release of metal atoms

3.1 Introduction

The development of carbon-based materials has received tremendous attention owing to their multifunctional properties. Free-standing carbon nano-onions (also known as carbon cages) have demonstrated useful properties for a wide range of applications, including catalysis, sensing, adsorption, bioimaging, water purification, or energy-storage and conversion.[1-8] In order to improve the properties of such carbon nanostructures, different synthetic approaches for controlling their growth and composition have been intensively investigated in recent years.[9-10] For example, the size of the carbon nano-onions and the thickness of their graphene layers can be selectively controlled by factors such as temperature and time, and the size of the catalyst nanoparticle (NP) selected as template.[11]

Similar to the recently reported three dimensional (3D) carbon nanotube/graphene architectures,[12] nanostructures composed of carbon nano-onions and graphene can potentially exhibit high surface area accompanied by an intrinsic high electrical conductivity. Generally, the strategy for the synthesis of such carbon architectures involves the deposition of metallic NPs on graphene acting not only as a template, but also as a catalyst for the subsequent growth of carbon nanostructures at high temperatures.[13-14] In this way, Zhang and co-workers grew graphene shells on uniform copper nanoparticles supported on graphene by a one-step in situ chemical vapour deposition (CVD) process.[15]

Interestingly, such carbon-coating on nanoparticles offers an effective protection to the metallic core and prevents the agglomeration of NPs not only during the carbonization process at high temperatures but, more importantly, during the utilisation of such hybrid nanostructures as electrodes materials for energy storage.[16] For example, carbon-coated Fe_2O_3 nanoparticles dispersed on graphene sheets (Fe_2O_3@C@graphene) have shown outstanding Li^+ storage properties when used as anode materials for lithium ion batteries, due to the semipermeable carbon shell (made of two to five layers).[17] These hybrid nanostructures reported by Tour et al. were obtained by a two-step CVD growth (initial reduction and carbon coating of Fe_3O_4 supported on graphene (Fe_3O_4@graphene) to Fe@C@graphene under methane atmosphere) followed by oxidation of the metal core to Fe_2O_3 in air.

In order to take full advantage of the inner confined space of carbon nano-onions and, therefore, to increase of the surface area and porosity, acid treatments are usually applied that can cause detrimental effects on the physicochemical properties of the resultant nanostructures.[18-19] Thus, hollow carbon spheres anchored on the surface of carbon nanotubes were reported by Fan et al. after etching MnO_2 NPs used as a template.[20] Interestingly, the preparation of unsupported hollow carbon nanocages by iodine or NH_4Cl-assisted heat treatment have been recently reported.[21-22] In these studies, the formation of a soluble intermediate iron salt that can be easily removed is demonstrated to be the key factor for the preparation of hollow carbon nano-onions.

One-step synthetic methods allowing the decoration of carbon surfaces with hollow carbon nano-cages in a controllable manner are highly desirable.[23] Quintana et. al., reported recently the synthesis of hollow carbon nano-onions at the edges of few layer graphene by ultrasonication of fullerenes in organic solvent, however the formation of nano-diamonds as side product reveal the lack of knowledge about the real mechanism.[24] To the best of our knowledge, the synthesis of carbon nano-onions with special attention to the nanoparticle-support has not been investigated.

In this work, we study the formation process of carbon nano-onions (or nano cages) and the role of the presence of chemical defects on the carbon surface when preformed Fe_3O_4 NPs are supported on a two-dimensional carbon substrate. Unlike previous studies where the catalytic nanoparticle is covered by graphitic carbon at high temperatures due to the saturated carbon atmosphere (i. e. methane in CVD), here, the effect of the carbon substrate in the catalytic formation of nano-cages is investigated by thermal treatment in a protective atmosphere (i. e. argon) in the absence of any carbon-containing gas, allowing the migration and coalescences of nanoparticles.

3.2 Results and discussion

Small pseudo-spherical iron oxide nanoparticles (Fe_3O_4NPs) of 4 nm diameter on the surface of graphite flakes were selected for studying the formation of carbon nano-onions, as they are prone to form carbon nanostructures at high temperatures in inert atmosphere due to their catalytic properties (Appendix III, Figure 1). The selected Fe_3O_4NPs were previously synthetized via the thermal decomposition of iron (III) acetylacetonate in phenyl ether solvent in the presence of 1,2-hexadecanediol acting as reducing agent and, oleic acid and oleylamine as surfactants to control the nucleation and growth.[25]

In order to appraise the effect of the presence of anchoring points on the basal plane of the carbon support during thermal annealing at high temperatures under inert atmosphere, two different graphite flakes were employed for the study, named as GF and GF_{OX}. While GF_{OX} was used as received from the company, GF was ball-milled to reduce its original size from natural graphite flake to powder (Appendix III, Figure 2). After the milling, GF size was successfully reduced as observed by SEM, being slightly larger than GF_{OX} flakes, 2µm and 300nm, respectively (Appendix III, Figure 3). More importantly, neither their graphitization, as confirmed by the sharp diffraction peak at 26.4^0 (Appendix III, Figure 4), nor chemical composition were affected during the ball milling. In fact, X-ray photoelectron spectroscopy (XPS) showed higher oxygen content on the surface of as received GF_{OX} (O/C = 0.08) with respect to GF (O/C = 0.02), which indicates the superficial chemical functionalization of GF_{OX} (Appendix III, Figure 5) and allows the use of GF as a background structure to elucidate the relevance of electrostatic interaction (NP-GF_{OX}) with respect to van der Waals interactions (NP-GF) between the nanoparticle and carbon support during thermal annealing.

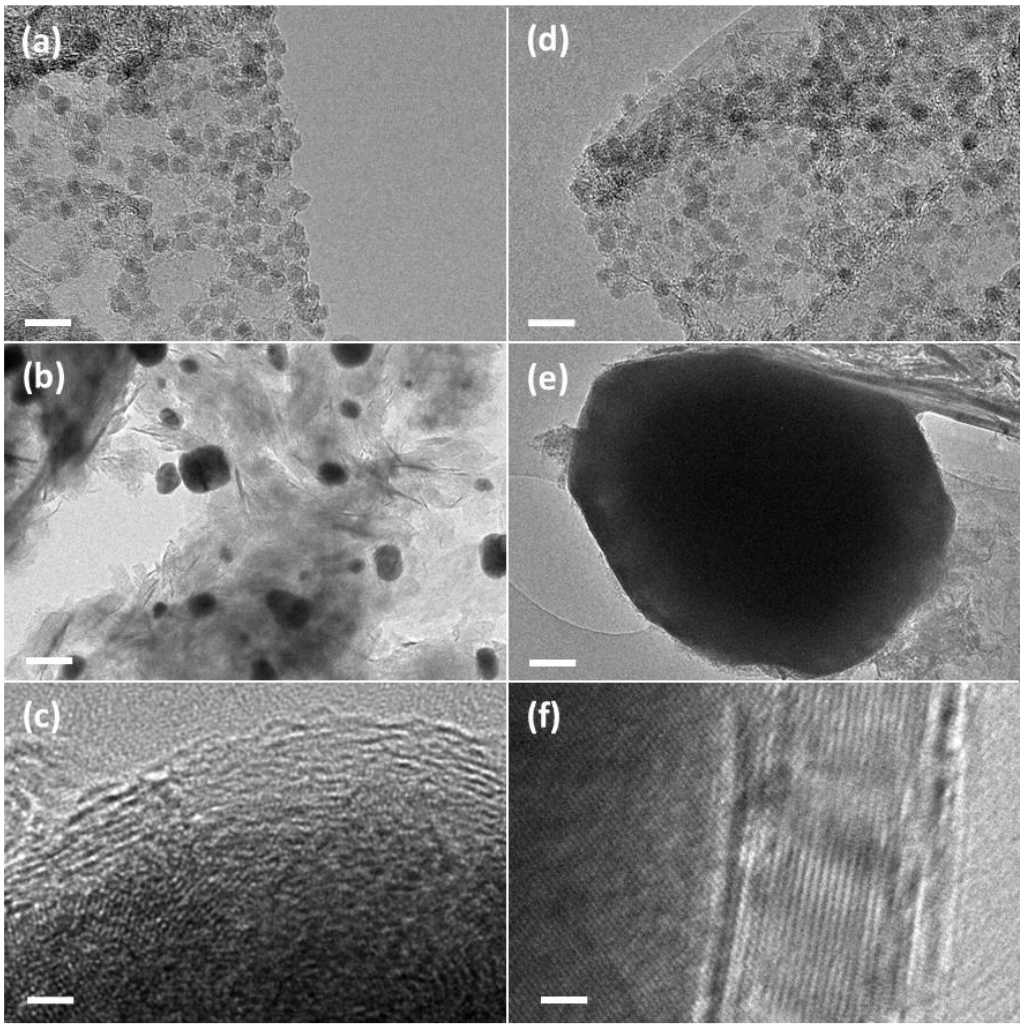

Figure 1. Bright-field TEM images of initial (a) Fe_3O_4/GF_{OX} and (d) Fe_3O_4/GF. (b-c) $Fe@C/GF_{OX}$ and (e-f) Fe@C/GF after annealed hybrids at 1000^oC for 2 hours in argon. Scale bars are 200 (b), 50 (e), 10 (a,d) and 2 nm (c,f).

For the hybrid formation, after purification the as-synthetized Fe_3O_4NPs (50 mg) were dispersed via sonication in organic solvent (120 ml of hexane) in the presence of graphite flakes (GF or GF_{OX}) (100 mg) to yield Fe_3O_4/GF_{OX} (Scheme 1a) and Fe_3O_4/GF (Scheme 1b), respectively. Transmission electron microscopy (TEM) studies showed that both hybrids have supported NPs with identical sizes, as the sonication does not affect the size of the NP, which were measured as 3.9 ± 1 and 4 ± 0.6 nm in Fe_3O_4/GF_{OX} and Fe_3O_4/GF respectively (Appendix III, Figure 6). In addition, they have also comparable NP assembly on the surface of both carbon supports, revealing neither nanoparticle agglomeration nor carbon support dependence (Figure 1a and Figure 1d). However, thermogravimetric analysis (TGA) of the hybrids indicated that the residual weight remaining after annealing the hybrid samples at 1000^0C in air

that can be attributed to Fe_2O_3 is slightly higher for Fe_3O_4/GF_{OX} (25.6%) than for Fe_3O_4/GF (20.5%) (Appendix III, Figure 7). Fe_3O_4/GF_{OX} hybrid is expected to be slightly more decorated with nanoparticles than Fe_3O_4/GF hybrid, because of the presence of polar oxygen-groups on the basal plane of GF_{OX} that can act as anchoring points. Moreover, Fe_3O_4NPs are expected to interact stronger with GF_{OX} surfaces than with GF ones where only van der Waals forces are mainly present.[26-29] Thus, the formed hybrids (Fe_3O_4/GF and Fe_3O_4/GF_{OX}) with identical NPs on the surface are ideal platforms for studying the role of chemical defects (mainly carboxylic groups COOH) on the carbon nano-onions growth.

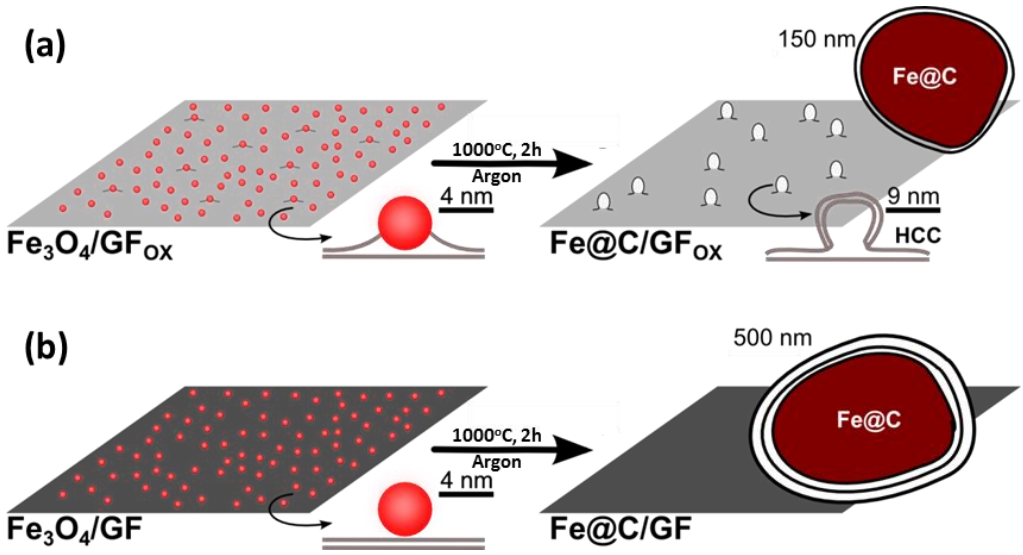

Scheme 1. Schematic representation of the annealing treatment of initial (a) Fe_3O_4/GF_{OX} and (b) Fe_3O_4/GF hybrids, respectively, where preformed nanoparticles are homogeneously dispersed on the carbon surface. After thermal treatment, large metal-carbon core-shell nanoparticles (Fe@C) and hollow carbon cages (HCC) are observed on the surface of the carbon substrate (GF_{OX}) whereas only large metal-carbon core-shell nanoparticles (Fe@C) are observed in annealed Fe_3O_4/GF hybrid.

Annealing Fe_3O_4/GF_{OX} hybrid at 1000^0C for 2 hours in argon ($Fe@C/GF_{OX}$) produces a dramatic change on the nanoparticle morphology (Scheme 1a). The initial monodispersed 4 nm Fe_3O_4 NPs (Figure 1a) are transformed into larger nanoparticles (Figure 1b) with diameters of 150 ± 50 nm (Appendix III, Figure 8). A more pronounced effect was observed when nanoparticles supported on a more graphitized (low O/C) carbon surface (GF) are subjected to the same thermal treatment (Scheme 1b). As shown in Figure 1e, nanoparticles agglomerate to form larger nanoparticles in Fe@C/GF, for possessing the diameter much larger (with a maximum size of 500 nm) than the nanoparticles

in Fe@C/GF_{OX} (Figure 1b). Larger carbon-coated iron nanoparticles in Fe@C/GF (500nm) than in Fe@C/GF_{OX} (150 nm) suggest that the nanoparticles can migrate and coalesce more easily when supported on a graphitized carbon surface (GF) at 1000^{o}C. In fact, it is worth mentioning that the observed nanoparticle agglomeration was not reported before when iron oxide nanoparticles, also located on a two-dimensional carbon support, were treated via CVD at high temperatures conditions.[17] In such conditions, a protective graphitized carbon layer covers immediately the nanoparticle surface, retaining their size. In contrast, in our study, the nanoparticles are not in the presence of such a saturated carbon environment, which does not result in the immediate protective carbon shell, so nanoparticles are able to migrate along the surface and coalesce into larger nanoparticles facilitated by the high thermal conditions.

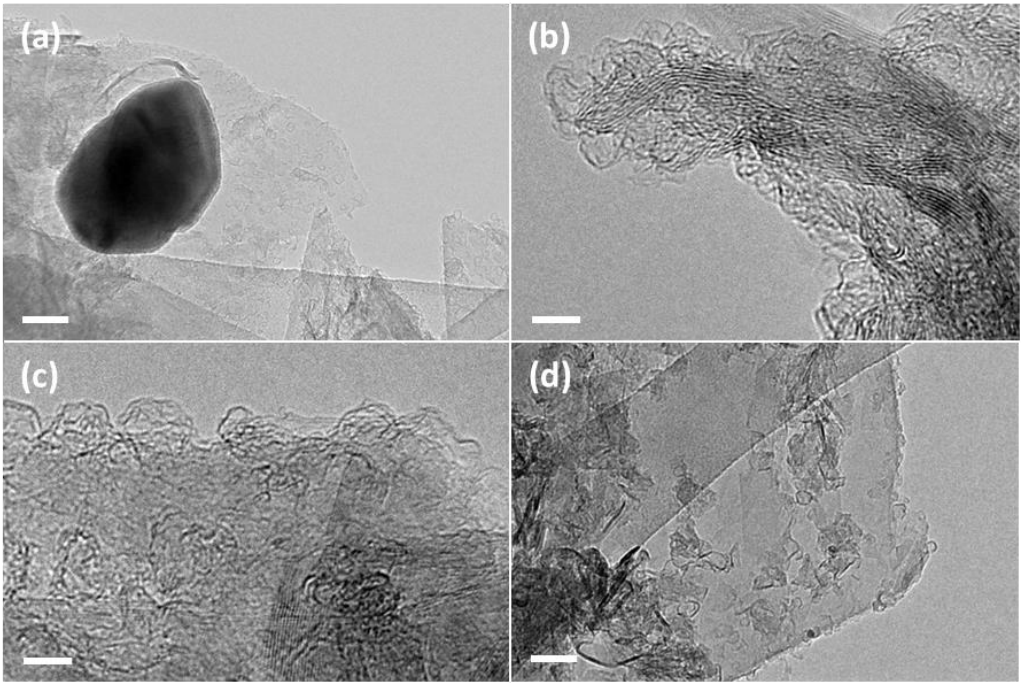

Figure 2. Bright-field TEM images of (a-c) Fe@C/GF_{OX} showing the presence of hollow carbon cages (HHC) on the surface of graphene (GF_{OX}). (d) TEM images of Fe@C/GF hybrid with no superficial transformation. Scale bars are 50 (a,d), 10 (b) and 5 nm (c).

Surprisingly, the surface of the carbon support in Fe@C/GF_{OX} is drastically modified during annealing at 1000^{o}C for 2 hours under inert atmosphere (Figure 2a), forming numerous hollow carbon cages (HCC). The resulting hollow carbon cages, which are mostly made of 2-3 graphene layers, are uniformly distributed along the carbon surface (Figure 2b-c). Statistical

analysis of the hollow carbon cages, which would be presumably created by iron nanoparticles, reveals a larger average size (9 ± 2 nm) with respect to the initial 4 nm metal oxide nanoparticle (Appendix III, Figure 9), suggesting the agglomeration of the nanoparticles during the thermal treatment. In contrast, the carbon surface after annealing Fe_3O_4/GF (Figure 2d) after the same procedure remains practically unchanged, with scarce amount of hollow carbon cages are observed along the carbon surface (Appendix III, Figure 10). Hence, the observed differences on the carbon surface after thermal treatment suggest that interaction between the catalytic nanoparticles with its support plays an important role.

The presence of mainly van der Waals interactions between nanoparticles and the graphitized carbon surface (GF) enables mostly the free migration and coalescence of nanoparticles, leading to the observed large carbon-coated iron nanoparticles in Fe@C/GF (Appendix III, Figure 11). In contrast, the stronger interaction with a more defective carbon surface (GF_{OX}) (based on electrostatic interaction) would hinder nanoparticle migration (Figure 3a, inset). To prove this point, Fe_3O_4/GF_{OX} hybrid was heated in air (300^{o}C) to remove the surfactant which acts as a stabilizer. The complete removal of the surfactant does not promote the agglomeration of nanoparticles (Figure 4a-b), even after heating the hybrid at 300^{o}C for a long period of time in air (Appendix III, Figure 12), as the nanoparticles retain their pseudo-spherical shape and size. The removal of the surfactant is confirmed by thermal gravimetric analysis (Figure 4c) and also electrochemically (Figure 4d), improving the pseudo-capacitance of the hybrid due to a more accessible nanoparticle surface.

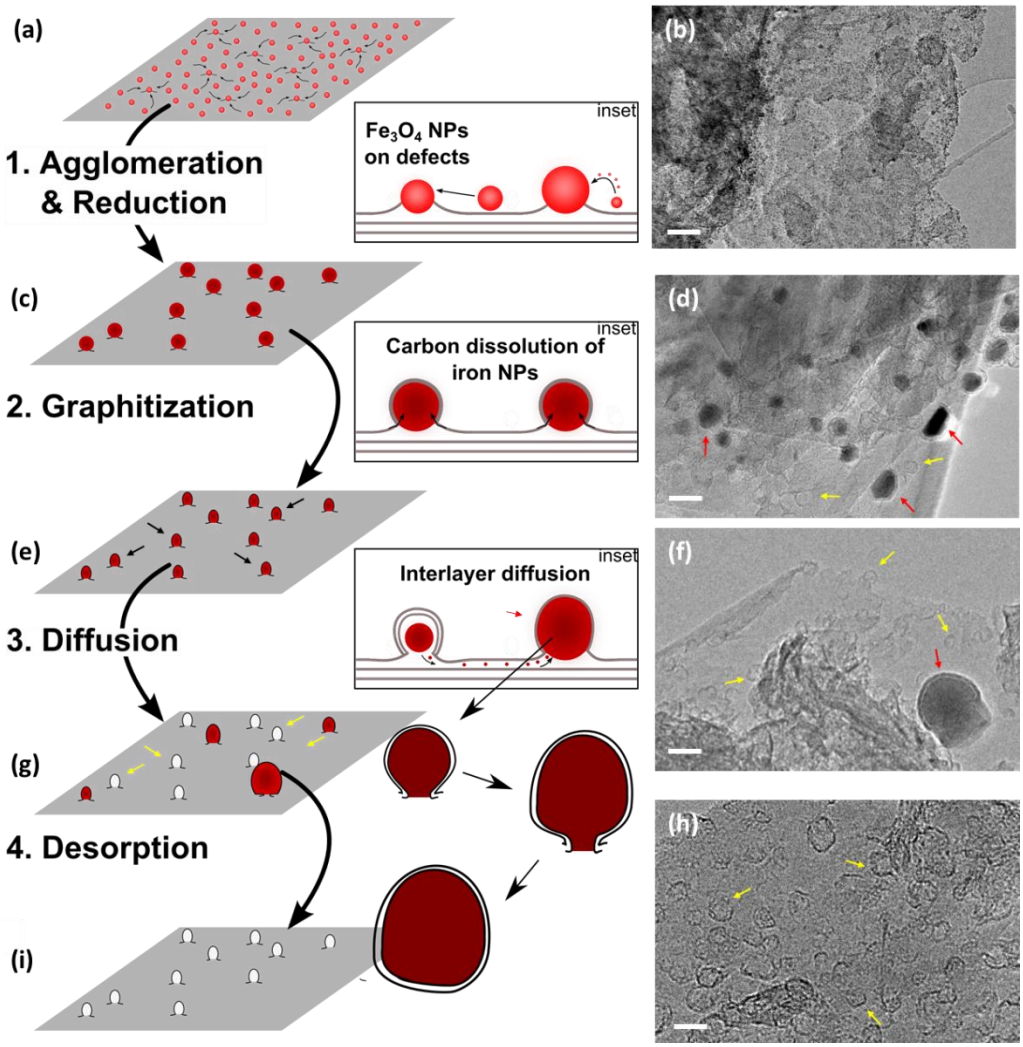

Figure 3. Proposed mechanisms for the formation of hollow carbon cages (HCC) on the surface of GF_{OX} templated by iron nanoparticles during annealing at 1,000°C in argon. Initially, (a-b) iron nanoparticles supported on carbon agglomerate around those nanoparticles anchored on defective carbon surface via Ostwald ripening and coalescence (a-inset). Subsequently, the reduction of iron oxide to iron (0) at high temperatures in argon followed by the dissolution of carbon from the carbon substrate and surfactant (c-inset) leads to carbon oversaturation and, hence, graphitic carbon at the nanoparticle surface is observed (d). Due to the high temperature, large nanoparticles, which are surrounded by few carbon graphitic layers, grow at the expense of the small ones by the diffusion of iron clusters between the graphitic layers of the substrate (e-inset). It would result into small and hollow carbon cages decorating the carbon surface (f) while large metal-carbon core-shell nanocages (f, red arrow) finally detached from the substrate (i) forming large metal-carbon core-shell nanoparticles and (h) hollow carbon cages on the surface of GF_{OX}. Scale bars are 50 (b), 20 (d,f) and 10 nm (h).

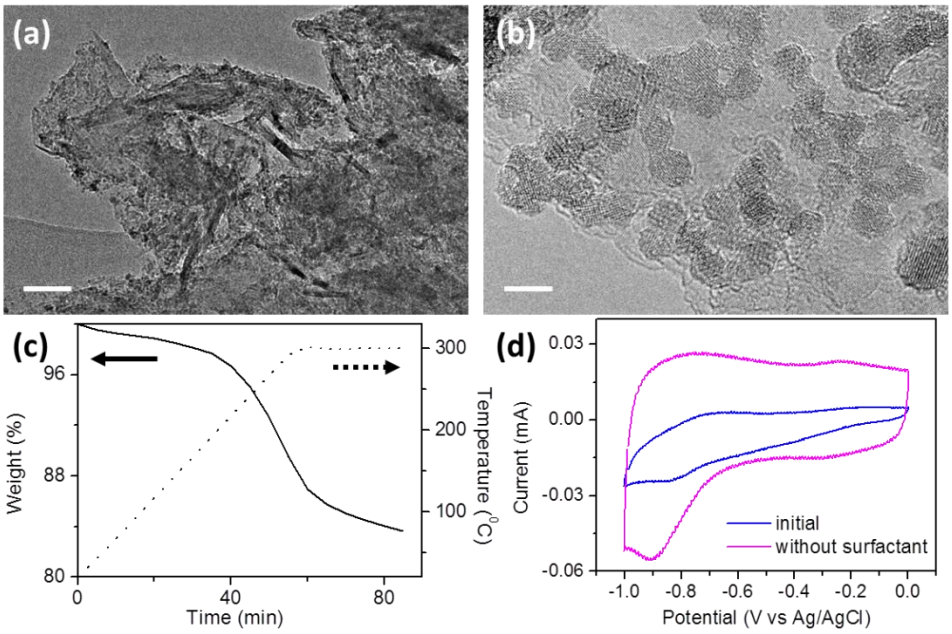

Figure 4 (a-b) Bright-field TEM images of Fe_3O_4/GF_{OX} after heating in air at 300^0C for 2 hours. (c) Thermogravimetric analysis of the elimination of surfactant in air of Fe_3O_4/GF_{OX} hybrid, showing a total removal after 82 minutes. (d) Cyclic voltammogram of initial Fe_3O_4/GF_{OX} hybrid (blue) and heated Fe_3O_4/GF_{OX} hybrid for 82 minutes in air (pink) in 2M KCl at 0.1 V/s. It is important to highlight that more active surface area of iron nanoparticles is available by removing the surfactant. Scale bars are 50 (a) and 5 nm (b).

Based on the widely-accepted vapor-liquid-solid (VLS) mechanism, iron oxide would be thermally reduced to metallic iron at high temperatures under argon atmosphere, and dissolve some carbon thus forming iron carbide.[30] Small amounts of amorphous carbon present on the carbon surface together with the surfactant which initially surround the preformed Fe_3O_4 NPs can simultaneously act as source of carbon.[31-33] The X-ray diffraction pattern of $Fe@C/GF_{OX}$ (Figure 5a, red line), which is completely different with respect to before annealing treatment (Figure 5a, blue line), confirms the formation of metallic Fe (*, JCDPS No. 06-0696) and Fe_3C (▪, JCDPS No. 35-0772) crystalline phases and it is associated to the dark nanoparticles observed by TEM (Figure 1b). Diffraction peak at 2Θ of 26.10^0 indexed to the diffraction from (002) plane of the graphite flake.

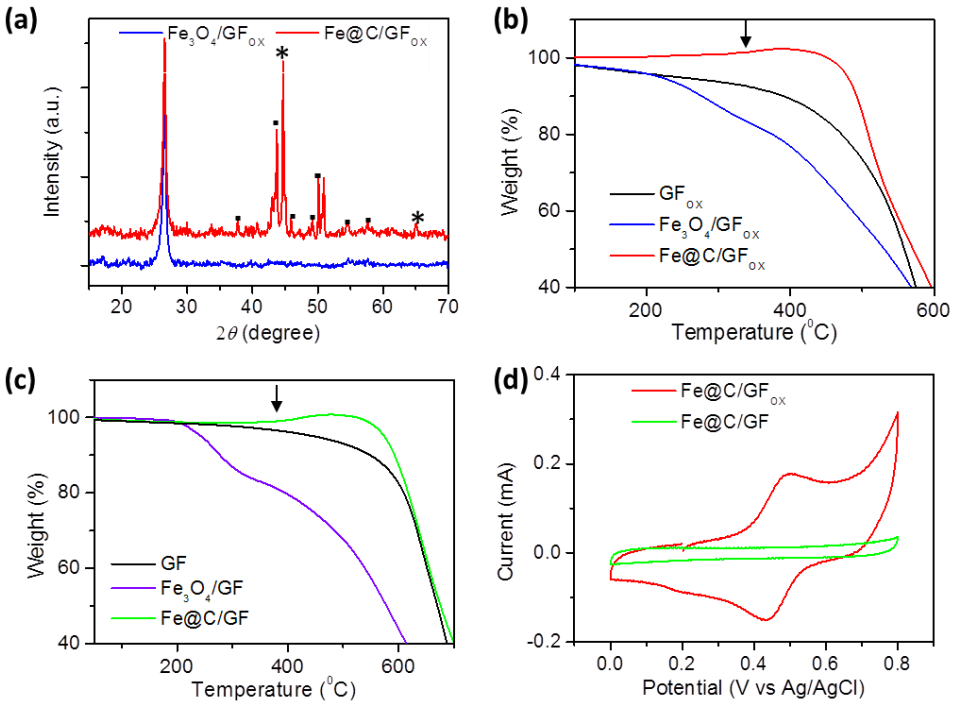

Figure 5. (a) X-ray diffraction pattern and (b) thermal gravimetric analysis in air of Fe_3O_4/GF_{OX} before (blue, Fe_3O_4/GF_{OX}) and after (red, $Fe@C/GF_{OX}$) annealing. (c) Gravimetric analysis in air of Fe_3O_4/GF before (purple, Fe_3O_4/GF) and after (green, Fe@C/GF) annealing. (d) Cyclic voltammogram of Fe_3O_4/GF_{OX} (red) and Fe_3O_4/GF (green) after thermal treatment (annealing at 1000^0C in argon) in 2M KCL at 0.1V/s. Iron redox process in $Fe@C/GF_{OX}$ hybrid suggests a porous shell on the iron-carbon core-shell nanoparticles. In contrast, purely double-layer behaviour is observed in Fe@C/GF hybrid so no redox process is measured.

The thermodynamically higher stability of graphitic carbon than iron carbide [34-36] results in the precipitation of graphitic carbon layers around the nanoparticle (Figure 3d-e), producing the carbon-coated iron nanoparticles. HRTEM studies reveal a highly graphitized carbon shell on the large iron nanoparticles with an average thickness between 4 and 7 nm (Figure 1c), confirming the formation of carbon-coated nanoparticles (nano-onions) after thermal treatment. Interestingly, the carbon shell increases the thermal stability of $Fe@C/GF_{OX}$ (Figure 5b, red line) with respect to the initial Fe_3O_4/GF_{OX} hybrid (Figure 5b, blue line) as the oxidation of the carbon support occurs at a higher temperature (480 and 380^0C, respectively). A more significant increase of the thermal stability in air (~200^0C, based on the onset of GF oxidation) is observed in Fe@C/GF (Figure 5c, green line) with respect to the initial hybrid (Fe_3O_4/GF), being in agreement with the around three times thicker carbon-shell measured in Fe@C/GF (Figure 1f) than $Fe@C/GF_{OX}$ (9 nm vs 4 nm

respectively). The small weight gain around 350^0C in Fe@C/GF_{OX} (Figure 5b, black arrow,) and around 400^0C in Fe@C/GF can be associated with the simultaneous oxidation of the carbon shell and the iron Fe^0 core. Thus, the increase of the thermal stability in air of the heated hybrids (Fe@C/GF_{OX}, Fe@C/GF) with respect to initial hybrids (Fe_3O_4/GF_{OX}, Fe_3O_4/GF) reveals a complete inhibition of iron as a catalyst, suggesting the protection of the spontaneous oxidation of the metallic iron core in air at room temperature.[37] It is important to highlight that the thin carbon coating of Fe@C NPs would be directly related the lower carbon saturation on the reduced iron nanoparticles in Fe@C/GF_{OX} with respect to Fe@C/GF as some of the carbon has been employed for the preparation of HCC on the surface of GF_{OX}. Hence, the absence of HCC in Fe@C/GF leads to a carbon oversaturation on large Fe@C nanoparticles which results in thick carbon-coating as well as tubular structures (Appendix III, Figure 13).

Electrochemistry is used to gain more information about the carbon shell structure of the formed carbon nano-onions by studying the interface between the electrolyte and the metal-carbon nano-onions. As shown in Figure 5d, both hybrids have a dramatically different electrochemical response in 2M KCl. Iron from the core of large nano-onions is detected ($Fe^{3+/2+}$, E^0= 0.41V vs Ag/AgCl) in Fe@C/GF_{OX} hybrid. In contrast, no redox process is observed in Fe@C/GF, showing purely double-layer behaviour. These observations suggest a porous carbon shell structure in Fe@C/GF_{OX} whereas iron is completely isolated in Fe@C/GF, being in agreement with the measured carbon shell thickness by TEM analysis and its high thermal stability in air by TGA. Additionally, the acid treatment of Fe@C/GF_{OX} hybrid confirms the possibility of dissolving the iron core (Appendix III, Figure 14), being in agreement with the proposed porous carbon shell structure.

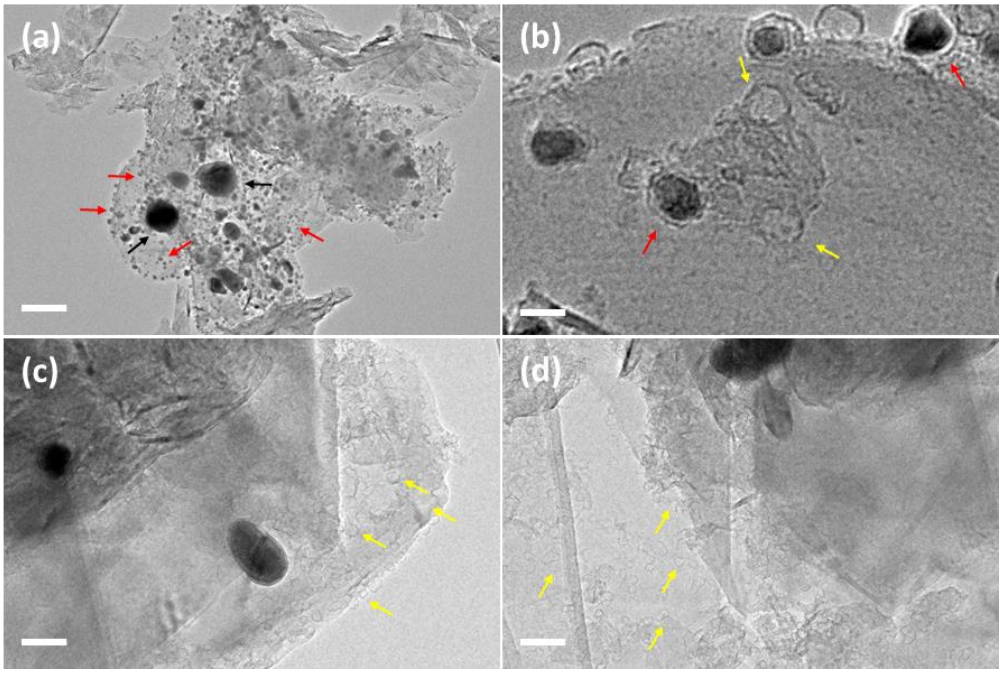

Figure 6. Bright-field TEM images of annealed hybrid ($Fe@C/GF_{OX}$) at 1000°C for 45 min in argon. Scale bars are 200 nm (a), 20 nm (c-d) and 10 nm (b). Short arrows indicate free-standing and large metal-carbon core-shell nanoparticles (black), supported and small iron-carbon core-shell nanoparticles (red) and hollow carbon nano-onions (yellow).

On the other hand, the investigation of thermal treated Fe_3O_4/GF_{OX} hybrid after 45 minutes (instead of 2 hours) at 1000°C allows a further insight into the formation process of the hollow carbon cages on the surface of GF_{OX}. As shown in Figure 6, dark and large nano-onions are already formed after a short thermal treatment (Figure 6a, black arrows). However, not all the iron is encapsulated in large carbon-coated nanoparticles as in $Fe@C/GF_{OX,}$ smaller carbon-coated iron nanoparticles are still decorating the carbon surface (Figure 6a, red arrows). A close examination of the carbon surface reveals that the iron nanoparticles are not the initial 4 nm size but their size increases to 9 nm, being all the nanoparticles surrounded by a carbon shell structure (Figure 6b). This observation is crucial to confirm that hollow carbon cages on the surface of GF_{OX} (Figure 6b-d, yellow arrows) are initially filled with iron, which acts as a template. It is important to mention that the stabilization of nanoparticles around 9 nm size is not fully-understood yet but electronic and structural factors have to be considered, such as in the case of other nanoparticles (i. e. Au) on the surface of graphene. [38-40]

More interestingly, iron-filled carbon cages larger than 15 nm were found in the intermediate sample heated for 45 min (Figure 3d, red arrows), being in sharp contrast to the statistical analysis of Fe@C/GF_{OX} after annealing for 2 hours, which does not show any hollow carbon cages larger than 14 nm and suggest the desorption of large iron-filled carbon cages from the carbon support. Such process would be a result of iron diffusing from small carbon cages towards larger nano cages (>14nm) via Ostwald ripening, leaving the small carbon cages empty (Figure 3d-g, yellow arrows). This hypothesis is in agreement with the observed large iron-filled carbon cage on the surface of GF_{OX} (Figure 3f, red arrow), being surrounding by hollow carbon cages. It is important to mention that the diffusion from one metal-carbon cage to another is proposed to take place between the graphitic layers of GF_{OX} rather than from the surface so the graphitic layers of the carbon cages would hinder the diffusion of iron both outwards and inwards the cage. In fact, heat-promoted expansion at high temperatures (i. e. thermal exfoliation),[41] as well as the successful intercalation of many metals and semiconductors between the graphene layers[42-43] suggests that iron atoms can diffuse between the graphitic carbon layers in order to connect metal-carbon nanocages during annealing at 1000^{o}C in argon (Figure 3e-inset, black arrow). The successive increment in size of the iron-carbon nanocages would decrease the interaction of iron-filled carbon cages with its support, producing the completely detachment of the former nanostructure and forming the observed large carbon-coated iron nanoparticles (Fe@C) (Figure 4i).

Metallic iron has been extensively utilized as a hard catalyst for the formation of a carbon coating in previous examples;[44] however, in these studies, iron has not spontaneously diffusedd from the core to form hollow carbon structures but has formed carbon-coated iron nanoparticles. In sharp contrast, we observe the diffusion of iron from the core, resulting in hollow carbon nanostructure after long (2 hours) annealing times (Figure 2a-c), at lower temperatures than iron evaporation (1000^{o}C with respect to 1900^{o}C) [45] and in the absence of any oxidizing agent.[21-22]

3.3 Conclusions

We have found that the carbon support plays an important role in the growth process of carbon-coated iron nanoparticles when the catalyst (iron nanoparticles) is supported on flat carbon nanostructures, suggesting the interactions between nanoparticle and support are crucial parameters. Thus, 4 nm nanoparticles agglomerate and lead to large metal-carbon nano-onions (500 nm, Fe@C) when they are supported on a highly graphitised nanostructure (i.e. GF), showing the low nanoparticle-support interaction. In contrast, the carbon support can have a stronger interaction with the nanoparticles via the chemical defects located at the carbon surface (i.e. GF_{OX}). During thermal treatment, nanoparticles anchored to the defects serve as a nucleation points during the agglomeration process, in which smaller nanoparticles migrate along the surface dissolving carbon atoms from the surfactant and carbon support. The reduction of iron at high temperatures that is concomitant with the formation of graphitic shells gives rise to small carbon-coated iron cages on the surface. Hollow carbon cages (9 nm) on the surface and large carbon-coated iron nano-onions (150 nm) that desorb from the surface appear as a result of the diffusion of iron atoms through the graphitic layers (Ostwald ripening). The resulted hollow carbon cages on the carbon surface demonstrate promising results for electrochemical storage devices such as supercapacitors or batteries due to the increased surface area with respect pristine "smooth" carbon nanostructures.

3.4 Experimental part

Synthesis of preformed Fe_3O_4 nanoparticles.

The preparation of 4-nm Fe_3O_4 nanoparticles was made following Zeng's procedure.[25] Briefly, $Fe(acac)_3$ (2 mmol) was mixed in phenyl ether (20 mL) with 1,2-hexadecanediol (10 mmol), oleic acid (6 mmol), and oleylamine (6 mmol) under nitrogen and was heated to reflux for 30 min. After cooled to room temperature, the dark-brown mixture was treated with ethanol under air, and a dark-brown material was precipitated from the solution. The product was dissolved in hexane and reprecipitated with ethanol to give 4-nm Fe_3O_4 nanoparticles.

Milling GF flakes

Graphite flakes (GF and GF_{OX}) were purchased from Asbury Carbons. While GF were used as received, graphitic natural flakes material (GF, 200 mg) was placed inside a ball milling cylinder (5 ml) with an SS ball (10 mm). The cylinder was vibrated at a frequency of 20Hz for 90 min four times. The milled material was recovered from the cylinder and use without further purification.

Synthesis of Fe_3O_4/GF_{OX} (and Fe_3O_4/GF).

Graphite flakes (GF_{OX} or GF, 100 mg) were suspended in hexane (100 mL) and sonicated for 20 minutes. Subsequently, a hexane suspension of 4-nm preformed Fe_3O_4 nanoparticles (50 mg/20 mL) was sonicated while the graphite flakes suspension was added drop by drop. The mixture was stirred vigorously for 3 hours. Then, the suspension was sonicated for 15 minutes and filtered onto a PTFE filtration membrane (0.2 μm pore size), thoroughly washed with hexane, ethanol and acetone and dried in air to yield Fe_3O_4/GF_{OX}, 125 mg (or Fe_3O_4/GF,134 mg).

Annealing treatment of metal-carbon hybrids.

Metal-carbon hybrid (20 mg) was first sealed in a quartz tube under argon atmosphere. Subsequently, the quartz tube was introduced in a furnace pre-heated at 1000^0C. After 2 hours, the tube was taken out from the furnace and let it cool down at room temperature.

Structural characterization.

Thermogravimetrical analysis (TGA) was carried out on a SDDT Q-600 TA instrument over the range of 25-1000 ^{0}C in air at a scan rate of 5^{0}C/min. Powder X-Ray diffraction measurement of the materials were taken using X-Pert Pro PANalytical-XRD diffractometer using Cu Kα radiation (λ = 1.5406Å). XPS were recorded using a Kratos with monochromated Al Kα radiation (10 kV anode potential, 15 A emission current) in fixed analyser transmission mode (80 eV pass energy). High resolution transmission electron microscopy (TEM imaging, were performed using a Jeol 2100F transmission electron microscope at an accelerating voltage of 200kV. TEM specimens were prepared by casting several drops of a suspension of the composite in hexane onto a copper grid mounted "lacey" carbon film before drying under a stream of nitrogen. Statistical analysis was performed using Gatan Digital Micrograph. Electrochemical experiments were carried out on a computer-controlled potentiostat (Autolab 302N) at room temperature using a conventional three-electrode cell with a nitrogen saturated 2M KCL aqueous solution as electrolyte. A Pt wire and a Ag/AgCl electrode were used as the counter and the reference electrode, respectively. All potentials were measured and reported versus the Ag/AgCl electrode at room temperature. Working electrodes were prepared using 1:1 mixture of the active material with deionized water by sonication for 15 min and 1% PTFE binder. The prepared sample was dropped onto the glassy carbon electrode (GCE) surface using a micro syringe (10 µg) and the electrode was allowed to dry at room temperature before carrying out the measurements. Prior to use, the working glassy GCE (3 mm in diameter) was polished mechanically with aqueous slurries of alumina powder (0.05 µm) and rinse with Mill-Q water and acetone, and allowed to dry under nitrogen.

3.5 References

1. J. K. McDonough and Y. Gogotsi, Electrochem. Soc. Interface 2013, **22**, 61-66.
2. J. Liu, N. P. Wichramaratne, S. Z. Qiao and M. Jaroneic, Nat. Mater. 2015, **14**, 763-774.
3. M. E. Plonska-Brzezinska and L. Echegoyen, J. Mater. A 2013, **1**, 13703-13714.
4. F. Zheng, M. He, Y. Yang and Q. Chen, Nanoscale, 2015, **7**, 3410-3417.
5. S-M. Kim, Y-K. Heo, K-T. Bae, Y-T. Oh, M-H. Lee and S-Y. Lee, Carbon, 2016, **101**, 420-430.
6. J. Yang, Y. Zhang and D. Y. Kim, Carbon, 2016, **98**, 74-82.
7. K. M. Tripathi, A. Bhati, A. Singh, N. R. Gupta, S. Verma, S. Sarkar and S. K. Sonkar, RSC Adv. 2016, **6**, 37319-37329.
8. H. Jabee, K. C. Kemp and V. Chandra, J. Environ. Manage. 2013, **130**, 429-435.
9. K. Flavin, M. N. Chaur, L. Echegoyen and S. Giordani, Org. Lette., 2010, **12**, 840-843.
10. G. Wu, M. Nelson, S. Ma, H. Meng, G. Cui and P. K. Shen, Carbon, 2011, **49**, 3972-3982.
11. S-M. Yoo, W. M. Choi, H. Baik, H-J. Shim, I. Song, M-S. Kwon, J. J. Bae, H. Kim, Y. H. Lee and J-Y. Choi, ACS Nano, 2012, **6**, 6803-6811.
12. R. Sun, H-B. Zhang, J. Yao, D. Yang, Y-W. Mai and Z-Z. Yu, Carbon, 2016, **107**, 138-145.
13. M. Tavakkoli, T. Kallio, O. Reynaud, A. G. Nasibulin, C. Johans, J. Sainio, H. Jiang, E. I. Kauppinen and K. Laasonen, Angew. Chem. Int. Ed., 2015, **54**, 4535-4538.
14. B. Zhang, Z-L. Xu and J-K. Kim, RSC Adv., 2014, **4**, 12298-12301.
15. X. Zhang, C. Shi, E. Liu, J. Li, N. Zhao and C. He, Nanoscale, 2015, **7**, 17079-17087.
16. L. McCafferty, V. Stolojan, S. G. King, W. Zhang and S. Haq, S. R. P. Silva, Carbon, 2015, **84**, 47-55.
17. H. Fei, Z. Peng, L. Li, Y. Yang, W. Lu, E. L. G. Samuel, X. Fan and J. M. Tour, Nano Research 2014, **7**, 502-510.
18. G. H. Jeong, I. Lee, J-G. Kang, H. Lee, S. Yoon and S-W. Kim, RSC Adv., 2015, **5**, 731119-73125.
19. Q. Li, K. Yao, G. Zhang, J. Gong, E. Mijowska, K. Keirzek, X. Chen, X. Zhao and T. Tang, Part. Part. Syst. Charact., 2015, **32**, 874-879.
20. Q. Wang, J. Yan, Y. Wang, G. Ning, Z. Fan, T. Wei, J. Cheng, M. Zhang and X. Jing, Carbon, 2013, **52**, 209-218.
21. S. J. Teng, X. X. Wang, B. Y. Xia and J. N. Wang, J. Power Sources, 2010, **15**, 1065-1070.
22. S. J. Teng, J. N. Wang, B. Y. Xia and X. X. Wang, Chem. Eur. J., 2010, **16**, 13603-13608.
23. L. Jiang, J. Wang, X. Mao, X. Xu, B. Zhang, J. Yang, Y. Wang, J. Zhu and S. Hou, Carbon, 2017, **111**, 207-214.
24. J. I. Tapia, E. Larios, C. Bittecnourt, M. J. Yacamán and M. Quintana, Carbon, 2016, **99**, 541-546.
25. S. Sun and H. Zeng, J. Am. Chem. Soc., 2002, **124**, 8204-8205.
26. B. C. Satishkumar, E. M. Vogl, A. Govindaraj and C. N. R. Rao, J. Phys. D: Appl. Phys. 1996, **29**, 3173-3176.
27. L. Jiang and L. Gao, Carbon, 2003, **41**, 2923-2929.
28. B. R. Azamian, K. S. Coleman, J. J. Davis, N. Hanson and M. L. H. Green, Chem. Commun., 2002, **4**, 366-366-367.
29. C. A. Dyke and J. M. Tour, J. Phys. Chem. A, 2004, **108**, 11151-11159.

30. W-J. Jiang, L. Gu, Y. Zhang, X. Zhang, L-J. Zhang, J-Q. Wang, J-S. Hu, Z. Wei and L-J. Wan, J. Am. Chem. Soc., 2016, **138**, 3570-3578.
31. R. G. Mendes, A. Bachmatiuk, A. A. El-Gendy, S. Melkanova, R. Klingeler, B. Büchner and M. H. A. Rümmeli, J. Phys. Chem. C, 2012, **116**, 23749-23756.
32. D. A. J. Herman, S. Cheong, M. J. Banholzer and R. D. Tilley, Chem. Commun., 2013, **49**, 6203-6205.
33. F. B. Romdhane, J. A. Rodriguez-Manzo, A. Andrieux-Ledier, F. Fossard, A. Hallal, L. Magaud, J. Coraux, A. Loiseau and F. Banhart, **Nanoscale**, 2016,**8**, 2561-2567.
34. Y. Homma, H. Liu, D. Takagi and Y. Kobayashi, Nano Res., 2009, **2**, 793-799.
35. J. Hoekstra, M. Versluijs-Helder, E. J. Vlietstra, J. W. Geus and L. W. Jenneskens, ChemSusChem 2015, **8**, 985-989.
36. J. Hoekstra, A. M. Beale, F. Soulimani, M. Versluijs-Helder, J. W. Geus and L. W. Jenneskens, J. Phys. Chem. C, 2015, **119**, 10653-10661.
37. D. Kang, J. Y. Kwon, H. Cho, J-H. Sim, H. S. Hwang, C. S. Kim, Y. J. Kim, R. S. Ruoff and H. S. Shin, ACS Nano, 2012, **6**, 7763-7769.
38. Z. Luo, L. A. Somers, Y. Dan, T. Ly, N. J. Kybert, E. J. Mele and A. T. C. Johnson, Nano Lett., 2010, **10**, 777-781.
39. S. U. Yu, B. Park, Y. Cho, S. Hyun, J. K. Kim and K. S. Kim, ACS Nano, 2014, **8**, 8662-8668.
40. A. La Torre, M. C. Gimenez-Lopez, M. W. Fay, C. Herreros-Lucas, P. D. Brown and A. N. Khlobystov, Small, 2015, **11**, 2756-2761.
41. C. Zhang, W. Lu, X. Xie, D. Tang, C. Liu and Q-H. Yang, Carbon, 2013, **62**, 11-24.
42. A. M, Shikin, G. V. Prudnikova, V. K. Adamchuck, F. Moresco and K. H. Rieder, Phys. Rev. B, 2000, **62**, 13202-13208.
43. A. Dahal and M. Batzill, Sci. Rep., 2015, **5**, 11378.
44. C. Scheliehe, J. Yuan, S. Glatzel, K. Siemensmeyer, K. Kiefer and C. Giordano, Chem. Mater., 2012, **24**, 2716-2721.
45. S. Boncel and K. K. K. Koziol, Appl. Surf. Sci. 2014, **301**, 488-491.

Part B

Hybrid metal-carbon nanostructures towards energy-related applications

General Statement

The combination of carbon nanostructure with functional nanomaterials (i.e. molecules, nanoparticles or metal-coordination polymers) has shown promise for the development of the next generation of materials, mainly, due to the underlying synergistic effects within the hybrid material. While the active additives provide a rich variety of electronic processes via reversible Faradaic oxidation/reduction reactions, carbon nanostructures, which act as a support, facilitate both the electron and the ionic transfer due to their intrinsic high conductivity and high surface area. In this Part, we will focus our attention on the combination of carbon nanostructures with a multi-electron molecular metal cluster (Chapter 4), metal oxide nanoparticles (Chapter 5) and metal coordination polymers (Chapter 6).

Molecular metal clusters can undergo multi-electron redox reaction and have been already proposed for energy related applications (i. e. Lithium batteries via the insertion/extraction of Li^+ ions).[1-2] Even though their intrinsic potential, their current application is limited by their low stability during the electrochemical process, restricting their commercialization. In Chapter 4, we aim to investigate the extreme confinement (<10 nm internal diameter) of molecular clusters inside hollow tubular carbon nanotubes as new strategy to increase the cluster stability during the reduction/oxidation process and hence, increase their durability. The composite material, which was previously synthesized by Dr. Maria Gimenez-Lopez, is extensively studied using different electrochemical techniques. To test the protective behaviour of the host-container, electrochemical measurements are carried out under harsh conditions (i. e. acid media). In addition, the insertion/removal of K^+ ions from the composite will be discussed from both thermodynamic and kinetic point of view.

The overall performance of nanoparticles is limited by their agglomeration, which drastically decreases their active surface area. The combination with carbon nanostructure is the common approach to overcome such a limitation and recent trends are based on synthesizing the nanoparticle in the presence of the carbon substrate (*in situ* or one-pot synthesis). Interestingly, despite the great knowledge about free-standing nanoparticle synthesis, being able to

selectively control the composition, shape or size, the new synthetic pathway could be significantly affected by the presence of carbon nanostructures during the *in situ* (or one-pot) reaction. In Chapter 5, we aim to develop a simple *in situ* approach using hollow carbon nanofibers for the synthesis of metal-carbon hybrids, facilitating the nanoparticle encapsulation while increasing the nanoparticle-carbon contact. Carbon nanofibers (CNF) are proposed as the host-container because of their wide internal diameter and, more importantly, their internal corrugated interior which not only would act as anchoring points, leading to 1D arrangement, but also it has shown the ability of stabilizing nanoparticles in harsh conditions (i. e. thermal treatment). One of the main objectives here is to encompass the control of the synthesis of nanoparticles (i. e. chemical composition, shape and size) with their confinement within CNF. The effect of chemical defects (i. e. oxygen containing groups) on the surface of CNF will be evaluated as a strategy to control the synthesis of nanoparticles either inside or outside the carbon nanofiber. Subsequently, the resulted hybrid materials will be analysed extensively from an electrochemical point of view in order to elucidate the advantages of confinement as well as the proposed in situ synthetic approach (vs ex situ).

Metal coordination polymers, such as Prussian blue, have gathered much the attention for the insertion of cations due to their intrinsic three-dimensional open framework. In Chapter 6 we aim to relate the structure and chemical composition (i. e. vacancies and oxidation states of metal centres) of a Prussian blue analogue with its electrochemical performance and stability. In contrast to previous examples in the literature that focus on developing different synthetic methods for controlling the ratio of metal vacancies and, hence, the water content, our approach would produce from a PBA with a specific composition, different mixed-valence systems (MVS) by thermally removing coordinated water molecules. The advantage of our approach is that the initial number of vacancies within the structure would remain intact and will allow a direct comparison of the factors involved. Interestingly, such thermal treatment simultaneously triggers an internal electron transfer from one metal centre (M'-NC) to the other (M-CN). Prior to preparing and analysing PBA@carbon hybrids, the electrochemical conditions of pristine PBA as well as the annealing temperature to prepare MVS-PBA are optimized. Then, the effect of

carbon nanostructure during the in situ synthesis of PBA@carbon hybrids is investigated to, finally, focus on the specific capacitance and electrochemical stability of MVS-PBA@carbon hybrid.

Part B1

Isolated systems in carbon nanostructures

Chapter 4

Molecule clusters encapsulated in carbon nanotubes as new working principle for energy-storage

4.1 Introduction

Hybrid metal-carbon nanostructures have recently attracted a great deal of attention as electrode materials for high-energy and high-power density supercapacitors.[3-5] They store energy by combining two different charge storage mechanisms: electrical double-layer (EDL) capacitance and pseudocapacitance. Carbon-based electrodes operate under the first mechanism, in which the energy is stored at the electrode interface through reversible electrolyte ion adsorption during charging-discharging, showing excellent cyclic stability and long service lifetime.[6] On the contrary, pseudocapacitors materials that are typically transition metal oxides depend on the fast and reversible redox reactions at the electrode surface for charge storage providing the source of high specific capacitance in the hybrid supercapacitors.

High aspect ratio carbon nanostructures such as carbon nanotubes that show high electronic conductivities provide an excellent means to achieved this charge storage combination.[7] They not only serve as the physical support of the metal oxide nanoparticles but also provide fast transport pathways for both electrons and ions through the interconnected tri-dimensional porous network structure.[8–10] Since the redox reactions take place solely on the outermost surface layer of the metal oxide nanoparticles, the charge transfer ability of the metal oxide-carbon nanotube composites[11] could be, in principle, further enhanced by increasing the interfacial contact area between the two components and reducing the thickness of the supported nanoparticles.[12–14] Thus, the full utilization of the electro active material might be then achieved, minimizing environmental impacts and reducing production costs.[15]

Molecular metal clusters that can be envisaged as the ultimate smallest particle size undergoing multi-electron redox reactions have been proposed as cathode-active materials for lithium-ion battery applications.[16–19] These polynuclear metal complexes can potentially show extreme high capacitance. However, previous attempts to fabricate molecular clusters batteries based on Mn_{12} molecules ($[Mn_{12}O_{12}(O_2CR)_{16}(H_2O)_4]$ R=CH_3, C_6H_5) (Figure 1a), which are well-known as single-molecule magnets (SMM), comprised of a physical mixture of Mn_{12} microcrystals with different types of carbon materials bound

together.[20] The strain developed during the charge–discharge processes accompanying the insertion and removal of lithium ions together with the poor electrode contact leads to low stability, slow rate and insufficient cyclability. Thus, nanostructuring of the hybrid composite electrode ensuring both an intimate contact at the molecule level and smooth electron transfer in a protected surrounding[21] would be the ideal scenario for achieving the full potential of these exciting magnetic molecules in energy storage devices.

Open-end multi-walled carbon nanotubes (MWNT) with diameters smaller than 10 nm are ideal one-dimensional containers for large molecules.[22–24] The confined space within these restricted nanotube diameters will hinder the formation of large aggregates of molecules maximizing molecule-nanotube contacts. Interestingly, these one-dimensional nanopore channels may also play an important role increasing the confinement of the electrolyte ions, which could lead to an increase of capacitance.[25] Very recently, theoretical studies have demonstrated the importance of the nanotube-like pore structure on the enhanced capacitance.[26–28] The efficiency of the storage process over that of a flat carbon-based capacitor arises from the confinement, where the charging and discharging process involves the exchange of ions with the bulk electrolyte. This ionic transport may be restricted in long carbon nanotubes with several tens of microns in length. However, by reducing the length of the one-dimensional nanocontainers the transport resistance of the electrolyte ions, and therefore (*i.e.* ion diffusion length), should become less important, allowing the exploitation of capacitance effects within the confined space of the nanotubes (Figure 1b).

4.2 Results and discussion

Coexistence of capacitance effects and multi-electron redox reactions within the internal cavity of carbon nanotubes has not yet been realized. This unique molecule-carbon nanotube hybrid approach can serve as new working principle for high-performance energy-storage devices. To test this hypothesis, we have designated a hybrid material ($Mn_{12}Ac$@MWNT) in which $Mn_{12}Ac$ (Ac for R=CH_3) molecules (Figure 1a) are encapsulated inside short graphitised MWNT (mean internal diameter of *ca.* 6.5 nm and average length of *ca.* 400 nm) by van der Waals forces (*i.e.* non-covalent interactions) that allow the

guest-molecules to stay mobile within the internal cavities of the host-containers (Figure 1c).[23] The functional properties of $Mn_{12}Ac$ SMM, which are very sensitive to the oxidation states of the manganese centres, are fully retained after the encapsulation within the carbon nanotubes that acts as a shield protecting the guest-molecules from harsh environment.[23,29] This distinctive well-defined hybrid nanostructure $Mn_{12}Ac$@MWNT (Appendix IV, Figures 1–6) will provide a unique scenario for studying simultaneously capacitance effects and multi-electron redox processes in a confined space of a few nanometers for charge storage.

The electrochemical performance of a thin-film of $Mn_{12}Ac$@MWNT deposited on a glassy carbon electrode has been extensively investigated in our study by galvanostatic charge–discharge measurements, cyclic voltammetry, and electrochemical impedance spectroscopy in a three-electrode electrochemical cell using a 2 M KCl aqueous electrolyte. Short and open MWNT used for the preparation of the hybrid material and a crystalline sample of $Mn_{12}Ac$ were also carefully analysed under the same experimental conditions to ascertain the behaviour of the host nanocontainer and the confinement effect on the capacitance performance. Electrochemical studies on $Mn_{12}Ac$ (Appendix IV, Figure 7) reveals a rich redox chemistry involving several oxidation and reduction process. Several of the latter appear to be reversible by electrochemical criteria, suggesting that $[Mn_{12}Ac]^{n-}$ are stable species. In fact, monoanionic and dianionic members of the Mn_{12} family have been isolated.[30–32]

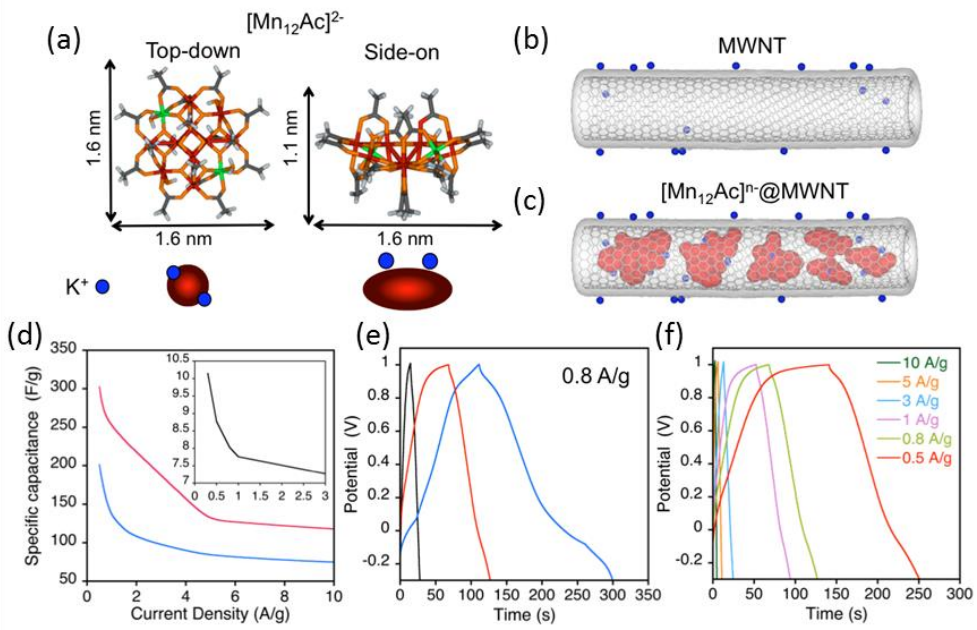

Figure 1. Coexistence of capacitance effects and multi-electron redox reactions within the internal cavity of carbon nanotubes. (a) Structure of a two-reduced $[Mn_{12}O_{12}(O_2CCH_3)_{16}(H_2O)_4]$ ($[Mn_{12}Ac]^{2-}$) that is expected to be formed within the studied potential range in which two of the outer Mn(III) atoms shown in green have been reduced to Mn(II). Dimensions are indicated by double-headed arrows. Carbon, hydrogen, manganese, and oxygen atoms are shown as grey, light-grey, red and orange, circles, respectively. Schematic representation of $K_2[Mn_{12}Ac]$ where the potassium ions are located slightly above the x–y plane of the $Mn_{12}Ac$ cluster. (b) Diagrams of the charge storage mechanisms for a short and open MWNT and (c) a MWNT hosting $Mn_{12}Ac$. (d) Specific capacitance (F/g of $Mn_{12}Ac$) as a function of the current density for $Mn_{12}Ac$ (blue) and $Mn_{12}Ac$@MWNT (red) in 2M KCl. Inset: Capacitance of short and open graphitized MWNT per nanotube mass. (e) Comparison of the galvanostatic charge–discharge curves for $Mn_{12}Ac$@MWNT (red), $Mn_{12}Ac$ (blue) and short and open graphitized MWNT (black) at a current density of 0.8 A/g. (f) Charge–discharge curves for the hybrid $Mn_{12}Ac$@MWNT at different current densities (0.5-10 A/g).

An important synergistic effect of the nanoscale hybridization on the rate capability is clearly revealed when variations of the specific capacitance with the current density for $Mn_{12}Ac$@MWNT and a crystalline sample of $Mn_{12}Ac$ are compared, showing much higher values for the hybrid material in the investigated range (0.3-10 A/g) (Figure 1d). At a current density of 0.5 A/g (Appendix IV, Figure 8), the experimental value of the specific capacitance found for the hybrid (302 F/g) is almost an order of magnitude higher than the one calculated (36 F/g) taking into account both the amount of $Mn_{12}Ac$ inside nanotubes (14.2% wt, Appendix IV, Figure 3) and experimental values obtained for only $Mn_{12}Ac$ (201 F/g) and nanotubes (9 F/g).[33] In contrast to $Mn_{12}Ac$ electrode, a less merited decrease in capacitance at low current

densities (< 5 A/g) is observed for the hybrid material (Figure 1d), which is in agreement with an enhancement of both the electrochemical utilization of the $Mn_{12}Ac$ molecules and the ionic transport as a consequence of the nanoscale dispersion.[34]

Comparison of galvanostatic charge–discharge curves for $Mn_{12}Ac$@MWNT, $Mn_{12}Ac$ and MWNT electrodes at the same current density of 0.8 A/g (Figure 1e) demonstrates a behaviour for the hybrid electrode that is a combined contribution from double-layer capacitance and redox pseudocapacitance. A shorter discharging time is expected for $Mn_{12}Ac$@MWNT, as the amount of encapsulated $Mn_{12}Ac$ molecules in the hybrid is only a small fraction of the amount of $Mn_{12}Ac$ deposited on the electrode. However, the charge–discharge curves for $Mn_{12}Ac$@MWNT are more symmetric (quick current/voltage response) and with much lower IR drop (lower contact resistance) than those obtained for $Mn_{12}Ac$ electrode (Appendix IV, Figure 9). The latter is in agreement with the reduction in the internal resistance observed from the hybrid electrode with respect to the $Mn_{12}Ac$ electrode on the electrochemical impedance measurements (Appendix IV, Figure 10). As a consequence of the nanoscale hybridization the energy and power densities values (Appendix IV, Figure 11) obtained from the charge–discharge curves at a current density of 0.5 A/g for the hybrid electrode (71.1 Wh/kg and 2323.0 W/kg, respectively) are, much higher than those found for the $Mn_{12}Ac$ electrode (45.9. Wh/kg and 320.6 W/kg, respectively).

The protective effect of the host nanocontainer on the encapsulated $Mn_{12}Ac$ molecules combined with a rapid electron transfer can be clearly evidenced from cyclic voltammetry studies at a scan rate of 0.1 V/s (Figure 2a) showing an interesting activation process. In contrast to the insufficient rate cyclability of the $Mn_{12}Ac$ crystals (Figure 2b and Appendix IV, Figure 12 and Figure 13) (capacitance retention of 8 % after 100 cycles), the hybrid electrode shows a significant increase in capacitance with increasing cycle number in the first 100 cycles with a maximum change in capacitance of ten times followed by a steady decrease for the first 2000 cycles (Figure 1c). Since no capacitance increase with increasing cycle number can be observed for the carbon nanotubes (Figure 1c and Appendix IV, Figure 14), the activation effect of the

hybrid electrode can be attributed solely to the encapsulated material. Cyclic stability studies of a sample of $Mn_{12}Ac$@MWNT thermally treated at 340 °C to form Mn_3O_4 inside nanotubes (Mn_3O_4@MWNT) that is an expected decomposition product of $Mn_{12}Ac$ were performed to ascertain the observed activation in the hybrid material to structurally intact $Mn_{12}Ac$ molecules. As shown in Figure 2c (pink), a gradual decrease of the capacitance in the first 300 cycles is found for Mn_3O_4@MWNT until a constant retention value of ca. 53 % is reached[35] (Appendix IV, Figure 15), which is in sharp contrast to the hybrid electrode. Hence, the activation process observed cannot be attributed to the decomposition of the $Mn_{12}Ac$ cluster, but instead to the $Mn_{12}Ac$ molecules that remain structurally intact after cycling (Appendix IV, Figure 16). To unequivocally prove the chemical stability enhancement of the confinement of $Mn_{12}Ac$ within the nanoscopic cavities of MWNT, cyclic voltammetry for $Mn_{12}Ac$@MWNT and $Mn_{12}Ac$ was performed under acidic conditions ($HClO_4$ aqueous electrolyte, pH = 4). Stability studies for the hybrid electrode show the presence of a rapid activation process for the first 100 cycles followed by a gradual capacitance increase (Figure 2c and Appendix IV, Figure 17), whereas an instant decomposition can be observed for the $Mn_{12}Ac$ electrode as a consequence of the protonation of the acetate groups (pk_a = 4.75) (Appendix IV, Figure 18).

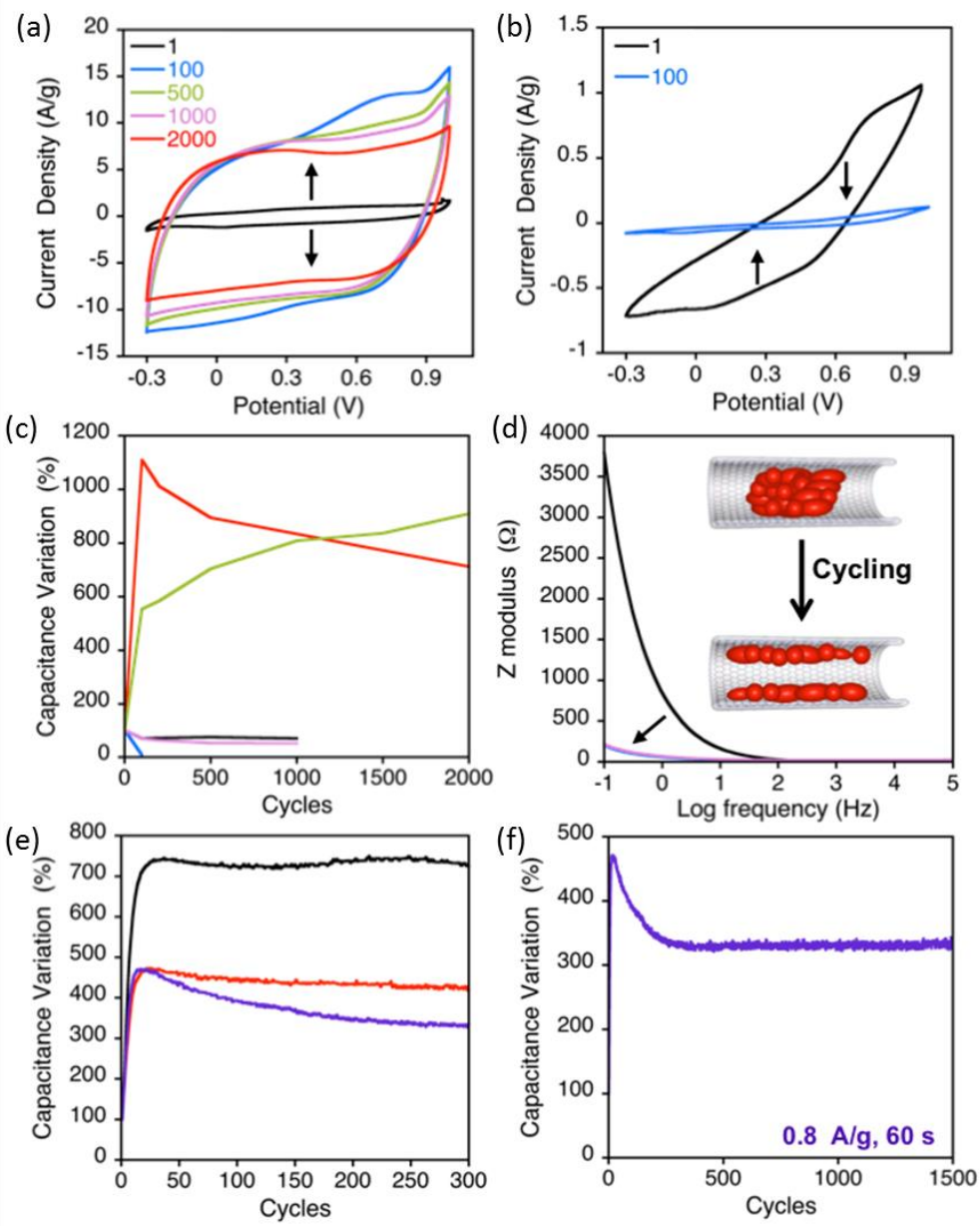

Figure 2. Confinement effect on the cycling performance of molecule metal clusters encapsulated within carbon nanotubes. Cyclic voltammetry (CV) of (a) $Mn_{12}Ac$@MWNT and (b) $Mn_{12}Ac$ electrodes at a scan rate of 0.1 V/s with increasing cycling. (c) Variation of the specific capacitance (%) from CV measurements as a function of increasing cycle number for $Mn_{12}Ac$@MWNT in KCl (red) and $HClO_4$ (pH=4) aqueous solution (green), Mn_3O_4@MWNT (pink), short and open MWNT (black) and $Mn_{12}Ac$ (blue). (d) Bode type representation of the impedance (Z) modulus as a function of applied frequency for the hybrid $Mn_{12}Ac$@MWNT electrode for the 1st (black), 100th (blue) and 1000th (pink) cycle. (e) Cycling performance of $Mn_{12}Ac$@MWNT at a current density of 0.4 (black) and 0.8 A/g with (60 s) (purple) and without (0 s) (red) time delay between each charge–discharge cycle for the first 300 cycles. The potential range is -0.3 to 1 V (vs. saturated Ag/AgCl). (f) Cycling stability of $Mn_{12}Ac$@MWNT for 1500 cycles (8 A/g, 60 s).

In order to investigate further the activation process observed with the increase in area of the cyclic voltammograms for the $Mn_{12}Ac$@MWNT electrode, electrochemical impedance spectroscopy was performed before

(cycle 1) and after electrode activation (cycle 100 and 1000) in a 2 M KCl aqueous electrolyte (Figure 2d). A Bode-type representation of the modulus of the impedance (Z_{mod}) *versus* the l*ogarithm* of the frequency shows that the capacitance of the $Mn_{12}Ac$@MWNT electrode increases with the first 100 cycles and remains unchanged after 1000 cycles that is consistent with cycling voltammetry measurements. The overall reduction on the electrode resistance can be understood in terms of continuous improvement of the contact resistance between the $Mn_{12}Ac$ and the nanotube that enhances the ionic diffusion leading to capacitance activation. This only can be explained with the disaggregation of the $Mn_{12}Ac$ nanoclusters into very small clusters and these into molecules within the host nanocontainers after cycling. An increase of the electro-active surface area is expected, as a result of this process that is induced by the electron reduction of $Mn_{12}Ac$ that takes place during the discharging.

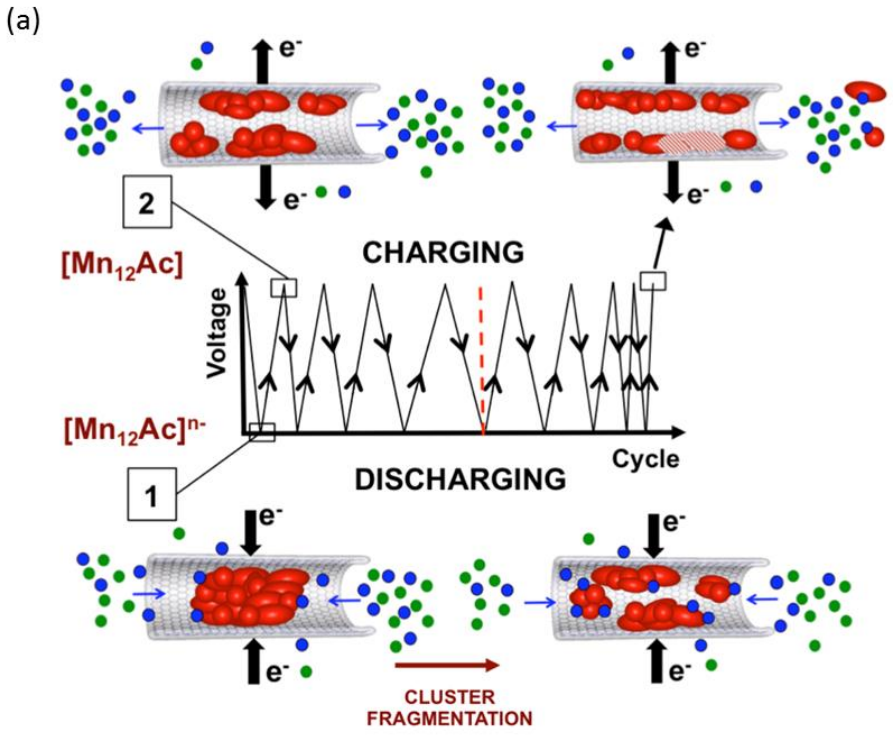

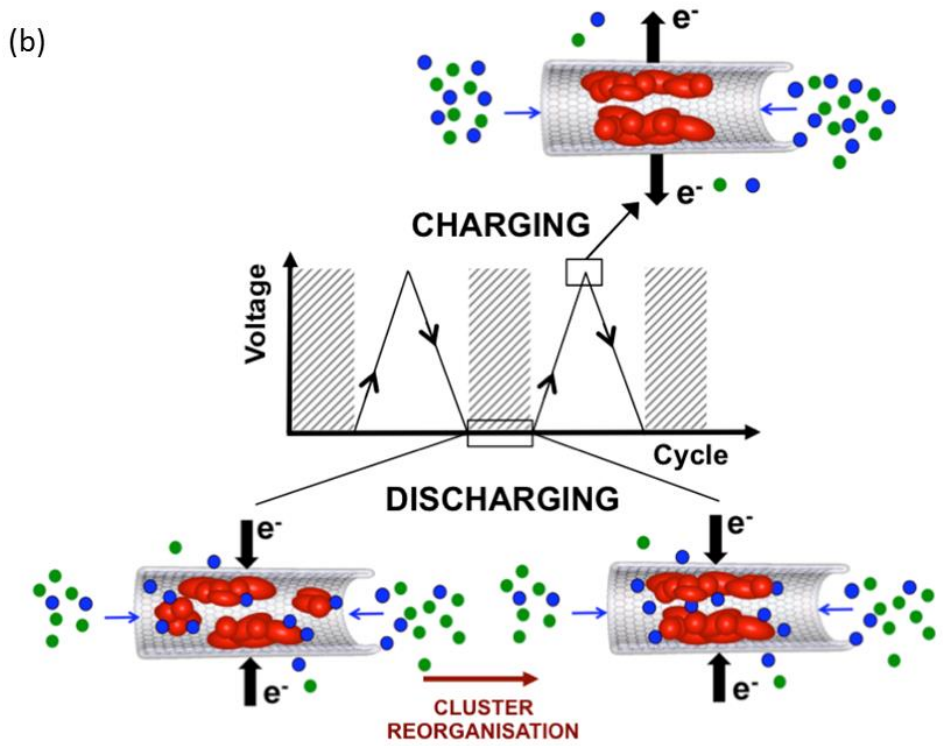

Figure 3. Dynamic behaviour of guest $Mn_{12}Ac$ molecules encapsulated within a carbon nanotube under (a) continuous and (b) discontinuous charge–discharge cycling. (a) upon discharging the cluster aggregation is reduced as a consequence of the electron reduction of $Mn_{12}Ac$ concomitant with the penetration of K^+ within the carbon nanotube channels. The decomposition of $Mn_{12}Ac$ via electron reduction into Mn_3O_4 and/or the release of $[Mn_{12}Ac]^{n-}$ from the internal cavities of the host-nanocontainers may explain the decrease in capacitance observed after an outstanding number of cycles. (b) The fragmented nanoclusters $[Mn_{12}Ac]^{n-}$ are likely to reorganize into thermodynamically more stable aggregations, as a consequence of the time delay between charge-discharge cycles. K^+, Cl^- and $Mn_{12}Ac$ are shown as blue, green and red circles, respectively.

The dynamics of the activation process can be understood from galvanostatic charge–discharge studies. As it is shown in Figure 2e, when $Mn_{12}Ac$@MWNT undergoes continuous cycling at a current density of 0.8 A/g the activation leads to an increase in capacitance of almost 5 times after just 20 cycles that decreases very slowly to be negligible after 7000 cycles (Appendix IV, Figure 20). A similar behaviour is found at lower current density (0.4 A/g), however, as the ionic transport is less diffusion-limited under these conditions, a greater increase in capacitance is observed for the activation (more than seven times after 30 cycles) (Appendix IV, Figure 21). Although we are not able to visualise the actual mechanism of the activation process, it is quite likely that K^+ ions would be strongly attracted to the negatively charge nanoclusters that break into smaller clusters due to columbic repulsions in the

discharging where the electron reduction of the $Mn_{12}Ac$ takes place (Figure 3a). The breaking up of the nanoclusters after reduction might be induced by the penetration of K^+ ions into the nanotube channels and, vice versa. Considering that the $[Mn_{12}Ac]^{n-}$–nanotube interactions are driven by columbic forces, the fragmented nanoclusters are likely to be highly mobile on the nanotube sidewalls, leading to disorder aggregations within a one-dimensional restrictive space. If this process takes place in an unconfined space, the fragmented nanoclusters would quickly disassemble from the nanotube, abandoning the electrode surface and reducing the cycling stability. When the potassium ions are desorbed after charging, it is plausible that the formed aggregates rapidly reorganise to assemble on the nanotube walls by van de Waals forces. This spatial reorganisation together with the size reduction of the fragmented nanoclusters is expected to facilitate ionic diffusion within the nanotube channels and give rise to less disrupted transport pathways. This is in agreement with the gradual capacitance increase observed for cyclic voltammetry experiments under acid conditions after 200 cycles (Figure 2c), as the solvated ion size for protons (900 pm) is larger than for potassium (300 pm).[36-38] It is worth mentioning that no activation has been previously observed for molecule metal clusters adsorbed on the external surface of carbon nanotubes in which the stability of these systems is restricted only a few cycles.[16]

When a time delay between each charge–discharge cycle is considered at a current density of 0.8 A/g, the activation leads to the same increase in capacitance as in the experiment with continuous cycling (Figure 2e and 2f). However, after 50 cycles the activation readily decreases reaching a constant capacitance value (330 %, > 400 cycles) that is in sharp contrast with the gradual capacitance decrease observed for the experiment under continuous cycling (Appendix IV, Figure 19). Thus, $[Mn_{12}Ac]^{n-}\ldots[Mn_{12}Ac]^{n-}$ interactions must be considered to explain the differences in behaviour. By inserting a time delay after each cycle, the disordered fragmented nanoclusters are likely to reorganize into thermodynamically more stable aggregations contributing to the energy dissipation at the electrode (Figure 3b). As this cluster–cluster aggregation is kinetically unfavourable, a continuous size reduction of the fragmented nanoclusters is expected under constant cycling. The gradual

decrease in capacitance activation might be then explained due to the decomposition of the formed isolated $Mn_{12}Ac$ molecules. However, the fact that the Coulombic efficiency remains unchanged with the loss of capacitance activation may suggest that $Mn_{12}Ac$ molecules may leach out of the carbon nanotubes instead of decomposing.

The structure of the one- and two-electron reduced complexes remains practically unchanged with respect to the neutral complex $[Mn_{12}]^0$ and the added electrons in $[Mn_{12}]^-$ and $[Mn_{12}]^{2-}$ go to the outer Mn(III) atoms converting them to Mn(II) (Figure 1a).[30-32] It is worth noting that in the solid state the electrons are known to be valence-trapped and the positions of the cations in the $[Mn_{12}]^{-/2-}$ salts are located slightly above the x–y plane of the Mn_{12}.[39–41] Thus it can be concluded that, the adsorption/desorption of K^+, concomitant with the reduction/oxidation of the fragmented $Mn_{12}Ac$ nanoclusters encapsulated within the carbon nanotubes, is the origin of capacitance enhancement, but not the only one. To prove that the enhancement in capacitance can also be attributed to a deviation from unity of the ratio of numbers of ions of different charge (i.e. K^+ and Cl^-) within the host-nanotubes[42] open circuit potential measurements were performed after applying a negative potential to the activated $Mn_{12}Ac$@MWNT electrode that became negatively charged (Figure 4). A clean glassy carbon electrode was tested under the same conditions as background experiment (Appendix IV, Figure 22). As shown in Figure 4, a positive increase in the potential of the hybrid electrode relative to the reference electrode is always observed when the cell is allowed to equilibrate after external stimulus (negative potential). Under these conditions only the K^+ ions that are not bonded to the $[Mn_{12}Ac]^{n-}$ would be able to migrate out of the carbon nanotube channels to compensate the charge difference in the bulk electrolyte. Interestingly, the time for the cell to equilibrate decreases drastically with increasing number of open circuit potential experiments (from 60 min. to 26 min. after the electrode is negatively charge ten times). This indicates that during the insertion and removal of K^+ within the nanotubes channels a structural reorganisation of the encapsulated nanoclusters is taking place facilitating the ionic migration.

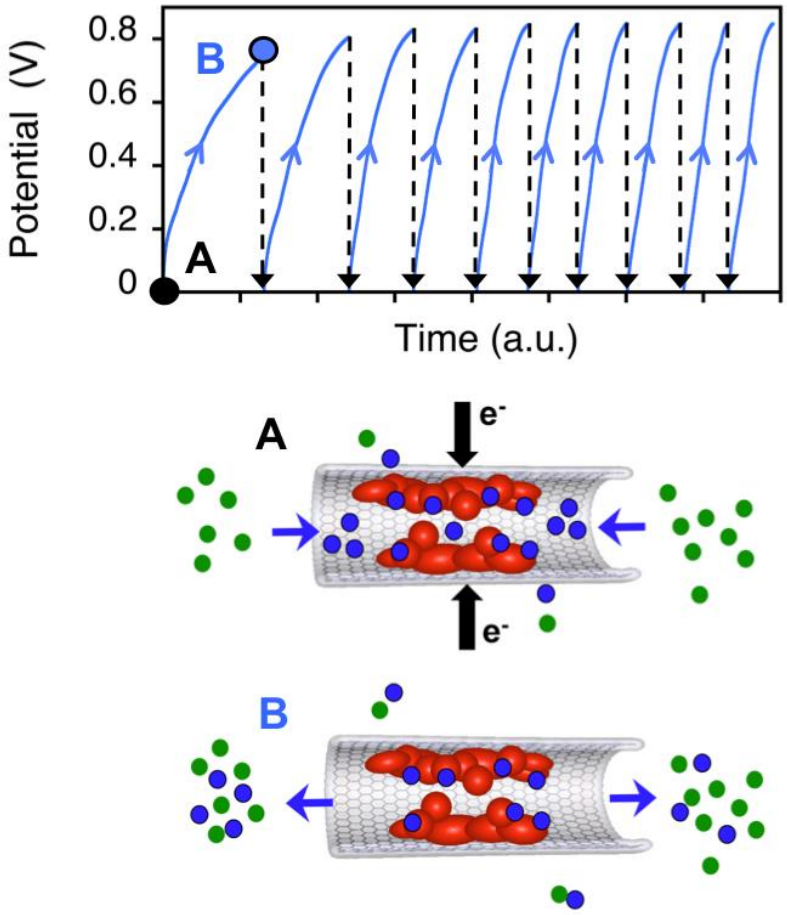

Figure 4. Capacitance enhancement can also be attributed to the deviation from unity of the ratio of K^+ and Cl^- within the host-nanotubes. Open circuit measurements were carried for one hour after applying a negative potential. Schematic representations in A and B show that only the K^+ ions that are not bonded to the $[Mn_{12}Ac]^{n-}$ would be able to migrate out of the carbon nanotube channels. K^+, Cl^- and $Mn_{12}Ac$ are shown as blue, green and red balls, respectively.

4.3 Conclusion

In conclusion, this study outlines a new strategy for energy storage devices. Our strategy exploits the multi-electron redox properties of molecular metal clusters confined within the internal cavities of carbon nanotubes. The carbon nanotubes act as both host-containers, ensuring both an intimate contact at molecule cluster level, and as a conduit for smooth electron transfer in a protected surrounding. We identify the key processes that lead to capacitance activation: (1) fragmentation of confined $Mn_{12}Ac$ nanoclusters which undergo oxidation/reduction that is concomitant with the adsorption/desorption of K^+ ions, and (2) insertion/removal of K^+ ions within the nanotubes channels. Experimental evidence suggests the coupling of these two processes under a

potential change (external stimulus). This is the first example reporting the synergetic coexistence of capacitance effects and multi-electron redox reactions within the internal cavity of carbon nanotubes. The one-dimensional confinement allows clustering aggregation that triggers the long-term cyclic stability (chemical stability). The nanoscale hybridization of the $Mn_{12}Ac$ nanoclusters improves the rate capability and accounts for the high values on energy a power density found.

The surprising capacitance activation observed in $Mn_{12}Ac$@MWNT may open new avenues for energy storage devices that have not been considered so far. The electrochemical properties of $Mn_{12}Ac$@MWNT and the complex dynamic behaviour of the confined $Mn_{12}Ac$ nanoclusters studied here may pave the way for future applications of these materials in smart electrochemical devices (brain-type memories) for the development of neural implant electrodes and spintronic applications.

4.4 Experimental part

Preparation of short and open graphitized MWNT via oxidative cutting

GMWNT (200 mg) were added to a 16 M solution of nitric acid (50ml) and the resulting black suspension was treated with ultrasound in a water bath for 30 min at room temperature. The suspension was then heated in air under reflux for 5h. The resulting mixture was then diluted with deionized water (200 ml), filtered using a 0.45m pore size PTFE membrane filter, washed thoroughly with water until neutral pH and ethanol (50 ml) and dried under vacuum to yield a black solid (192 mg). The product was then placed in an alumina crucible and heated in air at 700°C until weight loss of 80% was achieved.

Preparation of $Mn_{12}Ac$@MWNT and Mn_3O_4@MWNT

Mn_{12} was synthesized following the procedure described previously.[23,43] Subsequently, freshly annealed short and open graphitized MWNT (10 mg) were added to a suspension of $Mn_{12}Ac$ (30 mg) in hexane (8 ml), and the resulting black suspension was transferred into a 10 ml autoclave that was topped up with supercritical carbon dioxide (40 °C, 275 bar). The pressure was cycled between 270 bar and 120 bar for 20 h. The resulting black solid was then washed with 250 ml acetonitrile and filtered using 0.2 m pore size PTFE membrane filter to give $Mn_{12}Ac$@MWNT (14.2% wt of $Mn_{12}Ac$). After heating at 340 °C on air, Mn_3O_4 is formed as a product of thermal decomposition of $Mn_{12}Ac$ in MWNT to yield Mn_3O_4@MWNT (5.6% wt of Mn_3O_4). Details for the preparation of short and open graphitized MWNT via oxidative cutting and the quantification of the amount of $Mn_{12}Ac$ inside nanotubes can be found in supplementary material.

Electrochemical tests

Electrodes were tested on PGSTAT 304 (Autolab) in a three-electrode electrochemical cell using 2M KCl aqueous solution as electrolyte at room temperature. For the experiment under acid conditions an aqueous solution of $HClO_4$ (pH = 4) was used as electrolyte instead. Prior to modification, the glassy carbon electrode (GCE) was well polished with aqueous slurries of alumina powder (0.05 μm), rinsed and ultrasonicated in distilled deionized

water. A Pt wire and Ag/AgCl (saturated KCl) were used as the counter and the reference electrode, respectively. The modified electrode was prepared by mixing the active material ($Mn_{12}Ac$@MWNT, $Mn_{12}Ac$, GMWNTs and Mn_3O_4@MWNT), carbon black and poly(tetrafluoroethylene) (PFTE) in a mass ratio of 70:20:10 to form a homogeneous suspension in hexane. The suspension was dropped cast onto the GCE and let it to dry under a stream of nitrogen before measurements.

Characterisation

Cylic voltamograms were performed at 0.1 V/s in a potential window of -0.3 to 1V. Charging-discharging curves were carried out at different current densities (0.3, 0.5, 0.8, 1, 3, 5 and 10 A/g) from -0.3 to 1V. For the hybrid electrode ($Mn_{12}Ac$@MWNT), the specific capacitance (F g^{-1}) was calculated based on the total mass of the active material ($Mn_{12}Ac$) using the next equation $C_{sp}= I•t/ (\Delta V•m)$, where I is the constant discharge current, t is the discharging time, ΔV is the voltage drop upon discharging and m is the mass of the electrode material. EIS measurements were performed by applying an AC voltage with 5 mV amplitude in a frequency range from 0.1 Hz to 100 kHz at open circuit potential (OCP). OCP protocol was as follow: a negative potential (-0.3V) was applied to the modified electrode for 10 min. Subsequently, an open circuit measurement was run for 1 hour. High-resolution TEM imaging and energy-disperse X-ray analyses were performed using a Jeol 2100F transmission electron microscope using an accelerating voltage of 100kV. TEM samples were prepared by casting several drops of hexane suspension of $Mn_{12}Ac$@MWNT and Mn_3O_4@MWNT onto copper-grid mounted ‘lacey’ carbon films before drying under a stream of nitrogen. TGA measurements were carried out on a SDT Q-600 TA instrument over the range 25–1,000°C in air and at a scan rate of 5°Cmin^{-1}.

4.5 References

1. A. K. Cuentas-Gallego, R. Martinez-Rosales, M. Baibarac, P. Gomez-Romero and M. E. Rincon, Electrochem. Commun. 2007, 9, 2088-2092.
2. K. Kume, N. Kawasaki, H. Wang, T. Yamada, H. Yoshikawa and K. Awaga, J. Mater. Chem. A., 2014, 2, 3801-3807.
3. C. J. Shearer, A. Cherevan, and D. Eder, Adv. Mater. 2014, **26**, 2295–2318.
4. M. Zhi, C. Xiang, J. Li, M. Li, and N. Wu, Nanoscale, 2013, **5**, 72, 72–88.
5. N-S. Choi, Z. Chen, S. A. Freunberger, X. Ji, Y-K. Sun, K. Amine, G.Yushin, L. F. Nazar, J. Cho and P. G. Bruce. Angew. Chem. Int. Ed. 2012, **51**, 9994–10024.
6. T. Kim, G. Jung, K. S. Suh and R. S. Duoff, ACS Nano, 2013, **7**, 8, 6899–6905.
7. L. Dai, D. W. Chang, J-B. Baek and W, Lu, Small, 2012, **8**, 8, 1130–1166.
8. S. W. Lee, J. Kim, S. Chen, P. T. Hammond and Y. Shao-Horn, ACS Nano, 2010, **4**, 7, 3889–3896.
9. M. Zhi, A. Manivannan, F. Meng and N. Wu, Journal of Power Sources, 2012, **208**, 345–353.
10. J-G. Wang, Y. Yang, Z-H. Huang and F. Kang, Electrochemica Acta, 2011, **56**, 9240–9247.
11. C. Zhou, Y. Zhang, Y. Li and J. Liu, J. Nano Lett. 2013, **13**, 2078–2085.
12. R. B. Rakhi, W. Chen, D. Chan and H. N. Alshareef, Nano Lett., 2012, **12**, 2559–2567.
13. X. Yu, B. Lu and Z. Xu. Adv. Mater., 2014, **26**, 1044–1051.
14. S. Santhanagopalan, A. Balram and D. D. Meng. ACS Nano, 2013, **7**, 3, 2014–2125.
15. X. Zhang, W. Shi, J. Zhu, D. J. Kharistal, W. Zhao, B. S. Lalia, H. H. Hag and Q. Yan, ACS Nano, 2011, **5**, 3, 2013–2019.
16. N. Kawasaki, H. Wang, R. Nakanishi, S. Hamanaka, R. Kitaura, H. Shinohara, T. Yokoyama, H. Yoshikawa and K. Awaga. Angew. Chem. Int. Ed., 2011, **50**, 3471–3474.
17. H. Wang, Z. Zeng, N. Kawasaki, H. Eckert, H. Yoshikawa and K. Awaga, Chem. Eur. J., 2013, **19**, 11235–11240.
18. H. Wang, S. Hamanaka, Y. Nishimoto, S. Irle, T. Yokoyama, H. Yoshikawa and K. Awaga, J. Am. Chem. Soc., 2012, **134**, 10, 4918–4924.
19. A. K. Cuentas-Gallego, M. Lira-Cantú, N. Casañ-Pastor and P. Gómez-Romero, Adv. Funct. Mater., 2005, **15**, 1125–1133.
20. H. Yoshikawa, C. Kazama, Awaga, M. Satoh and J. Wada, Chem. Commun, 2007, 3169–3170.
21. M. C. Giménez-López, A. La Torre, M. W. Fay, P. D. Brown and A. N. Khlobystov, Angew. Chem. Int. Ed., 2013, **125**, 7, 2105–2108.
22. M. C. Giménez-López, A. Chuvilin, U. Kaiser and A. N. Khlobystov, Chem. Commun., 2010, 47, 2116–2118.
23. M. C. Giménez-López, F. Moro, A. La Torre, C. J. Gómez-García, P. D. Brown, J. Slageren and A. N. Khlobystov, Nat. Commun., 2011, 2:407.
24. A. Chuvilin, E. Bichoutskaia, M. C. Gimenez-Lopez, T. W. Chamberlain, G. A. Rance, N. Kuganathan, J. Biskupek, U. Kaiser and A. N. Khlobystov, Nature Materials, 2011. 10, 687–692.
25. C. Merlet, B. Rotenberg, P. A. Madden, P-L. Taberna, P. Simon, Y. Gogotsi and M. Salanne, Nature Materials, 2012, **11**, 306–310.

26. J. Chmiola, C. Largeot, P-L. Taberna, P. Simon and Y. Gogotsi, Y. Angew. Chem. Int. Ed., 2008, **47**, 3392–3395.
27. J. Chmiola, G. Yushin, Y. Gogotsi, C. Portet, P Simom and P. L. Taberna, Science, 2006, **313**, 1760-1763.
28. C. Largeot, C. Portet, J. Chmiola, P-L. Taberna, Y. Gogotsi and P. Simon, J. Am. Chem. Soc., 2008, **130**, 9, 2730–2731.
29. K. Sun, K. Park, J. Xie, J. Luo, H. Yuan, Z. Xiong, J. Wang and Q. Xue, ACS Nano, 2013, **7**, 8, 6825–6830.
30. R. Bagai, and G. Christou, Chem. Soc. Rev., 2009, **38**, 1011–1026.
31. M. Soler, W. Wernsdorfer, K. A. Abboud, J. C. Huffman, E. R. Davidson, D. N. Hendrickson and G. Christou. J. Am. Chem. Soc., 2003, **125**, 12, 3576–3388.
32. M. Soler, K. S. Chandra, D. Ruiz, E. R. Davidson, D. N. Hendrickson and G. Christou, Chem. Commun., 2000, 2417–2418.
33. S. H. Aboutalebi, A. T. Chidembo, M. Salari, K. Konstantinov, D. Wexler, H. Liu and S. X. Dou, Energy Environ. Sci., 2011, **4**, 1855–1856.
34. X. Zhao, L. Zhang, S. Murali, M. D. Stoller, Q. Zhang, Y. Zhu and R. S. Ruoff, ACS Nano, 2012, **6**, 6, 5404–5412.
35. W. Chen, Z. Fan, L. Gu, X. Bao and C. Wang, Chem. Commun., 2010, **46**, 3905–3907.
36. J. Kielland, J. Am. Chem. Soc., 1937, **59**, 1675–1678.
37. B. Tansel, J. Sager, T. Rector, J. Garland, R. F. Strayer, L. Levine, M. Roberts, M. Hummerick and J. Bauer. Separation and Purification Technology, 2006, **51** 40–47.
38. J. Zhou, X. Lu, Y. Wang and J. Shi, Fluid phase equilibria, 2002, **194–197**, 257–270.
39. H. J. Eppley, H. L. Tsai, N. Devries, K. Folting, G. Christou and D. N. Hendrickson, J. Am. Chem. Soc., 1995, **117**, 301–317.
40. N. E. Chakov, M. Soler, W. Wernsdofer, K. A. Abboud and G. Christou. Inorg. Chem., 2005, **44**, 5304–5321.
41. R. Bagai and G. Christou, Inorg. Chem., 2007, **46**, 25, 10810–10818.
42. Z-S. Wu, K. Parvez, X. Feng and K. Mullen, Nat. Commun., 2013, 4:2487.
43. T. Lis, Acta Crystallogr. Sec. B, 1980, **36**, 2042-2046.

Chapter 5

Templating effect of carbon nanofibers for the in situ synthesis of metal oxide nanoparticles: effect of nanoscale-confinement

5.1 Introduction

Nowadays, a significant effort is being made in developing functional nanomaterials which can offer new solutions for catalysis, bioimaging, electronics and renewable energy.[1] However, the shortage of some technologically important chemical elements, including many transition metals, demands long-term stability of the material to ensure that functional properties are retained during the exploitation cycle.

In this context, manganese compounds have received considerable attention not only for their relatively high abundance, low cost, environmental benignity, and structural versatility[2] but also because they offer a wealth of applications and excellent performance in the field of electrochemical energy storage and conversion.[3] For example, manganese oxides (Mn_xO_y) are the most promising electrode materials for charge storage applications in cathodes of secondary lithium batteries, electrochromic devices and electrochemical supercapacitors.[4] Similar to other transition metal oxides, they store electrochemical energy by the simultaneous injection of electrons and adsorption of cations. Manganese-based oxides have been combined with different carbon nanostructures in order to improve not only a higher surface area of the active material but also film conductivity, due to the carbon nanostructures.[5] For example, Mn_3O_4 nanocrystals have been successfully dispersed on reduced graphene oxide, delivering higher lithium storage capacity in comparison to pure Mn_3O_4.[6] However, there is a general consensus that the manganese dissolution during the charge-discharge cycle is the key problem hindering the application of electroactive Mn_xO_y as electrode material.[7] Mn cation dissolution not only adversely affects capacity retention through the loss of active material but also can cause the formation of an undesired solid electrolyte interphase (SEI) on the negative electrode of a lithium battery. Delacourt et.al, revealed that manganese cations trapped in the solid electrolyte interphase undergo a multiphase transformation reactions leading to severe structural changes and electrolyte decomposition,[8] which illustrates the detrimental effects caused by manganese dissolution.

Three main approaches have been explored to combat the problem of dissolution. The first is based on the substitution of manganese in a $LiMn_2O_4$

crystal lattice by cations such as Co^{2+}, Al^{3+} and Ti^{4+}, which also reduce the electrochemical activity of the material due to the dopant cations.[9-10] An alternative approach involves coating the surface of manganese oxide with a thin layer of less soluble metal oxide, such as ZnO, NiO and Co_3O_4.[11-13] These core-shell electrodes possess remarkable stability and retention of 97% over 100 cycles at high temperature, which is a significant improvement on the performance of the core electrode which drops 35.3% under the same conditions.[14] However, uniformity and continuity of the coating layers may make it difficult to control the insulating nature of the coated oxide, and may block ionic and electronic transportation channels, therefore decreasing the storage ability. More recently Zhan et.al reported an effective approach to supress manganese dissolution via a nanoscale surface-coating by atomic layer deposition of electrochemical inactive cations incorporated only into the surface of the spinel $LiMn_2O_4$ both protecting the bulk $LiMn_2O_4$ from acid corrosion, such as a surface-coating layer, but maintaining the ion and charge transport channels on the surface.[15] Protective coating with a polymer can also enhance the electrochemical utilization of well-dispersed manganese oxide nanoparticles while suppressing the dissolution related to the structure evolution during cycling.[16] For example, mesoporous carbon/MnO_2 composite covered with polyaniline showed a capacitance retention of 88% after 1000 galvanostatic charge-discharge cycles in acid media.[17] As an alternative to the protective coating methodology which may have negative impact on the electrode rate capability, dissolution of manganese compounds can be supressed by adding to the electrochemical media either $NaHCO_3$ or Na_2HPO_4, improving electrode cyclability to over 1800 cycles, as demonstrated by Komaba et. al.[18]

The present study explores an alternative and simple approach to mitigate manganese dissolution via encapsulation in hollow tubular carbon nanostructures, which does not require any chemical modification of the manganese oxide nanoparticles nor the composition of electrolyte. Carbon nanofibers (CNFs) stands as the ideal candidate due to their low cost as well as their large internal diameter (63 ± 26 nm), which exhibit corrugated surfaces due to their internal layers composed by 13-15 nm stacked-nanocones (Appendix V, Figure 1). These corrugated graphitic cavities have already

shown an effect on the nanoparticles by controlling the nanoparticle positions [19] and growth.[20] Additionally, CNFs can provide excellent electrical contact between the nanoparticles and the macroscopic electrode due to the high conductivity of CNFs.[21] Most importantly, the nanoscale confinement prevents the dissolution of nanoparticles without detrimental effects on ion or charge mobility, thus yielding a new hybrid material with superior electrochemical stability. This study is specifically focused on Mn_3O_4 phase which is known to be kinetically more likely to dissolve as compared to other oxides, such as Mn_2O_3 or MnO_2.[22]

5.2 Results and discussion

Synthesis and characterization of metal oxide-carbon hybrids. The synthesis of pseudo-spherical Mn_3O_4 NP is based on the developed approach for Hyeon's group[23] which requires a basic reaction medium obtained by the hydrolysis of acetate:[24]

$$CH_3COO^- + H_2O \rightarrow CH_3COOH + OH^- \quad (1)$$

$$3Mn^{2+} + 6OH^- + (1/2)O_2 \rightarrow Mn_3O_4 + 3H_2O \quad (2)$$

Briefly, manganese acetate is added to a solution of oleylamine, which acts as a ligand stabilising the surface of the growing nanoparticle, in xylene and subsequently heated to 90^0C in air atmosphere. Once the temperature is achieved, 1 mL of DI water was injected into the solution under vigorously stirring and aged for 3 hours. Subsequently, pseudo-spherical nanoparticles of 11 ± 3 nm diameter are obtained after purification (Appendix V, Figure 2). A similar procedure was followed to synthesise nanoparticles of Mn_3O_4 within CNF cavity by immersing open CNFs into a solution of manganese acetate with oleylamine/xylene. With the aim of tuning the number of nanoparticles that are synthesized inside the carbon nanofibers (CNFs), the carbon surface was previously oxidized by acid treatment (HNO_3). X-ray photoelectron spectrometry (XPS) confirms the differences in oxygen content (O%) on the surface a different nanofibers labelled as CNF_G, CNF, CNF_{AC} and CNF_{OX} according to their oxygen content, 0.4, 1.2, 2 and 11.4, respectively (Appendix V, Figure 3). Hence, when the nanofibers surface is oxidised by acid treatment (i. e. CNF_{AC} and CNF_{OX}) prior Mn_3O_4 formation, the nanoparticles are formed

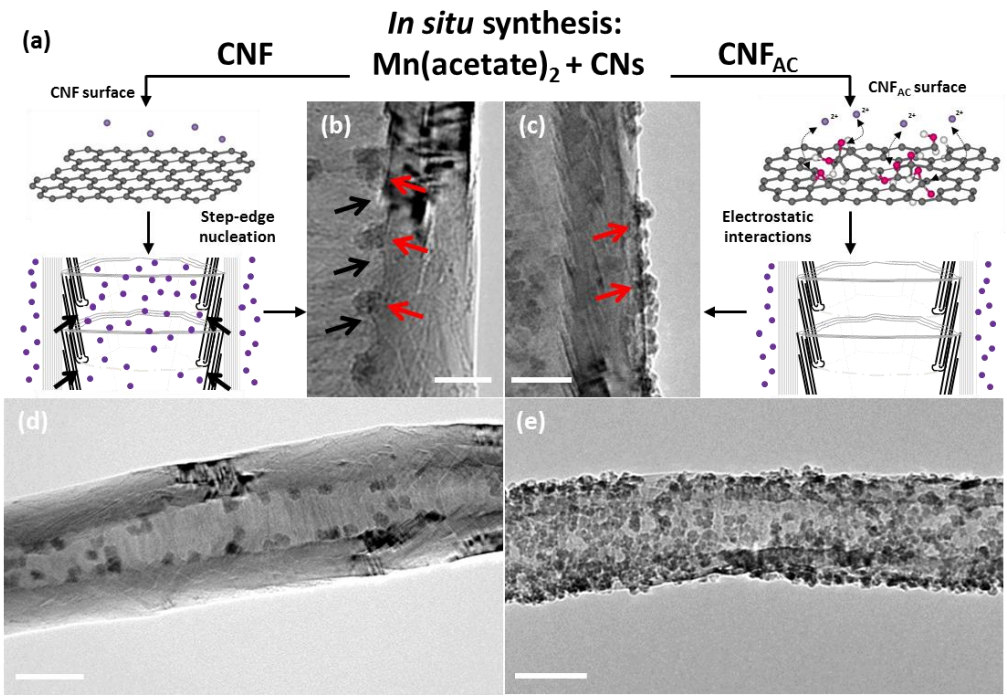

Figure 1. (a) Schematic synthesis of Mn_3O_4@CNF (left-hand-side) and Mn_3O_4/CNF_{AC} (right-hand-side) showing both the smooth exterior and corrugated interior (black arrows) of CNFs. (b) The In situ synthesis of Mn_3O_4 NPs was performed in the presence of pristine CNF, leading to the formation of nanoparticles (red arrows) located inside CNF (Mn_3O_4/CNF). (c) In order to study the effect of nanoparticle encapsulation, a similar nanoparticle synthesis was carried out in the presence of acid treated CNF (CNF_{AC}), forming Mn_3O_4/CNF_{AC} hybrid where nanoparticles were mostly deposited on the outer surface of CNF_{AC} due to initial electrostatic interaction between Mn^{2+} cations (purple) and oxygen groups (pink) at the carbon surface. (d) TEM image of Mn_3O_4/CNF, showing nanoparticles positioned inside CNF cavity at the step-edges. (e) TEM image of Mn_3O_4/CNF_{AC}, showing that most of the nanoparticles are located outside the CNF_{AC}. Scale bars, 20 nm (b,c) and 50 nm (d,e) respectively.

predominately on the exterior of CNF_{AC} (Figure 1c and Appendix V, Figure 4). As the oxidative treatment of CNF leads to the structural defects in the sp^2-carbon lattice, and functionalisation with oxygen-containing groups, such as carboxyl, epoxide or hydroxyl groups, on the surface of CNF_{AC} which are able to bind manganese cations during the nanoparticle synthesis, resulting in the nucleation and growth of nanoparticles mainly on the outer surface and acting as anchoring sites for Mn_3O_4 NPs (Figure 1e).[25-26] In pristine CNFs, the absence of such defects on the surface ensures that manganese cations to interact equally with both the outer and the inner carbon surface of CNF during the synthesis. However, the internal CNF step-edges of 3-4 nm high ensure a larger surface of contact with growing nanoparticles than the smooth outer

surface, thus providing more effective nucleation centres and the anchoring points for Mn_3O_4 NP inside CNF (Figure 1d).[20]

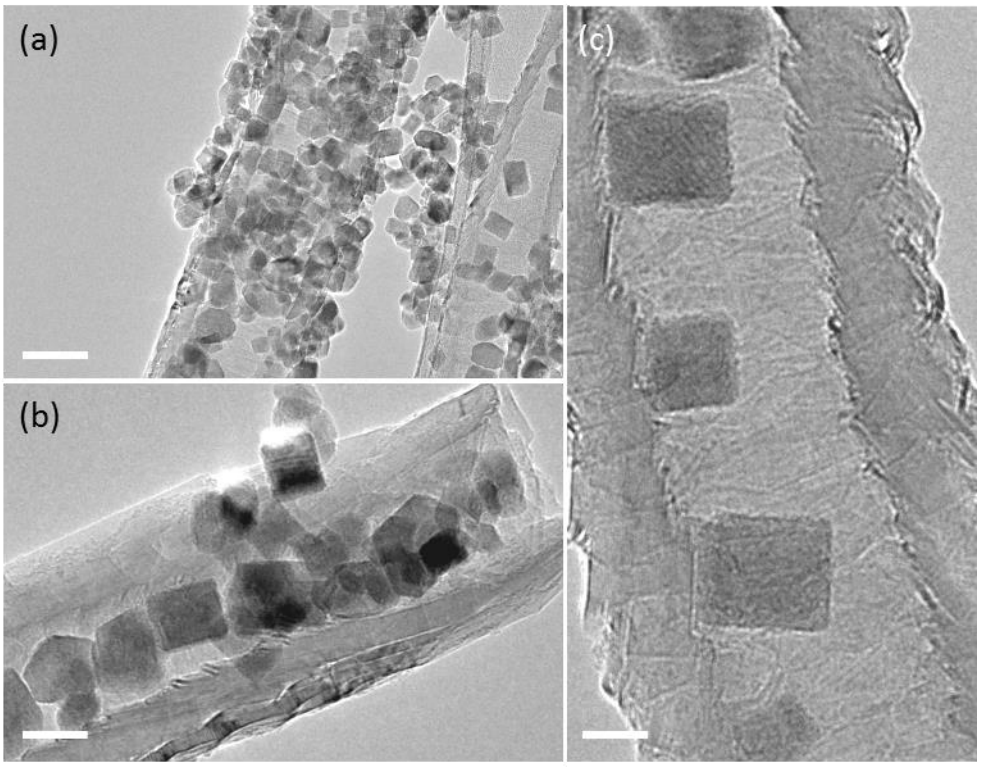

Figure 2. TEM images Mn_3O_4/CNF_G. Scale bars are (a) 50, (b) 20 and (c) 10 nm, respectively

When the in situ synthesis is carried out in the presence of low oxygen content carbon nanofibers (CNF_G, O < 1%), synthesized Mn_3O_4 NPs were larger and more faceted (Figure 2a) compared to free-standing Mn_3O_4 NPs. A close inspection at the carbon nanofiber interiors by TEM reveals the existence of NPs, proving carbon nanofibers as nanoreactors for the synthesis of metal-oxide nanoparticles (Figure 2b). Analysis of the side dimension of the encapsulated nanoparticles in Mn_3O_4/CNF_G reveals a size similar to the step length, formed by few layers graphene-stacked (18 ± 6 nm length), enabling the nanoparticles to grow and arrange within a chain in just one step synthesis (Figure 2c and Appendix V, Figure 5). It is important to highlight that large and faceted nanoparticles (Appendix V, Figure 6) are also observed after repeating the same synthetic procedure in the presence of graphitized MWNTs (Appendix V, Figure 7). Nanoparticles were not synthesized inside GMWNTs due to their narrower internal diameter (4 ± 2 nm) with respect to CNFs (63 ± 23 nm). Thus, these observations suggest that the carbon surface can tune the

morphology of Mn_3O_4 NPs from small and pseudo-spherical to large and faceted nanoparticles.

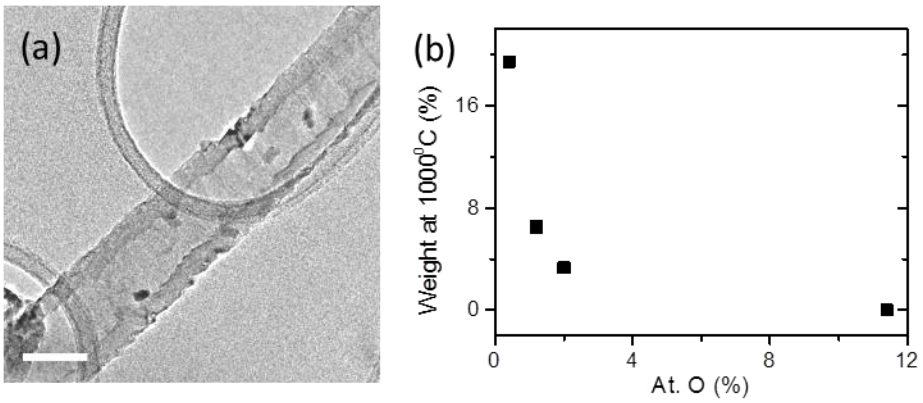

Figure 3. (a) TEM image of Mn_3O_4/CNF_{AC} hybrid after purification (named as $Mn_3O_4@CNF_{AC}$), showing small amount of nanoparticles inside. (b) Correlation of the total metal oxide loading in the purified hybrids (based on TGA measurements in air) with respect to the superficial oxygen content (based on XPS measurement) on the carbon nanostructure (0.4, 1.2, 2 and 11.4 for CNF_G, CNF, CNF_{AC}, and CNF_{OX}, respectively). Scale bar is 50 nm.

Previous studies have shown that the morphology (size and shape) of nanocrystals are very sensitive to changes on experimental conditions such as precursors/surfactant ratio, temperature, time, solvents, pH, mechanical agitation and even a magnetic field.[27-31] However, to the extent of our knowledge, graphitized carbon nanostructures (i. e. small oxygen content) have not being shown to affect the synthesis of nanoparticles. Based on the experimental results, we may propose the nucleation and growth mechanisms of Mn_3O_4 nanoparticles during the in situ synthesis. In our system, the carbon nanostructure, and specially, their superficial functionalization, plays a role during the in situ synthesis of the metal oxide-carbon hybrid material, as other experimental parameters such as temperature, solvents or reaction time are similar in all the experiments. The Hyeon group performed several experiments to fully understand the formation mechanism of free-standing Mn_3O_4 NP, proposing manganese oxide $Mn(OH)_2$, which can be generated during the hot-injection of DI water in the presence of oleylamine, as an intermediate that only contributes to the nucleation. In contrast, manganese-oleylamine (Mn-OAM) complex contributes to the shape-controlled growth process as the experimental results suggested a selective attachment onto the (001) plane of Mn_3O_4[32]. Therefore, any interaction of the carbon nanostructure with these

two intermediate species ($Mn(OH)_2$ and Mn-OAM) during the synthesis would have a dramatic impact on the final nanoparticle morphology.

In our experiments, the smaller nanoparticle size found in Mn_3O_4/CNF_{AC} with respect to free-standing Mn_3O_4 NPs (Appendix V, Figure 8), 8 ± 2 and 11 ± 3 nm, respectively, confirms that oxygen containing groups on the carbon surface additionally act as nucleation points. Thus, the presence of oxidized carbon nanofibers (i. e. CNF_{AC}) does not substantially modify the nanoparticle synthetic pathway as similar pseudo-spherical nanoparticles are observed, compared to free-standing Mn_3O_4 NPs. An indirect observation of a strong interaction of the Mn^{2+} with the oxidized carbon surface would be inversely related to the total Mn_3O_4 weight encapsulated inside hollow tubular nanostructures. To investigate this point further, all hybrid materials were purified after the synthesis by removing the NPs located on the outer surface of the nanofiber via sonication in hexane and subsequent filtration. As it can be observed in Figure 3a, a significant difference of the nanoparticle content is observed after purification ($Mn_3O_4@CNF_{AC}$) with respect to Mn_3O_4/CNF_{AC} (Figure 1e) so most of nanoparticles are located inside CNF (Appendix V, Figure 9). Thermal gravimetric analysis of the purified hybrid materials shows that higher amount of manganese oxide remains in $Mn_3O_4@CNF_G$ with respect to $Mn_3O_4@CNF_{AC}$, being the values 19.4 and 3.3% respectively. Hence, a correlation is stablished between the weight of manganese oxide of the purified hybrids at 1000^{o}C (encapsulated) with respect to the superficial oxygen content measured by XPS (Figure 3b), revealing a low nanoparticle content for a high oxygen-containing groups surface as a consequence of oxygen containing groups on the carbon surface acting as nucleation points via electrostatic interactions (Figure 4a).[33]

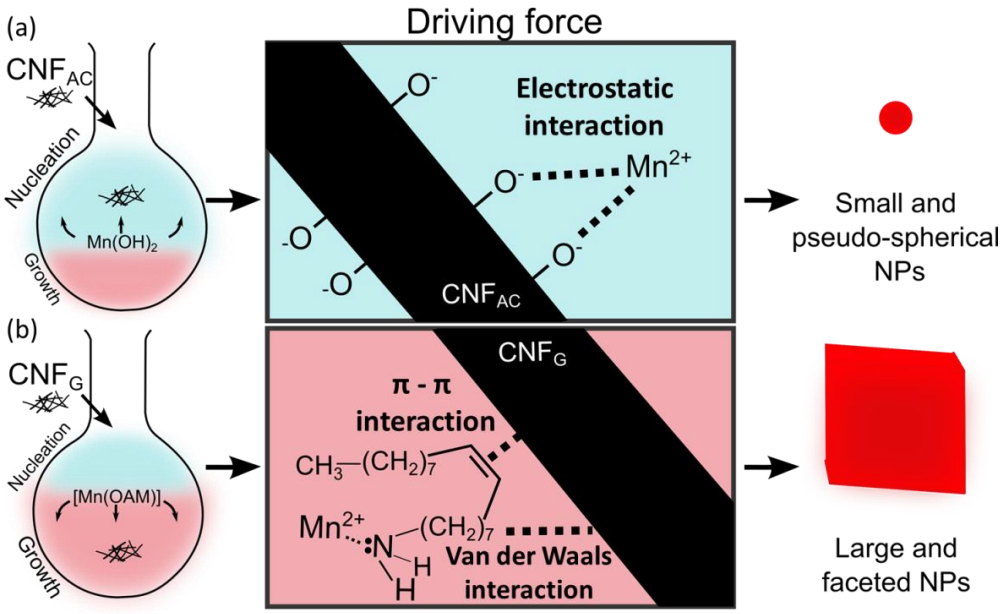

Figure 4. Schematic representation of in situ synthesis of Mn_3O_4 nanoparticles in the presence of (a) CNF_G and (b) CNF_{AC}. In the presence of CNF_{AC}, the nucleation process (represented by the blue zone) would be favoured with respect to the growth process as the oxygen-containing groups in the carbon surface would additionally acts as nucleation points via electrostatic interaction. Conversely, the non-covalently π-π stacking interaction between the alkenyl functional group (-CH=CH-) and the aromatic graphitized surface as well as van der Waals interaction with the alkali chain of oleylamine with the carbon surface would drive the Mn-OAM complex towards the carbon surface (both inside and outside), enhancing the growth (represented by the pink zone)over the nucleation process.

In contrast, the presence of large and faceted nanoparticles suggests a change on the nucleation/growth ratio when using low oxygen content carbon nanostructures (i. e. CNF_G or GMWNTs). Due to the lack of oxygen-containing groups or, in other words, the highly graphitized carbon surface, an interaction between the oleylamine with the carbon surface is expected via a non-covalent π- π stacking interaction between the alkenyl functional group (-CH=CH-) of oleylamine and the aromatic graphitized surface as well as van der Waals interaction of the long alkali chain (– $(CH_2)_7$–) with the carbon surface (Figure 4b). This effect would be the driving force for the Mn-OAM complex to completely surround the carbon surface (both inside and outside). Simultaneously, the hydrophobicity of the graphitized carbon nanostructure would hinder the formation of numerous $Mn(OH)_2$ nucleation points when the hot-injection of H_2O takes place. Thus, the combination of the mentioned effects together with the observed template effect of the internal nanocone would lead to large and faceted nanoparticles when the synthesis is performed

in the presence of highly graphitized carbon nanostructure (CNF_G and GMWNTs).

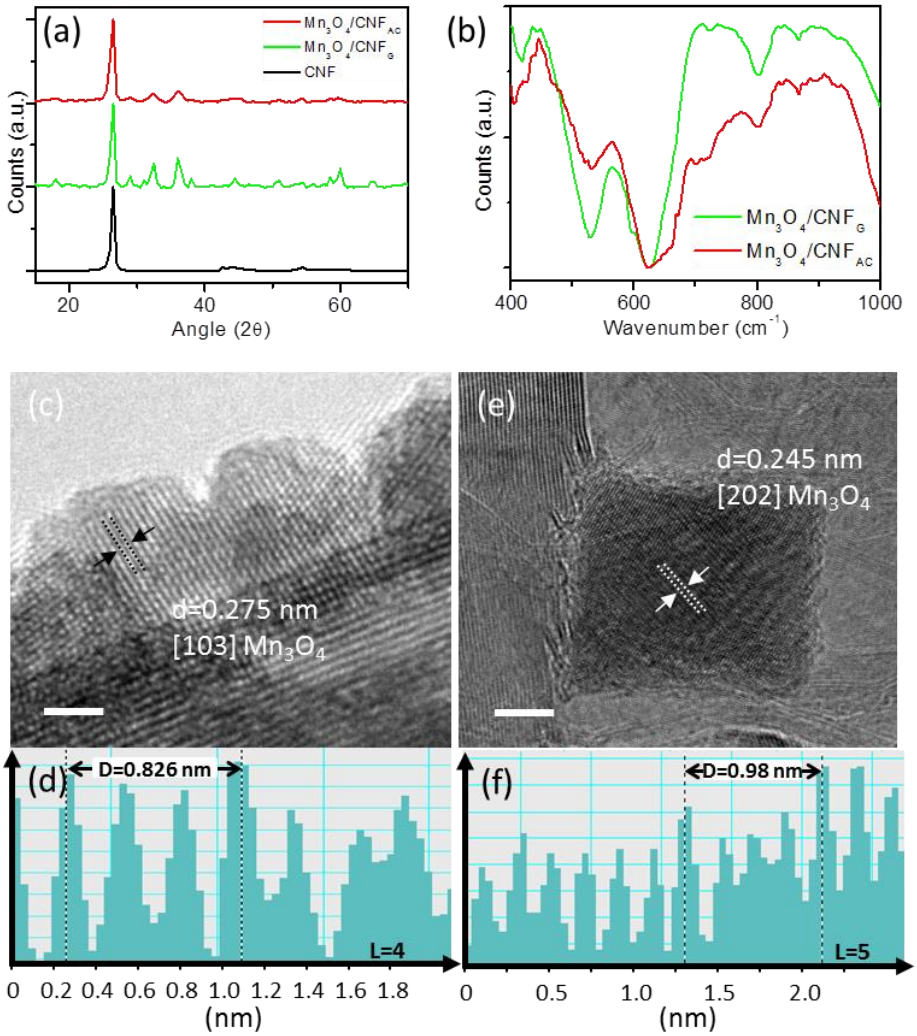

Figure 5. (a) Powder XRD pattern and (b) IR spectra of pristine CNF (black), Mn_3O_4/CNF_G (green) and Mn_3O_4/CNF_{AC} (red). High resolution TEM images of (c) Mn_3O_4/CNF_{AC} and (e) Mn_3O_4/CNF_G. (d,f) Interplanar spacing (d) is calculated using the equation: $d = D / (L\text{-}1)$, where D and L stand for the total distance and the numbers of layers, respectively, as measured in the line profiles (d,f) of the HRTEM images. Scale bars are (e) 5 and (c) 2 nm, respectively.

Despite the observed morphological differences between the nanoparticles with respect to the carbon nanostructure, only the Mn_3O_4 phase is successfully synthesized in all the hybrid materials. The XRD pattern is indexed to Hausmannite Mn_3O_4 (JCPDF file no. 80-0382) where sharp diffraction peaks in the XRD pattern of Mn_3O_4/CNF_G are indicative of highly crystalline nanoparticles (Figure 5a, green), which is in line with HRTEM observations (Figure 5e-f and Appendix V, Figure 10). Nanoparticles in Mn_3O_4/CNF_{AC} and

Mn_3O_4@CNF have lower crystallinity due to their small size, being confirmed by the slightly broader diffraction peaks in the XRD pattern (Figure 5a, red and Appendix V, Figure 11) as well as by HRTEM analysis (Figure 5c). The crystal lattice fringes can just be attributed to the Mn_3O_4 (Figure 5d-f and Appendix, Figure 12). In addition, the sharp peaks at 628 and 524 cm^{-1} observed by IR were assigned to the characteristic of coupling modes between Mn-O in tetrahedral and octahedral sites for Mn_3O_4 nanoparticles (Figure 5b and Appendix V, Figure 13). [34] Therefore, the carbon nanostructure surface does not appear to affect the chemical composition of the nanoparticles but their growth mechanism.

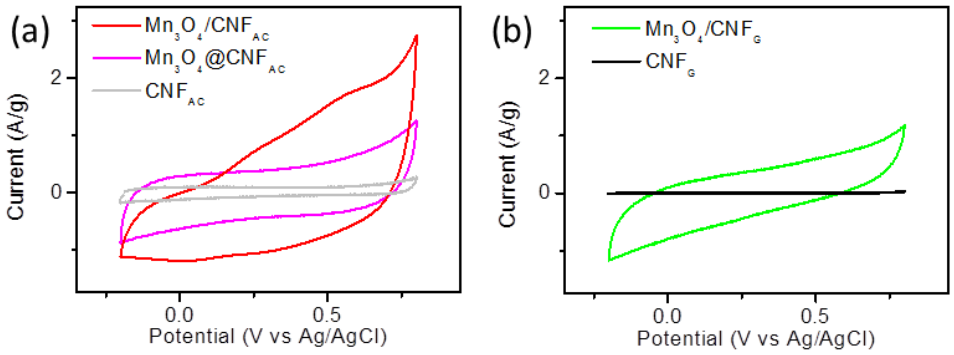

Figure 6. Cyclic voltammetry of (a) Mn_3O_4/CNF_{AC}, before (red) and after washing (pink), and (b) Mn_3O_4/CNF_G (green) with respect to the carbon nanostructure (CNF_{AC} grey and CNF black) at 0.1V/s in 2M KCl. Specific capacitances of Mn_3O_4/CNF_{AC}, Mn_3O_4@CNF_{AC} and Mn_3O_4/CNF_G are 17.8, 9.6 and 8.3 F/g, respectively.

Figure 6 shows that the Mn_3O_4/CNF_{AC} hybrid, where large amount of small pseudo-spherical nanoparticles decorating the surface of CNF_{AC}, shows the largest current response (Figure 6a, red) with respect to large faceted NPs in Mn_3O_4/CNF_G (Figure 6b, green). Their specific capacitances are 17.8 and 8.3 F/g respectively. In addition, the Mn_3O_4@CNF_{AC} hybrid, despite itss lower manganese oxide content with respect to Mn_3O_4/CNF_G (3.3 and 19.4%, respectively), exhibits a higher current response (Figure 6a, pink). Thus, small nanoparticles are a better candidate for electrochemical storage applications due to their high surface area in comparison to large and crystalline nanoparticles.

In this context, Mn_3O_4/CNF_{AC} and Mn_3O_4@CNF hybrids are ideal systems to investigate the confinement effect of nanoparticles within CNF. It is

important to highlight that large field of view TEM images clearly demonstrate that Mn_3O_4/CNF_{AC} (Figure 1e) contains more nanoparticles than Mn_3O_4@CNF (Figure 1d), which is corroborated by TGA measurements quantitatively showing that Mn_3O_4/CNF_{AC} have almost 4 times more Mn_3O_4 (by weight) than Mn_3O_4@CNF (Appendix V, Figure 14). Closer inspection of high-magnification TEM images reveals that while the nanoparticles have the same shape in both materials, they are slightly smaller in Mn_3O_4/CNF_{AC} as compared to Mn_3O_4@CNF, with the average diameters being 8 ± 2 and 10 ± 2 nm respectively (Appendix V, Figure 8). This small but measurable difference is likely to be a result of a higher number of nucleation points in CNF_{AC} than in pristine CNF leading to a larger number of smaller nanoparticles in the former case as previously discussed.

In order to further investigate the effect of nanoparticles confinement in CNF, a separate batch of Mn_3O_4 NPs was synthesized using the same conditions as for the preparation of Mn_3O_4@CNF, but without CNF, leading to free-standing spherical nanoparticles (s-Mn_3O_4, 11 ± 3 nm).[23] In parallel, another batch of Mn_3O_4NP was made by extending the reaction time from 3 to 8 hours yielding nanoparticles with the 'nanobrick' morphology (b-Mn_3O_4, approximately 10 nm x 10 nm with ~5.7 nm thickness). The pre-formed nanoparticles have been inserted into CNFs using previously reported methods,[20] producing s-Mn_3O_4@CNF_{AC} (Appendix V, Figure 15**)** and b-Mn_3O_4@CNF (Appendix V, Figure 16) which give ideal control systems for comparison with the Mn_3O_4@CNF where nanoparticles were formed *in situ* inside CNFs.

Electrochemical storage properties and stability. Overall, Mn_3O_4/CNF_{AC} and Mn_3O_4@CNF possess similar size, shape and chemical composition of the metal oxide nanoparticles but with significantly different environments around the Mn_3O_4 centres, such that comparison of electrochemical performance of these nanomaterials can help to assess the impact of nanoscale confinement on the functional properties of the nanoparticles and to harness them in practical applications (Figure 7a-b). In addition, electrochemical performance of s-Mn_3O_4@CNF_{AC} can stablish the advantages of *in situ* synthesis with respect to the conventional two-steps approach synthesis while comparison with b-

Mn_3O_4@CNF can illustrate the importance of the nanoparticle shape and size. The metal oxide-carbon nanostructures were deposited on a clean glassy carbon surface by drop casting and were studied in cyclic voltammetry measurements at 0.05V/s in 2M KCl. CV measurements indicate a capacitance (calculated from the area under the curve) of Mn_3O_4/CNF_{AC} 4 times higher than Mn_3O_4@CNF (Figure 7c), which is related to the higher amount of metal oxide and smaller nanoparticles in the former material. In addition, inorganic oxygen-containing groups on the CNF_{AC} may further contribute to the capacitance of Mn_3O_4/CNF_{AC} (Appendix V, Figure 17).

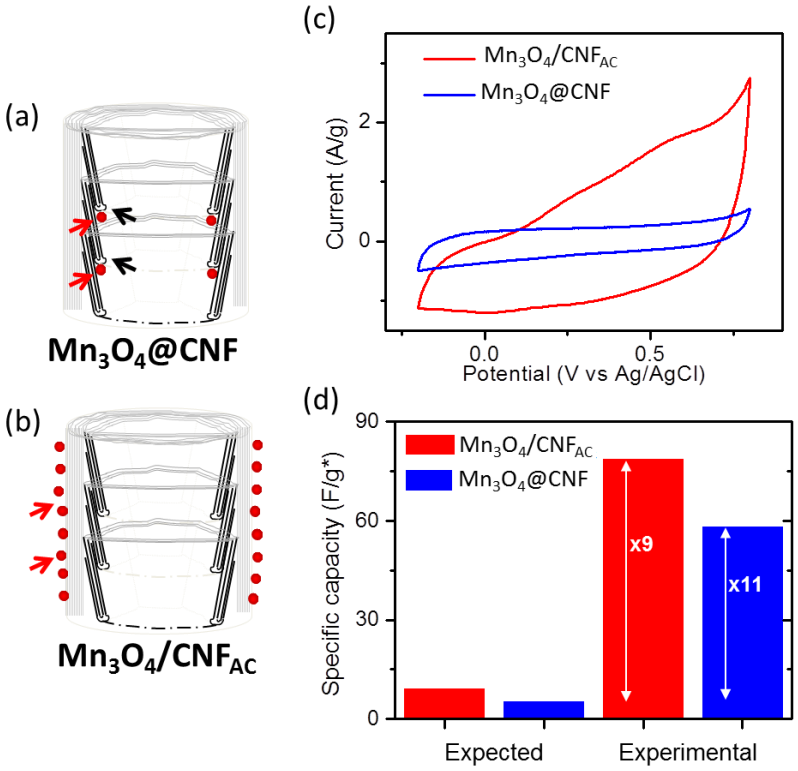

Figure 7. (a) and (b) are schematic representation of Mn_3O_4/CNF and Mn_3O_4/CNF_{AC} respectively. (c) Cyclic voltammogram of Mn_3O_4@CNF (blue) and Mn_3O_4/CNF_{AC} (red) at 0.05V/s in 2M KCl. (d) Expected (based on charge-discharge values of individual building blocks, e.g. Mn_3O_4NP and CNF in separation) and experimental specific capacitance (based on charge-discharge cycle at 0.5 A/g) of Mn_3O_4@CNF (blue) and Mn_3O_4/CNF_{AC} (red), showing a greater synergetic effect when nanoparticles are located inside CNF (Mn_3O_4@CNF) than outside CNF_{AC} (Mn_3O_4/CNF_{AC}). Because the two hybrid materials have different amounts of nanoparticles, the capacitance was normalized with respect to the amount of Mn_3O_4 of each sample for the sake of comparison (defined as specific capacitance).

It is important to mention that the specific capacitance of the hybrid material is not always a sum of the specific capacitance values of their building blocks (Appendix V, Table 1). For example, in contrast to agglomerated nanoparticles,

well-distributed nanoparticles on a surface would have larger surface available which would enhance the specific capacitance. Hence, the *in situ* synthesized Mn_3O_4/CNF_{AC} and Mn_3O_4@CNF show experimentally measured specific capacitances of 9 and 11 times higher than expected for the sum of the constituent components (Figure 7d). The greater synergy effect for Mn_3O_4@CNF suggests that nanoparticles inside CNF not only may have a better dispersion but, more importantly, a stronger interaction with the carbon support than nanoparticles located outside CNF_{AC}, highlighting the benefit of confinement for the effective electric contact between the Mn_3O_4NP and the carbon nanofiber. Interestingly, preformed s-Mn_3O_4 NPs inserted into CNF_{AC} (s-Mn_3O_4@ CNF_{AC}) have an experimental specific capacitance no more than twice of the expected for the separate components, exhibiting only a low synergetic effect (Appendix V, Figure 18), which is in sharp contrast to the remarkable synergetic effect observed in Mn_3O_4@CNF hybrid (Figure 8f). Thus, *in situ* synthesis of metal oxide nanoparticles directly in carbon nanostructures is demonstrated to be a more effective approach as compared to the conventional approach (pre-formed nanoparticles inserted in CNF) for the capacitance due to the formation of a more intimate nanoparticle-carbon contact.

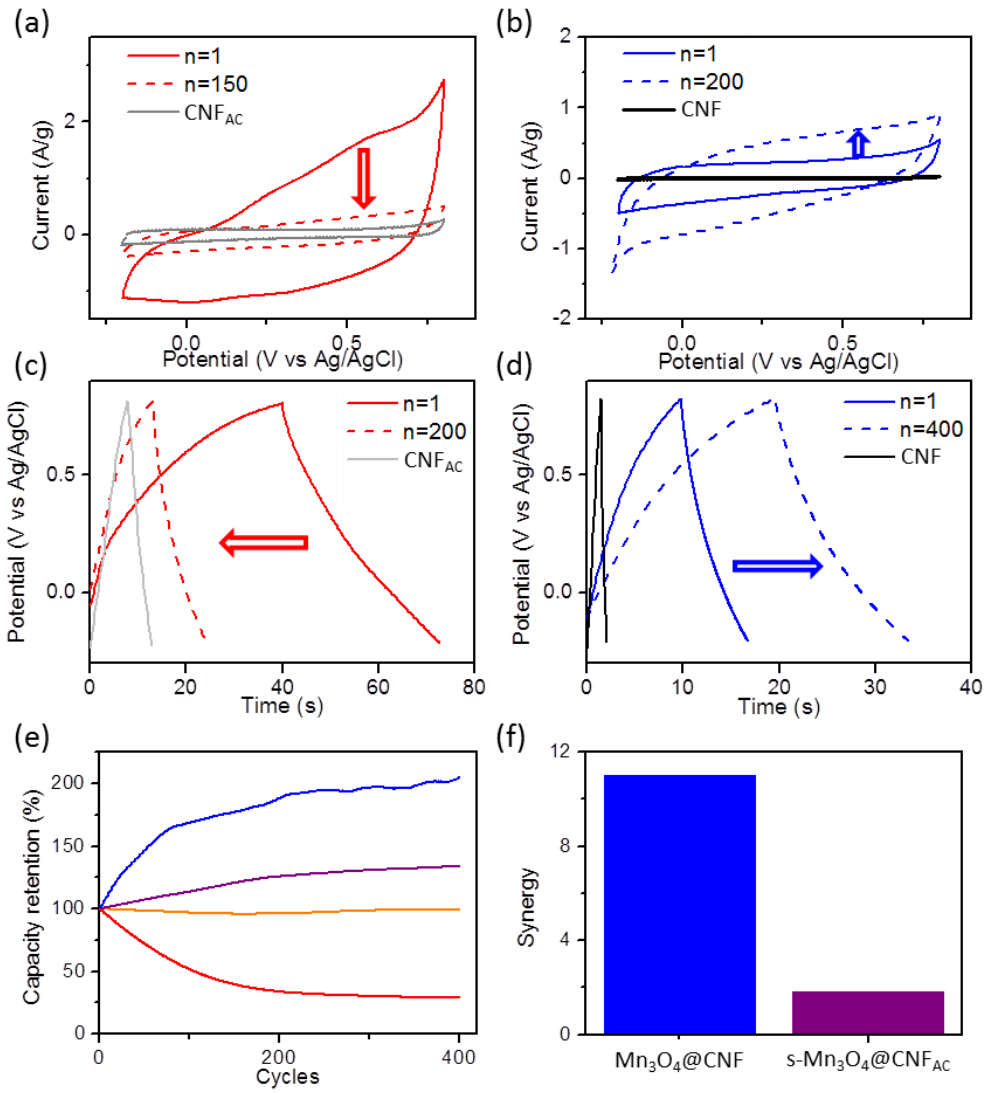

Figure 8. (a) Cyclic voltammograms of Mn_3O_4/CNF_{AC} (n=1, n=150 (dashed)) with respect to CNF_{AC} (grey) at 0.05V/s in 2M KCl, showing a low cycling stability. (b) Cyclic voltammograms of Mn_3O_4@CNF (n=1 and n= 200 (dashed)) with respect to pristine CNF (black), showing an increment in current after 200 cycles at 0.05V/s in 2M KCl. (c) Galvanostatic charge-discharge cycles of Mn_3O_4/CNF_{AC} (n=1, n=200 (dashed)) with respect to CNF_{AC} (grey) at 0.5A/g, showing a decrement of capacitance after cycling in 2M KCl. (d) Galvanostatic charge-discharge cycles of Mn_3O_4@CNF (n=1, n=400 (dashed)) with respect to CNF (black) at 0.5 A/g, showing an increment of capacitance after cycling in 2M KCl. (e) Capacitance retention of Mn_3O_4/CNF_{AC} hybrid (red), b-Mn_3O_4@CNF composite (orange), s-$Mn_3O_4@CNF_{AC}$ composite (purple) and Mn_3O_4@CNF hybrid (blue) during 400 cycles at 0.5 A/g in 2M KCl. (f) Synergy, being the ratio between experimental and theoretical specific capacitance, of Mn_3O_4@CNF hybrid (blue) with respect s-$Mn_3O_4@CNF_{AC}$ composite (purple) shows the benefits of *in situ* over conventional synthesis procedure.

Detailed CV measurements performed for both *in situ* synthesized hybrid materials under the same conditions (2M KCl electrolyte, room temperature) show significant differences in electrochemical stability of the two materials. The stability of nanoparticles outside CNF_{AC} appears to be relatively low

(Figure 8a) as the electrochemical response of Mn_3O_4/CNF_{AC} decreases dramatically after 150 cycles and approaches the response of empty CNF_{AC} (grey line). In stark contrast, nanoparticles located inside CNF (Mn_3O_4@CNF) not only retain their properties, but increase their electrochemical response after 200 cycles (Figure 8b) and maintain the improved electrochemical performance for 9,000 cycles (Appendix V, Figure 19). Electrochemical impedance spectroscopy confirms this improvement in the capacitance for the hybrid material after cycling at 0.05 V/s (Appendix V, Figure 20). Furthermore, charge-discharge measurements performed in both hybrid materials under the same conditions reveal an increase in capacitance of Mn_3O_4@CNF (Figure 8d) and a decrease in capacitance of Mn_3O_4/CNF (Figure 8c) with the number of cycles, which is consistent with the observed changes in the electrochemical responses of these materials. This clearly emphasises the advantages of charge storage for confined Mn_3O_4 NP and represents a significant improvement in the nanoparticle stability provided by the CNF nanoscale cavity. Additionally, b-Mn_3O_4@CNF and s-Mn_3O_4@CNF_{AC} show a high capacitance stability during charge-discharge cycles in 2M KCl at 0.5A/g (Figure 8e) similar to that for Mn_3O_4@CNF, confirming that the encapsulation of nanoparticles is essential for the enhanced durability of Mn_3O_4 NPs.

Surprisingly, in spite of their high stability, no measurable electrochemical activation was observed for b-Mn_3O_4@CNF after 400 cycles. Due to the synthetic protocol, preformed block-shaped b-Mn_3O_4 NPs are surrounded by almost twice as much surfactant as the more compact spherical Mn_3O_4 NPs (Appendix V, Figure 21). Such a highly protected surface may result in a lower specific capacitance of the b-Mn_3O_4@CNF composite (23.7F/g) with respect to spherical nanoparticles inside CNF (Mn_3O_4@CNF-58.1 F/g) (Appendix V, Figure 22). Furthermore, the almost constant electrochemical response during charge-discharge cycles (e.g. no decrease and no increase in the specific capacitance with the number of cycles, Figure 8e) may also be linked to a high concentration of surfactant surrounding the nanoparticle surface in b-Mn_3O_4@CNF. It is important to note that the fact that the surface of Mn_3O_4 crystal in the block-NP is flatter than in sphere-NP may also mean that the crystal facets in b-Mn_3O_4 are more stable and less likely to change during the

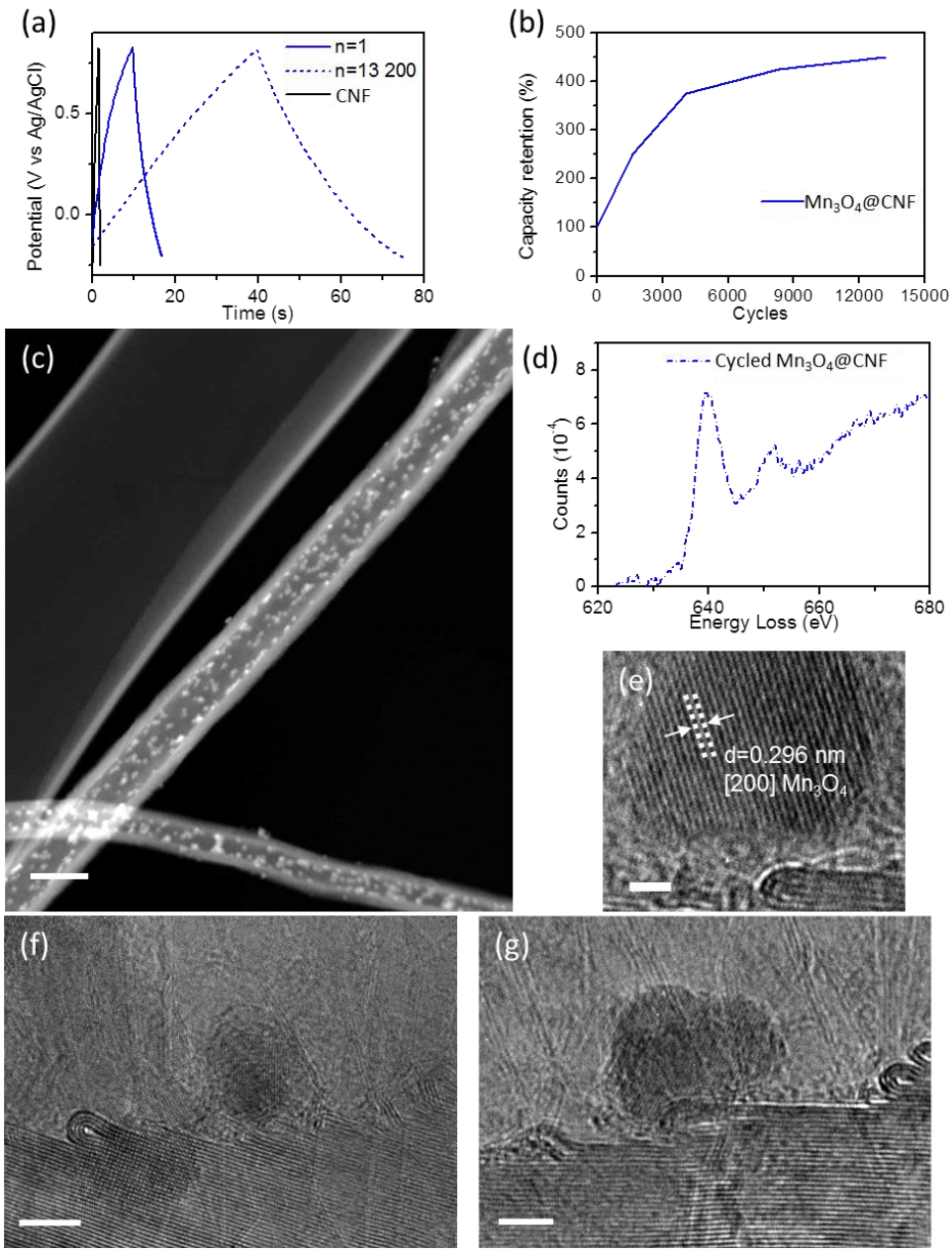

Figure 9. (a) Galvanostatic charge-discharge cycles of Mn_3O_4/CNF (n=1, n=13,200 (dashed)) with respect to CNF (black) at 0.5A/g, showing an increment of capacitance after cycling in 2M KCl. (b) Capacitance retention of Mn_3O_4/CNF during 13,200 cycles at 0.5 A/g in 2M KCl. (c) STEM image of Mn_3O_4@CNF after electrochemical stability experiment (13,200 cycles), revealing that nanoparticles remain inside CNF (inverse contrast to bright-field TEM: nanoparticles are bright white/grey and CNF walls pale grey, and vacuum is black). (d) Electron energy-loss spectrum of Mn_3O_4 NPs located inside CNF with peak intensity ratio of 2.7. (e) HRTEM image of Mn_3O_4 NPs inside CNF after 13,200 charge-discharge cycles at 0.5 A/g, showing characteristic inter planar distance of Mn_3O_4 (0.296 [200]). HRTEM of Mn_3O_4@CNF (f) before and (g) after 13,200 charge-discharge cycles at 0.5 A/g. Scale bars are 100 (c), 5 (f,g) and 2 nm (e).

charge-discharge cycling.[35] In addition, electrochemical activation appears to be directly related to nanoparticles loading. Although showing similar pseudo-

spherical nanoparticles, with similar sizes (Appendix V, Figure 2), s-Mn_3O_4@CNF_{AC} composite, which has 3.8 wt.% Mn_3O_4 (Appendix V, Figure 23), shows a smaller electrochemical response increment than Mn_3O_4@CNF hybrid with 6.4 wt.% Mn_3O_4 under the same conditions (Figure 8e).

As the Mn_3O_4@CNF hybrid shows the greatest activation among all the studied materials, the cycling stability experiment was extended over 13,000 cycles (Figure 9a). It is remarkable that this hybrid material becomes almost five times more active after such a long charge-discharge cycling (Figure 9b). Previous work showed a specific capacitance activation (between 1.4 to 3.5 times) triggered by the oxidation of Mn_3O_4 to MnO_2 (with the latter being more electrochemically active) due to Na^+ intercalation.[36-38] This transformation has previously been studied in detail, for instance, Komaba reported effects of different parameters, such as milling treatment, the potential range and electrolyte solution on the Mn_3O_4 to MnO_2 transformation.[39] To the best of our knowledge, the specific capacitance activation of Mn_3O_4NPs has not been previously reported in aqueous KCl solution.

Characterization of electrochemically activated Mn_3O_4@CNF. In order to gain a better understanding of the mechanisms of the electrochemical activation described above and to elucidate the chemical reasons for the continuously increasing capacitance of Mn_3O_4@CNF during the charging-discharging cycling, detailed TEM analysis was carried out on the Mn_3O_4@CNF material after it had been subjected to around 15,000 cycles. Remarkably, nanoparticles are retained inside CNFs even after around 15K cycles (Figure 9c) and, surprisingly, there is no measurable increase of the nanoparticle average size (10-11 nm) after the experiment, although the spread of the size distribution increases from 2 to 4 nm (Appendix V, Figure 24). HRTEM images of the inter-planar distances confirm that the nanoparticles remain as the Mn_3O_4 phase after the electrochemical cycling (Figure 9e and Appendix V, Figure 25) ruling out the oxidation to MnO_2 or any other chemical transformation of the manganese oxide as a potential mechanism for the activation. Additionally, electron energy-loss spectroscopy (EELS), a powerful local-probe chemical analysis method for determining the oxidation state of transition metals, shows the intensity ratio of $L_3(2p_{3/2})/L_2(2p_{1/2})$ for Mn EELS

edges as 2.7, as expected for the Mn_3O_4 phase (Figure 9d).[40-44] Therefore, the drastic improvement of the capacitance during the cycling is not related to any chemical transformation of Mn_3O_4, in particular to MnO_2, which is also consistent with the absence of Na^+ cations in the electrolyte (Appendix VI, Figure 26).

While no significant changes in size, composition or structure of the Mn_3O_4NPs can be detected after the extensive potential cycling, systematic TEM imaging reveals subtle changes in Mn_3O_4NP surface morphology which may be responsible for the observed increase in their capacitance (Figure 9f). Such surface transformation (Figure 9g) can be due to the pseudocapacitance (Faradaic) reactions occurring on the nanoparticle which are known to be the major charge storage mechanisms for manganese oxides. The initial superficial oxidation reaction of Mn_3O_4 to MnOOH ((1) to (2), Fig. 6c), involves the surface desorption of electrolyte cations (Cation = H^+).[45]

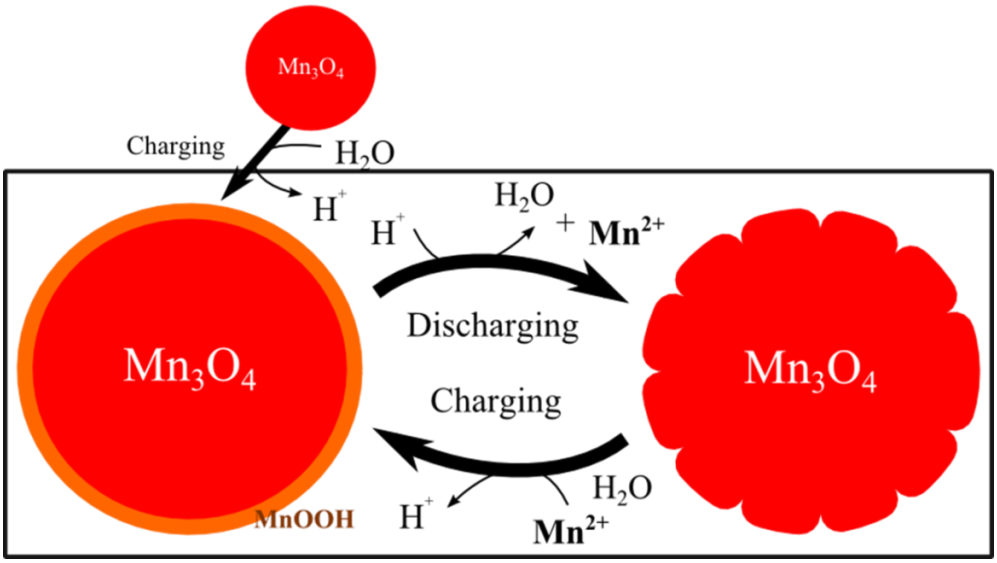

Figure 10. Proposed superficial transformation on nanoparticle (Mn_3O_4-red) based on initial oxidation or charging ($Mn_3O_4 + 2H_2O \rightarrow 3MnOOH$ (orange) + $H^+ + e^-$), subsequent reduction or discharge, releasing of Mn^{2+} ions ($4MnOOH + 8H^+ + 6e^- \rightarrow Mn_3O_4 + Mn^{2+} + 4H_2O$), and re-capture of dissolved Mn^{2+} upon oxidation ($Mn_3O_4 + Mn^{2+} + 4H_2O \rightarrow 4MnOOH + 8H^+ + 6e^-$). It is important to highlight that the dissolution of manganese from one nanoparticle and a subsequent reduction in a different one can explain the measured increase in the spread of size distribution.

The subsequent superficial reduction reaction of Mn_2O_3 ((2) to (3), Fig. 6c) gives rise to the formation of Mn^{2+},[46-47] which would deteriorate the performance of the nanoparticle over cycling (2), such as in the example

reporting the diffusion of the reduced Mn species, $[Mn(H_2O)_6]^{2+}$, from the MWNTs network into the electrolyte solution, and subsequent deposition upon oxidation on the electrode surface (not on MWNTs) thus deteriorating the electrode performance including the specific capacitance and cyclic stability.[48] In our case, the encapsulation of Mn_3O_4NPs in CNF hinders the diffusion of Mn^{2+} to the bulk electrolyte solution, making it easier the re-capture the manganese cations upon applying an oxidation potential without detrimental effects on the electrode performance ((3) to (4), Figure 10). The continuous dissolution and re-capture (3-4) process in the confines of CNF channel would not affect the manganese nanoparticle phase (staying Mn_3O_4) or the loss of the metal from the system, but a subtle structural modification of the nanoparticle surface, creating "dentate" nanoparticles with an increased surface area and, hence, higher specific capacitance would take place inside the CNF. This observation is also in agreement with the fact that b-Mn_3O_4@CNF showed no activation effects as the nanoparticle surface in this case is inaccessible (e.g. high surfactant content) and more stable (due to the lower curvature than in the spherical NP) in order to undergo increase in the NP surface roughness underpinning the increased capacitance.

5.3 Conclusion

A series of metal oxide-carbon nanostructures has been successfully synthesized via a facile in situ method where it was possible to control the final nanoparticle loading within the cavities of CNF by tuning the oxygen-containing groups (nucleation points) on the carbon surface. Interestingly, the absence of nucleation points (i. e. graphitized carbon surface) modifies the final nanoparticle morphology, from the expected small pseudo-spherical to large faceted, via non-covalently interactions between the surfactant with the carbon surface. It is observed that the unique corrugated internal structure of carbon nanofibers (CNF) not only allows the arrangement of nanoparticles in one dimension but also serves as template for the synthesis of faceted nanoparticles. Furthermore, we have introduced and developed confinement in carbon nanofibers as an alternative approach stabilising electrochemically active Mn_3O_4NPs against dissolution, oxidation and leaching during the charging-discharging cycle Mn_3O_4NPs synthesised directly inside the cavity of hollow, electrically conducting nanofibers yielded a hybrid material and most durable capacitance characteristics, with the specific capacitance increasing over 13,000 potential cycles. In contrast, the nanoparticles grown on outer surface of CNF or prepared separately and inserted in CNF, exhibited a lower durability in the charging-discharging cycling and/or weaker synergistic effects between the metal oxide and graphitic carbon components. The mechanism of the remarkable performance of Mn_3O_4NP formed inside CNF, increasing their specific capacitance by nearly a factor of 5, have been explored by HRTEM, STEM and EELS, revealing no chemical changes in structure or in composition of nanoparticles, and no significant changes in the NP average size. The remarkable electrochemical stability of Mn_3O_4 inside CNF is due to the nanoscale confinement allowing excellent electrical contact between the metal oxide and carbon and facilitating re-capture of desorbed Mn^{2+} due to the nanoscale confinement effects imposed by the CNF cavity. These newly discovered mechanisms of metal oxide interactions with carbon nanostructures contribute to the rational design of metal-carbon hybrid nanostructures for electrochemical applications such as efficient catalysts for energy storage and energy generation.

5.4 Experimental part

General

CNF (produced by chemical vapour deposition) were purchased from Pyrograph. All other reagents were purchased from Sigma-Aldrich (UK) and used without further purification. Thermogravimetrical analysis (TGA) was carried out on a SDT Q-600 TA over the range of 25 – 1000^{o}C in air at scan rate of 5^{o}C/min. Infrared (IR) spectra were measured as KBr discs on a Nicolet Avatar 380 FT-IR spectrometer over the range of 400-4000 cm^{-1}. High resolution transmission electron microscopy (TEM) imaging, energy-dispersive-x-ray (EDX) and energy electron loss analysis were performed using a Jeol 2100F transmission electron microscope at an accelerating voltage of 200 kV. TEM specimens were prepared by casting several drops of a suspension of nanofibers in hexane onto copper grid mounted "lacey" or "holey" carbon film before drying under a stream of nitrogen. Statistical analysis of TEM images was performed using Gatan Digital Micrograph software.

Electrochemical experiments were carried out on a computer-controlled potentiostat (Autolab 201A) at room temperature using a conventional three-electrode cell with a nitrogen saturated 2M KCl aqueous solution as electrolyte. A Pt wire and a reversible hydrogen reference electrode (Ag/AgCl) were used as the counter and the reference electrode, respectively. All potentials were measured and reported versus the Ag/AgCl at room temperature. 0.5 mg of active material (in situ hybrid and composites) was sonicated in 0.5 mL of hexane to form a homogeneous suspension after sonication. It is important to notice that no binder or conductive carbon was added to the electrode in order to avoid any side effects. Subsequently, 10 µg of the suspension was placed onto the surface of glassy carbon electrode (GCE) using a micro syringe and the electrode was allowed to dry at room temperature before measurements. Prior to use, the working glassy carbon electrode (3 mm in diameter) was polished mechanically with aqueous slurries of alumina powder (0.05 µm) and rinse with Mill-Q water and acetone, and allowed to dry under nitrogen. The capacitance of the hybrid material (C, in F/g) was calculated using

galvanostatic charging–discharging measurements using the following expression:

$C\ (F/g) = [t_d \bullet i]/\Delta V$

where t_d (s), i (A/g) and ΔV (V) are the discharging time in galvanostatic cycles, the current density and the voltage window, respectively.

In order to have a clear comparison between the performance of both hybrid, their capacitance was normalized to the amount of Mn_3O_4 using the following equation to calculate the specific capacitance:

$C_{sp}\ (F/g^*) = C\ (F/g) * 100 / \%Mn_3O_4$

Synthesis of CNF_{AC}

A 5M nitric acid solution (50 mL) was prepared and added to a carbon nanofibers sample (50 mg) the mixture was heated at reflux for 24 hours. After cooling, the mixture was diluted and filtered through a nylon membrane under vacuum. The solid was washed with excess deionised water until the filtrate had a neutral pH. The product was dried with acetone under vacuum and collected.

Synthesis of CNF_G

Carbon nanofibers (50 mg) were sealed in a furnace and purged with a flow of argon for 1 hour to purge the system before heating up the system to 900^0C. After keeping the temperature for 2 hours, the system was left to cool down.

Synthesis of Mn_3O_4 NPs (s-Mn_3O_4 NPs)

s-Mn_3O_4 NPs were synthesized using the previous modified protocol but without the presence of any carbon nanostructure during the synthesis. To precipitate the nanoparticles, ethanol (25 mL) was added to the reaction mixture, and Mn_3O_4 NPs were isolated by centrifugation. The resulting precipitate was dissolved in hexane and precipitated again by adding ethanol. This process was repeated three times to remove the excess of oleylamine. The obtained pseudo-spherical Mn_3O_4 can be well dispersed in organic solvents such as hexane, toluene or chloroform.

***In situ* synthesis of Mn_3O_4@CNF**

The synthesis of oleylamine stabilised Mn_3O_4 NPs was performed using a modified low-temperature Hyeon protocol.[25] In a typical experiment, a

mixture of manganese (II) acetate (1.1 mmol) and oleaylamine (13.5 mmol) in xylene (7 mL) was added a suspension of carbon nanofibers (CNF), previously sonicated for 15 min (25 mg/10mL). After heating the mixture in 90^0C in air, 1 mL of deionised water was added to the dark suspension under a vigorous stirring, and the resulting suspension was kept at 90^0C for 3 hours. The composite material was isolated by centrifugation at room temperature and filtration by using a nylon membrane, which was then thoroughly washed with hexane, ethanol and finally acetone. The resulting precipitate was sonicated in hexane (25 mL) for 15 minutes and filtrated again to remove nanoparticles from the outer surface.

***In situ* synthesis of Mn_3O_4/CNF_{AC}**

The synthesis of oleylamine stabilised Mn_3O_4 NPs was performed using a modified low-temperature Hyeon protocol.[23] A mixture of manganese (II) acetate (1.1 mmol) and oleaylamine (13.5 mmol) in xylene (7 mL) was added to a suspension of carbon nanofibers (CNF_{AC}), previously sonicated for 15 min (25 mg/10mL). After heating the mixture to 90^0C in air, 1 mL of deionised water was added to the dark suspension under a vigorous stirring, and the resulting suspension was kept at 90^0C for 3 hours. The composite material was isolated by centrifugation at room temperature and filtration by using a nylon membrane, which was then thoroughly washed with hexane, ethanol and finally acetone.

***In situ* synthesis of $Mn_3O_4@CNF_G$**

A similar procedure than in situ synthesis of $Mn_3O_4@CNF_{AC}$ was followed but in the presence of thermal treated carbon nanofibers (CNF_G) instead of CNF_{AC}.

Synthesis of $Mn_3O_4@CNF_{AC}$

The in situ synthesized Mn_3O_4/CNF_{AC} was sonicated in hexane (25 mL) for 15 minutes and filtrated again to remove nanoparticles from the outer surface.

Synthesis of nanobrick Mn_3O_4 NPs (b-Mn_3O_4 NPs)

The synthesis of oleylamine stabilised Mn_3O_4 nanobricks was performed using a reported protocol.[19] Briefty, 10 mmol of manganese (II) acetate and 120 mmol of oleylamine were dissolved in 150 mL of xylene. After heating at

90^0C in air over 6 hours, 1mL of deionised water was added to the brown solution under vigorous stirring, and the resulting suspension was kept at 90^0C for further 2 hours. To precipitate the nanoparticles, ethanol (100 mL) was added to the reaction mixture, and Mn_3O_4 NPs were isolated by centrifugation. The resulting precipitate was dissolved in hexane and precipitated again by adding ethanol. This process was repeated three times to remove the excess of oleylamine. The obtained Mn_3O_4 nanobricks can be well dispersed in organic solvents such as hexane, toluene or chloroform.

Synthesis of s-Mn_3O_4@CNF_{AC}

s-Mn_3O_4 NPs (25 mg) were sonicated in xylene (20mL) in the presence of CNF_{Ac} (25 mg). The suspension was stirred for 1 hour prior to filtration. The membrane was washed with hexane and acetone.

5.5 References

1. N. A. Frey, S. Peng, K. Cheng and S. Sun, S. Chem. Soc. Rev., 2009, **38**, 2532-2542; M. Zhou, H-L. Wang and S. Guo. Chem. Soc. Rev., 2016, **45**, 1273-1307; Z. Fan and H. Zhang. Chem. Soc. Rev., 2016, **45**, 63-82.
2. J. F. Bondi, K. D. Oyler, X. Ke P. Schiffer and R. E. Schaak. J. Am. Chem. Soc., 2009, **131**, 9144-9145;I. Djerdj, D. Arčon, Z. Jagličić and M. Niederberger. J. Phys. Chem. C., 2007, **111**, 3614-3623; Hyeon, T. et al, Eur. J. Inorg. Chem., 2012, 2148-2155.
3. C. Li, X. Han, F. Cheng, Y. Hu, C. Chen and J. Chen. Nat. Commun., 2015, **6**:7345.
4. J-S. Kim, K. Kim,W. Cho, W. H. Shin, R. Kanno and J. W. Choi. Nano Lett., 2012, **12**, 6358-6365; N. Sakai, Y. Ebina, K. Takada and T. Sasaki. J. Electrochem. Soc., 2005, **152**, E384-E389 (2005); X. Wang, B. D. Myers, J. Yan, G. Shekhawat, V. Dravid & P. S. Lee. Nanoscale, 2013, **5**, 4119-4122.
5. T. M. Higgins, D. McAtter, J. C. M. Coelho, B. M. Sanchez, Z. Gholamvand, G. Moriarty, N. McEvoy, N. C. Berner, G. S. Duesberg, V. Nicolosi and J. N. Coleman, ACS Nano, 2014, **8**, 9567-9579.
6. H. Huang, L. Zhang, Y. Xia, Y. Gan. X. Tao, C. Liang and W. Zhang. New J. Chem, 2014, **38**, 4743-4747.
7. X. Xiao, Z. Liu, L. Baggetto, G. M. Veith, K. L. More and R. R. Unocic. Phys. Chem. Chem. Phys., 2014, **16**, 10398-10402.
8. C. Delacourt, A. Kwong, X. Liu, R. Quiao, W. L. Yang, P. Lu, S. J. Harris and V. Srinivasan. J. Electrochem. Soc., 2013, **160**, A1099-A1107.
9. Y. Shao-Horn and R. L. Middaugh. Solid State Ionics, 2001, **139**, 13-25.
10. T. Yang, C. Xie, R. Ruffo, H. Peng, D. K. Kim and Y. Cui. Nano Lett., 2009, **9**, 4109-4114.
11. Y-K. Sun, K-J. Hong and J. Prakash. J. Electrochem. Soc., 2008, **150**, A970-A972.
12. S-T. Myung, K. Hosoya, S. Komaba, H. Yashiro, Y-K. Sun and N. Kumagai. Electrochim. Acta, 2006, **51**, 5912–5919.
13. K-S. Lee, S-T. Myung, H. Bang, K. Amine, D-W. Kim and Y-K. Sun. J. Power Sources, 2009, **189**, 494-498.
14. S-T. Myung, K-S. Lee, D-W. Kim, B. Scrosati and Y-K. Sun. Energy Environ. Sci., 2011, **4**, 935-939.
15. J. Lu, C. Zhan, T. Wu, J.Wen, Y. Lei, A. J. Kropf , H. Wu, D. J. Miller, J. W. Elam, Y-K. Sun, X. Qiu and K. Amine. Nat. Commun., 2014, 5:5693.
16. L. Wang, P. Zuo, G. Yin, Y. Ma, X. Cheng, C. Du and Y. Gao. J. Mater. Chem. A, 2015, **3**, 1569-1579.
17. Y. Yan, Q. Cheng, V. Pavlinek, P. Saha and C. Li. Electrochimica Acta, 2012, **71**, 27-32.
18. S. Komaba, A. Ogata and T. Tsuchikawa. Electrochem. Commun., 2008, **10**, 1435-1437.
19. M. C. Gimenez-Lopez, A. La Torre, M. W. Fay, P. D. Brown and A. N. Khlobystov. Angew. Chem. Int. Ed., 2013, **52**, 2051-2054.
20. A. La Torre, M. W. Fay, G. A. Rance, M. C. Gimenez-Lopez, W. A. Solomonsz, P. D. Brown and A. N. Khlobystov. Small, 2012, **8**, 1222-1228.
21. M. C. Gimenez-Lopez, A. Kuroglu, D. A. Walsh and A. N. Khlobystov. Adv. Mater., 2016, **28**, 9103-9108.

22. S. E. LeBlanc and H. S. Fogler. AIChE Journal, 1989, **32**, 1702-1709.
23. T. Yu, J. Moon, J. Park, Y. I. Park, N. H. Bin, B. H. Kim, I. C. Song, W. K. Moon and T. Hyeon, Chem. Mater., 2009, **21**, 2272–2279.
24. Y-X. Zhang and Y. Jia, New J. Chem., 2013, **37**, 3603-3606.
25. X.W. Yang, J.W. Zhu, L. Qiu and D. Li, Adv. Mater., 2011, **23**, 2833–2838.
26. Y. Li, J. Qu, F. Gao, S. Lv, L. Shi, C. He and J. Sun, Appl. Catal. B., 2015, **162**, 268-274.
27. Y.W. Jun, M.F. Casula, J.H. Sim, S.Y. Kim, J. Cheon and A.P. Alivisatos, J. Am. Chem. Soc., 2003, **125**, 15981–15985.
28. J. Duan, S. Chen, S. Dai and S. Z. Qiao, Adv. Funct. Mater., 2014, **24**, 2072-2078.
29. K. Chandra, K. S. B. Culver, S. E. Werner, R. C. Lee and T. W. Odom, Chem. Mater., 2016, **28**, 6763-6769.
30. X. Pang, Y. He, J. Jung and Z. Lin, Science, 2016, **353**, 1268-1272.
31. Y. Li, T. Wu, K. Jiang, G. Tong, K. Jin, X. Qian, L. Zhao and T. Lv, J. Mater. Chem. C, 2016, **4**, 7119-7129.
32. J-W. Seo, Y-W. Jun, S. J. Ko and J. Cheon, J. Phys. Chem. B, 2005, **109**, 5389-5391.
33. C-L. Liu, K-H. Chang, C-C. Hu and W-C. Wen, J. Power Sources, 2012, **217**, 184-192.
34. M. Ishii, M. Nakahira and T. Yamanaka, Solid State Commun., 1972, **11**, 209-212.
35. S. Cao, F. F. Tao,Y. Tang, Y. Li and J. Yu. Chem. Soc. Rev., 2016, **45**, 4747-4765.
36. T-H. Wu, D. Hesp, W. Dhanak, C. Collins, F. Braga, L. J. Hardwick, and C-C. Hu. J. Mater. Chem. A, 2015, **3**, 12786-12795.
37. C-K. Lin, K-H. Chuang, C-Y. Lin, C-Y. Tsay and C-Y. Chen. Surface & Coating Technology, 2007, **202**, 1272-1276.
38. L. Yang, S. Cheng, X. Ji, X. Jiang, Y. Zhou, Jun. and L. Meilin. J. Mater. Chem. A, 2015, **3**, 7338-7344.
39. S. Komaba, T. Tsuchikawa, A. Ogata, N. Yabuchi, D. Nakagawa and M. Tomita. Electrochimica Acta, 2012, **59**, 455-463.
40. J. H. Paterson and O. L. Krivanek. Ultramicroscopy, 1990, **32**, 319-325.
41. H. Kurata and C. Colliex. Phys. Rev. B, 1993, **48**, 2102-2108.
42. Z. I. Wang, J. S. Yin and Y. D. Jiang. Micron., 2000, **31**, 571-580.
43. H. K. Schimd and W. Mader. Micron., 2006, **37**, 426-432.
44. L. Laffont and P. Gibot. Mat. Characterization, 2010, **61**, 1268-1273.
45. W. Wei, X. Cui, W. Chen and D. G. Ivey. Chem. Soc. Rev., 2011, **40**, 1697-1721.
46. B. Messaoudi, S. Joiret, M. Keddam and H. Takenouti. Electrochimia Acta, 2001, **46**, 2487-2498.
47. A. Wang , M. Guo, N. Wang, J. Zhao, W. Qi, M. F. Chen, Y. Guo,N-T. Nguyen and G. Zhu. Nanoscale, 2014, **6**, 5270-5278.
48. Q. Li, J. M. Anderson, Y. Chen, and L. Zhai. Electrochimia Acta, 2012, **59**, 548-557.

Part B2

Functional networks with carbon nanostructures

Chapter 6

Stabilisation of low crystalline Prussian Blue Analogue by internal charge transfer

6.1 Introduction

The family of bimetallic cyanide complexes (also known as Prussian blue analogues, PBA)[1] having the general formula $A_xM'[M''(CN)_6]_{1-y}\cdot\square\cdot nH_2O$ (where A is the guest cation, M' and M'' stand for the transition metal ions, □ for the vacancies of $[M''(CN)_6]$ centres in the framework and n for both water molecules coordinated to metal centres and within the lattice)[2] have attracted attention for a wide range of applications in electrochromism, ion detection, hydrogen storage, biosensing, photocatalysis, and molecular magnets, amongst others.[3-5] Their three-dimensional open frameworks have received a great deal of attention for a range of different electrochemical applications including sensing[6-7], supercapacitors[8], batteries[9] or electrocatalysts[10] due to the possibility of ion-exchange[11-17]. However, the stability of bimetallic cyanide complexes has been always questioned. Their electrochemical aging during cycling has encouraged researchers to carry out further investigations to overcome this important limitation.[18]

So far, it is known that parameters such as the nature of anions,[19] the concentration of alkali cations[20] or the presence of structural defects (i. e. $M''(CN)_6$ vacancies) can dramatically affect the electrochemical performance of bimetallic cyanide complexes.[21] For example, the increase in the number of $M''(CN)_6$ vacancies induces lattice distortion, reduces the cation content in the lattice (due to charge balance) and, more importantly, introduces more coordinated water molecules into the framework.[22] Such coordinated molecules facilitate the collapse of the cyano-bridge framework due to side reactions arising from H_2O decomposition resulting in low specific capacitance, low Coulombic efficiency, and a deterioration of the electrochemical performance.[23-24] Consequently, more attention has been focussed on high crystalline PBAs with a low number of vacancies, and, thus, coordinated water molecules, resulting in rigid structures in comparison to low crystalline PBAs.[25-26] For instance, a gradual decrease of the total H_2O content (from 18.7 to 15.5%) was reported by increasing the sodium concentration during the synthesis of $Na_{1+x}Fe[Fe(CN)_6]$. Such decrease in water content increased the specific capacitance, being in agreement with the higher cation

content within the framework (from 1.26 to 1.56), and an improved (6%) the cycling stability during the charge-discharge processes.[27]

The combination of PBAs with carbon-based nanostructures has shown an improvement in their electrochemical performance with respect to the single PBAs due to the increase in conductivity and a much better distribution of the PBA (known as synergetic effect).[28-29] For example, nickel hexacyanoferrate on graphene (NiHCF/graphene hybrid) showed 13% higher capacitance retention with respect to single NiHCF[30] and Ni-Fe-HCF/graphene nanocomposite illustrated higher capacity (67.77 mAh/g) than graphene (32.5 mAh/g) and Ni-Fe-HCF (20.97 mAh/g) under same experimental conditions.[31] In addition, Zhao et. al., reported higher synergistic effects by a direct growth of PB nanocrystal in the presence of graphene in comparison with conventional physical mixing.[32]

Among all of the PBAs, cobalt hexacyanoferrate (CoHCF) is of particular interest as the switching in the magnetic response between the diamagnetic Co^{III}_{LS}-NC-Fe^{II}_{LS} (LS: low-spin) and the paramagnetic Co^{II}_{HS}-NC-Fe^{III}_{LS} (HS: high-spin) states, which have been activated by light [33], temperature [34], pressure[35-36] and pH[37], leads to a significant cell parameter variation.[38] This process arises from the fact that both cobalt and iron can exist in two common oxidation states (II, III), leading to compounds of multiple stoichiometry (or mixed valence systems, MVS). The stoichiometry can be initially controlled during the synthesis as the substitution reactions of the water molecules of the hexaaqua complex $[Co^{II}(H_2O)_6]^{2+}$ by $[Fe^{III}(CN)_6]^{3-}$ progressively increases the Co ligand field as oxygen atoms from water are replaced by nitrogen atoms derived from the cyanide ligands. For a sufficient number of donor atoms around the Co ion (i. e. $Co(N_5O_1)$),[33] the cobalt becomes low spin, resulting in a charge-transfer-induced spin transition (CTIST) to a more stable Co^{III}_{LS}-NC-Fe^{II}_{LS} diamagnetic pair. Therefore, such sensitive synthesis hinders the comparison between the works published so far, as each material has a different stoichiometry (i. e. materials have different number of vacancies with different Co^{III}/ Co^{II} ratio).

It is been demonstrated that water molecules within the CoHCF framework play a role in charge transfer, switching the oxidation states and, hence, the

structure and magnetic response.[39] For example, Hayami et al. reported that the colour of the crystal as well as its magnetic behaviour changes after the removal of both coordinated and lattice water molecules by heating.[40] As a consequence of the loss of coordinated water molecules after thermal treatment, it is expected an increase of the ligand-field around the cobalt centres triggers the internal charge transfer from the Co^{II} to the Fe^{III} centres via the cyanide bridges, and therefore, the increase of the number of Co^{III}_{LS}-NC-Fe^{II}_{LS} pairs with respect to the initial Co^{II}_{HS}-NC-Fe^{III}_{LS} ones. This internal charge transfer accompanies a reduction of the unit cell of the CoHCFe which, to the extent of our knowledge, have not been investigated from an electrochemical point of view.

In this Chapter, we will investigate the effect of increasing the number of Co^{III}-NC-Fe^{II} pairs on the electrochemical performance of an in situ synthesised CoHCF/carbon hybrid via thermolysis under an inert atmosphere. First, the electrochemical parameters for the characterization of a CoHCF nanocrystal will be thoroughly studied. Then, a series of mixed valence systems (MVS), produced by thermal annealing of CoHCF under an inert atmosphere, will be electrochemically investigated. The thermal approach used in this work allows the selective modification of the water content and, hence, the Co^{III}/ Co^{II} ratio, while the vacancies in the framework remain constant, overcoming the current synthetic limitation where each synthesis results in CoHCF with unique stoichiometry (Appendix VI, Figure 1) and, hence, electrochemical properties. Thus, we will be able to isolate the effect of water molecules from the vacancy effects as the number of vacancies will be firstly determined by the initial synthesis while the water content by the subsequent heating conditions. The combination of CoHCF with carbon nanostructures will be carried out by a one-pot synthesis to produce CoHCF directly on the surface of graphene flakes (CoHCF/graphene hybrid). The synthesis of a CoHCF/graphene hybrid will be optimized by varying the concentration of carbon during the synthesis. Finally, the modification of Co^{III}/ Co^{II} ratio in the CoHCF/graphene hybrid will be investigated, stablishing its relation with the cation insertion/extraction process.

6.2 Results and Discussion

Synthesis of cobalt hexacyanoferrate (CoHCF). CoHCF with a high number of vacancies and, hence, low population of the Co^{III}_{LS}-NC-Fe^{II}_{LS} pair is synthesised from its precursors by a precipitation method in excess of Co^{II}. Briefly, an aqueous solution of $CoCl_2$ was added at once to an aqueous solution of $K_3Fe(CN)_6$ under vigorous magnetic stirring until a total ratio of 2:1 (Co/Fe) was achieved. The production of insoluble dark violet colloids evidenced the reaction. The resulting product was centrifuged and washed with copious amount of deionised water. The obtained neutral three-dimensional network (Figure 1a) adopts a face-centered cubic (fcc) structure with a cell parameter ($\bar{a}$) of 10.26 Å (Appendix VI, Figure 2). It is important to mention that cell parameter strongly depends on the oxidation state of the metallic ions and the nature of the alkaline ions.[41] The vertices and the centres of the faces of the cubic unit cell are occupied by the Fe^{III} ions (yellow), while Co^{II} ions (red) are located at the octahedral sites (Figure 1a). Both metal centres are linked by cyanide bridges with Fe^{III} and Co^{II} being coordinated by carbon (brown) and nitrogen (light blue), respectively. The corresponding ligand field of both donor atoms leads to low spin Fe^{III} and high spin Co^{II} configuration. Thermogravimetric measurements in the temperature range of room temperature to 200^0C at a scan rate of 5^0C/min in nitrogen reveals water content in the structure of 27.6% (Appendix VI, Figure 3). Water molecules can fill the pores within the structure and also coordinate to the Co^{2+} centres (Figure 1, blue), leading to a coordination sphere of $(NC)_x(OH_2)_n$. The latter is associated to the absence of $[Fe(CN)_6]^{3-}$ centres (Figure 1, red arrow). Energy dispersive X-ray (EDS) analysis reveal a Co/Fe ratio of 1.49, leading to the final formula of $K_{0.1}Co_4[Fe(CN)_6]_{2.7}\cdot\square_{1.3}\cdot 18H_2O$ (CoHCF) with a high percentage of $[Fe(CN)_6]^{3-}$ vacancies (33%).[42]

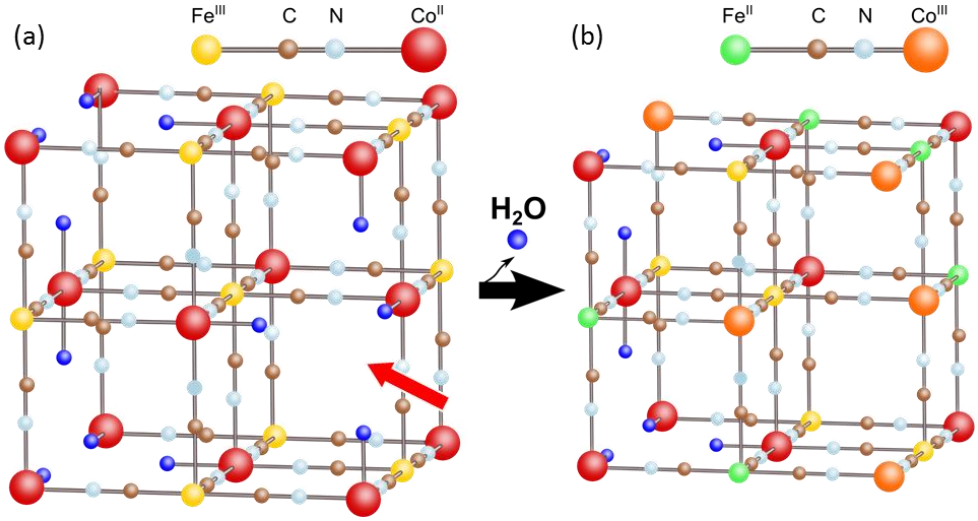

Figure 1. Schematic illustration of the formation of CoHFC mixed valence systems by thermal treatment. (a) Porous CoHCF framework presents intrinsic structural defects or $Fe(CN)_6$ (yellow) vacancies (red arrow), leaving the coordination of water molecules (blue) with Co^{II} center (red) possible. (b) the controlled removal of coordinated water molecules trigger the internal electron transfer from the Co^{II} centers to the Fe^{III}, resulting in the diamagnetic Fe^{II}-CN-Co^{III} pair. Simultaneously, there is a shrink in the cell unit due to the shortening of the Co^{III}-N bond with respect to Co^{II}-N bond, being 1.9 and 2.1Å, respectively[33]. The guests (zeolitic water molecules and cations, located at the centre of every eight sub-cubes) are omitted for clarity.

Electrochemical study of CoHCF. Prior to investigating the effect of the thermal treatment on the electrochemical properties of CoHCF, factors such as the nature of the guest cation (type of electrolyte selected) and the concentration of the electrolyte were carefully studied. Electrochemical performance was assessed by cyclic voltammetry (CV) dispersing the active material (CoHCF) on the surface of a glassy carbon electrode (no conducting additives were used for preparing the film). Pt wire and standard hydrogen electrode were utilised for the measurements, as counter and reference electrode, respectively. As it is shown in Figure 2a, despite the intrinsic low conductivity of CoHCF, a pair of pronounced redox peaks centred at 1V (E_0 vs RHE) that corresponds to the redox couple $Fe^{III/}$ Fe^{II} can be observed. It is accompanied by the release (during oxidation) and uptake (during reduction) of potassium ions (K^+) located at the tetrahedral sites in order to keep the neutrality of the framework. Their symmetric peak shape indicates high reaction reversibility.

Interestingly, the concentration of K^+ ions has an effect on the electrochemical response: the increase of the K^+ ions in the electrolyte facilitates their intercalation/de-intercalation within the CoHCF structure that is

reflected by a decrease of the separation of the redox peaks from 467 at 0.01M to 116mV at 2M. However, for a concentration higher than 0.5M the intercalation/deintercalation of K^+ ions remains unaffected, showing even a decrease of the peak current at high concentrations such as 2M (Figure 2b). In addition, the reversibility of the process ($\Delta i = i_{pa}/i_{pc}$, ratio between the peak anodic and cathodic current respectively) shows similar results with values close to 1 in the range of 0.5-1M. It is important to highlight that the de-intercalation or release of K^+ from CoHCF is found to be the greatest at 0.5M KCl, based on the anodic peak current (i_a) (Figure 2a-b). Electrochemical impedance spectroscopy suggests that initial CoHCF crystal is formed by a more porous and less crystalline outer structure in comparison with its interior as the experimental data fits with an equivalent circuit based on a solution resistance part (R_s), a porous layer (R-CPE) and a compact barrier (RW-CPE) (Figure 2d).[43] The solution resistance reflects the increase of ionic conductivity with the increase in concentration (from 1130Ω at 0.01M to 7.9Ω at 2M). More importantly, the total resistance of the material ($R_{ct2} + R_{ct2}$) shows the minimum value for 1M.

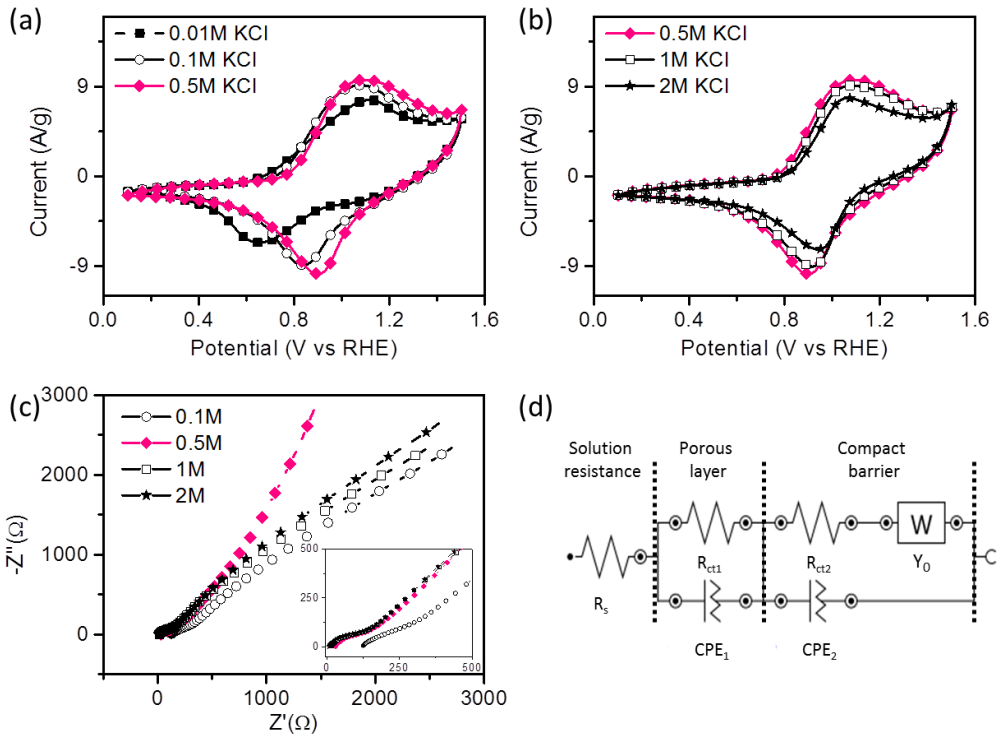

Figure 2 (a-b) cyclic voltammograms at 0.1V/s and (c) electrochemical impedance spectroscopy with (d) the simulated equivalent circuit of initial CoHCF at different KCl concentrations.

	Cyclic voltammograms				Equivalent circuit parameters						
KCl [M]	ΔE (V)	Δi [i_{pa}/i_{pc}]	E_o (V)	i_a (A/g)	R_s (Ω)	R_{ct1} (Ω)	R_{ct2} (kΩ)	CPE_1[n] (μF)	CPE_2[n] (μF)	Y_o (μS*$s^{1/2}$)	x^2
0.01	0.467	1.15	0.88	7.4	1130	-	-	-	-	-	-
0.1	0.232	1.1	0.95	8.8	122	127	10.6	74.2 [0.6]	289 [0.6]	424	0.02
0.5	0.188	1.04	1	9.3	27.1	94.8	9.54	27 [0.8]	284 [0.6]	448	0.02
1	0.157	1.02	1	8.9	14.5	98	5.61	21.5 [0.8]	266 [0.7]	324	0.03
2	0.116	1.09	1	7.5	7.9	102	7.49	14.4 [0.9]	267 [0.7]	253	0.05

Table 1 ΔE (peak separation), Δi (anodic and cathodic current ratio), E_o (formal potential), i_a (anodic peak current), R_s (electrolyte/electrode interface resistance), R_{ct1} (charge-transfer resistance in the porous layer), R_{ct2} (charge-transfer resistance in the compact barrier), CPE_1 and CPE_2 (constants phase elements indicates ideal capacitor if exponent [n] is equals to 1), Y_o (Admittance which is directly proportional to the diffusion (D) of the cation through the framework) and x^2 is the maximum change with respect to experimental data.[44]

Conversely, the total capacitance response (CPE_1+CPE_2) is higher at lower concentrations. As a combination of the two phenomena, the admittance (Y_0), which is directly proportional to the diffusion of the cation within the 3D porous structure, shows the highest value (448 μS·$s^{1/2}$) when the electrolyte is made of 0.5M KCl. Therefore, both cyclic voltammogram and electrochemical impedance analysis confirm 0.5M KCl as the best conditions to study the electrochemical properties of the CoHCF structure, having the highest electrochemical storage with the best diffusion of the cation through the framework.

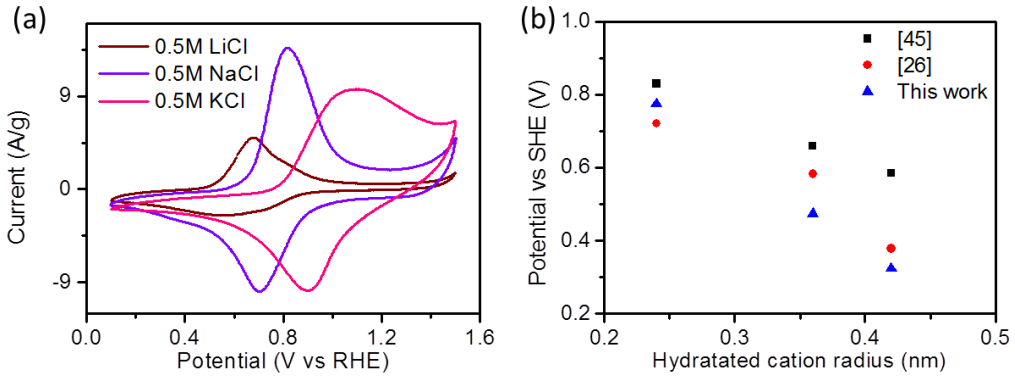

Figure 3 (a) Cyclic voltammogram of CoHCF in 0.5M LiCl (brown), NaCl (purple) and KCl (pink) at 0.1V/s, being ΔE (97, 120 and 188 mV), Δi (2.5, 1.6 and 1.04) and E_o (0.63, 0.76 and 1V) respectively. (b) Correlation of the formal potential with respect to the hydrated cation radius (Li^+ (0.42 nm), Na^+ (0.36 nm) and K^+ (0.24 nm), being the slopes -1.37 (R^2=0.999)[45], -1.8 (R^2=0.912)[26] and -2.5 (R^2=0.999) (this work).

Even though the synthesis of the CoHCF was carried out in the presence of K^+, other alkali cations can be stored within the framework.[46] It has been reported that the changes in the Gibbs free energy due to the alkali ion insertion ($\Delta G_i = -nF\Delta E_i$) is equal to the difference between the Gibbs free energy of "solvation" of the alkali ion in the CoHCF framework (ΔG_f) and the Gibbs free energy of solvation of the alkali ion in the solvent (ΔG_s):[47-48]

$$\Delta G_i = -nF\Delta E_i = \Delta G_f - \Delta G_s \quad \text{(Equation 2)}$$

Because the inserted ions are mostly dehydrated, the magnitude of ΔG_f is smaller than the free energy of solvation in solution (ΔG_s). Thus, the variation of insertion potential (ΔE_i) for different ions is mainly a function of just the Gibbs free energy of solvation of the insertion ion. Such value decreases as the ionic radius of the ion increases further down Group, since larger ions have lower hydration energies in solution.[49] In the present study, the same behaviour is observed (Figure 3a). Additionally, a linear correlation of the formal potential with respect to the hydrated cation radius suggest that alkali cations do not retain a complete hydration shell when they enter the crystal lattice (Figure 3b).[45,50]

Among the three alkali cations (Li^+, Na^+, K^+), K^+ showed the best electrochemical performance due to its symmetric shape (Figure 3a), meaning that a similar number of cations ingress in and out of the framework. In contrast, for larger cations such as hydrated lithium exhibiting a low cathodic current, the insertion in the framework is prevented. Overall, 0.5 M KCl is confirmed as the optimized conditions in order to investigate the electrochemical properties of CoHCF and the produced mixed valence systems (MVS) after thermal treatment.

Transformation of CoHCF into MVS by thermal treatment. Heating CoHCF at different temperatures between room temperature to 200^0C in nitrogen atmosphere enables the selective removal of water molecules from the structure (Appendix VI, Figure 4) from 5.5 to 17.4 water molecules. Due to their weak interaction, water molecules within the porous structure (solvated) would be removed first at low temperatures (< 100^0C). In contrast, higher temperatures would be required to remove water molecules coordinated to Co centre. As a consequence, the ligand field around this ion would increase;

destabilizing the electrons located in the orbitals of Co^{II} with the highest energy (e_g) and being transferred to the neighbor Fe^{III} orbitals with the lowest energy (t_{2g}). Thus, demagnetization and shortening of the unit cell would be observed as a consequence of the increase of diamagnetic Fe^{II}-CN-Co^{III} pairs, where the Co^{III}-CN distance bond is shorter than Co^{II}-CN, being 1.9 and 2.1Å respectively (Appendix VI, Figure 5). It is important to mention that no significant differences in the Fe-C bond length are expected with respect to the oxidation state of the iron centre (Fe^{II} or Fe^{III}), being 1.7935 and 1.7904 Å respectively.[51]

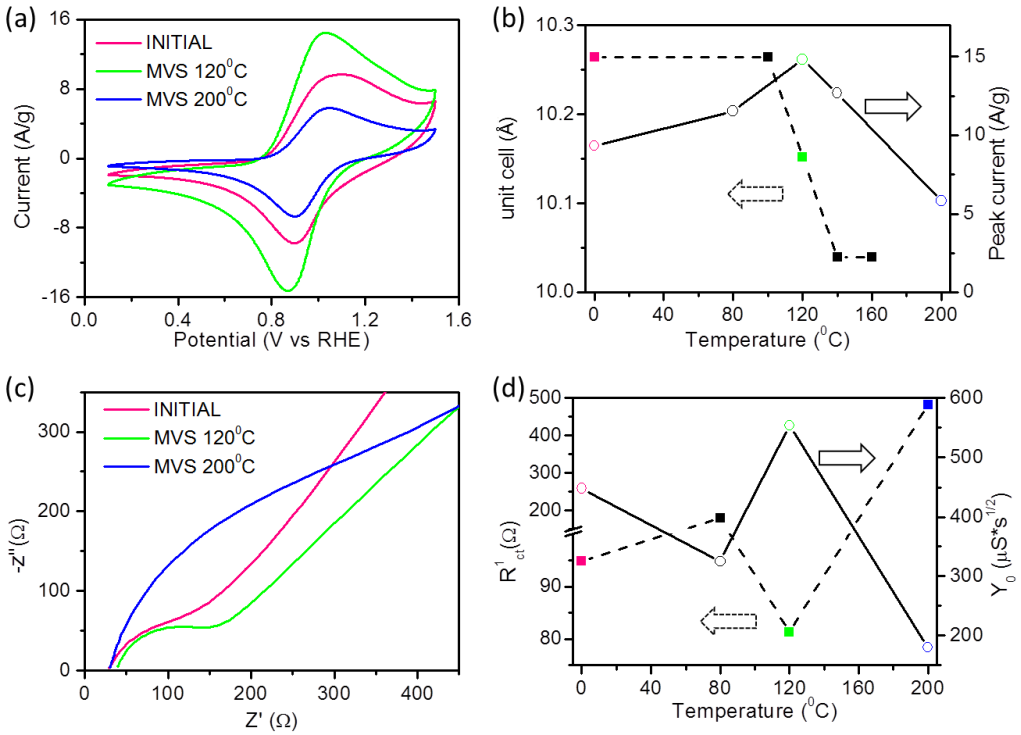

Figure 6. Electrochemical characterization of initial CoHFC and Mixed-Valence Systems (MVS). (a) Cyclic voltammogram and (c) Nyquist plot of initial (pink) and MVS after thermal treatment at 120^{0}C and 200^{0}C in N_2. (b) Correlation of the unit cell and the anodic peak current with respect the temperature. (d) Correlation of the charge-transfer resistance (R_{ct}^1) and the Warburg admittance (Y_0) with respect to the temperature. It is important to mention that Warburg admittance coefficient is proportional to the diffusion coefficient.[52]

As it can be clearly observed in Figure 6a, the heating of CoHCF at different temperatures produces MVS with different electrochemical performance. The heating at temperatures below 100^{0}C does not show a significant effect in the unit cell, where almost the 32% of water molecules are removed from the pores of the framework. Higher temperatures than 100^{0}C successfully removed the coordinated water molecules, decreasing steadily the unit cell ($\bar{a}$) to a

minimum size of 10.039Å. The controlled transformation from Fe^{III}-CN-Co^{II} to a Fe^{II}-CN-Co^{III} species is further confirmed by the demagnetization of the sample while increasing the temperature (Appendix VI, Figure 6). Interestingly, the shrinking of the unit cell (just 2.2% respect to initial unit cell ($\bar{a}$ = 10.264 Å) and 8% respect to the hydrated potassium diameter)[53] has a significant effect on the storage of K^+ within the CoHCF-MVS, showing an initial increase to 14.8 A/g after heating at 120^0C (MVS_{120}) and a subsequent decrease to 5.8 A/g after heating at 200^0C (MVS_{200}) (Figure 6b, solid line).

Additional experiments were performed to investigate the physical process that controls the kinetic behaviour of CoHCF during the cycling of the initial CoHCF and the MVS. Electrochemical impedance spectroscopy (EIS), carried out under the same conditions within the range of 0.1 to 10^6 Hz, shows that each system has different resistance response. The presence of a semi-circle at high-frequencies in the Nyquist plot (Figure 6c) reveals the charge transfer resistance associated to the $Fe^{III/II}$ redox process. Heating the sample at 120^oC (blue) reduces considerably the semi-circle with respect to the initial CoHCF sample (pink), being in agreement with the observed current increase by cyclic voltammogram. Further heating to 200^oC increases dramatically the resistance (blue) with a total value of 482Ω. The correlation of the charge transfer resistance with the ionic diffusion of the K^+ through the framework can be observed in Figure 6d where MVS_{120} shows the lowest charge-transfer resistance (81.3Ω) with the highest Warburg admittance (554 $\mu S \cdot s^{1/2}$). It is important to mention that these values were obtained from a simulated equivalent circuit (Appendix VI, Figure 7). Thus, removing thermally the coordinated water molecules affects the framework and, hence, the kinetic behaviour of charge carriers in and out of the structure.

In-situ synthesis of CoHCF@Carbon hybrid. The intrinsic electrical resistivity of CoHCF can be further reduced by the combination with carbon nanostructures, which show high conductivity. It is important to mention that the assembly was carried out during the synthesis of CoHCF (or *in situ*). To do so, graphene flakes (GF) were sonicated with the initial $K_3Fe(CN)_6$ solution and, subsequently, $CoCl_2$ was immediately added, enabling the in situ

precipitation of CoHCF in the presence of the carbon support. For comparison, CoHCF was combined with graphene flakes by conventional procedure (named as physically mixture) where CoHCF was sonicated in the presence of the carbon nanostructure, resulting in CoHCF/GF.

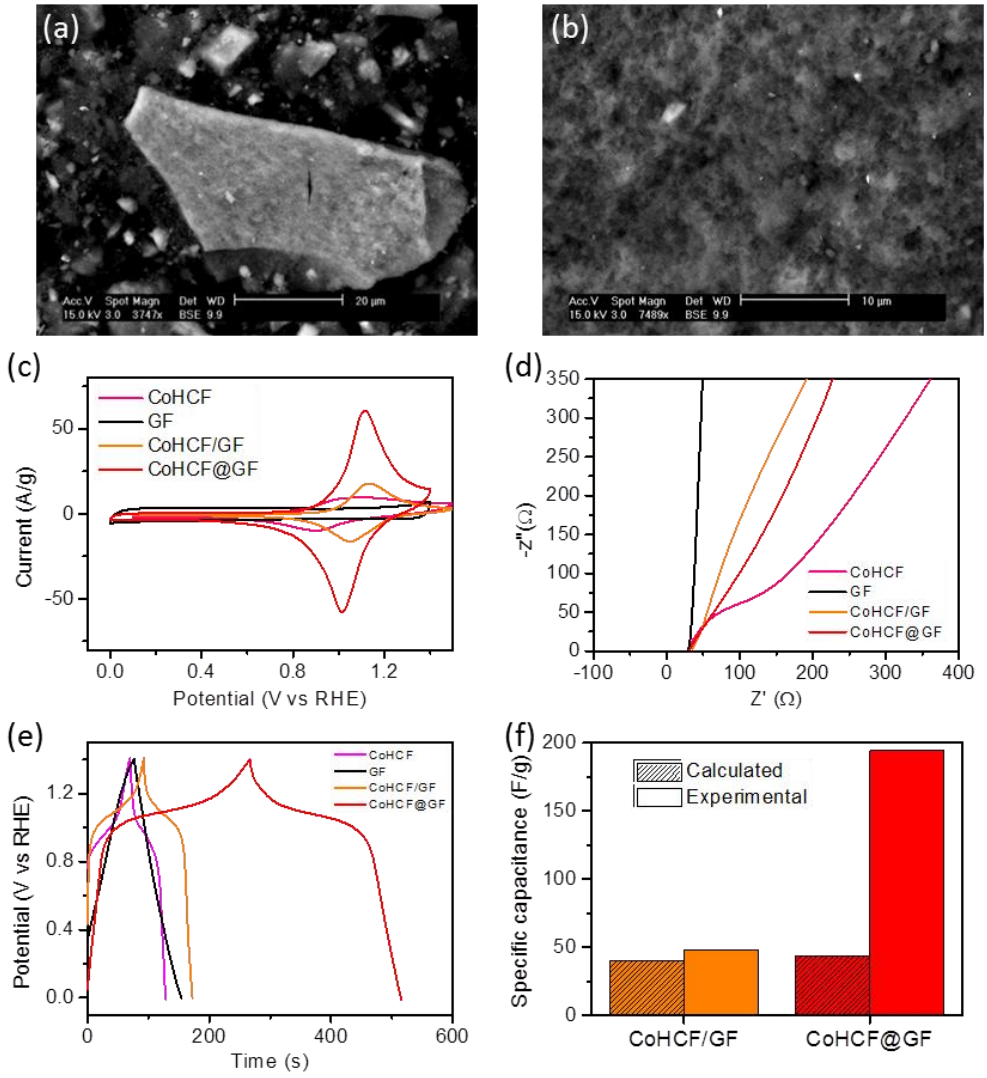

Figure 7. Synergetic effect of CoHCF@GF by in situ synthesis with respect to the conventional physical mixture (CoHCF/GF). Back-scattered scanning electron micrographs of (a) CoHCF/GF composite and (b) CoHCF@GF hybrid. (c) cyclic voltammogram at 0.1 V/s, (d) Nyquist plot and (e) galvanostatic charge-discharge cycle at 0.5 A/g in 0.5M KCl of initial CoHCF (pink), graphene flakes (black), CoHCF/GF composite (orange) and CoHCF@GF hybrid (red). (f) Synergy effect of the physical composite (CoHCF/GF) and the in situ hybrid (CoHCF@GF) based on their experimental and the calculated specific capacitance, being the ratio 1.2 and 4.4 respectively.

As it can be observed by SEM, the physically mixture of CoHCF with GF (Figure 7a, CoHCF/GF) exhibits a completely different morphology than the *in situ* CoHCF@GF hybrid (Figure 7b), showing the latter a smaller particle size (maximum of 2μm in CoHCF@GF with respect to 70 μm in CoHCF/GF) and a

much better dispersion of the CoHCF on the carbon support (Appendix VI, Figure 8).[54] It is important to note that back-scattered electrons (BSE) detected by SEM help to discriminate between the heavy (Fe or Co) and light elements (C), such that the former appears much brighter. As a consequence, the resultant metal-carbon hybrid (CoHCF@GF) reveals a much larger current density (i.e. 60.6 A/g anodic peak) in comparison to CoHCF/GF composite (i.e. 17.8 A/g anodic peak) while retaining the peak symmetry, highlighting the advantages of *in situ* synthesis over the conventional physical mixture for electrochemical applications (Figure 7c). It is important to mention that both the CoHCF@GF hybrid and CoHCF/GF composite have a similar amount of CoHCF, specifically 74.5 and 80.6% (Appendix VI, Figure 9).

Electrochemical impedance spectroscopy reveals the improvement of the conductivity in both CoHCF@GF hybrid (Figure 7d, red) and CoHCF/GF composite (Figure 7d, orange) with the addition of carbon by the absence of semi-circle at high frequencies. In contrast to the composite, the CoHCF@GF hybrid shows a more vertical line that is characteristic of facile ion transport such as in the case of ion adsorption on GF surface (Figure 7d, black).

Galvanostatic charge-discharge (CD) measurements at 0.5 A/g confirms CoHCF@GF hybrid material with the highest specific capacitance (194.2 F/g) with respect to CoHCF/GF composite (47.6 F/g), the initial CoHCF (31 F/g) and GF (37.8 F/g) by their own (Figure 7e). The specific capacitance of the hybrid material, which is in line with previous studies,[55-56] can be considered as a sum of specific capacitance values of their building blocks. Thus, the experimentally measured capacitance for the hybrid and the composite is 1.2 and 4.4 times higher than expected for these materials (Figure 7f). The greater synergetic effect for the hybrid material with respect to the composite is associated with a much better distribution and smaller size of CoHCF and suggests a stronger interaction with the carbon support. For example, We et al. synthesized *in situ* CoHCF in the presence of reduced graphene oxide (rGO), showing a maximum capacitance of 361F/g in Na_2SO_4 aqueous electrolyte for CoHCF/rGO (20% graphene) but with a smaller synergetic effect (1.4) as the specific capacitance of CoHCF and rGO were 263 and 168 F/g, respectively.[57]

Effect of carbon during the in-situ synthesis of CoHCF@GF hybrid. Although the XRD pattern of CoHCF@GF hybrid material seems initially a simple addition of both CoHCF and GF patterns, a closer examination reveals a slight shift of the peaks assigned to CoHCF, suggesting a 0.1% decrease of the unit cell (Appendix VI, Figure 10). To investigate whether the close CoHCF-carbon nanostructure interaction from the in situ synthesis can trigger the internal charge transfer in CoHCF, which would decrease the unit cell while enhancing the Co^{III}-CN-Fe^{II} state, several in situ synthesises of CoHCF@GF hybrid were performed. Specifically, the amount of carbon was increased by a factor of 2 (11.8 g/L), 3 (17.6 g/L), 4 (23.5 g/L) and 6 (35.3 g/L) with respect to the initial CoHCF@GF hybrid (5.9g/L), being these hybrids referred as CoHCF@GF_2, CoHCF@GF_3, CoHCF@GF_4 and CoHCF@GF_6, respectively.

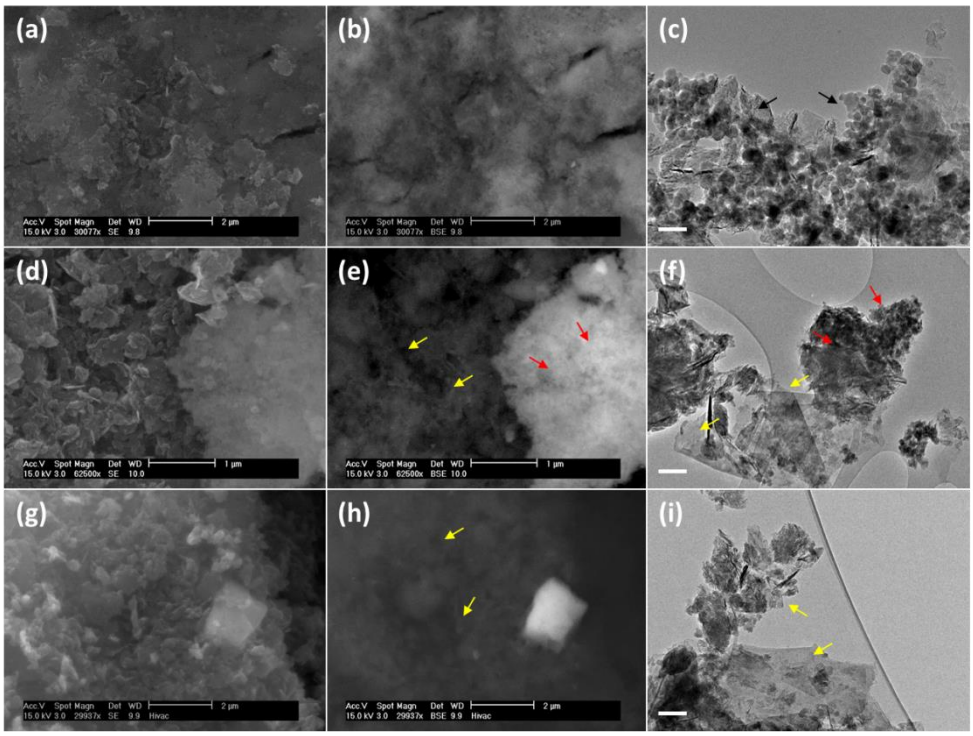

Figure 8. Structural characterization with the increase of carbon content during the in situ synthesis. FEG-SEM and TEM images of (a-c) CoHCF@GF_2, (d-f) CoHCF@GF_4 and (g-i) CoHCF@GF_6. Black and red arrows indicate CoHCF distributed on the carbon surface whereas yellow arrows indicate empty graphene flakes surface. Scale bars are (c) 100 and (f,i) 200 nm, respectively

As expected, the CoHFC/GF ratio decreases as the in situ reaction is carried out in the presence of more carbon material (Appendix VI, Figure 11). Interestingly, the addition of carbon seems to have a structural effect on the CoHCF nanoparticles during the in situ synthesis (Figure 8). Hence, at low

concentration of carbon (i. e. CoHCF@GF_2, Figure 8a-c), individual CoHCF nanoparticles are homogeneously distributed along the carbon surface (Figure 8c, black arrows). The increase of carbon content does not improve the distribution but, surprisingly, produces the agglomeration of CoHCF nanoparticles (Figure 8d-f, red arrows) while the surface of graphene flakes is mostly clear (Figure 8d-f, yellow arrows). This effect is more significant when the in situ synthesis is performed with a high concentration of carbon flakes (i. e. CoHCF@GF_6, Figure 8g-i), as not only the surface of GF is clear (Figure 8i, yellow arrows) but a few large nanocrystals (~200 nm) were found (Figure 8.g-h).

Energy-dispersive X-ray spectroscopy (EDS) analysis confirms the effect of GF concentration on the chemical composition of CoHCF during the in situ synthesis. The Co/Fe ratio varies slightly by increasing the concentration of graphene flakes, with a sharp decrease when the carbon content is higher than of 30g/L (Figure 9a). The latter observation suggests the important structural role of the carbon nanostructure at high concentration hinders the synthesis of the CoHCF nanocrystals. Therefore, based on the synthetic protocol in which graphene flakes (GF) are initially mixed with $K_3Fe(CN)_6$ solution, we propose that the excess of GF captures $Fe(CN)_6^{3-}$, hindering the diffusion of the added Co^{2+} and, hence, the synthesis of CoHCF (Appendix VI, Figure 12).

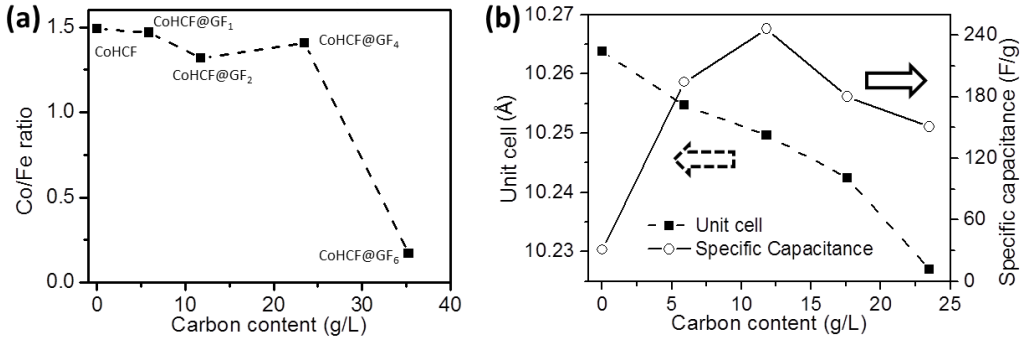

Figure 9. (a) Co/Fe ratio and (b) correlation of unit cell and specific capacitance with the increasing of carbon content in the volumetric flask during the in situ synthesis, resulting in CoHCF@GF (5.9 g/L), CoHCF@GF_2 (11.8 g/L), CoHCF@GF_3 (17.6 g/L), CoHCF@GF_4 (23.5 g/L) and CoHCF@GF_6 (35.3 g/L) hybrids. It is important to note that the unit cell for CoHCF (0g/L), CoHCF@GF (5.9 g/L), CoHCF@GF_2 (11.8 g/L), CoHCF@GF_3 (17.6 g/L) and CoHCF@GF_4 (23.5 g/L) hybrids is $\bar{a}$ = 10.26 ± 0.01 Å, $\bar{a}$ = 10.255 ± 0.007 Å, $\bar{a}$ = 10.250 ± 0.004 Å, $\bar{a}$ = 10.242 ± 0.006 Å and $\bar{a}$ = 10.227 ± 0.006 Å, respectively.

As a consequence of the proposed diffusion limitation of Co cations in such high carbon concentration conditions (CoHCF@GF_6), large FeHCF nanocrystals are found (Figure 8g-h and Appendix VI, Figure 13). This finding suggests the reduction of Fe^{3+} cations, which has been reported to be enhanced under irradiation with visible light. More importantly, the light-induced ligand-to-metal charge transfer (light-induced LMCT) associated with the reduction to Fe^{2+} cations is being further enhanced by the presence of dissolved organic carbon (such as citric acid or humic substances).[58-60] In our experiments at high carbon content (CoHCF@GF_6), the chemical functionalization on the surface of GF (i. e. hydroxyl groups, Appendix VI, Figure 14) could show similar interaction with Fe^{3+} cations, triggering their reduction and promoting the synthesis of FeHCF nanostructures. As a consequence of the mentioned heterogeneity, CoHCF@GF_6 is not going to be discussed further.

The correlation of the unit cell with the increase of carbon content can be observed in Figure 9b. As initially proposed, the increase of carbon content causes a decrease in the lattice parameter of the resultant complex, measuring a total 0.36% reduction from the initial CoHCF crystal (10.26 Å) to the CoHCF@GF_4 hybrid (10.227 Å). Thus, such shrinkage of the unit cell with the addition of carbon (<25 g/L) is associated to an increase of the Co^{III}-NC-Fe^{II} population during the in situ synthesis. [61-62] It is important to note that no new peaks appeared during the in situ synthesis, being a single-phase transformation (Appendix VI, Figure 15).

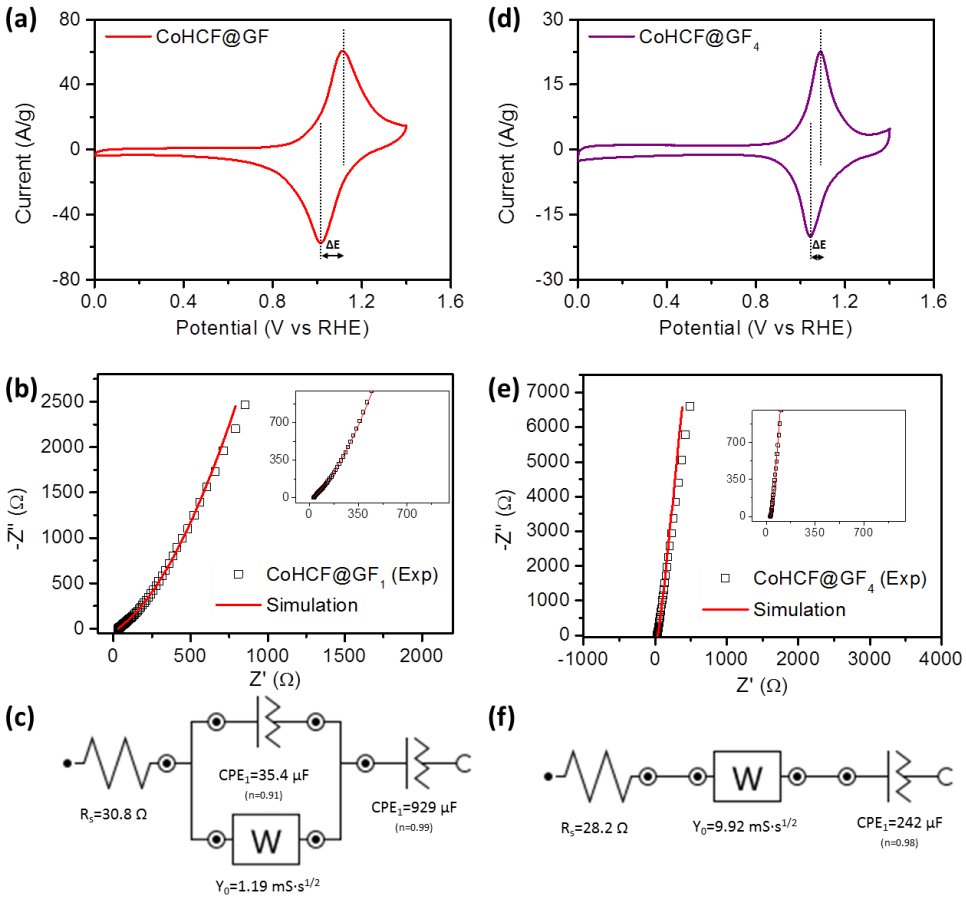

Figure 10. Cyclic voltammogram of (a) CoHCF@GF and (d) CoHCF@GF_4 at 0.1V/s in 0.5M KCl, showing their peak separation (ΔE). Nyquist plot of (b) CoHCF@GF and (e) CoHCF@GF_4 with (c,f) their simulated circuits respectively.

Conversely, the specific capacitance does not show a clear trend with respect to the addition of carbon (Figure 4h), suggesting that additional factors (i.e. potassium content, unit cell, water content) may play a role. Based on the potassium content, which is inversely dependent on the Co/Fe ratio in order to maintain the neutrality of the framework, CoHCF@GF_2 and CoHCF@GF_1 hybrids show the highest and lowest specific capacitance with Co/Fe ratio of 1.32 and 1.47 respectively. Even though this tendency is in agreement with the measured specific capacitance of CoHCF@GF_2 (246.4F/g for 11.8g/L), CoHCF@GF_1 have slightly higher specific capacitance than CoHCF@GF_4 (194.2 and 180.1 F/g respectively). It could be considered that the smaller unit cell, due to the increase of the Co^{III}_{LS}-NC-Fe^{II}_{LS} pair in CoHCF@GF_4 with respect to CoHCF@GF_1 could inactivate some iron centres (Fe^{II} vs Fe^{III}), what would reduce the amount of release and uptake of potassium ions, confirming the decrease in specific capacitance.

Surprisingly, despite that the unit cell shrinkage can limit the amount of ions going in and out of the framework; such a reduction in size enhances the diffusion of the ions through the structure, which would positively affect the stability during cycling. Analysis of the cyclic voltamograms of CoHCF@GF_1 and CoHCF@GF_4 at 0.1V/s (Figure 10a,d) illustrates an increase in reversibility (current ratio, Δi equals to 1.11 and 1.06 respectively) of the latter with also a much lower resistance (peak separation: ΔE equals 97 and 44 mV, respectively). The electrolyte/electrode interface resistance (solution resistance, R_s) is lower for CoHCF@GF_4 (28.2 versus 30.8Ω), which could be related to its high water content (Figure 10b,e and Appendix VI, Figure 16), and the diffusion of cations within CoHCF@GF_4 is more than 8 times higher with respect to CoHCF@GF_1. (9.92 $mS \cdot s^{1/2}$and 1.19$mS \cdot s^{1/2}$ respectively) (Figure 10c,f). In addition, the capacitance retention after 400 charge-discharge cycles at 1 A/g (Appendix VI, Figure 17) of CoHCF@GF_1 (45.4%) was slightly lower in comparison to CoHCF@GF_4 (48.2%). Therefore, it is shown that the shrinkage of the unit cell, triggered by the carbon support, decreases the specific capacitance while increases the stability of the framework.

Finally, it is important to mention that the presence of carbon substrate has an enormous effect on the intrinsic stability of CoHCF framework. It is worth mentioning that in the area of heritage science, the aging of Prussian blue pigments by light in air has attracted special attention regarding to conservation of artwork. Despite to the absence of the clear structural and electronic reorganization of Prussian blue upon fading, numerous studies have investigated the degradation of the pigment as a consequence of the formation of iron (III) oxohydroxide and demonstrated its dependence on several factors (pH, substrate, atmosphere and light).[63] Specifically, the substrate acts an mediator during the reorganization to maintain the electroneutrality of the framework.[64] For example, it is been demonstrated that Prussian blue is more stable on linen rather than cotton, being the latter a natural cation reservoir which generates hydroxyl radical when exposed to UV and blue light.[65-66]

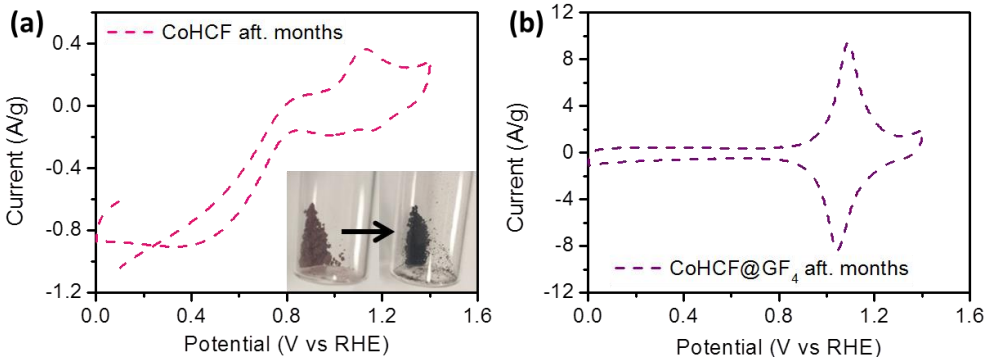

Figure 11. Cyclic voltammogram at 0.1V/s in 0.5M KCl of (a) CoHCF crystals and (b) CoHCF@GF_4 hybrid after 6 months of synthesis.

In our work, we observe that the electrochemical properties of the CoHCF crystal decreases dramatically (Figure 11) together with its initial violet colour after being in storage for 6 months (Figure 11, inset). In contrast, a clear and defined redox process is still observed when CoHCF is in contact with GF (i. e. CoHCF@GF_4 hybrid) after the same period of time, revealing the activity of the redox centres is maintained. As a consequence of the great stability of carbon nanostructures in environmental conditions, graphene flakes do not promote the decomposition of CoHCF but hinder the process. Therefore, the synthesis of hybrid nanostructures enhances the stability of CoHCF not only during electrochemical performance but also during their synthesis and subsequent storage.

Electrochemical evaluation of CoHCF@GF after thermal treatment. Aiming to investigate further the relation between the unit cell shrinkage with the electrochemical stability of the metal framework, CoHCF@GF_4 was heated in nitrogen at 120^{0}C for 1 hour (CoHCF@GF_4 120^{0}C). As it can be clearly observed in Figure 12a using the GF peak at 26.5 [002] as a reference, there is a shift in the CoHCF peak position [220] after thermal treatment as a consequence of the internal charge transfer from Co^{II}-NC-Fe^{III} to Co^{III}-NC-Fe^{II}. Using for the calculation the four most intense peaks of CoHCF in CoHCF@GF_4 120^{0}C, the unit cell of the metal framework is 10.119Å (1.1% smaller with respect to CoHCF in CoHCF@GF_4).

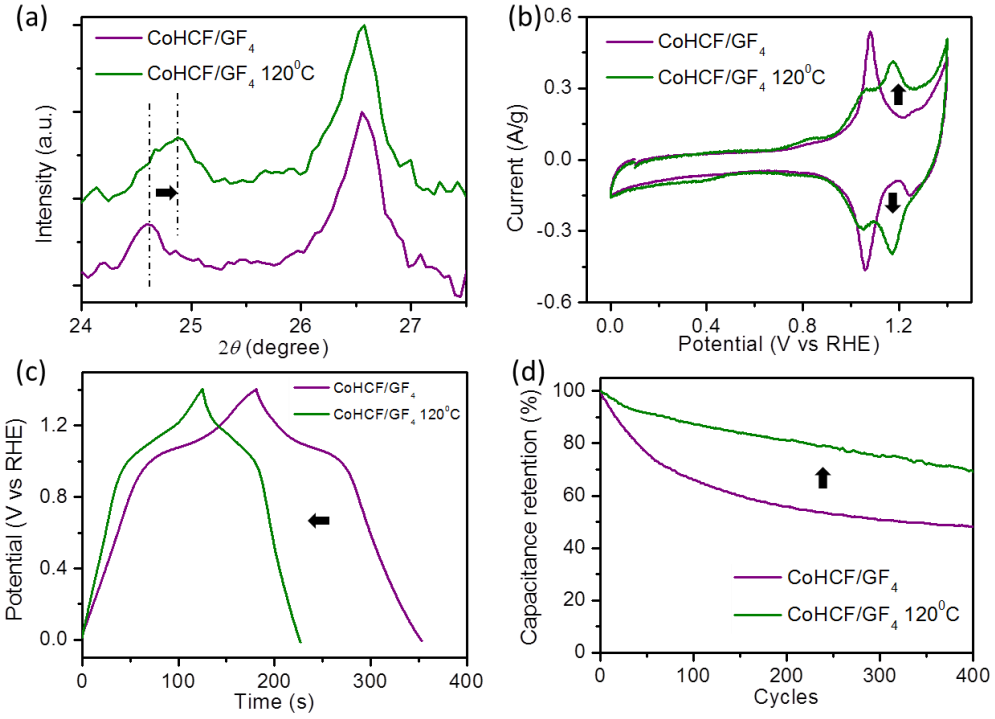

Figure 12. Structural and electrochemical characterization of CoHCF@GF_4 after thermal treatment at 120°C in nitrogen. (a) Powder XRD, (b) cyclic voltammogram at 5mV/s in 0.5M KCl, (c) charge-discharge cycle at 0.5 A/g and (d) capacitance retention after 400 cycles at 1 A/g of CoHCF@GF_4 before (purple) and after (green) thermal treatment at 120°C.

Cyclic voltammograms reveal that the internal charge transfer triggered by the thermal treatment is associated with a new redox couple (centred at 1.13V) (Figure 12b, arrows) with respect to CoHCF@GF_4 before treatment, which could be related to the formation of a Co^{III}-NC-Fe^{II} pair. In fact, the Fe-C bond would be less covalent because Fe centre would be surrounded by a more positive environment (due to the presence of the Co^{III}) and, hence, increasing

the formal potential from 1.07 (in CoHCF@GF_4) to 1.13V (in CoHCF@GF_4 120^{o}C).[67] The decrease in the energy couple could also inactivate some Fe centres, which would be in agreement with the observed decrease in the specific capacitance after thermal treatment (Figure 12c). More interestingly, the Warburg admittance of potassium ions within the framework in CoHCF@GF_4 120^{o}C is higher with respect to CoHCF@GF_4, being 12.5 and 9.92 $mS \cdot s^{1/2}$, respectively (Appendix VI, Figure 18). As a consequence, the thermally treated CoHCF@GF_4 shows a significant improvement of 21% higher capacitance retention after 400 cycles at 1 A/g (Figure 12d).

Overall, the low stability of CoHCF@GF_4 120^{o}C (80% after 250 cycles) is in agreement with previous studies as high PBA with better electrochemical performance (i. e. smaller capacity loss (<10%) after longer cycles (1000-5000)) can be found in the literature.[68,55] However, it is important to note that those PBAs had a low percentage of $Fe(CN)_6$ vacancies within the framework, having a beneficial effect on their stability. For example, You et al. compared the electrochemical performance of two different FeHCF (i.e. $Na_{0.61}Fe(Fe(CN)_6]_{0.94}\square_{0.06}$ and $Na_{0.13}Fe(Fe(CN)_6]_{0.68}\square_{0.32}$) which were labelled as high and low quality respectively according to their percentage of $[Fe(CN)_6]$ vacancies (6 and 32%, respectively). The low quality material, which indeed has similar percentage of vacancies with respect to CoHCF@GF_4 (32% and 30%, respectively), exhibited a smaller capacitance retention (36.5% after just 70 cycles) in contrast to the high quality material (zero-capacity loss after 150 cycles).[69]

6.3 Conclusion.

Here, we investigated the effect of Co^{II}/Co^{III} ratio on the electrochemical performance of cobalt hexacyanoferrate (CoHCF) triggering the internal electron transfer by thermal annealing. This alternative methodology enables us to specifically study the coordinated water contribution while retaining the number of vacancies constant. Interestingly, thermal treatment leads to an internal electron transfer from the Co to the Fe centres, selectively increasing the concentration of the Co^{III}_{LS}-NC-Fe^{II}_{LS} with respect to the initial Co^{II}_{HS}-NC-Fe^{III}_{LS} pair, which modifies the crystal structure (shrinking the unit cell) and, hence, the cation insertion/extraction process. Optimization of both the thermal conditions as well as the electrochemical parameters is discussed within this work. Furthermore, graphene flakes (GF) are used in the study to overcome the intrinsic low conductivity of CoHCF crystals. The hybrid composite reveals a much better electrochemical performance that the analogous composite due to a higher synergistic effect. Surprisingly, a structural and chemical effect of GF was observed during the in situ synthesis of CoHCF@GF hybrids, showing a small shrinkage of the CoHCF unit cell as well as the synthesis of FeHCF at high concentrations of GF. In addition, it appears that CoHCF in contact with GF is more stable when compared to CoHCF crystal, suggesting the combination of carbon nanostructures to enhance not only their electrochemical properties but also their stability during storage.

Overall, the thermal treatment of the resulant hybrids shows an improvement in the stability during cycling which indicates that the partial removal of coordinated water molecules introduce flexibility into the framework, facilitating the reversibility of the insertion/extraction of the K^+ . These findings would have an impact on the preparation of electrochemical storage devices such as supercapacitors and batteries.

6.4 Experimental information

Synthesis of CoHCF. $K_3[Fe(CN)_6]$ (0.494 g, 1.5 mmol) were dissolved in DI H_2O (8 mL) and stirred while a solution of $CoCl_2$ H_2O (0.713 g, 3 mmol) was added. The mixture was stirred for 10 minutes and the brown-red solid was separated by centrifugation (7000 rpm, 15 min). The solid was washed with water untill no chlorides were detected by adding $AgNO_3$ in the wash water. Finally, the solid was dried under vacuum at room temperature.

Synthesis of CoHCF@GF composite. Graphene nanoflakes (GF, 0.245 mg) and CoHCF (immediately mixed, 0.745 mg) were put together in a vial in 1ml DI H_2O and sonicated for 15 minutes.

Synthesis of CoHCF/GF hybrid. $K_3[Fe(CN)_6]$ (0.0119 g, 0.036 mmol) were dissolved in DI H_2O (1 mL) and graphene nanoflakes (10, 20, 30, 40 or 60 mg) was added to the solution and sonicated for 15 minutes. $CoCl_2 \cdot H_2O$ (0.0171 g. 0.072 mmol) solution was added immediately dropwise. The mixture was stirred for 1 hour and the brown-red solid was separated by centrifugation (7000 rpm, 15 min). The composite was washed with water until no chlorides were detected in the wash water and then filtered through a wet PTFE membrane. The composite was dried on the vacuum system.

Materials characterization.

All the reagents were purchased from Sigma-Aldrich (UK) and used without further purification. Thermogravimetrical analysis (TGA) was carried out on a SDT Q-600 TA over the range of 25 – 1000^0C in air at scan rate of 5^0C/min. Infrared (IR) spectra were measured as KBr discs on a Nicole Avatar 380 FT-IR spectrometer over the range of 400-4000 cm^{-1}. High resolution transmission electron microscopy (TEM) imaging, energy-dispersive-x-ray (EDX) and energy electron loss analysis were performed using a Jeol 2100F transmission electron microscope at an accelerating voltage of 200 kV. TEM specimens were prepared by casting several drops of a suspension of the hybrid material in hexane onto copper grid mounted “lacey” or “holey” carbon film before drying under a stream of nitrogen.

Electrochemical measurements. Electrochemical measurements were conducted with a Autolab 201 un an aqueous KCl electrolyte (0.5 M) in a

conventional, three-electrode cell where a Pt wire serves as the counter electrode and a standard hydrogen electrode as the reference electrode. Prior to measurement, oxygen was removed from all solutions by bubbling nitrogen and the working electrode (glassy carbon) was polished with 0.05 μm alumina and rinsed in a sonicated, distilled water bath. For the electrochemical measurements of the CoHCF and CoHCF-MVS, the working electrode was prepared by only using electroactive material without the presence of conductive or binder additives. For the case of CoHCF/GF composite and CoHCF@GF hybrid, the working electrode was prepared by mixing the electroactive material with a polymer binder (polytetrafluoroethylene) in a weight ratio of 90:10. The mass loading is about 0.14 mg/cm^2.

The specific capacitance is calculated by following the equation:

$$C = \frac{t_d \Delta t}{m \Delta V}, \qquad (1)$$

Where t_d is the discharge current, Δt is the discharge time, ΔV is the voltage range and m is the mass of active material.

Fabrication of mixed valence systems (MVS) of CoHCF and CoHCF/GF hybrids. Sample of interest was heated in an inert N_2 atmosphere using TGA at a 5^0C/min scan rate up to temperature of interest (80, 120, 140, 160 or 200^0C) with a subsequent 60 minutes isothermal period.

6.5 References

1. B. H. Berrie, Artist's Pigments: A Handbook of Their History and Characteristics Volume 3, Chap. 7. Edited by RL. Feller, E. W. FitzHugh, D. C. Washington: National Gallery of Art, 1997, 191-217.
2. M. Okubo and I. Homma, Dalton Trans., 2013, **42**, 15881-15884.
3. F. Ricci and G. Palleschi, Biosens. Bioelectron., 2005, **21**, 389-407;
4. S. Ohkoshi, T. Iyoda, A. Fujishima and K. Hashimoto, Phys. Rev. B, 1997, **56**, 11642
5. S. S. Kaye and J. R. Long, J. Am. Chem. Soc., 2005, **127**, 6506-6507.
6. A. A. Karyakin, Electroanalysis, 2001, **13**, 813-819.
7. R. Pauliukaite, M. Florescu and C. M. A. Brett, J. Solid State Electrochem., 2005, **9**, 354-362.
8. J. Chen, K. Huang and S. Liu, Eletrochem. Commun., 2008, **10**, 1851-1855.
9. K. Lu, B. Song, X. Gao, H.Dai, J. Zhang and H. Ma, J. of Power Sources, 2016, **303**, 347-353.
10. H. T. Bui, D. Y. Ahn, N. K. Shrestha, M. M. Sung, J. K. Lee and S-H. Han, J. Mater. Chem. A, 2016, **4**, 9781-9788.
11. T. Matsuda, J. Kim and Y. Moritomo, J. Am. Chem. Soc., 2010, **132**, 12206-12207.
12. R. Y. Wang, C. D. Wessells, R. A. Huggins and Y. Cui, Nano Lett., 2013, **13**, 5748-5752.
13. L. Lipson, B. Pan, S. H. Lapidus, C. Liao, J. T. Vaughey and B. J. Ingram, Chem. Mater., 2015, **27**, 8442-8447.
14. T. Shiga, H. Kondo, Y. Kato and M. Inoue, J. Phys, Chem. C, 2015, **119**, 27946-27953.
15. H. Zhang, Y. Yu, L. Zhang, Y. Zhai and S. Dong, Chem. Sci., 2016, **7**, 6721-6727.
16. P. Higel, F. Villain, M. Verfaguer, E. Riviere and A. Bleuzen, J. Am. Chem. Soc., 2014, **136**, 6231-6234.
17. D. Dedovets, P. Bauduin, J. Causse, L. Girad and O. Diat, Phys. Chem. Chem. Phys., 2016, **18**, 3188-3196.
18. V. Noel, H. Randriamahazaka and C. Chevrot, J. Electroanal. Chem., 2000, **489**, 46-54.
19. S. Yagi, M. Fukuda, R. Makiura, T. Ichitsubo and E. Matsubara, J. Mater. Chem. A, 2014, **2**, 8041-8047.
20. G. Kasiri, R. Trocoli, A. B. Hashemi and F. La Mantia, Electrochimica Acta, 2016, **222**, 74-83.
21. S. J. Reddy, A. Dostal and F. Scholz, J. Electroanal. Chem., 1996, **403**, 209-212.
22. N. Imanishi, T. Morikawa, J. Kondo, Y. Takeda, O. Yamamoto, N. Kinugasa and T. Yamagishi, J. Power Sources, 1999, **79**, 215-219.
23. Y. You, X. Yu, Y. Yin, K-W. Nam and Y-G. Guo, Nano Res., 2015, **8**, 117-128.
24. X. Wu, W. Deng, J. Qian, Y. Cao, X. Ai and H. Yang, J. Mater. Chem. A, 2013, **1**, 10130-10134
25. X. Wu, Y. Luo, M. Sun, J. Quian, Y. Cao, X. Ai and H. Yang, Nano Energy, 2015, **13**, 117-123.
26. H-W. Lee, M. Pasta, R. Y. Wang, R. Ruffo and Y. Cui, Faraday Discuss., 2014, **176**, 69-81.
27. W-J. Li, S-L. Chou, J-Z. Wang, Y-M. Kang, J-L. Wang, Y. Liu, Q-F. Gu, H-K. Liu and S-X. Dou, Chem. Mater., 2015, **27**, 1997-2003.
28. S. Yang, G. Li, G. Wang, J. Zhao, M. Hu and L. Qu, Sens. Actuators B, 2015, **208**, 593-599.
29. L. Han, Q. Wang, S. Tricard, J. Liu, J. Fang, J. Zhao and W. Shen, RSC Advances, 2013, **3**, 281-287.
30. Y. Yang, Y. Hao, J. Yuan, L. Niu and F. Xia, Carbon, 2015, **84**, 174-184.

31. S. Ghasemi, S. R. Hosseini and P. Asen, Electrochimica Acta, 2015, **160**, 337-346.
32. B. Kong, X. Sun, C. Selomulya, J. Tang, G. Zheng, Y. Wang and D. Zhao, Chem. Sci,. 2015, **6**, 4029-4034.
33. A. Bleuzen, C. Lomenech, V. Escax, F. Villain, F.; Varret, C. Cartier dit Moulin and M. Verdaguer, J. Am. Chem.Soc. 2000, **122**, 6648-6652.
34. O. Sato, Y. Einaga, A. Fuhishima and K. Hashimoto, Inorg. Chem., 1999, **38**, 4405-4412.
35. V. Ksenofontov, G. Levchenko, S. Reiman, P. Gütlich, A. Bleuzen, V. Escax and M. Verdaguer. Phys. Rev. B 2003, **68**, 024415.
36. A Bleuzen, J-D. Cafun, A. Bachschmidt, M. Verdaguer, P. Münsch, F. Baudelet and J-P. Itie. J. Phys. Chem. C 2008, **112**, 17709-17715.
37. P. Higel, F. Villain, M. Verdaguer, E. Riviere and A. Bleuzen, J. Am. Chem. Soc., 2014, **136**, 6231-6234.
38. V. Escax, A. Bleuzen. C. Cartier dit Moulin, F. Villain, A. Goujon, F. Varret and M. Verdauer, J. Am. Chem. Soc., 2001, **123**, 12536-12543.
39. T. Liu, Y-J. Zhang, S. Kanegawa and O. Sato, Angew. Chem. Int. Ed., 2010, **49**, 8645-8648
40. H. Ohmagari, R. Ohtani, M. Nakaya, M. Ohba, M. Nakamura, L. F. Lindoy, O. Sato and S. Hayami, Dalton Trans., 2016, **45**, 16784-16788
41. M. P. Shores, L. G. Beauvais and J. R. Long, J. Am. Chem. Soc., 1999, **121**, 775-779.
42. L. Wang, Y. Lu, J. Liu, M. Xu, J. Cheng, D. Zhang and J. B. Goodenough, Angew. Chem. Int. Ed., 2013, **52**, 1964-1967.
43. Z. Gao, J. Bobacka and A. Ivaska, Electrchim. Acta, 1993, **38**, 379-385
44. Bard and Faulkner, "Electrochemical Methods, Fundamentals and Applications", Wiley (2000). Sect. 10.3.
45. R. O. Lezna, R. Ramognoli, N. R. de Tacconi and K. Rajeshwar, J. Phys. Chem. B, 2002, **106**, 3612-3621.
46. D. J. Kim, Y. H. Jung, K. K. Bharathi, S. H. Je, D. K. Kim, A. Coskun and J. W. Choi, Adv. Energy Mater., 2014, 1400133.
47. F. Scholz and A. Dostal, Angew. CHem. Int. Ed. Engl., 1996, **34**, 2685-2687.
48. M. B. Soto and F. Scholz, J. Electroanal. Chem., 2002, **521**, 183-189.
49. Y. Marcus, J. Chem. Soc., Faraday Trans., 1991, **87**, 2995-2999.
50. Y. Mizuno, M. Okubo, E. Hosono, T. Kudo, H. Zhou and K. Oh-ishi, J. Phys. Chem. C, 2013, **117**, 10877-10882.
51. M. Takachi, T. Matsuda and Y. Moritomo, Appl. Phys. Express, 2013, **6**, 025802.
52. L. Wang, J. Zhao, X. He, J. Gao, J. Li, C. Wan and C. Jiang, Int. J. Electrochem. Sci., 2012, **7**, 345-353.
53. P. J. Kulesza,, M. A. Malik, M. Berrettoni, M. Giorgetti, , S. Zamponi, R. Schmidt and R. Marassi, J. Phys. Chem., 1998, **102**, 1870-1876.
54. B. Kong, X. Sun, C. Selomulya, J. Tang, G. Zheng, Y. Wang and D. Zhao, Chem. Sci., 2015, **6**, 4029-4034.
55. F. Zhao, Y. Wang, X. Xu, Y. Liu, R. Song, G. Lu and Y. Li, ACS Appl. Mater. Interfaces, 2014, **6**, 11007-11012.
56. M. Luo, Y. Y. Dou, H. Kang, Y. H. Ma, X. Y. Ding, B. Liang, B. J. Ma and L. Li, J. Solid Sate Electrochem., 2015, **19**, 1621-1631.

57. J-G. Wang, Z. Zhang, X. Liu and B. Wei, Electrochim. Acta, 2017, **235**, 114-121.
58. T. D. Waite and F. M. M. Morel, Environ, Sci. Technol., 1984, **18**, 860-868.
59. M. Fukushima and K. Tatsumi, Colloids Surf. A., 1999, **115**, 249-258.
60. T. D. Waite and F. M. M. Morel, J. Colloid, Interface Sci., 1984, **102**, 121-137.
61. H. Zhou, C. Qiu, Z. Liu, H. Yang, L. Hu, J. Liu, H. Yang, C. Gu and L. Sun, J. Am. Chem. Soc., 2010, **132**, 944-946.
62. F. P. Van der Zee, I. A. E. Bisschops and G. Lettinga, Environ. Sci. Technol., 2003, **37**, 402-408.
63. C. Gervais, M-A. Languille, G. Moretti and S. Reguer, Langmuir, 2015, **31**, 8168-8175.
64. L. Samain, B. Gilbert, F. Grandjean, G. J. Long and D. Strivay, J. Anal. At. Spectrom., 2013, **28**, 524-535.
65. K. R. Millington and L. J. Kirschenbaum, Coloration Technol., 202, **118**, 6-14.
66. C. Gervais, M-A. Languille, S. Reguer, M. Guillet, S. Pelletier, C. Garnier, E. P. Vicenzi and L. Bertrand, J. Anal. At. Spectrom., 2013, **28**, 1600-1609.
67. T. Muraliganth and A. Manthiram, J. Phys. Chem. C, 2010, **114**, 15530-15540.
68. M Pasta, C. D. Wessells, R. A. Huggins and Y. Cui, Nat. Commun., 2012, 3:1149.
69. Y. You, X-L. Wu, Y-X. Yin and Y-G. Guo, Energy Environ. Sci., 2014, **7**, 1643-1647.

Chapter 7

Conclusions

Technological advances, which have a crucial impact in society, are intimately related to the development of new nanostructured materials. Hence, the main motivation of this work was to expand the strategies for the preparation of functional nanomaterials by designing hybrid carbon nanostructures suitable for energy storage applications containing a range of electrochemically active nanocomponents including molecules, nanoparticles and metal coordination polymers. An overview of the current approaches within the energy area for the preparation of both uncoupled carbon nanostructures and the approaches to combine them with a wide range of active components (i. e. molecular clusters, nanoparticles and metal coordination polymers) is provided in Chapter 1. This chapter highlights that rational thinking is required for the development of nanomaterials with functional properties by targeting the combination of two or more nanocomponents with different properties, and preparation methodologies while ensuring the utilisation of cheaper and abundant materials such as non-precious metals.

In chapter 2, a large-scale, green, simple and cost-effective method for the production of 2D graphene nanoplatelets (GNP) from one-dimensional hollow carbon nanofibers (CNF) is proposed. It was found that high-energy ball milling can lead to few-layer GNP in just 20 min which reveals a higher specific capacitance (119 F/g) due to the combination of double-layer and redox pseudocapacitance mechanisms with respect to pristine CNF (3.7F/g). Interestingly, the produced GNP stands as an alternative to commercially available graphene nanoplatelets due to their higher electrochemical performance at a lower price (615.5F/$ and 264F/$, respectively). The effect of milling as well as the increase the hydrophilicity on electrochemical capacitance was thoroughly investigated. For example, the increase in oxygen content on the GNP nanostructure by acid treatment showed increase in the internal resistance as a consequence of a morphological change.

The formation of carbon nanostructures by using hard template catalyst (i. e. Fe_3O_4 nanoparticles) supported on a two-dimensional carbon substrate at high temperatures (1000^oC) in inert atmosphere (argon) was investigated in Chapter 3. Despite the thermal treatment of Fe_3O_4 NPs (4 nm) leads to large carbon-iron nano-onions (> 100nm) independently of the carbon substrate, it was

demonstrated that the presence of oxygen containing groups on the carbon surface had a dramatic effect on the formation pathways of those large nano-onions as a consequence of the nanoparticle-support interaction. Thus, the highly graphitized carbon surface (GF, low oxygen content) is mostly intact after thermal treatment whereas a large number of small hollow carbon cages (HCC, 9 nm) decorate the surface of the partly oxidized carbon surface (GF_{OX}) after 1000^{o}C for 2 hours. It was suggested that defects on the carbon surface would act as nucleation points during the agglomeration of nanoparticle at high temperatures. In fact, TEM analysis of thermal treated material for a shorter period of time (45 min instead 2 hours) demonstrated that hollow carbon cages were initially filled with iron. Subsequently, the hollow carbon cages and large carbon-coated iron nano-onions that desorb from the surface were a result of the diffusion of iron atoms through the graphitic layers via Ostwald ripening at high temperatures.

In chapter 4, the confinement of molecular metal clusters (i. e. Mn_{12} molecules) within the cavities of carbon nanotubes was investigated in order to overcome their intrinsic low cyclability of these polynuclear metal complexes. It is important to note that the carbon nanotubes acted as host-containers, ensuring the intimate contact with the molecule cluster, and as conductor for rapid electron transfer. Hence, the capacitance enhancement during electrochemical cycling was associated to two key factors. Firstly, the disaggregation of confined Mn_{12}Ac nanoclusters into very small clusters and these into molecules within the host nanocontainers during the oxidation/reduction process that leads to an increase of electro-active surface area. The second factor is the structural reorganisation of the encapsulated nanoclusters during the insertion and removal of K^{+} ions within the nanotube channels, which facilitates the ionic migration.

In chapter 5, the encapsulation effect is further investigated but using larger hollow tubular carbon nanostructures than carbon nanotubes. To do so, an in situ approach for the synthesis of metal oxide-carbon nanostructures was successfully developed where Mn_3O_4 nanoparticles were synthesized in the presence of hollow carbon nanofibers (CNF). It was demonstrated the control on the final nanoparticle loading inside the cavities of CNFs by tuning the

oxygen-containing groups, which act as nucleation points, on the carbon surface. It is important to highlight that the absence of nucleation points dramatically modified the nanoparticle morphology (from pseudo-spherical to large faceted), suggesting an effect of the graphitized carbon surface in the synthetic pathway. The electrochemical properties of all the hybrids lead to two main conclusions. First, large faceted nanoparticles showed a smaller specific capacitance with respect to small pseudo-spherical nanoparticles as a consequence of a smaller surface area. Secondly, the confinement of the nanoparticles increases their electrochemical stability. Hence, the nanoparticles grown on outer surface of CNF or prepared separately and inserted in CNF exhibited a low durability in the charging-discharging cycling and weak synergistic effects between the metal oxide and the carbon component. In contrast, nanoparticles synthesized directly inside the cavity of hollow CNF yielded a hybrid material with a high durable capacitance, increasing the specific capacitance over 13,000 cycles. The mechanism of the remarkable performance of NPs formed inside, which increases their specific capacitance by nearly a factor of 5, was explored by HRTEM, STEM and EELS, revealing no chemical changes in the structure or in composition of nanoparticles, and no significant changes in the NPs average size. Thus, the confinement facilitates the re-capture of desorbed Mn^{2+} on the nanoparticle surface, creating "dentate" nanoparticles with an increased surface area.

In Chapter 6, the effect of Co^{II}/Co^{III} ratio on the electrochemical performance of cobalt hexacyanoferrate (CoHCF) was thoroughly investigated. The proposed methodology was based on triggering the internal electron transfer (increasing the Co^{III}_{LS}-NC-Fe^{II}_{LS} with respect to the initial Co^{II}_{HS}-NC-Fe^{III}_{LS} pair) by thermal annealing, studying specifically the coordinated water contribution while retaining the number of vacancies constant within the structure. Different thermal conditions as well as the electrochemical parameters were thoroughly studied. In addition, CoHCF was synthesized in the presence of graphene flakes (GF) to overcome the intrinsic low conductivity of CoHCF crystals. It is important to highlight that the hybrid material exhibited a much better electrochemical performance that his analogue composite due to a higher synergy. Overall, the thermal treatment of the resulted hybrid improved the stability during cycling (+21% after 400 cycles)

which indicated that the partial removal of coordinated water molecules introduced flexibility into the framework, facilitating the reversibility of the insertion/extraction of the K^+.

Appendix I

List of abbreviations

EDL: electrochemical double-layer

EJ: exajuoles (10^{18}J)

EV: Electric vehicles

CNF: Carbon nanofibers

MWNTs: multi-walled carbon nanotubes

SWNTs: single-walled carbon nanotubes

F/g: Faraday per gram (

CNs: carbon nanostructures

AAQ: 2-aminoanthraquinone

TTF: tetrathiafulvalene

CNTs: carbon nanotubes

PANI: polyaniline

AQ: 9,10-anthraquinone

PhQ: 9,10-phenantreneuquinone

POMs: Polyoxometalates

rGO: reduced graphene oxide

PDDA: poly(dimethyl diallyl ammonium chloride)

NPs: nanoparticles

ORR: oxygen reduction reaction

OER: oxygen evolution reaction

GO: graphene oxide

Ac: acetate

DFT: density functional theory

MCPs: metal-coordination polymers

MOF: metal-organic framework

PBA: Prussian blue analogues

MHCFs: metal hexacyanoferrate

PPy: polypyrrole

GNP: graphene nanoplatelets

CVD: chemical vapour deposition

DMF: N,N-dimethylformamide

FESEM: Field emission scanning electron microscopy

EDS: Energy-dispersive X-ray spectroscopy

AFM: Atomic force microscope

TEM: Transmission electron microscope

SEM: Scanning electron microscope

XRD: X-ray diffraction

TGA: Thermogravimetric analysis

XPS: X-ray photoelectron spectroscopy

CV: Cyclic voltammogram

EIS: Electrochemical impedance spectroscopy

R_s: Solution resistance

C_{sp}: Specific capacitance

GCE: Glassy carbon electrode

PTFE: Polytetrafluoroethylene

OCP: Open circuit potential

HHC: Hollow carbon cages

GF: Graphene flakes

E^0: Formal potential

ΔE: Peak separation

MVS: Mixed-valence systems

Appendix II

Quick chemical-free exfoliation of carbon nanofibers for high-performance few-layer graphene nanoplatelet supercapacitors

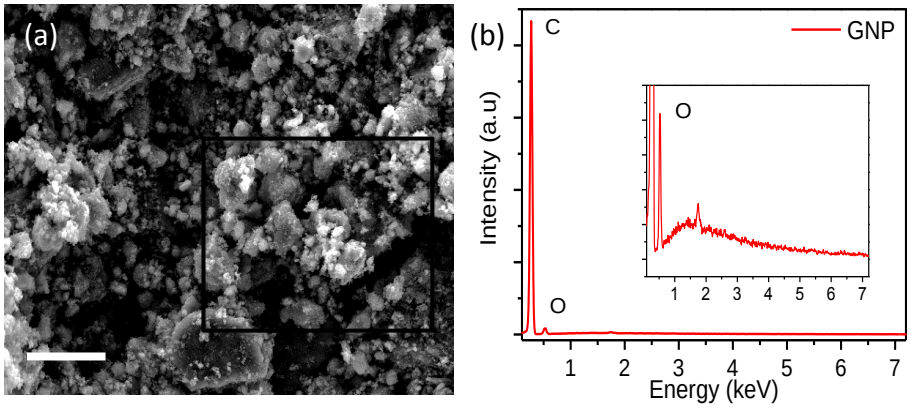

Figure 1. (a) FESEM image (scale bar: 25 µm) and (b) EDS of GNP showing C (93% weight) and O (6.8%). Inset in b shows traces of Si (0.2%) but no contamination from the milling process (in form of metallic impurities) is observed.

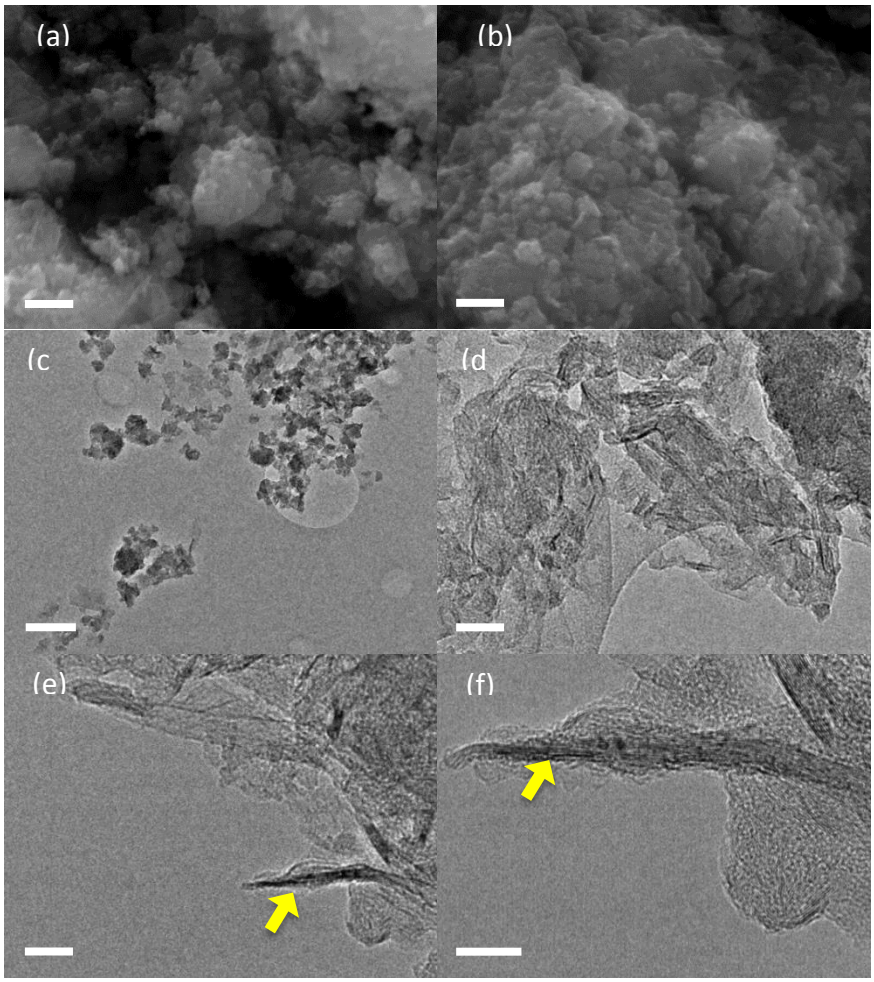

Figure 2. (a-b) FESEM (scale bars: 1 and 0.5 µm) and (c-f) HRTEM (scale bar: 200, 50, 20, 10 nm, respectively) images of GNP. Yellow arrows highlight the thickness of few-layer GNP.

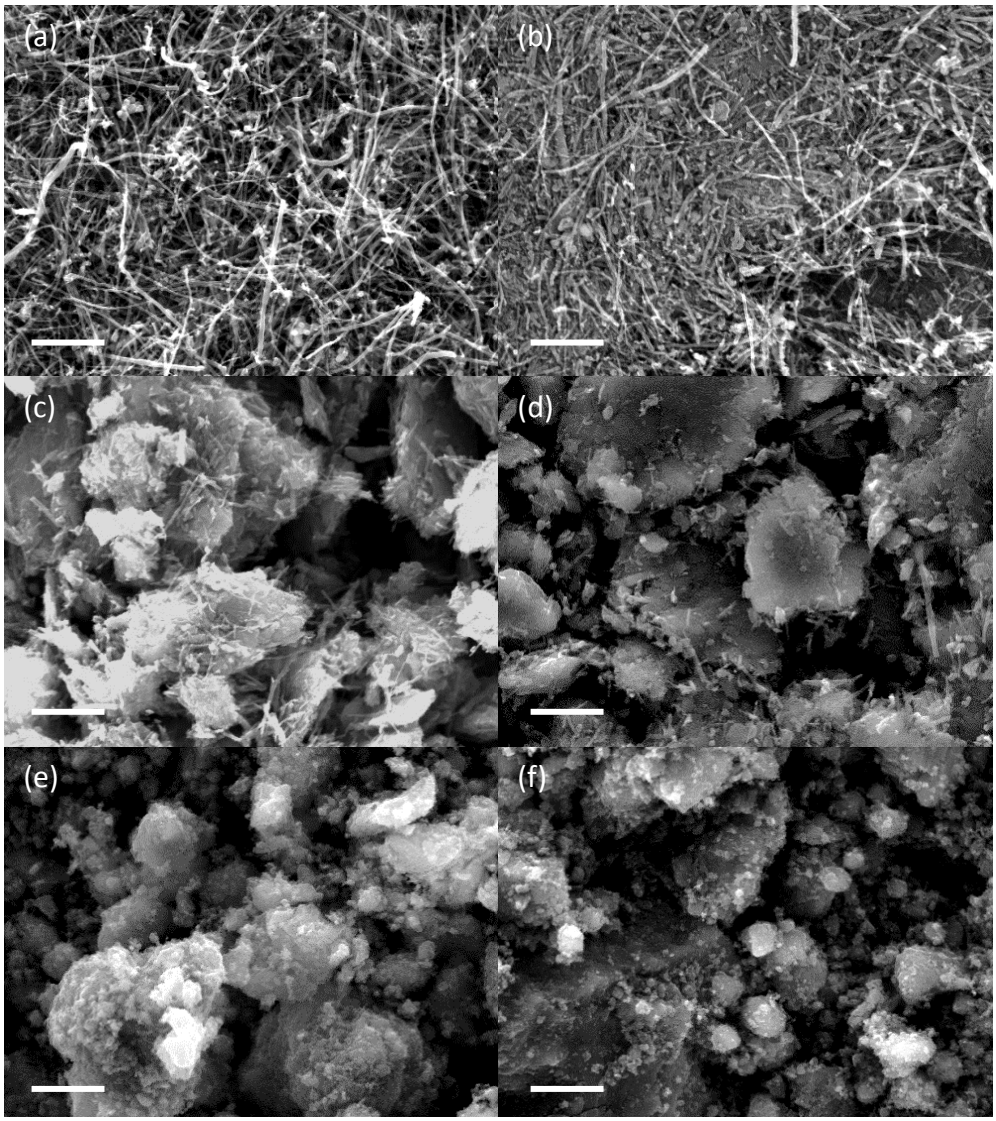

Figure 3. FESEM images of (a) pristine CNF and CNF milled for (b) 1, (c) 5, (d) 10, (e) 20 and (f) 30 minutes. The scale bars for all the images are 5 µm.

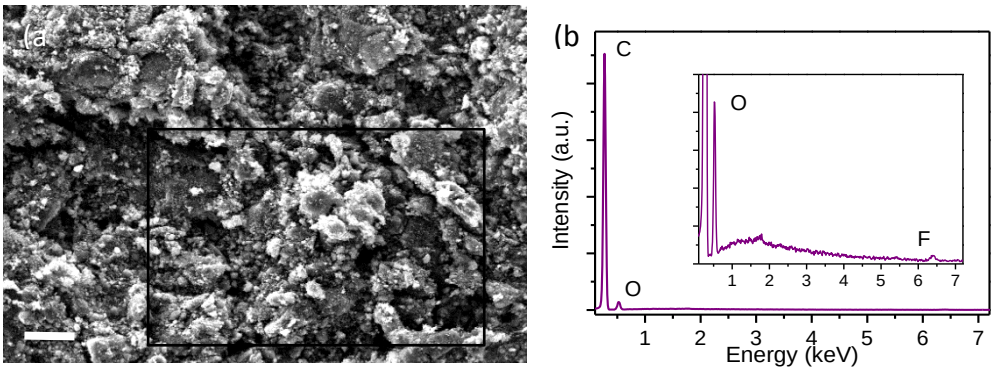

Figure 4. (a) FESEM image (scale bar: 25 µm) and (b) EDS of CNF milled after 30 minutes confirming the presence of metallic impurities (0.5% in weight of Fe) as result of the ball milling process.

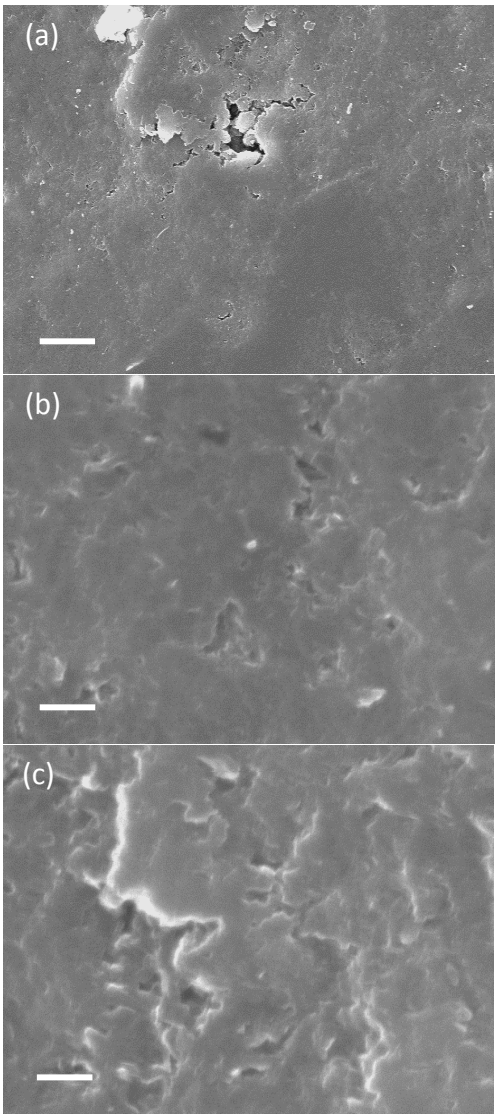

Figure 5. FESEM images of GNP after acid treatment (GNP_{AC}). Scale bars: 10 µm in a and 0.5 µm in b-c.

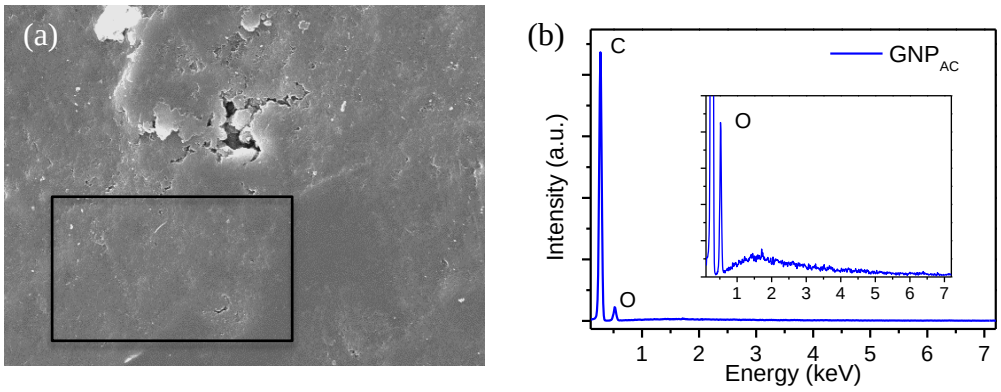

Figure 6. (a) FESEM image (scale bar: 10 µm) and (b) EDS of GNP_{AC} showing a O/C ratio (% weight) of 0.18.

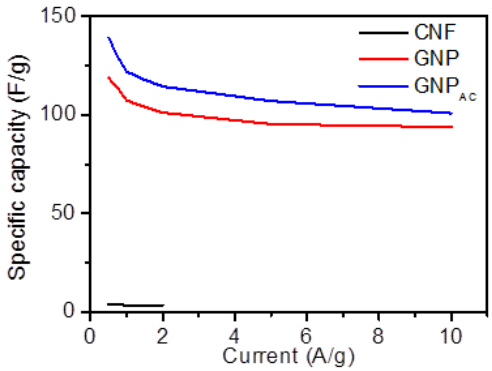

Figure 7. Specific capacitance (F/g) as a function of the current density (A/g) for CNF, GNP and GNP_{AC}.

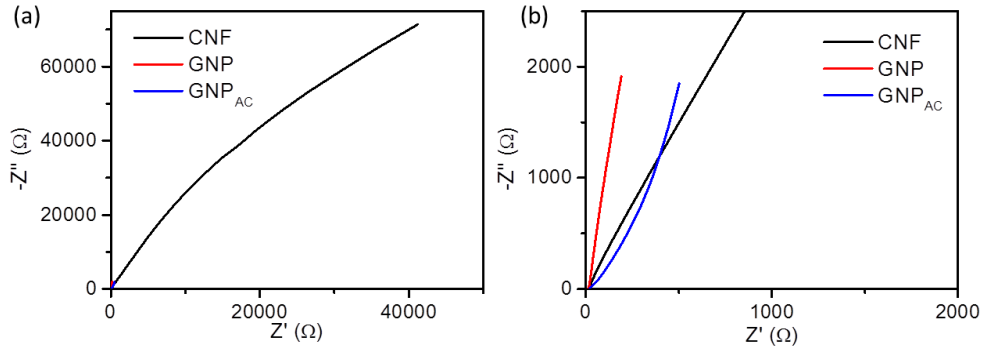

Figure 8. Nyquist plot for CNF, GNP and GNP_{AC} (a) at low and (b) high frequencies.

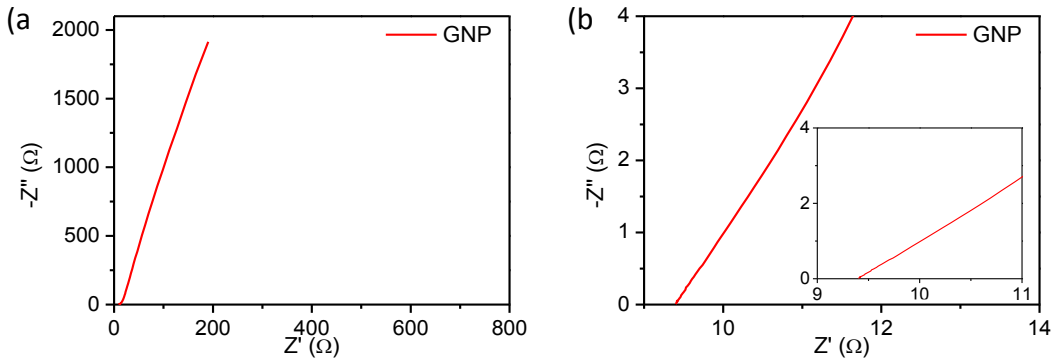

Figure 9. (a) Nyquist plot for GNP showing a high slope at low frequency and (b) the absence of a semi-circle at high frequency.

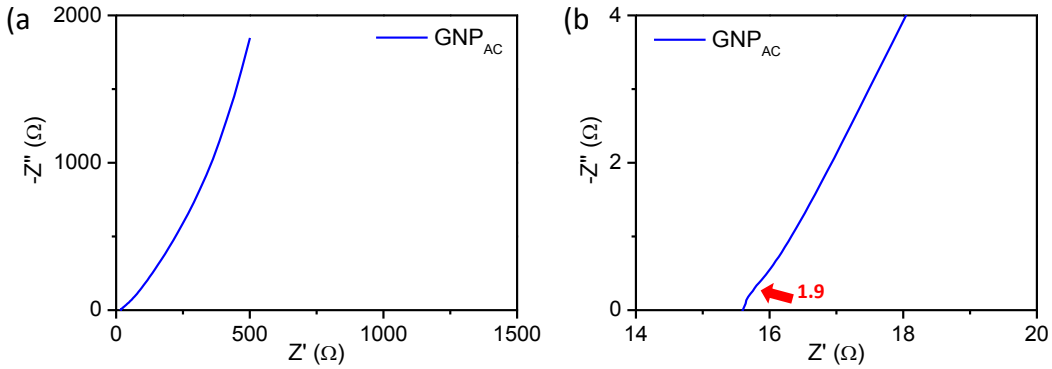

Figure 10. (a) Nyquist plot for GNP_{AC} showing a moderate slope at low frequency and (b) the presence of a semi-circle at high frequency.

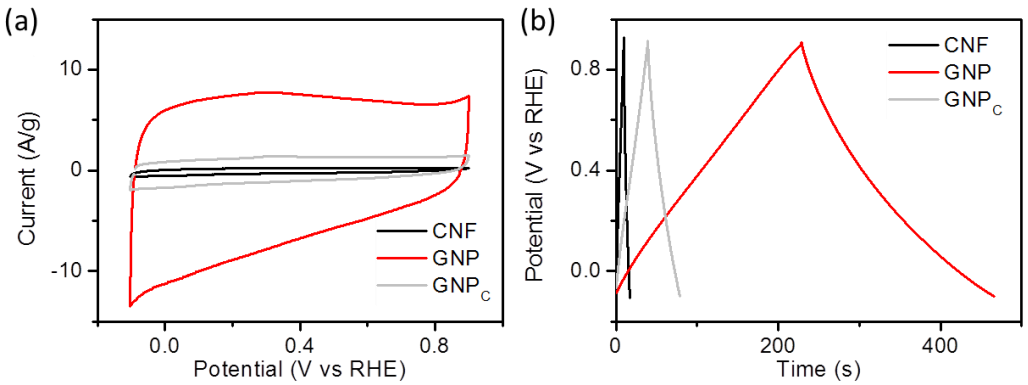

Figure 11. (a) Comparison of CV at 0.1V/s and (b) galvanostatic charging-discharging measurements at 0.5 A/g in 1M KOH of pristine CNF (black), graphite nanoplatelets, produced after milling CNF for 20 min(GNP), and commercially available GNP (GNP_C, Asbury 2299 GNP).

Appendix III

Growth of hollow nano-cages on defective graphene flakes driven by the agglomeration and release of metal atoms

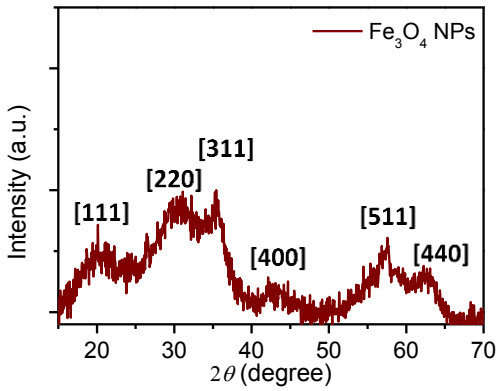

Figure 1. Powder XRD pattern of Fe_3O_4 NPs (brown), showing the characteristic inter-planar distance of Fe_3O_4 despite of their small size (4nm).

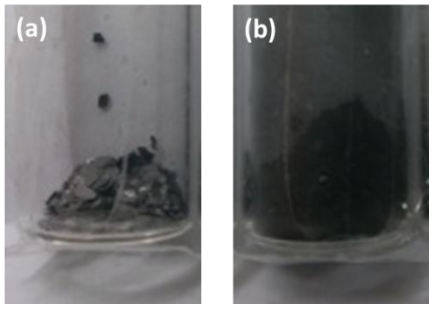

Figure 2. (a) Natural graphite flakes as received and (b) after milling treatment (GF).

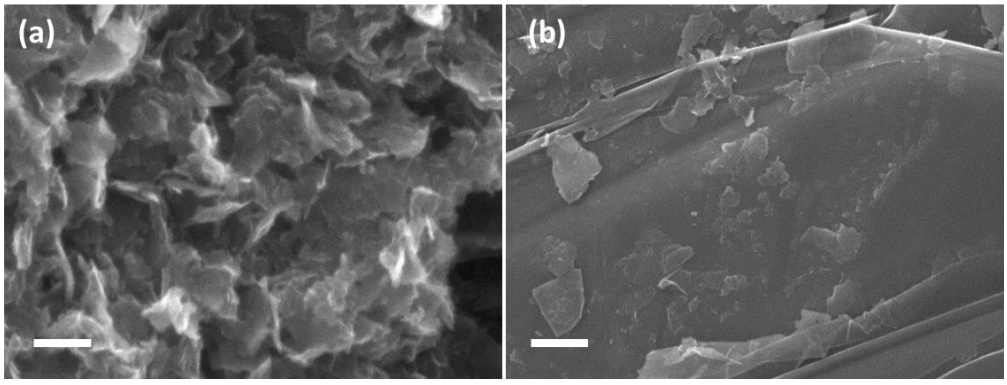

Figure 3. SEM images of (a) GF_{OX} and (b) GF (after milling treatment). Scale bar are (a) 500 nm and (b) 2 µm.

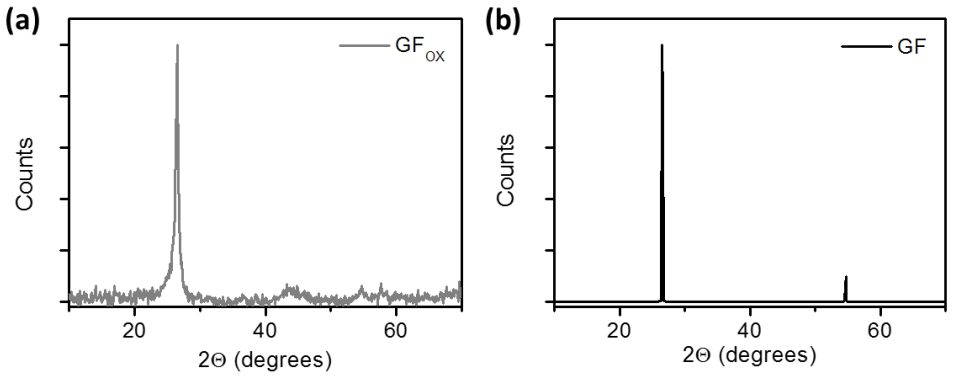

Figure 4. Powder XRD pattern of (a) GF_{OX} and (b) GF, showing the characteristic peaks of graphite located at 26.5^0, 44.3^0 and 54.5^0 corresponding to planes (002), (101) and (004), respectively.

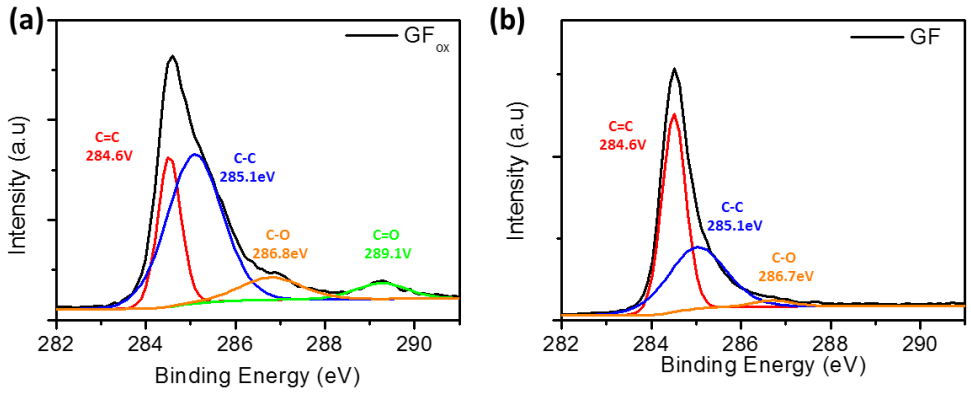

Figure 5. C 1s high-resolution XPS measurement of (a) GF_{Ox} and (b) GF, being fitted with four and three components respectively. It is important to highlight the high oxygen content on GF_{OX} is larger than GF (0.08 and 0.02, respectively).

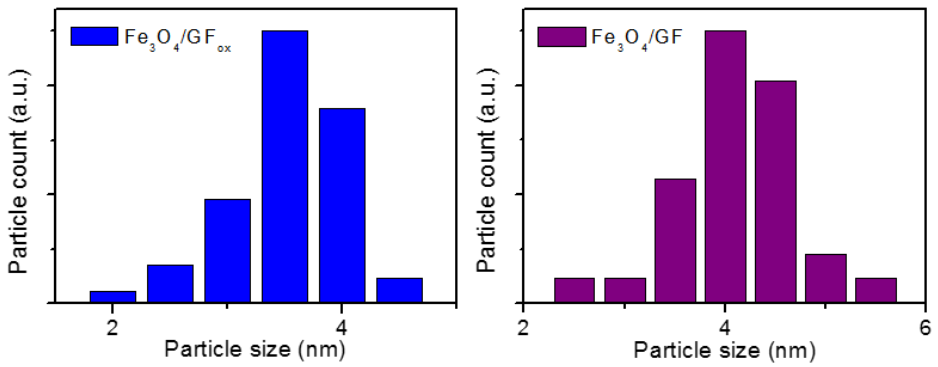

Figure 6. Statistical analysis of Fe_3O_4 nanoparticles supported on GF_{OX} (Fe_3O_4/GF_{OX}, blue) and GF (Fe_3O_4/GF, purple), being their sizes 3.9 ± 0.5 and 4 ± 0.6. It can be observed that the preparation of the composite does not modify the structure of the nanoparticles.

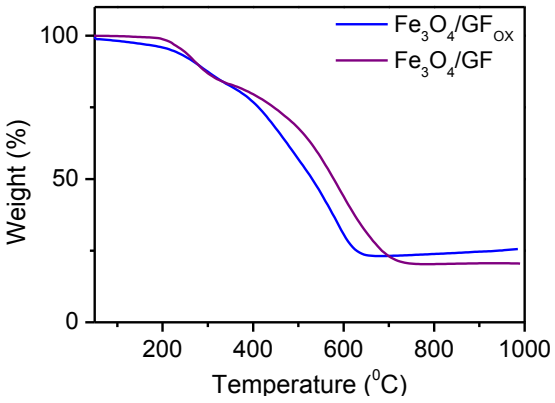

Figure 7. Thermal gravimetric analysis of Fe_3O_4/GF_{OX} (blue) and Fe_3O_4/GF (purple) in air at scan rate of 5^0C/min before thermal treatment (annealing at 1000^0C in argon) showing similar loading of nanoparticles, being related with the final weight at 1000^0C.

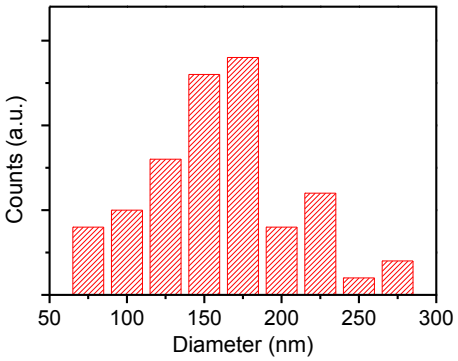

Figure 8. Statistical analysis metal-carbon nano-onions in $Fe@C/GF_{OX}$ composite, being their sizes 150 ± 50 nm.

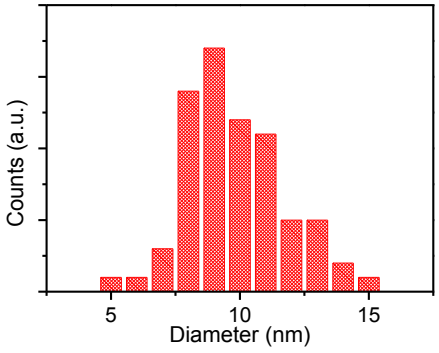

Figure 9. Statistical analysis hollow carbon cages supported on $Fe@C/GF_{OX}$ composite, being their sizes 9 ± 2 nm.

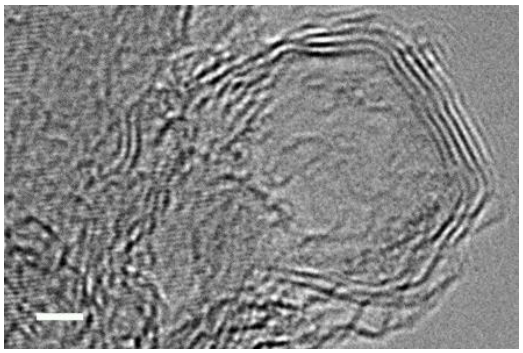

Figure 10. TEM image of a single hollow carbon cage on Fe@C/GF, being located at the more active site of the graphene flake (at the edge). Scale bar is 2 nm.

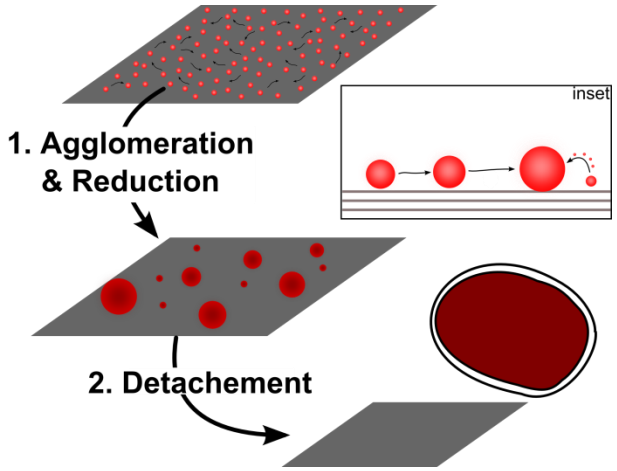

Figure 11. Proposed mechanism for the selective formation of metal-carbon nano-onions during annealing Fe_3O_4/GF at 1000°C for 2 hours in argon. Due to the low nanoparticle-carbon support interaction, nanoparticles agglomerate into large metal-carbon core-shell nanoparticles.

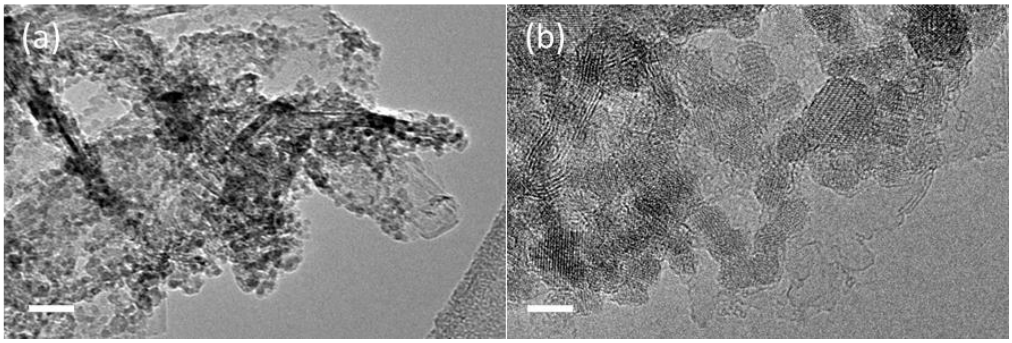

Figure 12. HRTEM image of Fe_3O_4/GF_{OX} after heating in air at 300^{0}C for 24 hours. Scale bars are (a) 20 and (b) 5 nm.

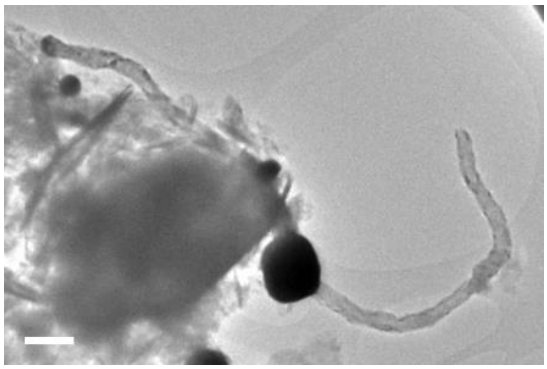

Figure 13. Bright-field TEM image of a-Fe_3O_4/GF at 1000^0C for 2 hours in argon showing the heterogeneity of the sample. Scale bar is 500 nm.

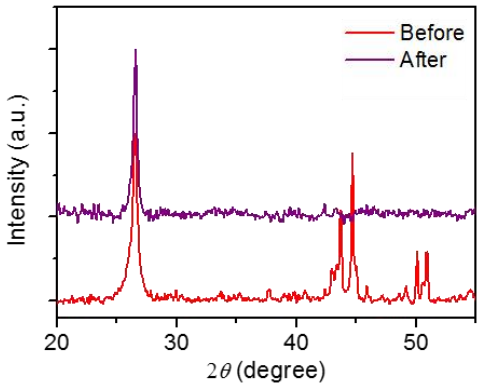

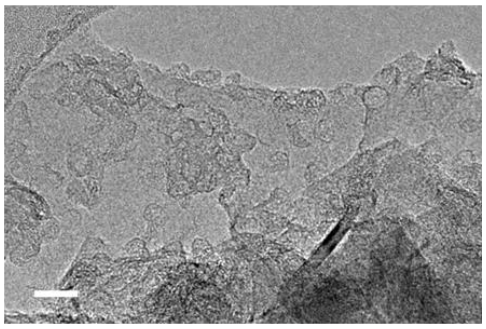

Figure 14. XRD pattern of a- Fe_3O_4/GF_{OX} before (red) and after (purple) acid treatment in chloric acid. TEM image shows that hollow carbon nanostructures are retained after treatment. Scale bar is 20 nm.

Appendix IV

Molecule clusters encapsulated in carbon nanotubes as new working principle for energy-storage

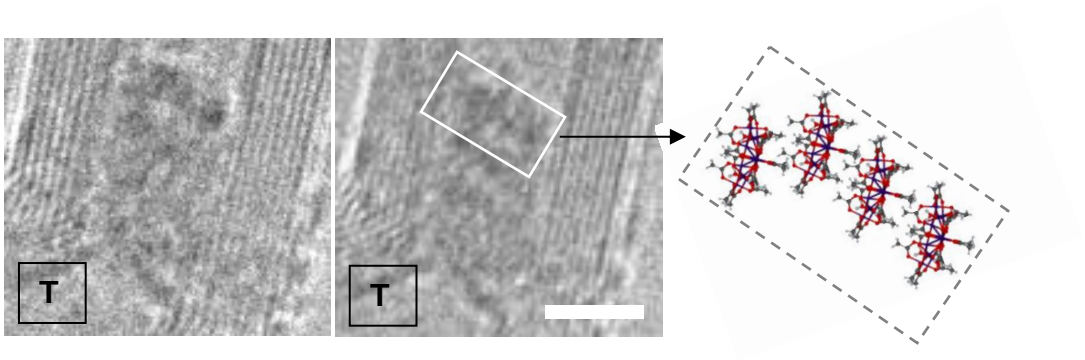

Figure 1: Time series of bright field transmission electron micrographs of Mn12Ac@MWNT (100 kV) and a schematic representation of the packing of Mn12Ac molecules in a NT. White scale bar is 5 nm.

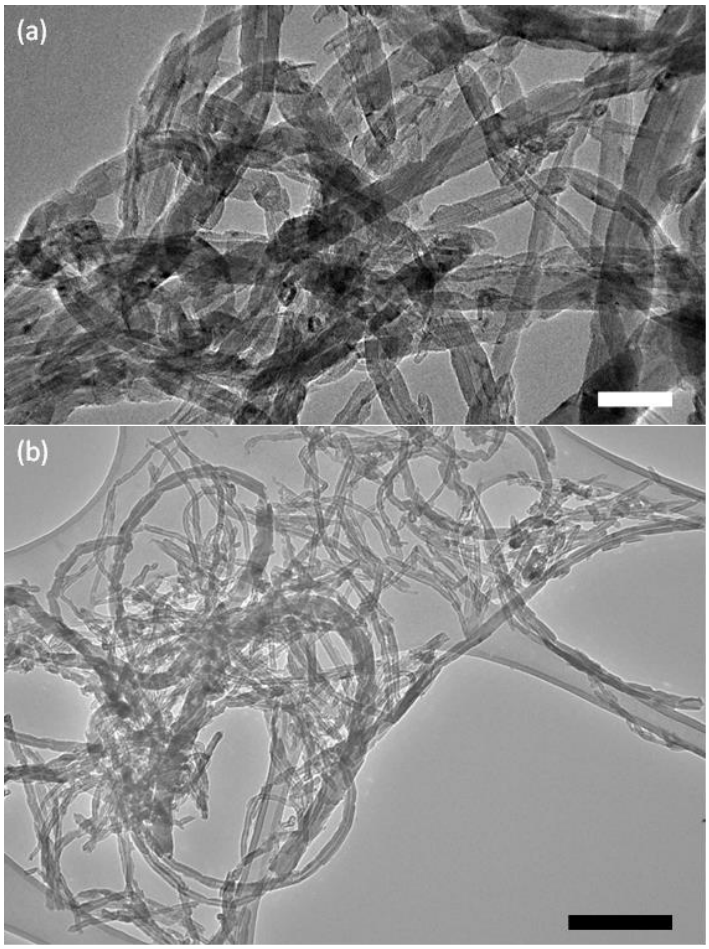

Figure 2: Bright field transmission electron micrographs of Mn_{12}Ac@MWNT (100 kV). White scale bar is 50 nm and black scale bar is 0.2 µm.

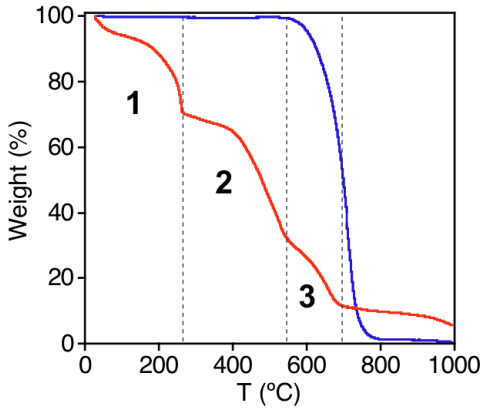

Figure 3: TGA of $Mn_{12}Ac$@MWNT (red) and empty (short and open) GMWNT (blue). Step 1 corresponded to decomposition of $Mn_{12}Ac$ with the loss of all coordinated ligands and, hence, the consequent formation of Mn_3O_4. Step 2 corresponded to the catalytic oxidation of the graphitized MWNTs in the presence of the Mn_3O_4 formed inside the nanotubes, and the third step corresponded to thermal oxidation of the graphitized MWNT themselves (that is, sections of nanotubes that are not in direct contact with Mn_3O_4)[1,2] The residual weight remaining at 1,000 °C was attributed to Mn_3O_4 (5.6% wt) that does not decompose further.

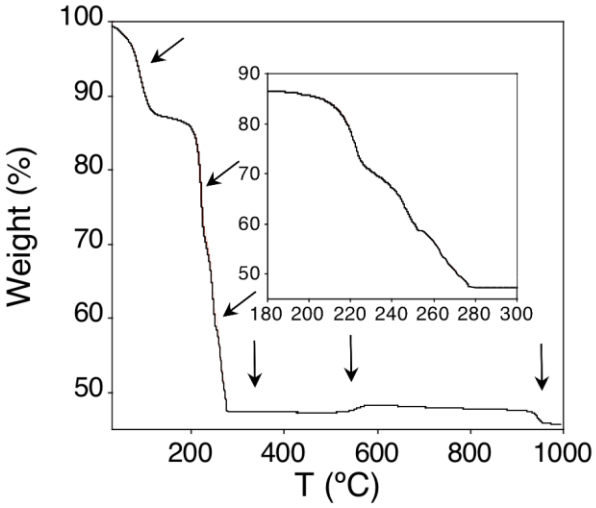

Figure 4. TGA of $Mn_{12}Ac$. Three weight loss steps were observed on air. The first step corresponded to the loss of crystallisation solvent molecules and the second and third weight losses to the subsequent decomposition of the cluster. At *ca.* 280 ºC, all organic moieties are removed upon heating and Mn_3O_4 was formed. Moreover, the oxidation of Mn_3O_4 to Mn_2O_3 was observed at 560 ºC, followed by the decomposition of Mn_2O_3 at higher temperatures (930 ºC).[3]

Quantification of the amount of $Mn_{12}Ac$ inside nanotubes. The amount of $Mn_{12}Ac$ in $Mn_{12}Ac$@MWNT can be estimated from TGA measurements (11.6% wt). From TGA measurements, the amount of $Mn_{12}Ac$ has been deduced by comparing the amount of manganese oxide remaining at 1,000°C after all carbon of $Mn_{12}Ac$@ GMWNT being burnt out (5.6% of the total weight, Figure 3) with the residual manganese oxide found at the same temperature for pristine $Mn_{12}Ac$ (47.2% of the total weight, Figure 4).

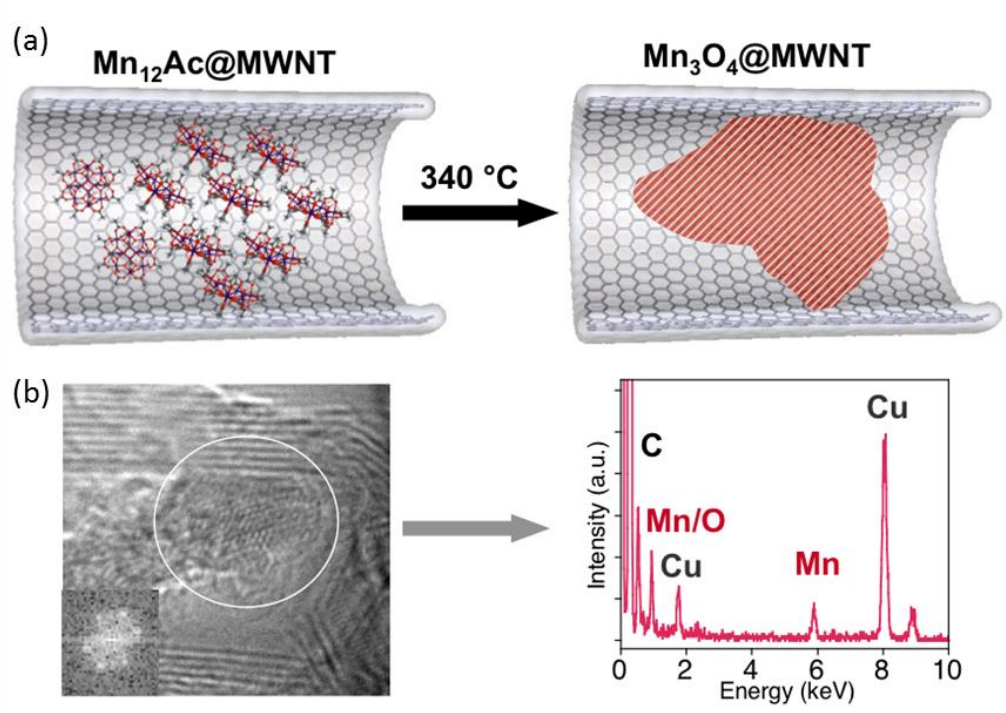

Figure 5: a) Schematic representation of the decomposition of $Mn_{12}Ac$ into Mn_3O_4 inside NT. b) On the left: bright field transmission electron micrographs of Mn_3O_4 nanoparticles inside NTs (100 kV); (inset) optical diffractogram showing *d*-spacing of 0.288 nm which corresponds to the [200] planes of Mn_3O_4. On the right: EDX spectrum of Mn_3O_4 formed from $Mn_{12}Ac$ inside NT (area of the spectrum is marked with a white circle; Cu peaks are due to the copper grid).

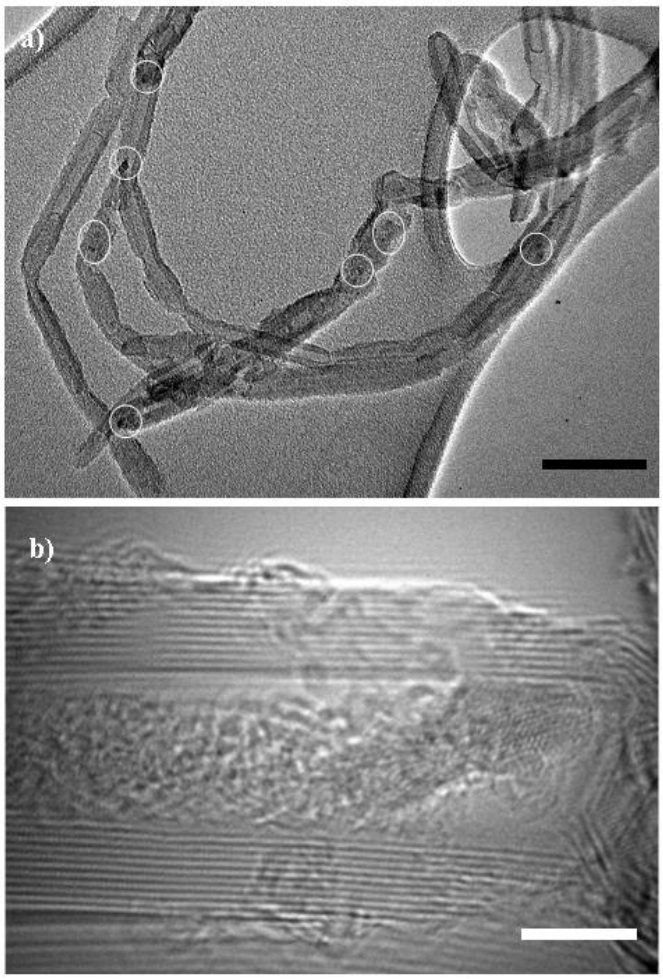

Figure 6: Bright field transmission electron micrographs of Mn_3O_4 nanoparticles inside nanotubes (100 kV). The white circles in (a) denote encapsulated nanoparticles. Black scale in (a) is 50 nm while white scale bar in (b) is 5 nm.

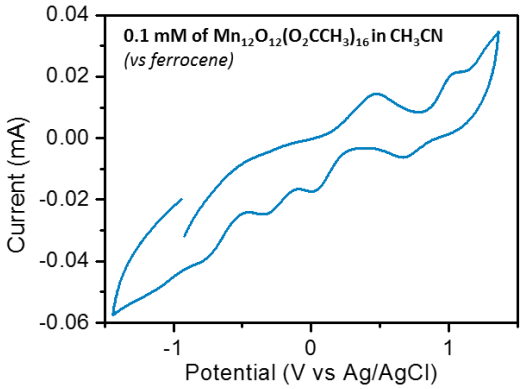

Figure 7: Cyclic voltammogram of $Mn_{12}Ac$ in MeCN. The potentials are given versus the Cp_2Fe/Cp_2Fe^+ couple under the same conditions.[4-8]

Synergistic effect of the nanoscale hybridization.

Calculation of the Theoretical Capacitance. The theoretical capacitance of the $Mn_{12}Ac$@MWNT hybrid electrode at a current density of 0.5 A/g can be calculated as follows:

$$C_{Hybrid} = P_{Mn12Ac} * C_{Mn12Ac} + (100\%\text{-}P)_{MWNT} * C_{MWNT}$$

being 201 F/g and 9 F/g the experimental values at 0.5 A/g of $Mn_{12}Ac$ and MWNT, respectively and 14.2% (*wt*) the percentage of $Mn_{12}Ac$ in the composite (*P*). Thus, the theoretical capacitance of the composite is 36 F/g.

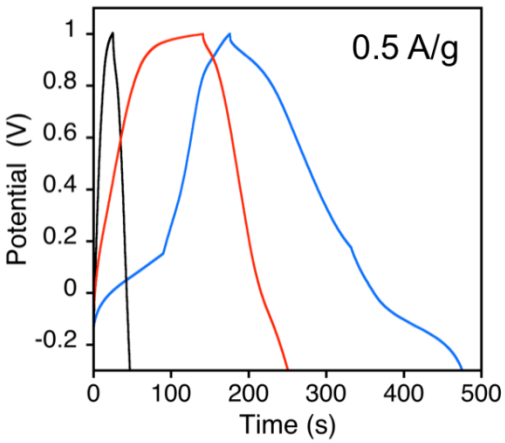

Figure 8: Comparison of charge–discharge curves of MWNT (black), $Mn_{12}Ac$ (blue) and $Mn_{12}Ac$@MWNT (red) at a constant current density of 0.5 A/g.

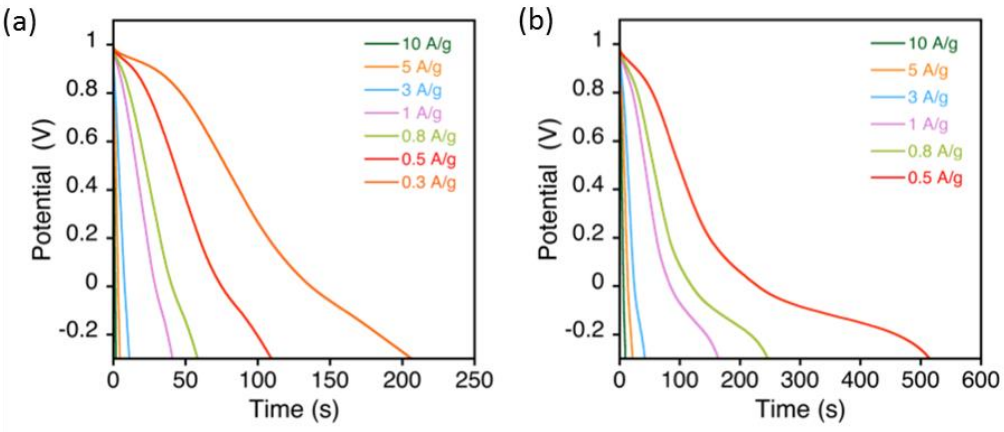

Figure 9: Discharge voltage profiles at various current densities (0.3, 0.8, 1, 3, 5, 10 A/g) for (a) Mn_{12}Ac@MWNT and (b) Mn_{12}Ac.

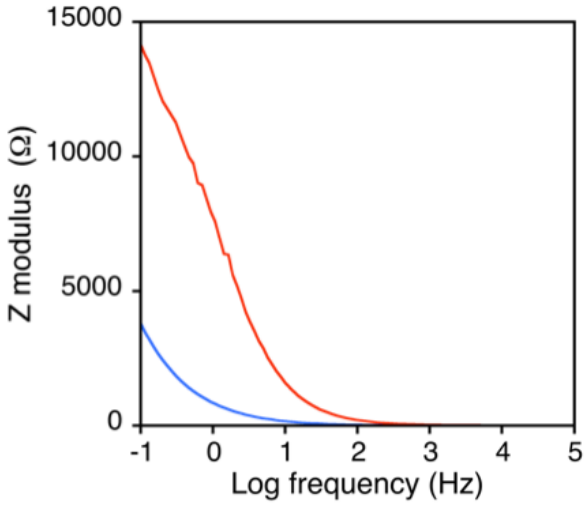

Figure 10: Bode plot representation of the electrochemical impedance for Mn_{12}Ac (blue) and Mn_{12}Ac@MWNT (red).

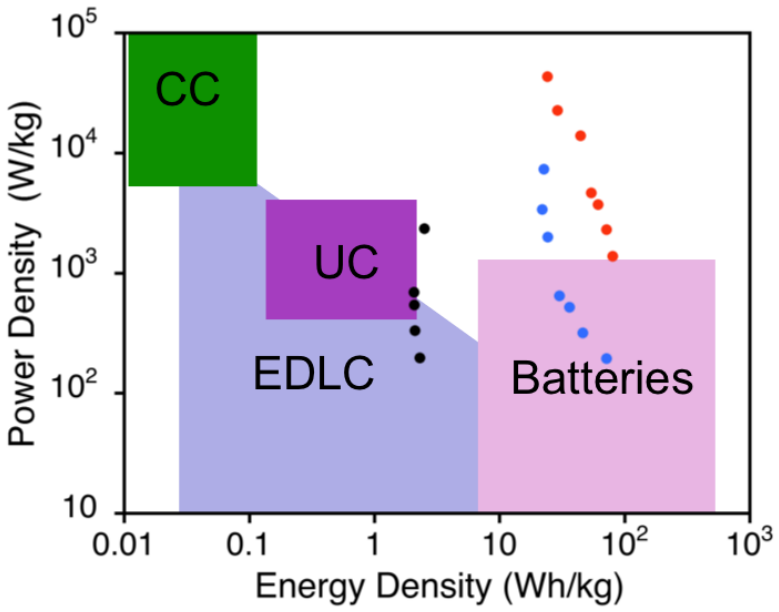

Figure 11: Ragone plot (power density *vs.* energy density) of MWNT (black), $Mn_{12}Ac$ (blue), $Mn_{12}Ac$@MWNT (red) electrodes and other power technologies (conventional capacitors (CC), ultra capacitors (UC), batteries and electrical double-layer capacitors (EDLC)).[9] The energy densities and power densities were derived from the charge–discharge curves at different current densities.

Protective effect of the host nanocontainer on the encapsulated $Mn_{12}Ac$ molecules.

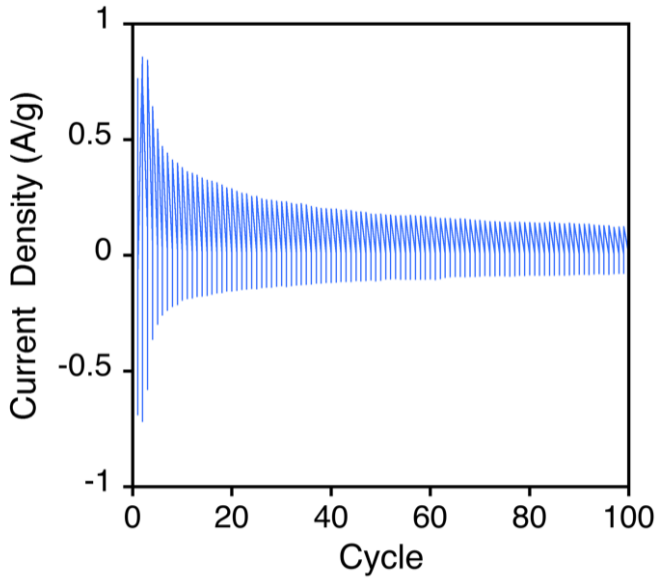

Figure 12: Variation of the current density with the increasing cycling for $Mn_{12}Ac$ electrode at a scan of 0.1 V/s.

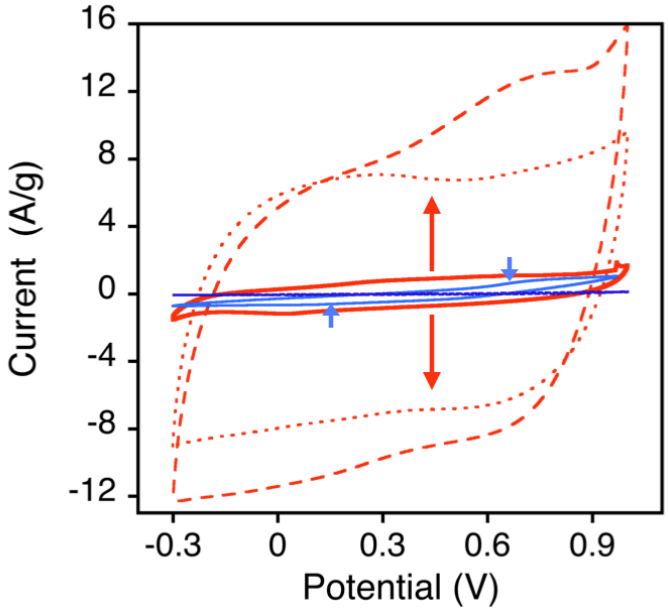

Figure 13: Comparison of cyclic voltammograms for $Mn_{12}Ac$ (bright and dark blue line for the 1st and 100th cycle, respectively) and $Mn_{12}Ac$@MWNT (solid, dashed and dotted red line for the 1st, 100th and 2000th cycle, respectively) at a constant scan rate of 0.1 V/s (based on the $Mn_{12}Ac$ mass).

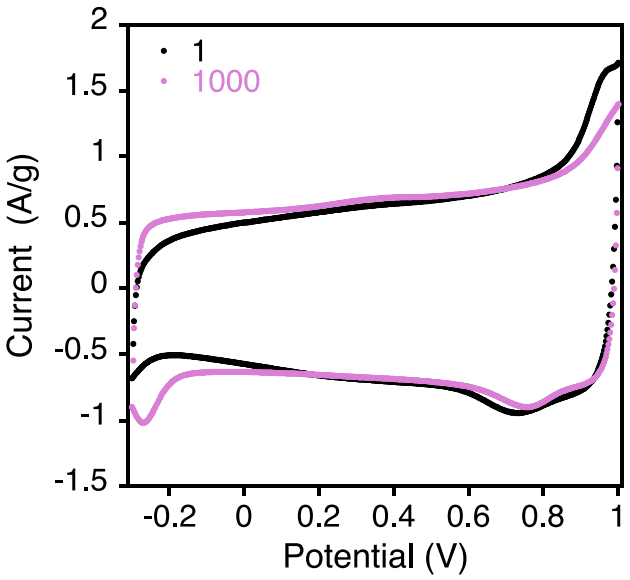

Figure 14: Cyclic voltammograms of MWNT at a constant scan rate of 0.1 V/s for the 1st (black) and 1000th (pink) cycle.

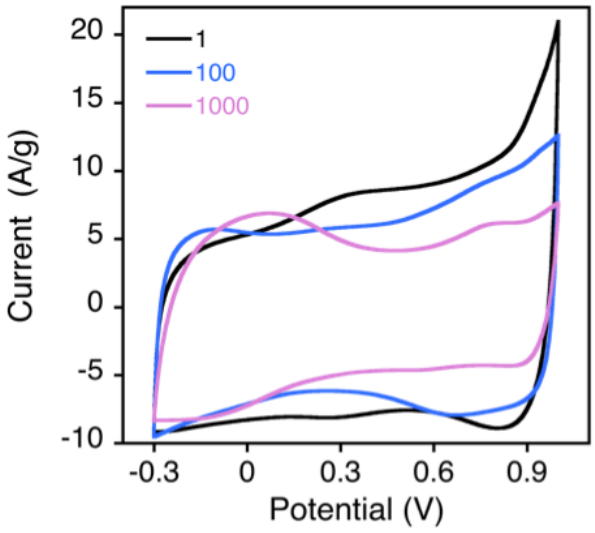

Figure 15: Cyclic voltammograms of Mn_3O_4@MWNT at a constant scan rate of 0.1 V/s for the 1st (black), 100th (blue) and 1000th (pink) cycle (based on the Mn_3O_4 mass).

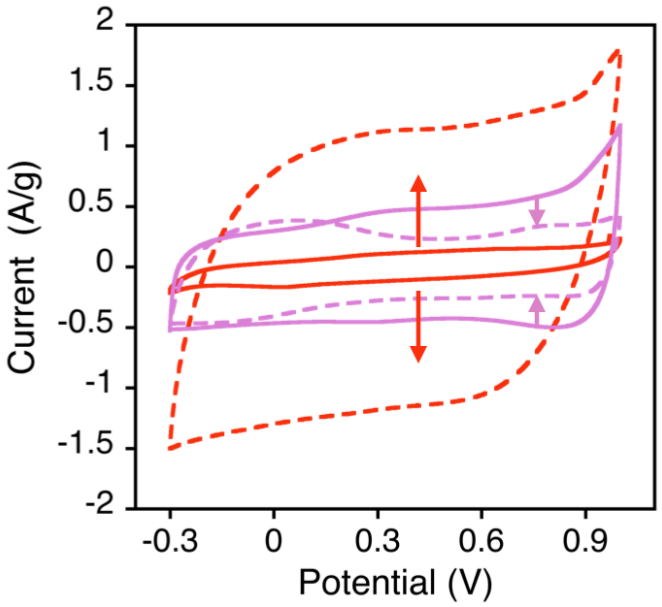

Figure 16: Comparison of the cyclic voltammograms of $Mn_{12}Ac$@MWNT (red) and Mn_3O_4@MWNT (pink) for the 1st (solid lines) and 1000th cycle (dashed lines) at a constant scan rate of 0.1 V/s. The total weight of the electrode is considered here.[10]

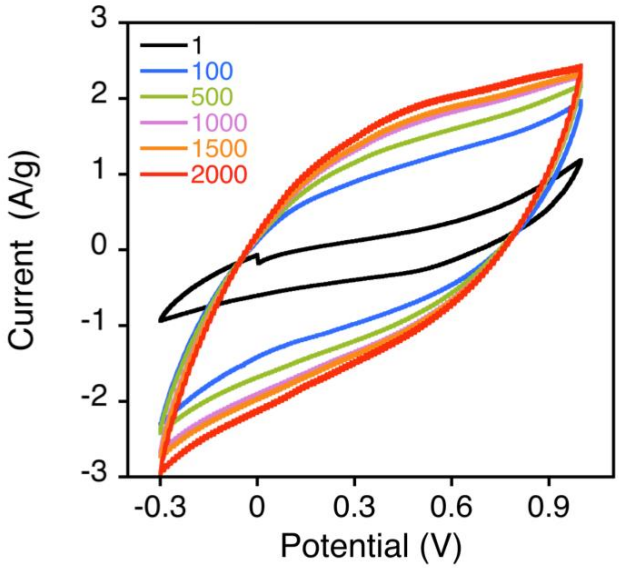

Figure 17: Cyclic voltammograms of $Mn_{12}Ac$@MWNT under acid conditions (aqueous solution of $HClO_4$, pH = 4) at a constant scan rate of 0.1 V/s with increasing cycling (1-2000 cycles) (based on the $Mn_{12}Ac$ mass).

(a)

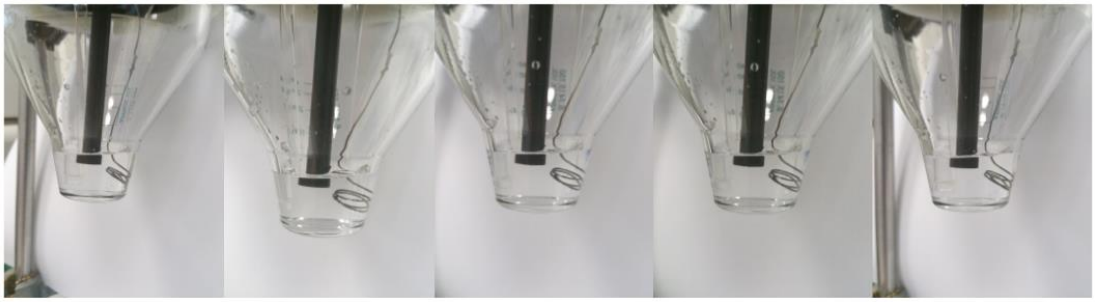

(b)

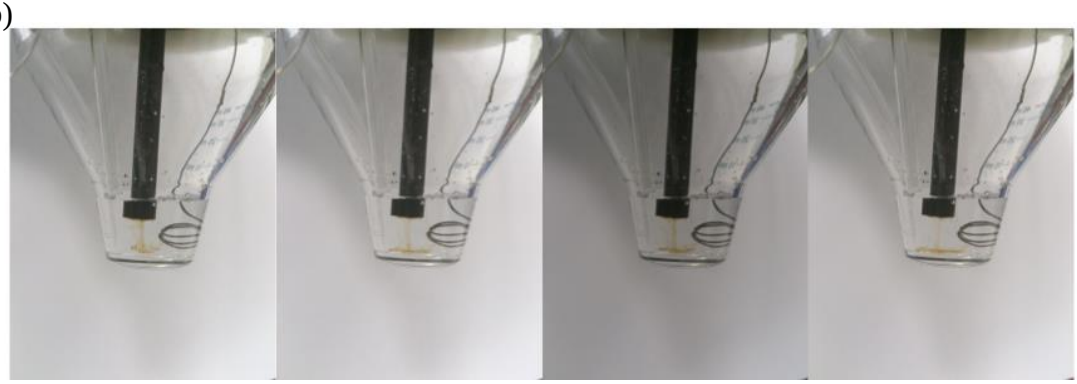

Figure 18: Time series of images for $Mn_{12}Ac$@MWNT (a) and $Mn_{12}Ac$ (b) electrodes with increasing time from left to right under acid conditions (aqueous solution of $HClO_4$, pH = 4).

Dynamics of the Activation Process.

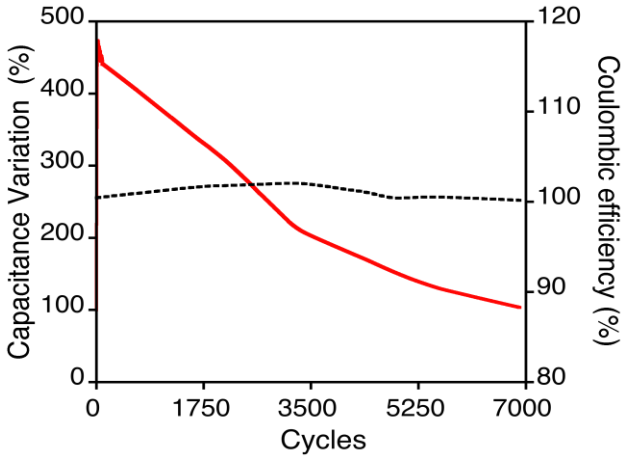

Figure 19: Cycling performance of $Mn_{12}Ac$@MWNT at a current density of 0.8 A/g with no time delay between each charge–discharge cycle is shown in red. Coulombic efficiency (%) as a function of increasing cycle number is shown in black (dashed line).

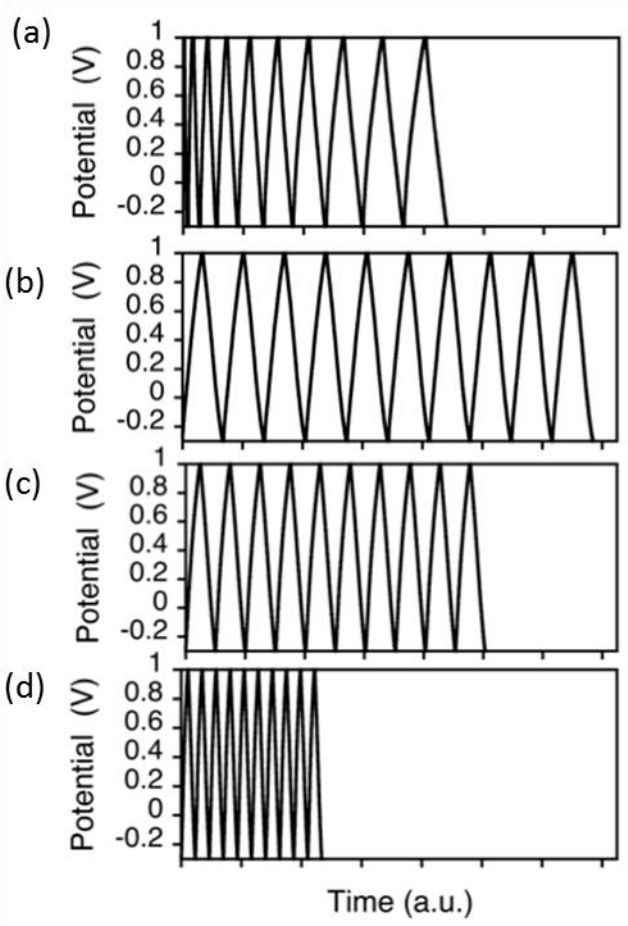

Figure 20: Charge–discharge profiles for $Mn_{12}Ac$@MWNT at a current density of 0.8 A/g for the initial first ten cycles (a) the first ten profiles after 990 cycles (b), 1990 cycles (c) and 4990 cycles (d) under continuous cycling.

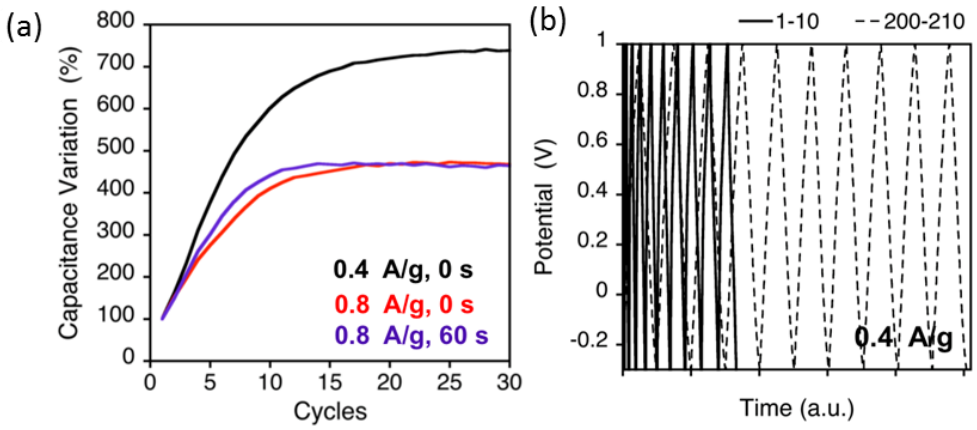

Figure 21: (a) Cycling performance of $Mn_{12}Ac$@MWNT at a current density of 0.4 and 0.8 A/g with (60 s) and without (0 s) time delay between each charge–discharge cycle for the first 30 cycles. The potential range is -0.3 to 1 V (vs. saturated Ag/AgCl). (b) Charge–discharge profiles at a current density of 0.4 A/g for the initial first ten cycles (solid line) and the ten profiles after 200 cycles (dashed line).

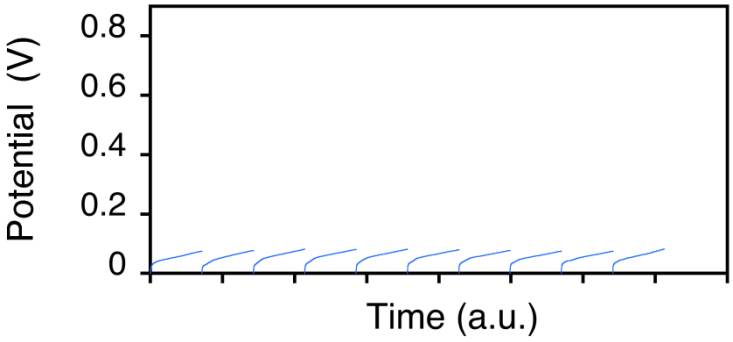

Figure 22: Open circuit potential experiments for a clean glassy carbon electrode.

References

1. X. Pan and X. Bao, Chem. Commun., 2008, 6271–6281.
2. B. Folch, J. Larionova, Y. Guari, C. Guerin, A. Mehdi and C. Reye. J. Mater. Chem., 2004, **14**, 2703–2711.
3. B. Liu, P. S. Thomas, A. S. Ray, and R. P. Williams, J. Therm. Anal. Cal., 2004, **76**, 115-122.
4. M. C. Giménez-López, F. Moro, A. La Torre, C. J. Gómez-García, P. D. Brown, J. Slageren and A. N. Khlobystov, Nat. Commun., 2011, 2:407.
5. M. Soler, K. S. Chandra, D. Ruiz, E. R. Davidson, D. N. Hendrickson and G. Christou, Chem. Commun., 2000, 2417–2418.
6. W. Jeon, M. K. Jin, Y. Kim, D-Y. Jung, B. S. Suh and S. Yoon, Bull. Korean Chem. Soc., 2004, **25,** 7, 1036–1040.
7. R. Bagai and G. Christou, Chem. Soc. Rev., 2009, **38**, 1011–1026.
8. R. Sessoli, H. L. Tsai, A. R. Schake, S. Wang, J. B. Vicent, K. Folting, D. Gatteschi, G. Christou and D. N. Hendrickson. J. Am. Chem. Soc., 1993, **115**, 5, 1804–1816.
9. J. Zang and X. Li, J. Mater. Chem., 2011, **21,** 10965–10969**.**
10. W. Chen, Z. Fan, L. Gu, X. Bao and C. Wang. Chem. Commun., 2010, **46**, 3905–3907.

Appendix V

Templating effect of carbon nanofibers for the in situ synthesis of metal oxide nanoparticles: effect of nanoscale-confinement

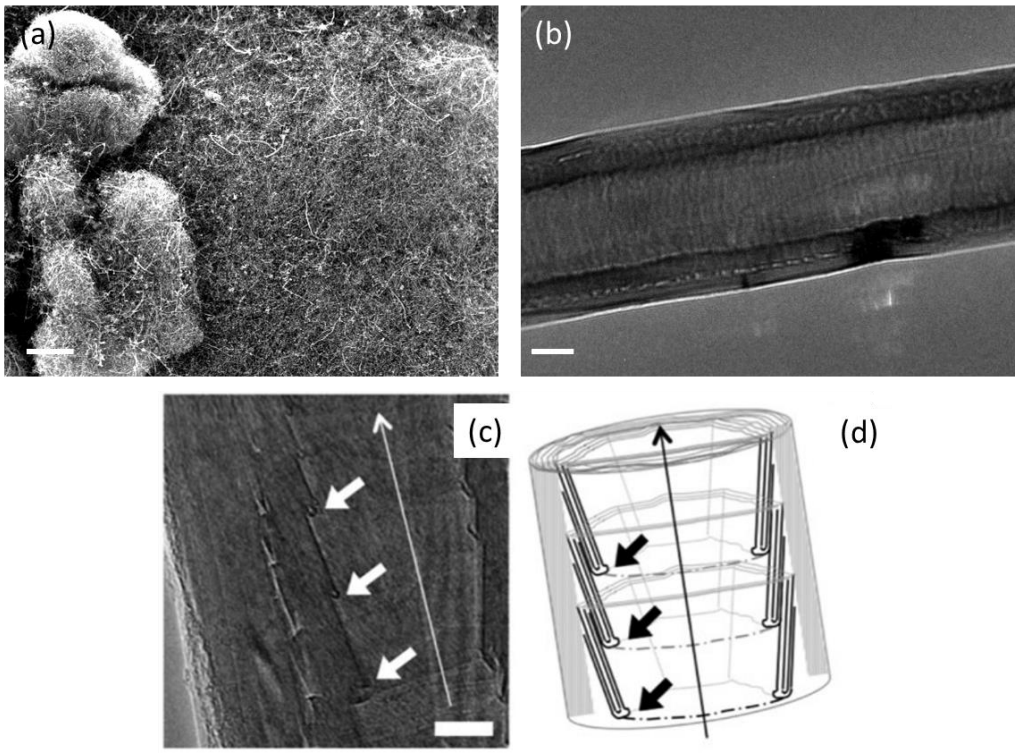

Figure 1. FESEM (a) and HRTEM (b-c) images of CNF at low and high magnification showing their internal corrugated structure (scale bars 25 µm, 100nm and 10 nm, respectively.) Schematic representation of a CNF (d). The long arrow in c and d indicates the main axes of the nanofibers, while the short arrows point to the internal step-edge of the CNF.

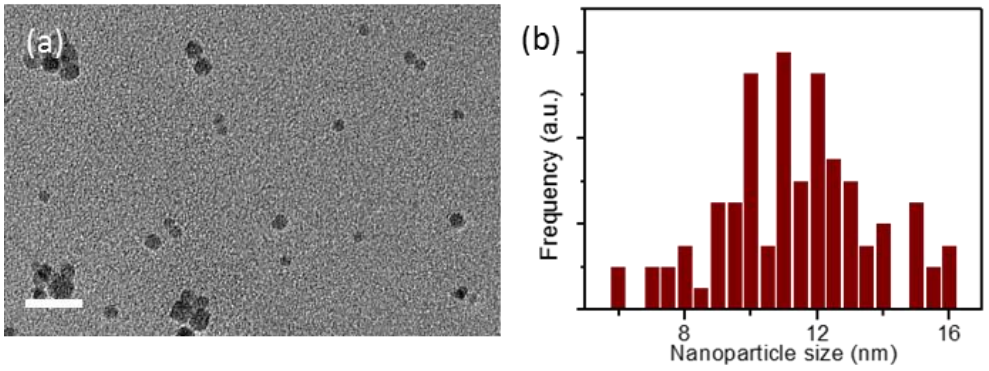

Figure 2. (a) TEM image and (b) nanoparticle size distribution of free-standing Mn_3O_4 NPs, showing an average size of 11 ± 3nm. Scale bar is 20 nm.

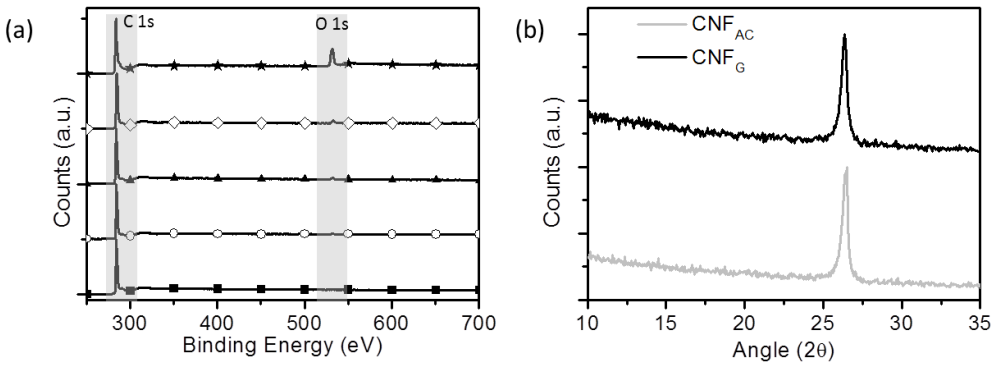

Figure 3. (a) Wide-scan XPS measurement of GWMNTs (square), CNF_G (circle), CNF (triangle), CNF_{AC} (diamond) and CNF_{OX} (star), being the atomic percentage of O (%) 0, 0.4, 1.2, 2 and 11.4, respectively. (b) Despite the superficial functionalization, the structure of both CNF_{AC} and CNF_G remains intact, as observed by TEM in Figure 1 and Figure 2a-b.

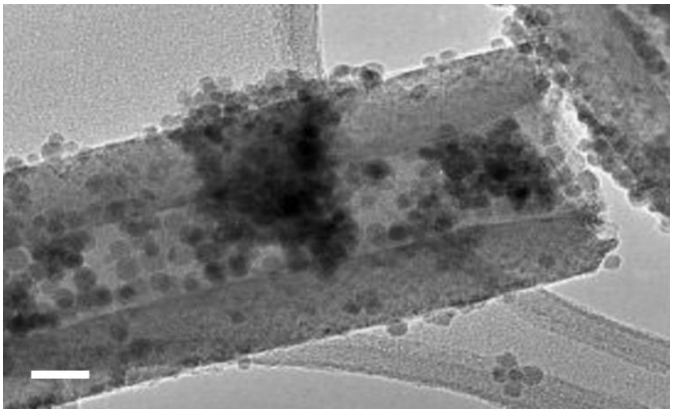

Figure 4. TEM image of Mn_3O_4/CNF_{OX} with an average size of 8± 2 nm. Scale bar is 20 nm.

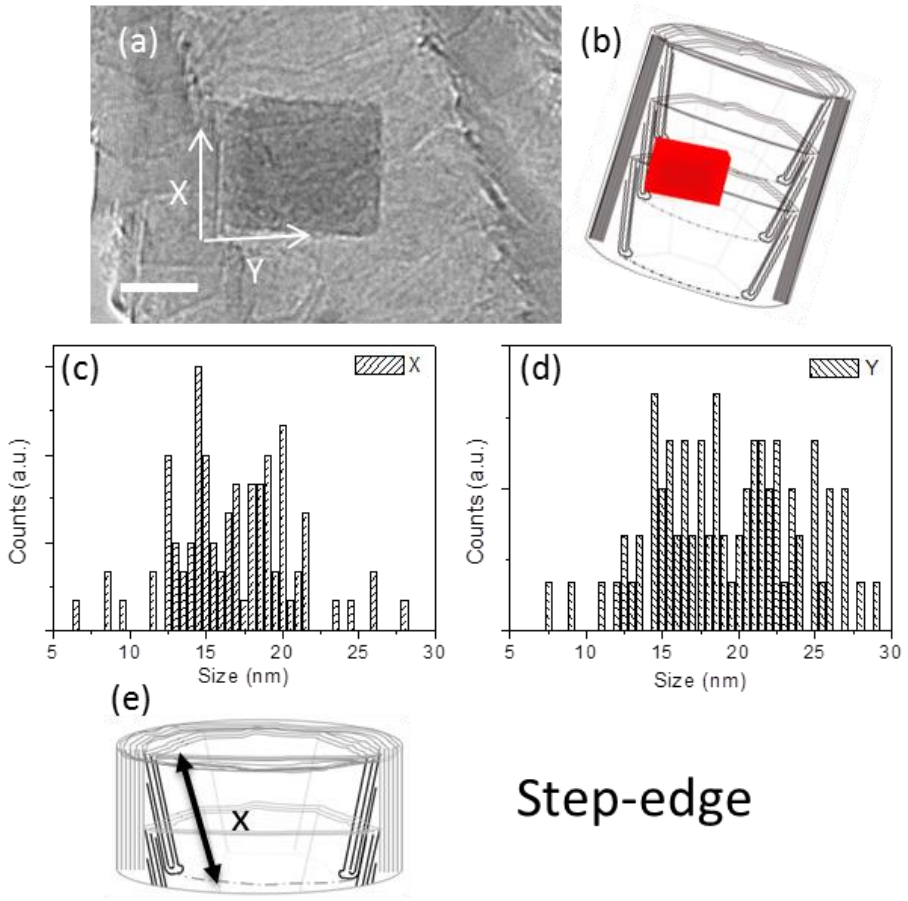

Figure 5. (a) TEM image, (b) schematic representation and (c-d) size distribution (X: 17 ± 4 and Y: 20 ± 5nm) of nanoparticles in Mn_3O_4/CNF_G), showing a good correlation with (e) nanocone length (18 ± 6). Scale bar is 10 nm.

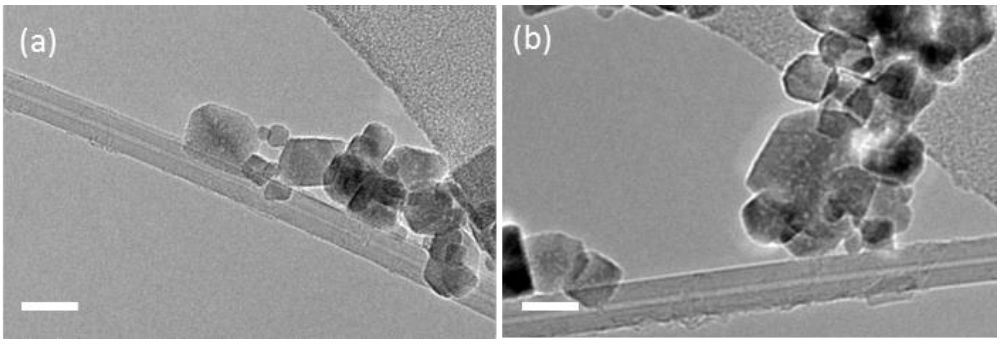

Figure 6. TEM images of Mn_3O_4 NPs synthesized in the presence of GMWNTs (Mn_3O_4/GMWNTs), showing a minimum and maximum nanoparticle size of 5 and 47 nm, respectively. Scale bars are 20 nm.

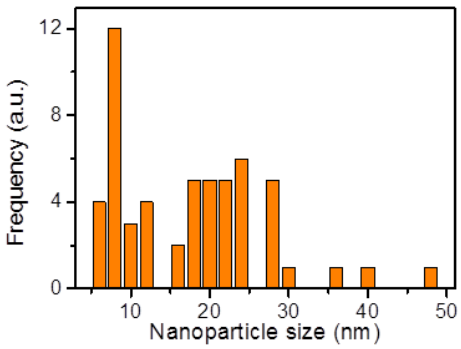

Figure 7. Histogram of Mn_3O_4 NPs synthesized in the presence of GMWNTs (Mn_3O_4/GMWNTs).

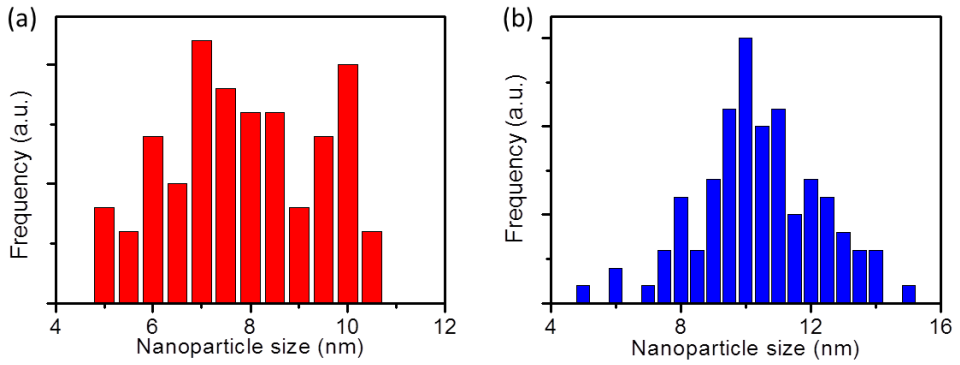

Figure 8. Nanoparticle size distribution of (a) Mn_3O_4/CNF_{AC} (red) and (b) Mn_3O_4@CNF (blue), being the average diameter 8 ± 2 and 10 ± 2 nm respectively.

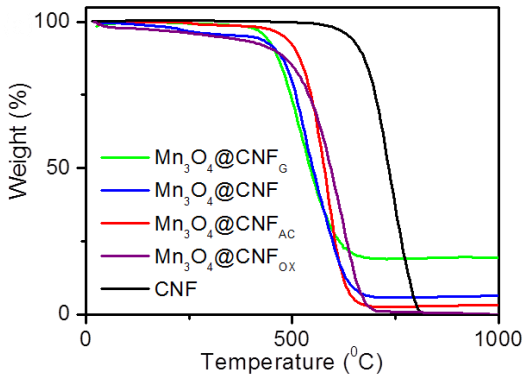

Figure 9. Thermogravimetric analysis at 5^0C/min in air of purified hybrids: Mn_3O_4@CNF_G (green), Mn_3O_4@CNF (blue), Mn_3O_4@CNF_{AC} (red), Mn_3O_4@CNF_{OX} (purple) and pristine CNF (black) with 19.4, 6.4, 3.3 and 0% of Mn_3O_4, respectively in each hybrid material.

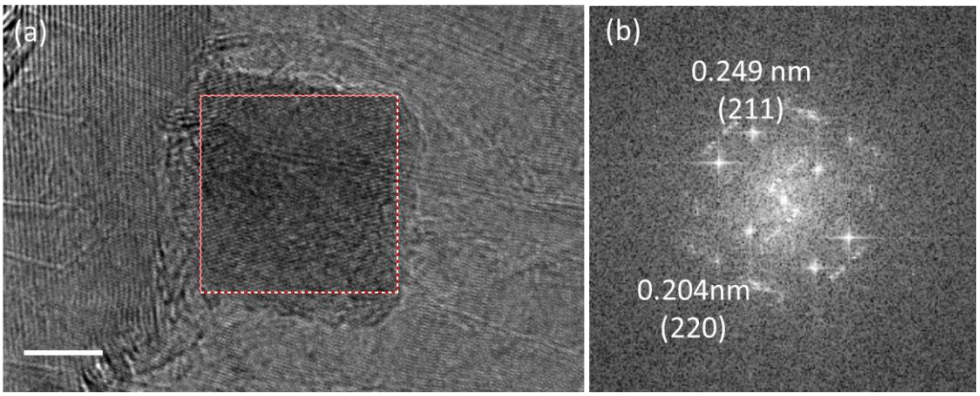

Figure 10. (b) Fourier transform of (a) Mn_3O_4/CNF_G TEM image revealing [211] and [220] planes of Mn_3O_4 phase. Scale bar is 5 nm.

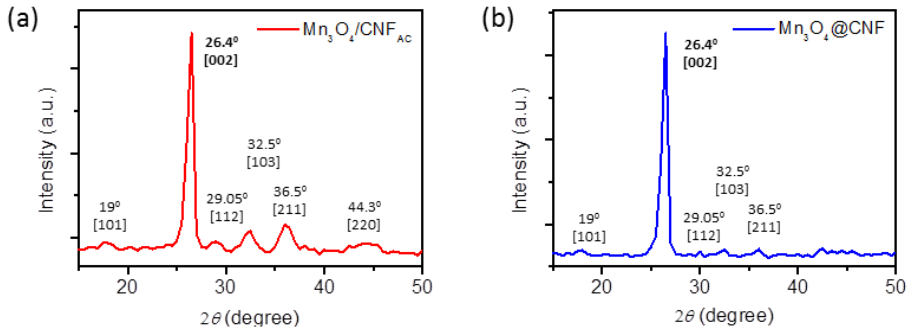

Figure 11. PXRD pattern of Mn_3O_4/CNF_{AC} (red) and Mn_3O_4@CNF (blue), being indexed to tetragonal hausmannite-Mn_3O_4 (JCPDS 24-0734, $I4_1/amd$, a = b = 5.76Å, c = 9.47 Å) even though their small size and their low amount in the composite. Sharp peak at 26^0 correspond to CNF [002].

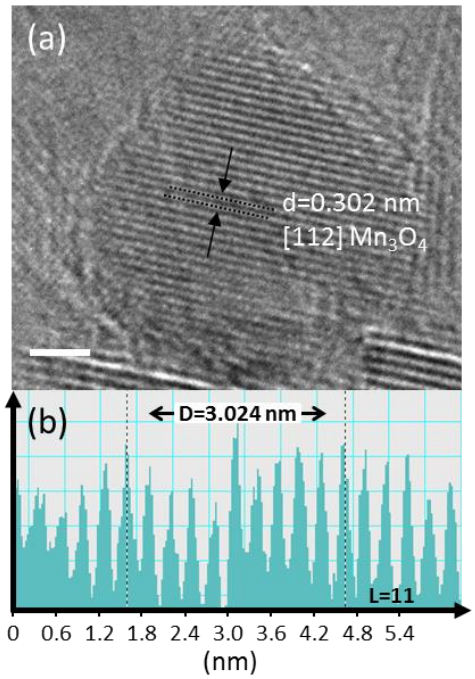

Figure 12. (a) HRTEM image of Mn_3O_4@CNF, resolving the nanoparticles interplanar spacing of 0.302nm ([112] plane of Mn_3O_4). (b) Interplanar distance (d) is calculated using the equation: $d = D / (L\text{-}1)$, where D and L stand for the total distance and the numbers of layers, respectively, as measured in the line profiles (a) of the HRTEM image. Scale bars is 2 nm.

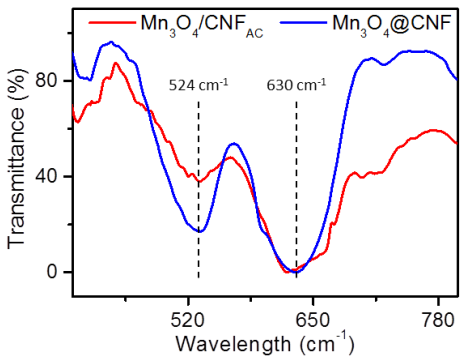

Figure 13. FT-IR spectrum for Mn_3O_4/CNF_{AC} (red) and Mn_3O_4@CNF (blue). In the region from 650 to 500 cm^{-1}, two absorption peaks were observed at 630 and 524 cm^{-1}, which may be associated with the coupling of the Mn-O stretching modes of tetrahedral and octahedral sites.

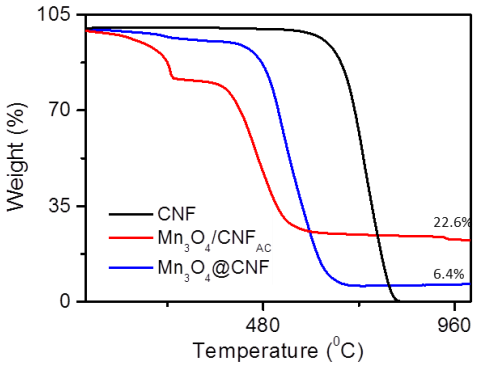

Figure 14. TGA of CNF (black), Mn_3O_4/CNF_{AC} (red) and Mn_3O_4@CNF (blue) at 5^0C/min in air. Surfactant loss is observed between 200-300^{0}C while the second loss is attributed to carbon oxidation. The remaining material is identified as Mn_3O_4 content, being 22.6 and 6.4% for Mn_3O_4/CNF_{AC} and Mn_3O_4@CNF respectively. It is worth noticing that manganese has a catalytic effect on the oxidation of carbon.

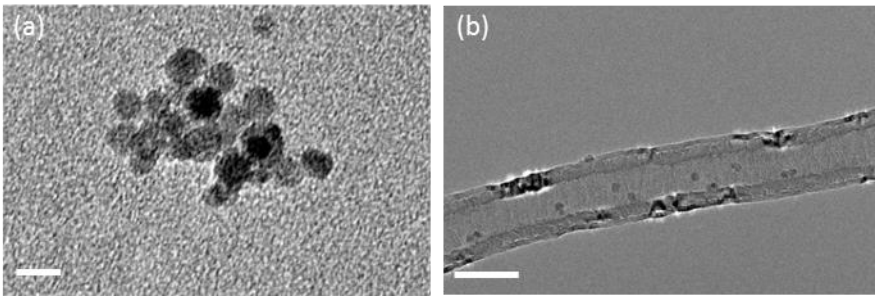

Figure 15. TEM images of preformed s-Mn_3O_4 NPs (a), and s-Mn_3O_4@CNF_{AC} composite (b), where nanoparticles are encapsulated inside CNF_{AC}. Scale bars are 10 (a) and 50 nm (b).

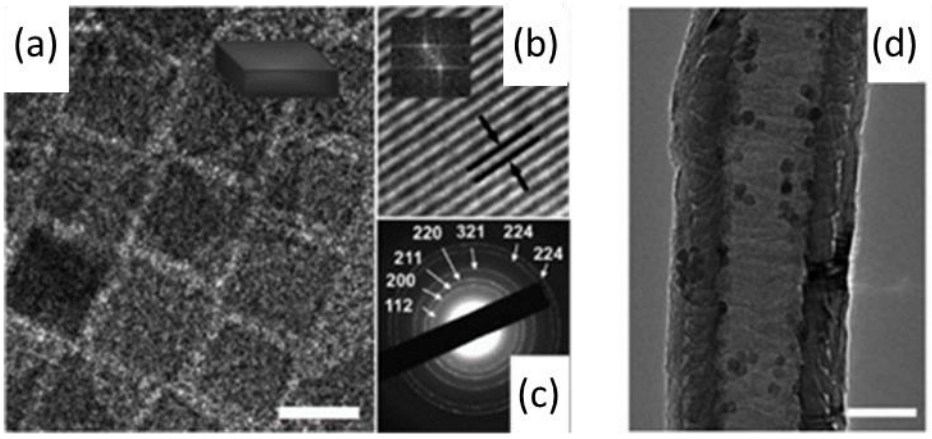

Figure 16. TEM images of (a) a close-packed array of b-Mn_3O_4 NPs (with size dimensions of 11.4 ± 1.6 nm and 10.1 ± 1.5 nm and thickness of 5.7 ± 0.9 nm). (b) lattice planes imaged parallel to the edge of a Mn_3O_4 NP with a d-spacing value of 0.288 nm (200). (c) Selected area electron diffraction (SEAD) pattern showing clear diffraction rings indexed to the Mn_3O_4 spinel structure. (d) TEM image of b-Mn_3O_4@CNF composite where nanoparticles are adsorbed on the step-edge of CNF. Scale bars are 10 (a) and 40 nm (d).

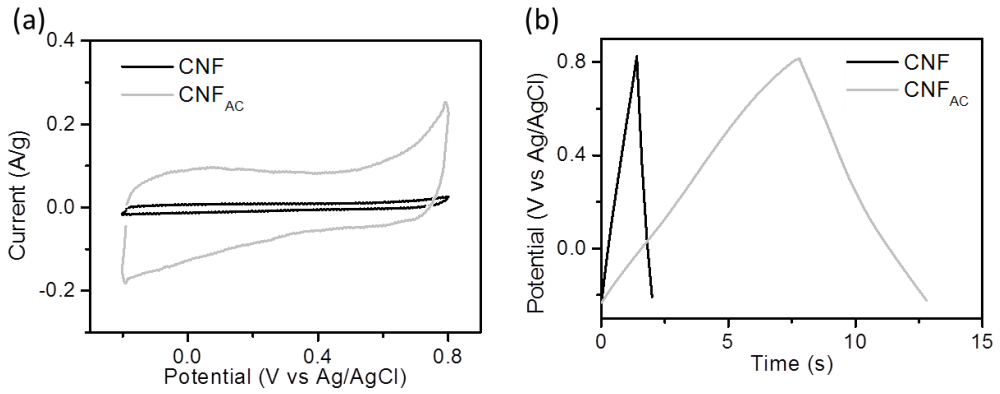

Figure 17. Cyclic voltammogram at 0.05V/s (a) and galvanostatic charge-discharge cycles (b) of CNF (black) and CNF_{AC} (grey) at 0.5 A/g, being their specific capacitance 0.3 and 2.4 F/g respectively.

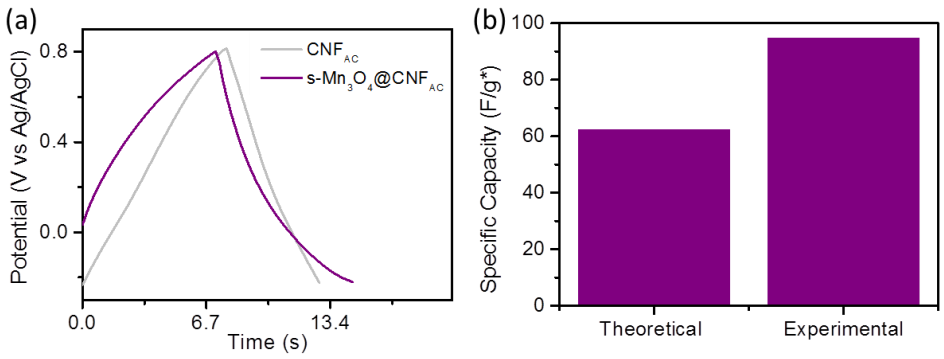

Figure 18. Charge-discharge cycle (a) of s-Mn_3O_4@CNF_{AC} (purple) with respect to CNF_{AC} (grey). Synergy (b) of 1.5, being the expected and experimental specific capacitance of the composite 62.2 F/g* (or 2.36 F/g) and 94.7 F/g* (or 3.6 F/g, having a 3.8% of Mn_3O_4) respectively.

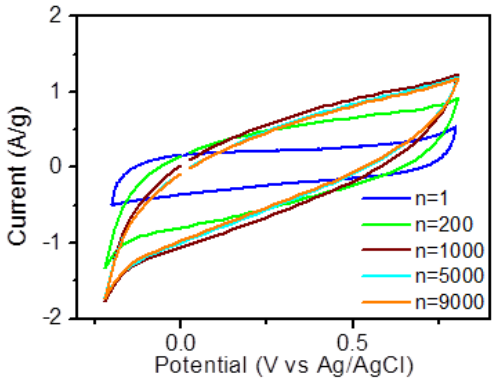

Figure 19. Cyclic voltammogram of Mn_3O_4@CNF at 0.05V/s in 2M KCl during 9 000 cycles.

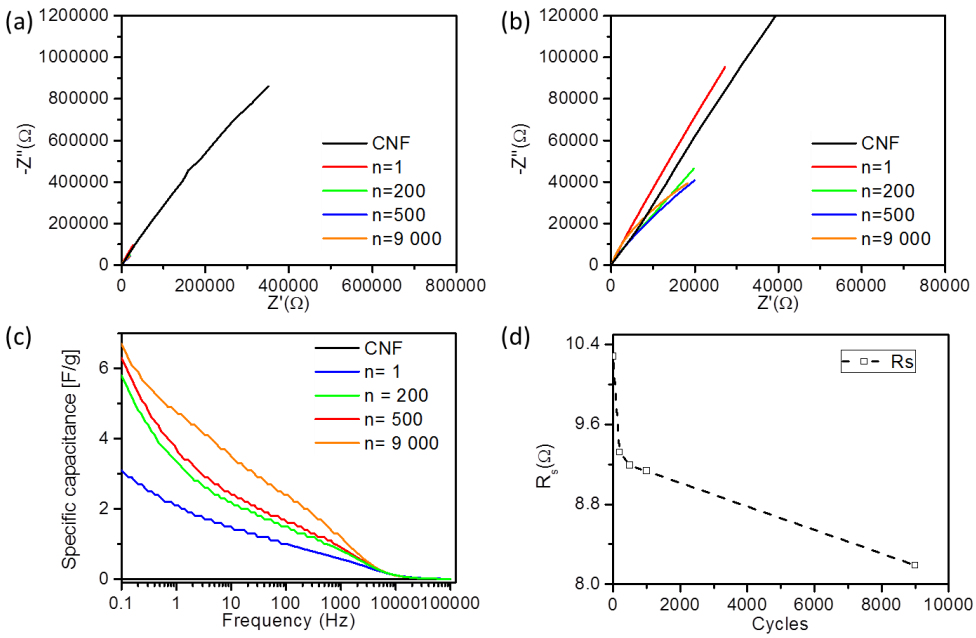

Figure 20. (a,b) Nyquist plot of initial Mn_3O_4@CNF (blue) and after different cycles at 0.05V/s (200, 500 and 9000) with respect to CNF (black). (c) Specific capacitance (calculated using equation 5) vs frequency and (d) solution resistance (R_s) over cycling, showing all a noticeable improvement on the electrochemical performance over cycling.

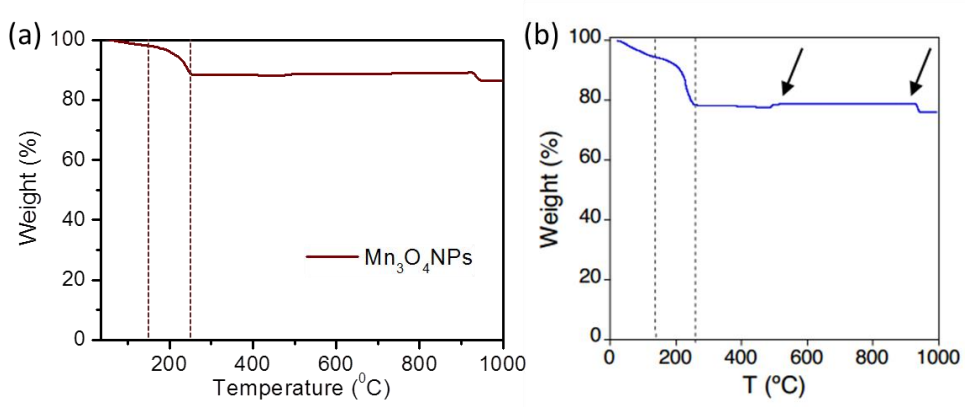

Figure 21. Thermal gravimetric analysis of (a) s-Mn_3O_4 and (b) b-Mn_3O_4 NPs at 5^0C/min in air, having a 12 and 22% surfactant loss respectively in the region 150-250 ^{0}C.

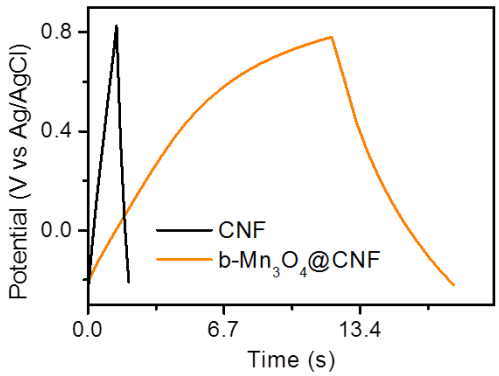

Figure 22. Charge-discharge cycle of b-Mn_3O_4@CNF composite at 0.5 A/g in 2M KCl with a specific capacitance of 3 F/g or 27.3 F/g* (with 11% of Mn_3O_4). It is important to notice that even though the composite has higher loading than Mn_3O_4@CNF hybrid, 11% with respect to 6.4%, its capacitance and, hence, its specific capacitance is smaller, 27.3 with respect to 58.1 F/g*.

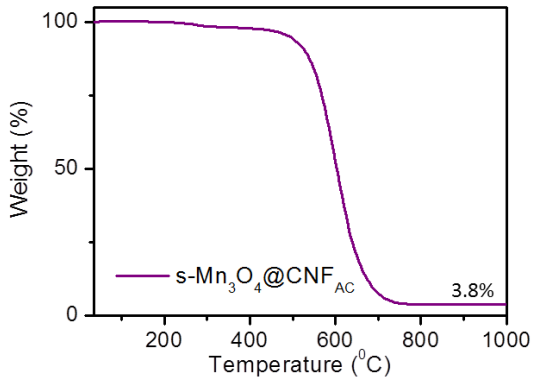

Figure 23. Thermal gravimetric analysis of s-Mn_3O_4@CNF_{AC} in air, showing a 3.8% of Mn_3O_4.

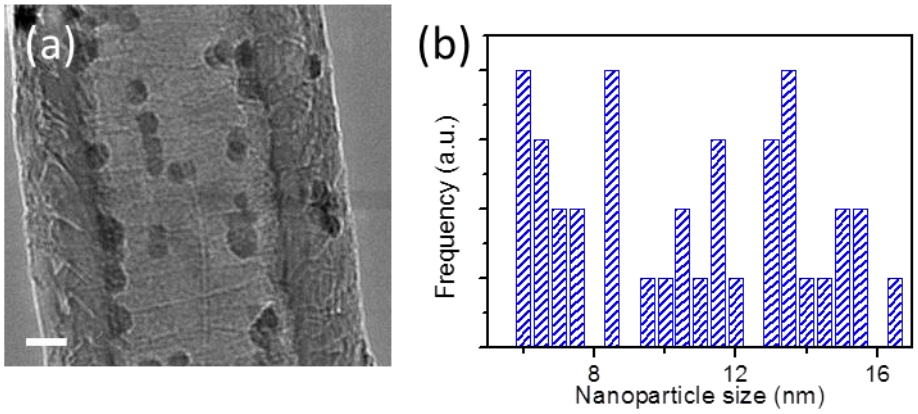

Figure 24. (a) TEM image of Mn_3O_4@CNF after 13 200 cycles at 0.5 A/g, showing no noticeable changes while nanoparticles are still inside CNF. (b) Nanoparticle size distribution with an average size of 11 ± 4 nm. Scale bar is 20 nm.

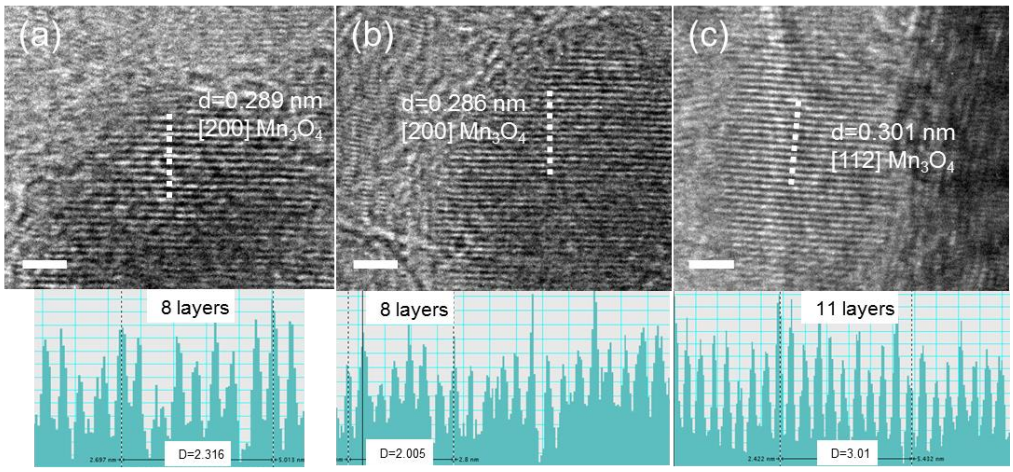

Figure 25. HRTEM images of Mn_3O_4 NPs inside CNF after 13 200 charge-discharge cycles at 0.5 A/g, showing the characteristic inter planar distance of Mn_3O_4. Scale bars are 2 nm.

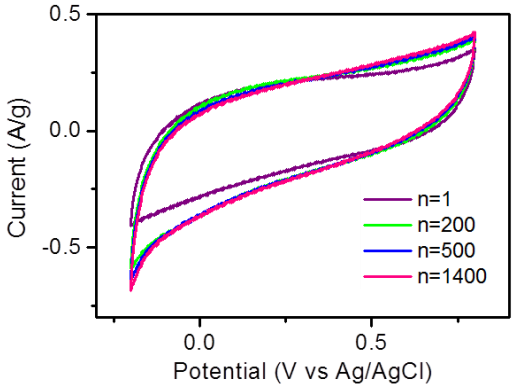

Figure 26. Cyclic voltammogram of Mn_3O_4@CNF in 2M LiCl at 0.05V/s shows high capacitance retention for 14 000 with a slightly capacitance increment.

	NPs Loading	Capacitance (F/g hybrid)		Specific Capacitance (F/g Mn_3O_4)		Synergy
	$\%Mn_3O_4$	M.	Exp.	M.	Exp.	
Mn_3O_4/CNF_{AC}	22.6	17.8	2.1	78.8	9.2	**9**
Mn_3O_4@CNF	6.4	3.7	0.3	58.1	5.3	**11**

Equation 1:

Synergy = Specific capacitance (Measured) / Specific capacitance (Expected)

Equation 2:

Expected capacitance = $(\%Mn_3O_4 * C_{NPs})/100 + [100-\%Mn_3O_4]/100 * C_{carbon}$

Equation 3:

Capacitance (F/g) = i (A/g) * t_d (s)/ V (V)

Equation 4:

Specific capacitance (F/g*) = Capacitance (F/g) * 100/ $\%Mn_3O_4$

Table 1. Calculation of synergy of metal carbon hybrid materials. Synergy effect is the relation between the measured (M.) versus the expected (Exp.) specific capacitance for the hybrid material (equation 1). To do so, the theoretical capacitance was calculated using equation 2, being 0.9, 0.3 and 2.4 F/g specific capacitance of building blocks at 0.5 A/g ($C_{NPs,}$ C_{carbon}: CNF and CNF_{AC}) respectively and $\%Mn_3O_4$ the loading of manganese oxide in the hybrid (obtained after heating the sample in air at 1 000^{0}C (Appendix V, Figure 9). It is important to mention that specific capacitance both with respect the hybrid (equation 3) and with respect to the amount of manganese oxide (equation 4) was calculated. The latter helps the comparison of material with different nanoparticle shape or size. C_{carbon} for the specific capacitance of either CNF (for Mn_3O_4@CNF) or CNF_{AC} (for Mn_3O_4/CNF_{AC}), i stands for current during galvanostatic discharge measurement, t_d for discharge time and V for voltage window.

Appendix VI

Stabilisation of low crystalline Prussian Blue Analogue by internal charge transfer

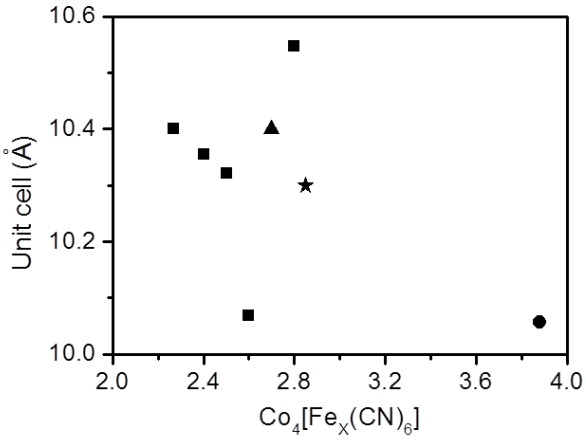

Figure 1. Relationship between the unit cell of CoHCF, which is related to the Co^{III}/Co^{II} ratio, with respect to the Fe content, which determines the $[Fe(CN)_6]$ vacancies, showing the difficulty to control simultaneously the number of vacancies and the oxidation state of Co centres during the synthesis. Thus, the number of vacancies as well as the Co^{III}/Co^{II} ratio is different in all of the examples. It is important to mention that the values are calculated from the literature (square[1], triangle[2], star[3] and circle[4]).

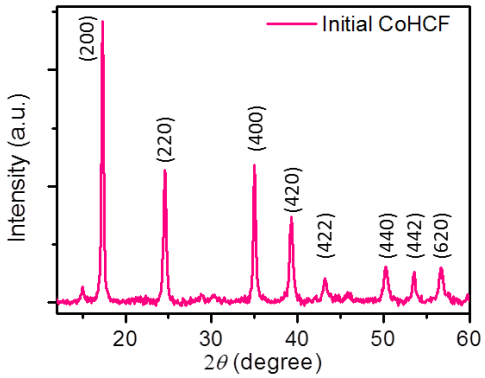

Figure 2. PXRD of CoHCF crystal. The indexation of a face-centred cubic unit (equation 1) leads to a unit cell parameter of $\bar{a}$ = 10.26 ± 0.01 Å, being the four most intense diffraction peaks at 17.30 (200), 24.40 (220), 35 (400) and 39.20 (420).

$$d_{hkl} = \frac{a}{\sqrt{h^2+k^2+l^2}} \quad \text{(Equation 1)}$$

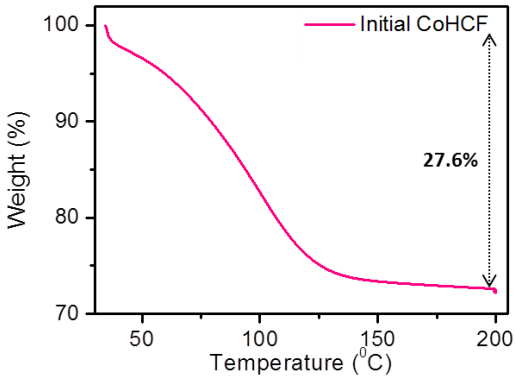

Figure 3. A total loss of 27.6% weight (associated to water molecules) was observed after heating the initial CoHCF crystal up to 200^{0}C in nitrogen atmosphere with a ramp of 5^{0}C/min.

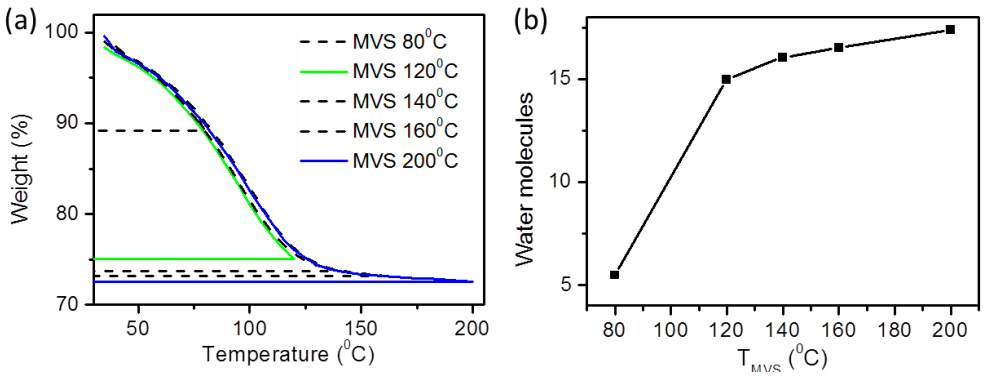

Figure 4. (a) TGA of initial CoHCF in nitrogen with a ramp of 5^{0}C/min, showing that the water content in the resulted MVS can be selectively determined in the range of RT to 200^{0}C by controlling the maximum achieved temperature. (b) Based on weight loss from Figure S4.a, the number of water molecules is calculated for every MVS.

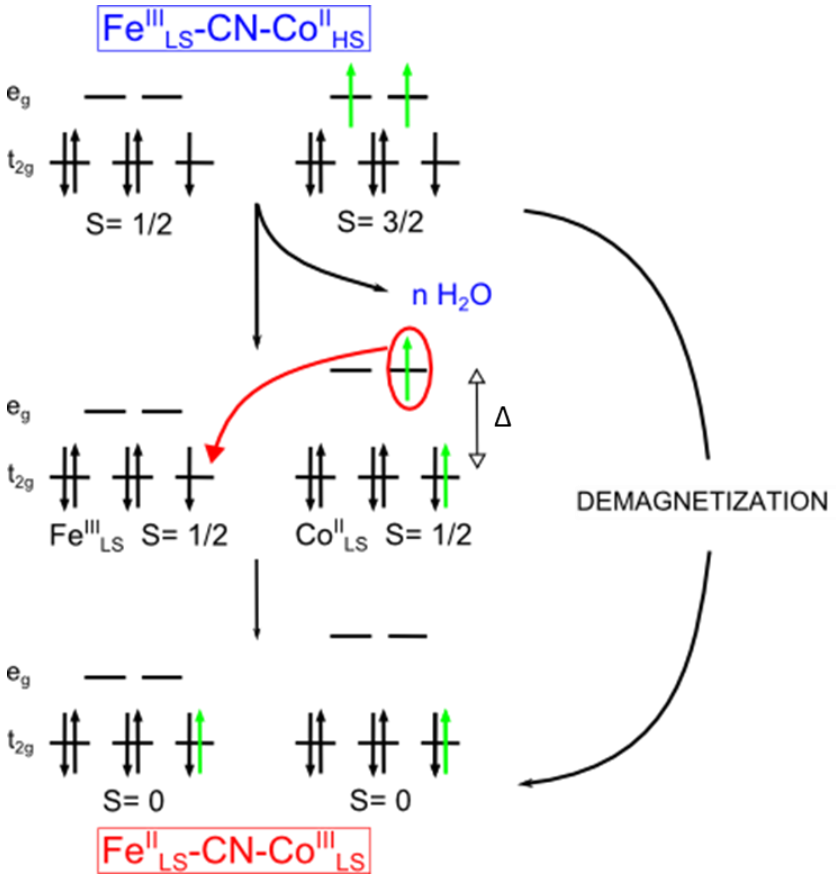

Figure 5. Schematic representation of the electronic configuration of Fe-Co pair and the mechanism associated to the internal charge transfer which produces the demagnetization of the sample.

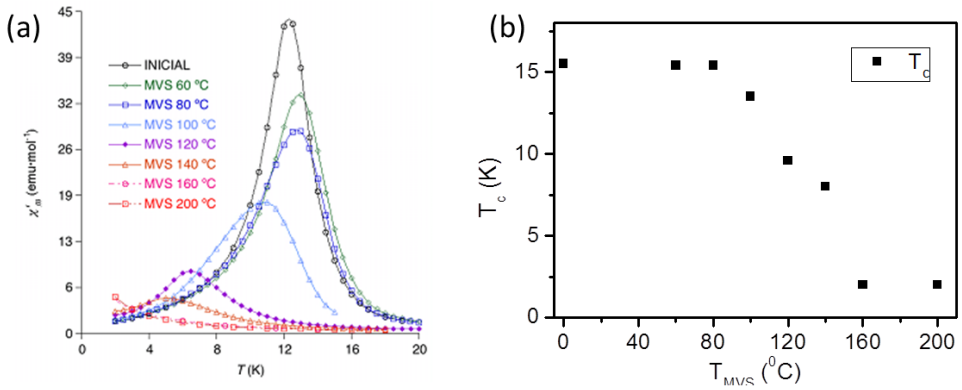

Figure 6. (a) Magnetic susceptibility in phase as a function of the temperature of MVS systems and initial CoHCF. (b) Curie temperature (T_c) of MVS and initial CoHCF (0^0C).

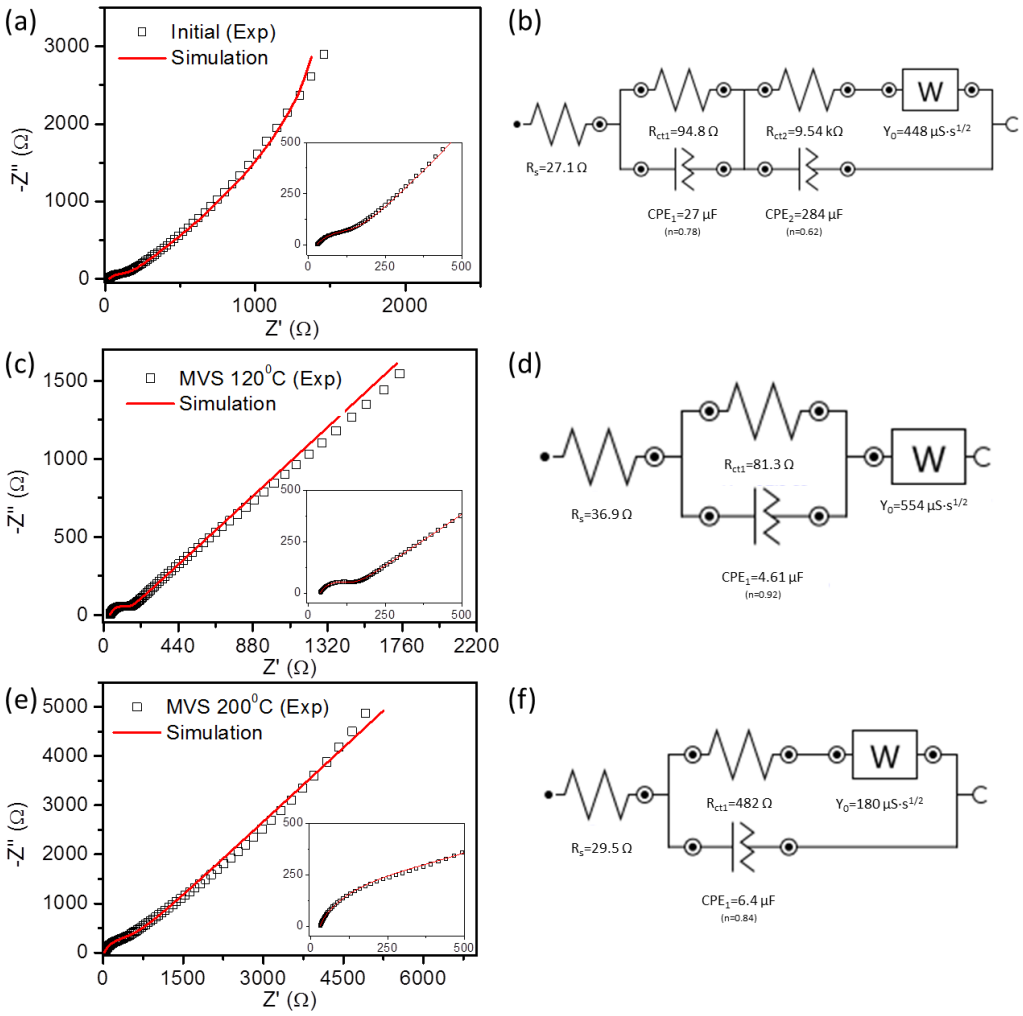

Figure 7. Nyquist plot of (a) initial CoHCF, (c) MVS 120^{0}C and (e) MVS 220-^{0}C with respect to the simulated calculation (red line) based on the proposed electrical circuits (b,d and f). x^2 for initial CoHCF, MVS 120^{0}C and MVS 220-^{0}C are 0.02, 0.03 and 0.08, respectively, showing a good fitting with experimental results.

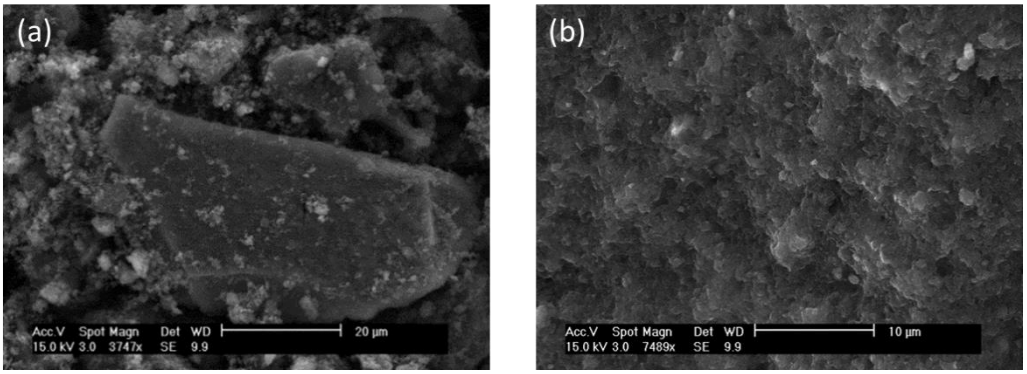

Figure 8. Scanning electron images of (a) CoHCF/GF composite and (b)CoHCF@GF hybrid using the secondary electron detector, which reveals the samples' surface topography.

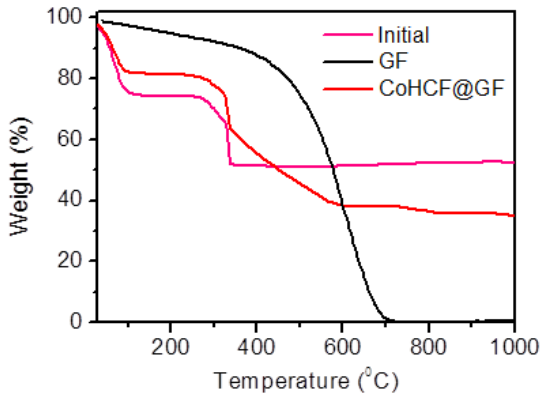

Figure 9. TGA of in situ CoHCF@GF hybrid (red) with respect to initial CoHCF (pink) and graphene flakes (black) in air with a ramp of 5^0C/min. In contrast to initial CoHCF, a 25.5% weight loss in the range of 350 to 600^0C in air is observed for the hybrid materials and it is assigned to the carbon nanostructure. Then, the in situ CoHCF@GF hybrid has a GF/CoHCF ratio of 25.5%/74.5%. It is important to mention that same ratio was employed for the fabrication of CoHCF/GF composite.

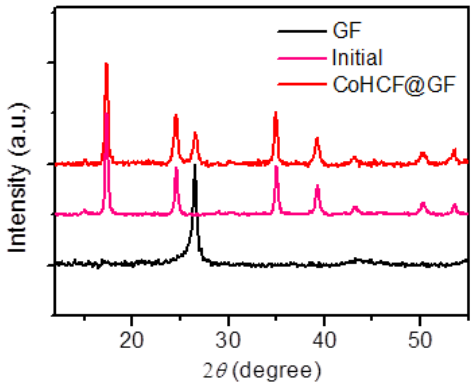

Figure 10. XRD diffraction pattern of in situ CoHCF@GF hybrid (red) with respect to initial CoHCF (pink) and graphene flakes (black). In contrast to initial CoHCF, a new peak at 26.5^0 is observed for the hybrid materials and it is assigned to the carbon nanostructure. Unit cell parameter of CoHCF in CoHCF@GF hybrid was calculated using the four most intense diffraction peaks (i. e. 17.28 (200), 24.54 (220), 34.93 (400) and 39.27 (420): $\bar{a}$ = 10.255 ± 0.007 Å (equation 1).

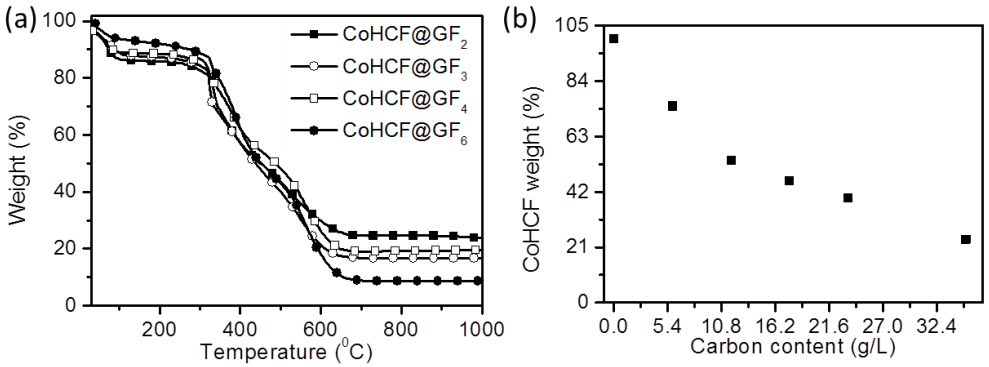

Figure 11. (a) TGA of in situ CoHCF@GF_x hybrid (x=2 to 6) in air with a ramp of 5^0C/min. (b) As expected, CoHCF weight decreases (from 100 to 24%) or, in other words, the amount of carbon in the hybrid increases as the amount of carbon during the synthesis increases from 0 in CoHFC to 76% in CoHCF@GF_6 (35.3g/L).

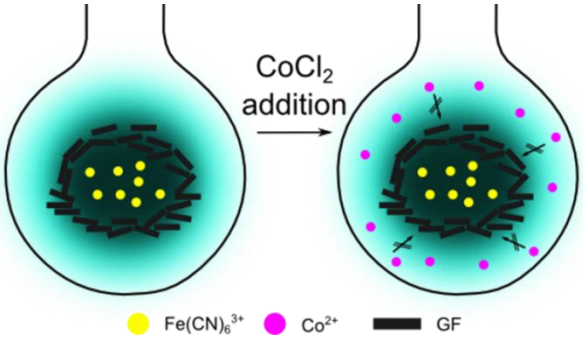

Figure 12. Schematic representation of initial high concentration of carbon nanostructure (GF) during the in situ synthesis of CoHCF@GF hybirds, which blocks the interaction of Co^{2+} with $Fe(CN)_6^{3-}$.

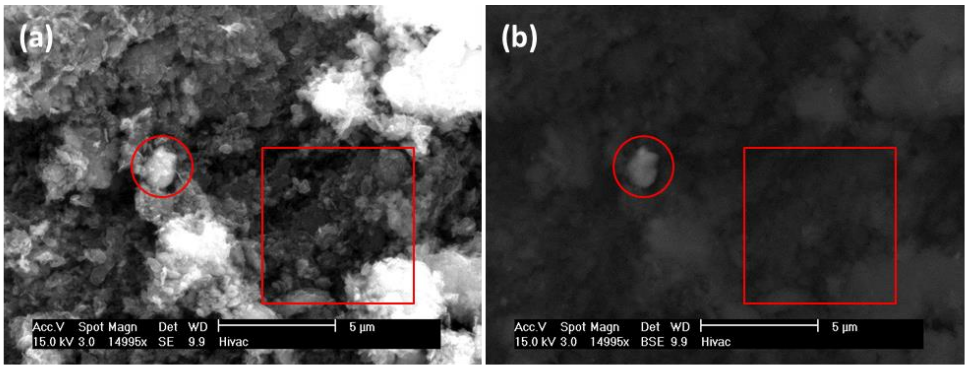

(c)

Sample	Fe Atomic %	Co Atomic%
Crystal (Circle)	3.43	-
Hybrid (Square)	0.37	0.34

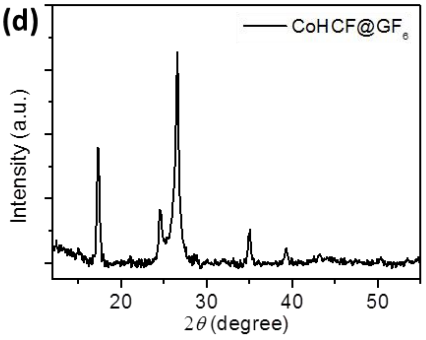

Figure 13. FESEM images of CoHCF@GF_6 using (a) secondary electron and (b) back-scattering electron. (c) EDS analysis shows that crystal structure (red circle) is mainly formed of iron while both iron and cobalt is observed in the rest of the sample (red rectangular). As no peaks corresponding to iron oxide whereas only the Prussian blue XRD pattern is identified (d), it is proposed that both FeHCF and CoCHF form the CoHCF@GF_6 hybrid.

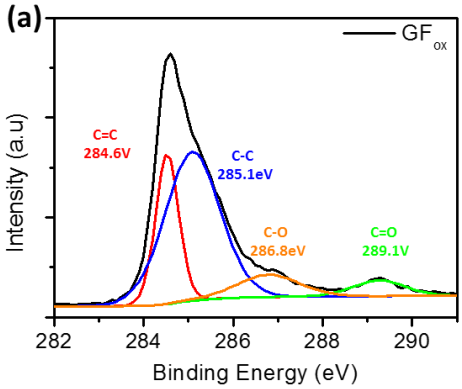

Figure 14. C 1s high-resolution XPS measurement of GF fitted with four components: nonoxygenated sp^2 C (284.6 eV), nonoxygenated sp^3 C (285.1eV), hydroxyl groups (286.8 eV) and carboxyl groups (289.1 eV). The chemical functionalization of the graphene flake surface enables the proposed interaction with iron cations.

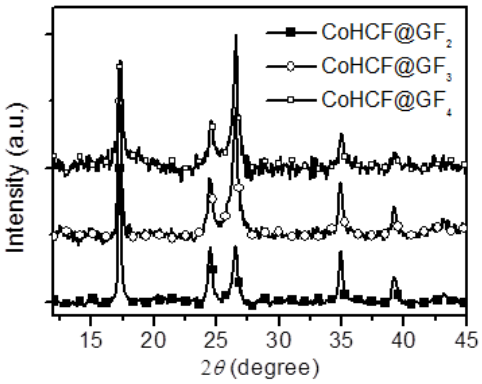

Figure 15. XRD diffraction pattern of in situ CoHCF@GF_x hybrid (x=2 to 4). It is important to notice that carbon peak at 26.5^0 increases with the increase of carbon content, being in agreement with TGA measurements (**Figure 10)**. Unit cell parameter of CoHCF in CoHCF@GF_x hybrid (x=2 to 4) was calculated using the four most intense diffraction peaks, leading to a unit cell parameter of $\bar{a}$ = 10.250 ± 0.004 Å, $\bar{a}$ = 10.242 ± 0.006 Å and $\bar{a}$ = 10.227 ± 0.006 Å, respectively (equation 1).

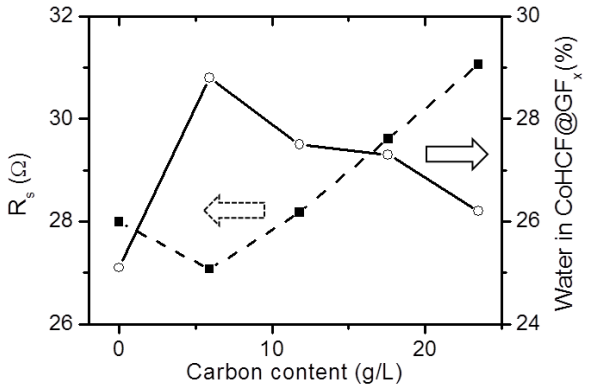

Figure 16. Solution resistance (R_s, dash line) from EIS measurements in the high frequency region and the water content (solid line) from TGA experiments are represented with respect to the carbon content during the in situ synthesis of CoHCF@GF$_x$ hybrids (CoHCF@GF (5.9 g/L), CoHCF@GF$_2$ (11.8 g/L), CoHCF@GF$_3$ (17.6 g/L), CoHCF@GF$_4$ (23.5 g/L) and CoHCF@GF$_6$ (35.3 g/L)). Initial CoHCF (carbon content = 0) is considered for the sake of comparison.

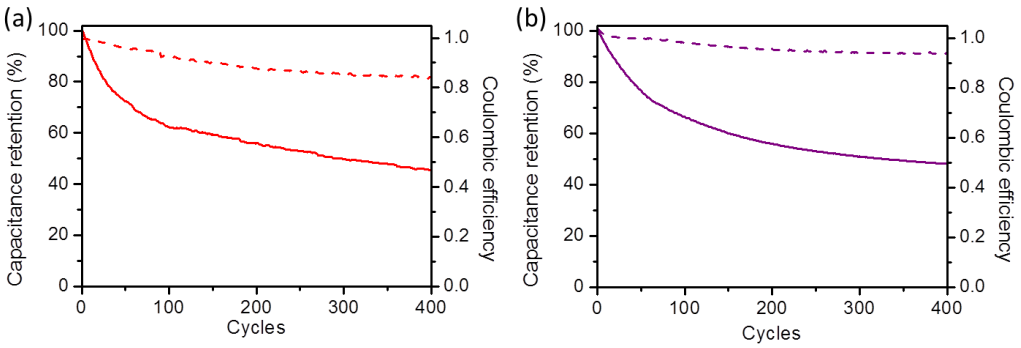

	Co/ Fe ratio	ΔE (mV)	E_0 (V)	Δi	R_s (Ω)	Y_0 (mS·s$^{1/2}$)	H_2O (%)	Cap. Ret. (%)
CoHCF@GF	1.47	97	1.06	1.11	30.8	1.19	25.07	45.4 (0.84)
CoHCF@GF$_4$	1.41	44	1.07	1.06	28.2	9.92	29.06	48.2 (0.94)

Figure 17. Capacitance retention (solid line) and coulombic efficiency (dash line) of (a) CoHCF@GF and (b) CoHCF@GF$_4$ after 400 cycles at 1A/g. The chemical composition and electrochemical parameters of CoHCF@GF and CoHCF@GF$_4$ are summarized in the table below, showing the capacitance retention after 400 cycles as well as the coulombic efficiency (in brackets).

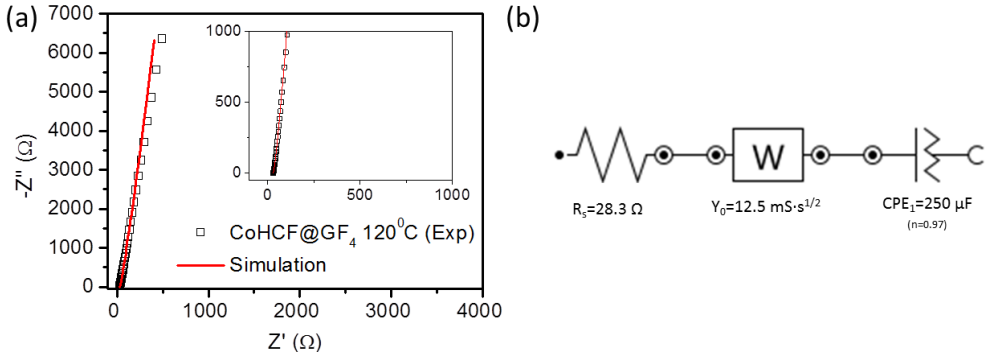

Figure 18. Nyquist plot of (a) CoHCF@GF_4 120^0C with respect to the simulated calculation (red line) based on the proposed electrical circuits (b). X^2 CoHCF@GF_4 120^0C is 0.002, showing a good fitting with experimental results.

References

1. L-H. Shi, T. Wu, M-J. Wang, D. Li, Y-J. Zhang and J-H. Li, Chin. J. Chem., 2005, **23**, 149-154.
2. A. Bleuzen, C. Lomenech, V. Escax, F. Villain, F.; Varret, C. Cartier dit Moulin and M. Verdaguer, J. Am. Chem.Soc. 2000, **122**, 6648-6652.
3. M. Berretoni, M. Giorgetti, S. Zamponi, P. Conti, D. Ranganatham, A. Zanotto, M. L. Saladino and E. Caponeti, J. Phys. Chem. C, 2010, **114**, 6401-6407.
4. T. Matsuda, J. Kim and Y. Moritomo, J. Am. Chem. Soc., 2010, **132**, 12206-12207.